Capturing the hot and violent Universe:

Multiwavelength studies of Galactic TeV-discovered Supernova remnant shells and of optically-selected galaxy clusters

Dissertation
der Mathematisch-Naturwissenschaftlichen Fakultät
der Eberhard Karls Universität Tübingen
zur Erlangung des Grades eines
Doktors der Naturwissenschaften
(Dr. rer. nat.)

vorgelegt von
Nhàn Thanh Stamer
aus Dak Lak, Vietnam

Tübingen
2025

Gedruckt mit Genehmigung der Mathematisch-Naturwissenschaftlichen Fakultät der Eberhard Karls Universität Tübingen.

Tag der mündlichen Qualifikation:	28.03.2025
Dekan:	Prof. Dr. Thilo Stehle
1. Berichterstatter:	Prof. Dr. Klaus Werner
2. Berichterstatter:	Dr. Gerd Pühlhofer

Declaration

I hereby declare that the thesis I submit for my doctorate with the title: "Capturing the hot and violent Universe: Multiwavelength studies of Galactic TeV-discovered Supernova remnant shells and of optically-selected galaxy clusters" is my own independent work, that I used only the sources and resources cited and have clearly indicated all content adopted either word-for-word or in substance. I declare that the University of Tübingen's guidelines to ensure good academic practice (Senate decision of 25.5.2000) have been observed. I solemnly swear that this information is true and that I have not concealed any relevant information. I am aware that making a false declaration is punishable by a fine or by a prison term of up to three years.

Date

Signature

Abstract

Supernova remnants (SNRs) and galaxy clusters represent the end points of stellar and cosmic evolution, respectively. They are formed via some of the most violent processes in the Universe, and play crucial roles in shaping the dynamics of galaxies and the Universe at large.

SNRs are the expanding structures left behind by supernova explosions. The explosion drives a shock wave outward, sweeping up and heating the surrounding interstellar medium (ISM). The interplay between the (forward and reverse) shocks, the ISM, and the ejected stellar material gives rise to many important astrophysical and astrochemical phenomena. These remnants therefore serve as natural laboratories for studying extreme physics processes, including the origin of cosmic rays (CRs). CRs are relativistic, charged particles, which are believed to be effectively accelerated at SNRs' shock fronts. In this work, we focus on SNR HESS J1534-571 and SNR candidate HESS J1614-518, both identified as strong TeV (tera electronvolt, 10^{12} eV) γ-ray emitters in the H.E.S.S (High Energy Stereoscopic System) Galactic Plane Survey. We investigate the multiwavelength morphology of the sources and the CR acceleration at their sites. Both HESS J1534-571 and HESS J1614-518 exhibit shell-like structures in radio and/or X-ray wavelengths, correlating with their TeV γ-ray shells. This correlation confirms the SNR nature of HESS J1614-518 for the first time and suggests that radiation across wavelengths originates from the same CR populations, allowing us to construct spectral energy distributions (SEDs).

XMM-Newton observations of HESS J1534-571 revealed no significant X-ray emission, placing an upper limit on the non-thermal component and constraining the CR spectra. The SED analysis suggests that a pure leptonic γ-ray production cannot be ruled out. Furthermore, our detection of a 3σ significant Fe Kα emission line with a clumpy morphology indicates an interaction between ambient gas and low energy protons, which are probably associated with the SNR. For HESS J1614-518, we identified non-thermal X-ray emission linked to TeV electron acceleration in a strong magnetic field. Its SED also favors a leptonic mechanism for high energy γ-ray production. Additionally, if the SNR is associated with the compact object J1616-5017, its distance is estimated to be 3.5 kpc. These findings are reported in Nguyen-Dang et al. (2023) and Pühlhofer et al. (2025).

On the one hand, *XMM-Newton* is well-suited for in-depth studies of designated SNR locations, particularly when complemented by archival data from recent observatories such as *Suzaku*. On the other hand, the findings from this study, along with other results reported by the SNR-ISM-Diffuse Emission working group of the SRG/eROSITA collaboration, highlight the exceptional capabilities of this state-of-the-art X-ray observatory in exploring SNRs, from identifying new candidates through survey modes to performing detailed spatial and spectral

analyses. This marks a significant advancement in the field, paving the way for future discoveries to address open questions about CRs and interstellar medium physics.

Galaxy clusters are the largest gravitationally collapsed objects in the Universe, consisting of thousands of galaxies, hot gas in the intracluster medium (ICM), and dark matter, making them detectable across a wide range of wavelengths. They are valuable probes to constrain cosmological parameters and to study large-scale physics. However, samples selected by different methods based on different wavebands may represent distinct populations of clusters. Therefore, it is crucial to understand the characteristics of cluster samples and the impact of selection methods for further cosmological and astrophysical application. This work analyzes the optically selected cluster sample CAMIRA from the Subaru-HSC observations overlapping the eFEDS survey of the SRG/eROSITA telescope. Initially focusing on 43 high-richness ($N > 40$) objects, we expanded the study to 997 clusters with $N > 15$, examining morphology, scaling relations, and selection effects.

In Ota et al. (2023), we found that up to 40% of the high-richness clusters are relaxed, indicating broader morphological diversity in optically selected samples compared to X-ray samples. Scaling relations such as X-ray luminosity - temperature ($L-T$) and X-ray luminosity - mass ($L-M$) for optical clusters exhibit shallower slopes than X-ray samples. In Nguyen-Dang et al. (2025), we report a relaxed fraction of up to 14% for the CAMIRA optical sample in the eFEDS field. Next, we conducted a stacking analysis weighted by the weak lensing signal-to-noise ratio to enhance statistical robustness. The $L-M$ slope aligns with high-richness results and is shallower than X-ray samples, while the optical richness - mass ($N-M$) relation matches literature values. CAMIRA clusters with X-ray counterparts in eFEDS exhibit a steeper $L-M$ slope and brighter, more centrally peaked X-ray profiles compared to the undetected ones. Given the high purity and completeness of the CAMIRA sample, we conclude that the optically-based method can effectively select a complete cluster population with diverse ICM characteristics. While optical properties remain relatively uniform across the sample, X-ray properties vary, influencing cluster detectability in X-ray surveys.

Our results highlight eROSITA's potential, particularly when integrated with HSC data in cluster studies up to high redshift $z > 1$. Current and future X-ray observatories, such as eROSITA and ATHENA, will enhance our ability to study the X-ray underluminous cluster populations, ushering in a new era of precision cosmology. Additionally, the newly launched, high-resolution X-ray telescope *XRISM* will facilitate detailed spectroscopic studies of gas motions in clusters and allow us to connect the impact of the non-gravitational processes to clusters' global properties such as scaling relations.

Zusammenfassung

Supernovaüberreste (SNRs) und Galaxienhaufen stellen die Endprodukte der stellaren und kosmischen Entwicklung dar. Sie sind durch einige der gewaltigsten Prozesse im Universum entstanden und spielen eine entscheidende Rolle bei der Gestaltung der Dynamik von Galaxien und des Universums insgesamt.

SNRs sind die sich ausdehnenden Strukturen, die von Supernova-Explosionen zurückbleiben. Die Explosion treibt eine Schockwelle nach außen, die das umliegende interstellare Medium (ISM) mit sich treibt und erhitzt. Das Zusammenspiel zwischen den (vorwärts- und rückwärtslaufenden) Schocks, dem ISM und dem ausgeworfenen Sternmaterial führt zu vielen wichtigen astrophysikalischen und astrochemischen Phänomenen. Diese Überreste dienen daher als natürliche Laboratorien zur Untersuchung extremer physikalischer Prozesse, einschließlich des Ursprungs der kosmischen Strahlung (CRs). CRs sind relativistische geladene Teilchen, von denen man annimmt, dass sie an den Schockfronten von SNRs effektiv beschleunigt werden. In dieser Arbeit konzentrieren wir uns auf zwei SNRs und SNR-Kandidaten, HESS J1534-571 und HESS J1614-518, die beide im HESS Galactic Plane Survey als starke TeV-Gammastrahlenemitter identifiziert wurden. Wir untersuchen die Multiwellenlängen-Morphologie der SNRs und die CR-Beschleunigung an ihren Positionen. Sowohl HESS J1534-571 als auch HESS J1614-518 zeigen schalenartige Strukturen bei Radio- und/oder Röntgenwellenlängen, die mit ihren TeV-Gammastrahlenschalen korrelieren. Diese Korrelation bestätigt zum ersten Mal den SNR-Charakter von HESS J1614-518 und legt nahe, dass die Strahlung bei allen Wellenlängen von denselben CR-Populationen stammt, was uns erlaubt, spektrale Energieverteilungen (SEDs) zu erstellen.

XMM-Newton-Beobachtungen von HESS J1534-571 ergaben keine signifikante Röntgenemission, wodurch die nichtthermischen Komponenten nach oben begrenzt und die CR-Spektren eingegrenzt wurden. Die SED-Analyse legt nahe, dass eine rein leptonische Gammastrahlenproduktion nicht ausgeschlossen ist. Darüber hinaus unterstützt unsere Entdeckung einer 3σ signifikanten Fe-Kα-Emissionslinie mit einer klumpigen Morphologie frühere Ergebnisse von Suzaku-Beobachtungen des SNR (Nguyen-Dang et al., 2023). Für HESS J1614-518 haben wir nichtthermische Röntgenemission identifiziert, die mit der Beschleunigung von TeV-Elektronen in einem starken Magnetfeld zusammenhängt. Die SED spricht auch für einen leptonischen Mechanismus zur Gammastrahlenerzeugung. Wir assoziieren das kompakte Objekt J1616-5017 mit diesem SNR und vermuten eine Entfernung von 3,5 kpc (Pülhofer et al. in prep.).

Einerseits eignet sich XMM-Newton hervorragend für detaillierte Studien ausgewählter SNR-Regionen, insbesondere in Kombination mit Archivdaten von neueren Observatorien wie

Suzaku. Andererseits unterstreichen die Ergebnisse dieser Studie sowie weitere Erkenntnisse der Arbeitsgruppe SNR-ISM-Diffuse Emission der eROSITA-Kollaboration die außergewöhnlichen Fähigkeiten dieses hochmodernen Röntgenobservatoriums bei der Erforschung von SNRs – von der Identifizierung neuer Kandidaten im Survey-Modus bis hin zu detaillierten räumlichen und spektralen Analysen. Dies stellt einen bedeutenden Fortschritt auf diesem Gebiet dar und ebnet den Weg für zukünftige Entdeckungen, um offene Fragen zu kosmischen Strahlen und der Physik des interstellaren Mediums zu klären.

Galaxienhaufen sind die größten gravitativ kollabierten Objekte im Universum, die aus Tausenden von Galaxien, heißem Gas im Intracluster-Medium (ICM) und dunkler Materie bestehen, so dass sie in einem breiten Wellenlängenbereich nachweisbar sind. Sie sind wertvolle Sonden zur Bestimmung grundlegender kosmologischer Parameter und zur Untersuchung der Physik im großen Maßstab. Allerdings können Haufenproben, die mit verschiedenen Methoden auf der Grundlage unterschiedlicher Wellenlängenbänder ausgewählt wurden, unterschiedliche Populationen repräsentieren. Daher ist es von entscheidender Bedeutung, die Eigenschaften der Proben und die Auswirkungen der Auswahlmethoden für weitere kosmologische und astrophysikalische Anwendungen zu verstehen. In dieser Arbeit wird die optisch selektierte Haufenprobe CAMIRA aus Subaru-HSC-Beobachtungen analysiert, die sich mit der eFEDS-Durchmusterung des SRG/eROSITA-Teleskops überschneidet. Anfänglich konzentrierten wir uns auf 43 reiche ($N > 40$) Haufen und erweiterten die Studie dann auf 997 Haufen mit $N > 15$ und untersuchten Morphologie, Skalierungsbeziehungen und Selektionseffekte.

In Ota et al. (2023) haben wir festgestellt, dass bis zu 40% der Haufen mit hohem Reichtum relaxiert sind, was auf eine größere morphologische Vielfalt in optisch ausgewählten Proben im Vergleich zu Röntgenproben hinweist. Skalierungsbeziehungen wie Röntgenluminosität - Temperatur $L-T$ und Röntgenluminosität - Masse $L-M$ für optische Haufen weisen flachere Steigungen als Röntgenproben auf. In Nguyen-Dang et al. (eingereicht 2025) berichteten wir über einen relaxierten Anteil von bis zu 14% für die optische CAMIRA-Probe im eFEDS-Feld. Als nächstes führten wir eine Stapelanalyse durch, die mit dem Signal-Rausch-Verhältnis des schwachen Gravitationslinseneffekts gewichtet wurde, um die statistische Robustheit zu erhöhen. Die Steigung von $L-M$ stimmt mit den Ergebnissen für hohen Reichtum überein und ist flacher als bei den Röntgenproben, während die Beziehung zwischen Reichtum und Masse $N-M$ den Literaturwerten entspricht. CAMIRA-Haufen mit Röntgengegenstücken in eFEDS zeigen eine steilere $L-M$-Steigung und hellere, zentralere Röntgenprofile als solche ohne Gegenstück. In Anbetracht der hohen Reinheit und Vollständigkeit der CAMIRA-Stichprobe schließen wir, dass die optisch basierte Methode effektiv eine vollständige Haufenpopulation mit verschiedenen ICM-Eigenschaften auswählen kann. Während die optischen Eigenschaften über die gesamte Probe hinweg relativ einheitlich bleiben, variieren die Röntgeneigenschaften und beeinflussen die Detektierbarkeit von Clustern bei Röntgenuntersuchungen.

Unsere Ergebnisse zeigen das Potenzial von eROSITA in Kombination mit HSC-Daten bei der Untersuchung von Galaxienhaufen bis hin zu hohen Rotverschiebungen ($z > 1$). Aktuelle und zukünftige Röntgenobservatorien wie eROSITA und ATHENA stehen bereit,

um eine große Anzahl von Haufen mit hoher Rotverschiebung und geringer Leuchtkraft zu entdecken, die bisher via ICM Emissionen nicht detektierbar waren. Dies wird weitere Verbesserungen und Überprüfungen der Auswahlmethoden ermöglichen und damit eine neue Ära der Präzisionskosmologie einleiten. Darüber hinaus wird das neu gestartete, hochauflösende Röntgenteleskop XRISM detaillierte spektroskopische Studien der Gasbewegungen in Haufen ermöglichen, um den Einfluss nichtgravitativer Prozesse mit globalen Eigenschaften der Haufen wie Skalierungsrelationen zu verknüpfen.

Nothing in life is to be feared, it is only to be understood.

– Marie Curie

The end and the beginning

Supernovae are among the most violent yet beautiful explosions in the universe, marking ***the end*** *of a star's life cycle. Whether resulting from the gravitational collapse of a massive star or the thermonuclear destruction of a low-mass star's remnant white dwarf, these events release an enormous amount of energy and eject the progenitor star's outer layers into the surrounding environment. Supernovae can briefly outshine their entire host galaxy, with peak luminosity lasting from a few days to several weeks. Historically, these brilliant outbursts were named "novae," reflecting the awe-inspiring appearance of what seemed to be a new star in the sky. While the name is still used to this day despite the opposite nature of the objects, in a way, supernovae lead to a* ***new beginning****. They enrich the galaxy with heavy elements for the next cycle of star formation and leave behind a residue, known as a supernova remnant (SNR), that continues to shape the evolution and dynamics of the host galaxy. Although the optically luminous phase of a supernova fades quickly, SNRs can evolve over tens of thousands of years, gradually merging into the interstellar medium. During this time, their interaction with the surrounding environment triggers various radiation processes observable across the electromagnetic spectrum (Fig. 1). This makes SNRs an ideal cosmic laboratory for studying extreme physical processes that cannot be replicated on Earth, including the mystery of relativistic, charged particles known as cosmic rays.*

On a broader cosmic scale, galaxy clusters mark ***the endpoints*** *of structure evolution, representing the largest gravitationally collapsed objects of the Universe. In the framework of cold dark matter, these massive systems are thought to form by merging smaller structures (see Fig. 2 for an example of a post-merger image). This hierarchical growth makes galaxy clusters a vital probe to study the history of the Universe and trace the initial conditions at* ***the beginning*** *of the Universe. Moreover, constraining cosmological parameters through cluster studies offers a glimpse into our Universe's eventual fate: Will it continue to expand indefinitely, and at what rate, or will it collapse at some point, only to start a whole new cycle of cosmic evolution?*

Fascinated by the astronomical objects described above, I chose to write this doctoral thesis and focus on leveraging archival and observational data to study their properties and attempt to address key scientific questions. Specifically, we examine the appearance of SNRs across different wavebands, their mechanisms for producing and accelerating relativistic cosmic rays, and their interactions with the interstellar environment. These aspects are explored in Nguyen-Dang et al. (2023) and Pühlhofer et al. (2025, in preparation). Additionally, we evaluate the dynamical state of galaxy clusters and compute their scaling relations. We compare observed properties of the cluster sample to theoretical models and investigate differences among cluster samples selected through various methods. These topics are discussed in Ota et al. (2023) and Nguyen-Dang et al. (2025, submitted).

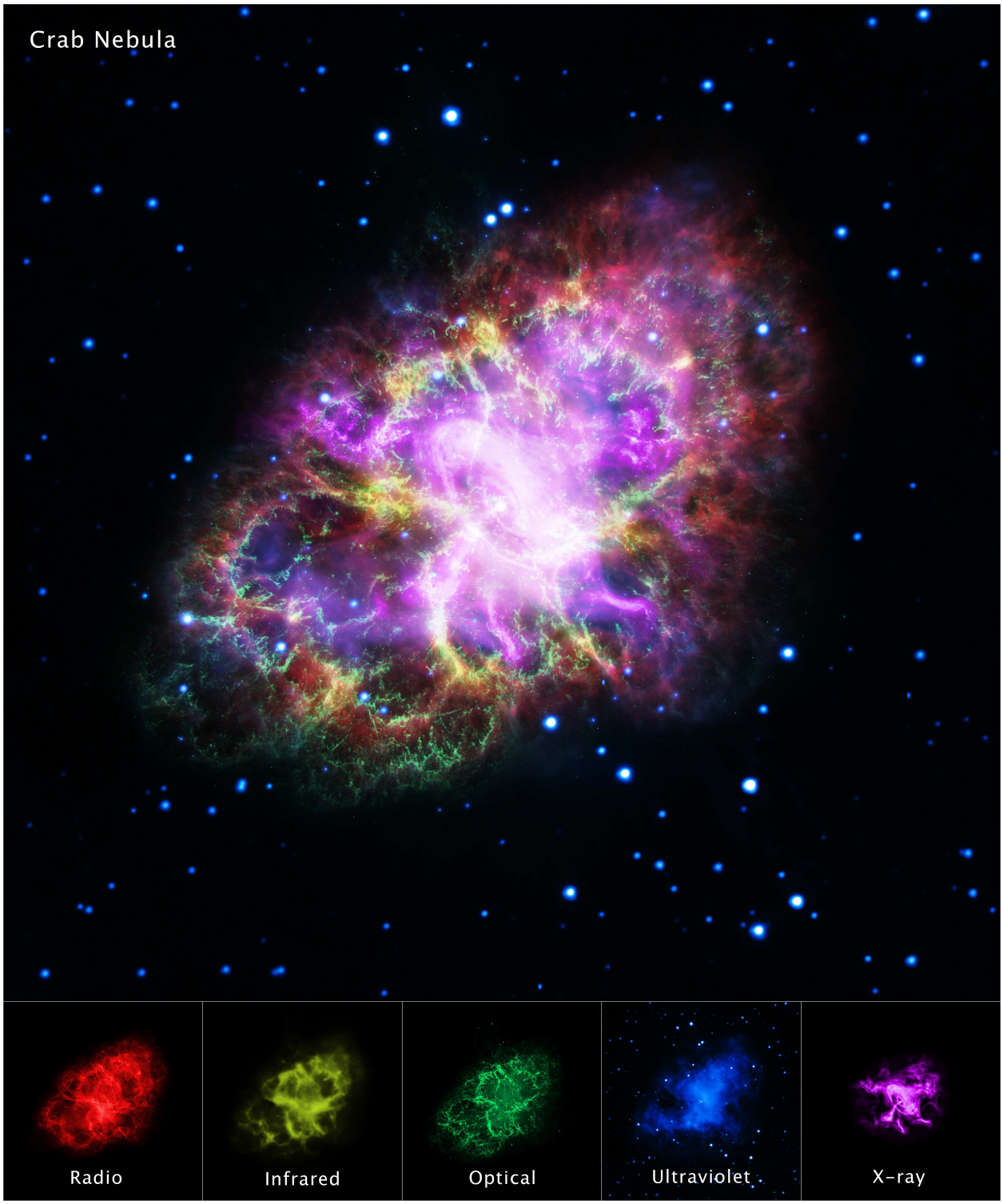

Figure 1: Supernova remnant Crab nebula as seen in different wavelengths. Credit: NASA, ESA, G. Dubner (IAFE, CONICET-University of Buenos Aires) et al.; A. Loll et al.; T. Temim et al.; F. Seward et al.; VLA/NRAO/AUI/NSF; Chandra/CXC; Spitzer/JPL-Caltech; XMM-Newton/ESA; and Hubble/STScI.

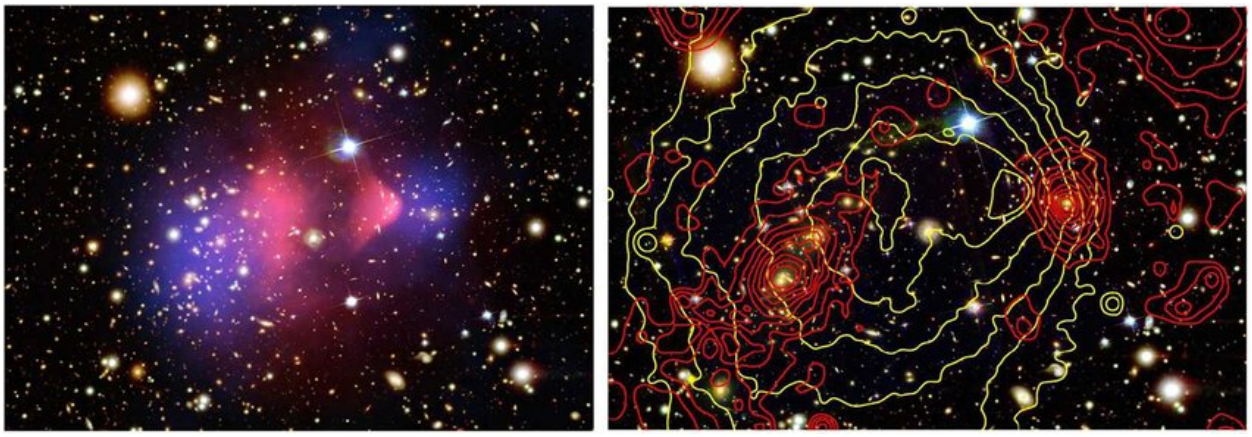

Figure 2: The Bullet cluster as seen in different wavelengths. Figure from Natarajan et al. (2024). *Left:* optical color composite image with superposition of X-ray emission in red and weak lensing mass reconstruction in blue. *Right:* Overlaid red contour is the combined strong and weak lensing map, yellow contour shows X-ray brightness. Credit: NASA/CXC/CfA/STScI/Magellan, Clowe et al. 2006; Bradač et al. 2006, 2009.

List of original publications

- **N. T. Nguyen-Dang**[1], G. Pühlhofer, M. Sasaki, A. Bamba, V. Doroshenk, and A. Santangelo. *XMM-Newton observation of the TeV-discovered supernova remnant HESS J1534-571.* In Astronomy & Astrophysics (A&A) (Nov. 2023), arXiv:2307.08656.

- G. Pühlhofer, M. Michailidis, **N. T. Nguyen-Dang**, A. Santangelo, M. Sasaki, W. Becker, G. Ponti. *Identification of HESS J1614-518 as Supernova remnant using GLEAM and eROSITA survey data.* In Astronomy & Astrophysics (A&A), to be submitted.
  My contribution: I analyzed the morphology of the SNR candidate in both the radio and X-ray wavebands. Using the derived fluxes across different energy regimes, I constructed potential models to explain the observed cosmic ray (CR) induced γ-rays. Additionally, I helped the corresponding author to set up the eROSITA analysis chain used for the paper and substantially contributed to the X-ray analysis process that led to the results reported in the paper.

- N. Ota, **N. T. Nguyen-Dang**, I. Mitsuishi, M. Oguri, M. Klein, N. Okabe, M. E. Ramos-Ceja, T. H. Reiprich, F. Pacaud, E. Bulbul, M. Brüggen, A. Liu, K. Migkas, I. Chiu, V. Ghirardini, S. Grandis, Y.-T. Lin, H. Miyatake, S. Miyazaki, and J. S. Sanders. *The eROSITA Final Equatorial-Depth Survey (eFEDS). X-ray properties of Subaru's optically selected clusters.* In Astronomy & Astrophysics (A&A) (Jan. 2023), arXiv:2206.09536.
  My contribution: I conducted the systematic search for the brightest cluster galaxies (BCGs) using a tool that I developed. I also calculated the morphological parameters of the selected clusters and derived their dynamical status. The results obtained from these morphological indicators played a key role in shaping the final conclusions regarding the impact of cluster selection methods.

- **N. T. Nguyen-Dang**, N. Ota, N. Okabe, M. Oguri, I. Mitsuishi, T. H. Reiprich, F. Pacaud, E. Bulbul, J. S. Sanders, M. Brüggen, A. Liu, Y. Tsujita, I. Chiu, V. Ghirardini, S. Grandis, M. Klein, Y.-T. Lin, K. Migkas, H. Miyatake, S. Miyazaki, and M. E. Ramos-Ceja. *The eROSITA Final Equatorial-Depth Survey (eFEDS): X-ray stacking analysis of Subaru's optically selected clusters spanning low richness regime.* In Astronomy & Astrophysics (A&A), submitted (Jan. 2025).

[1] My name in scientific publications remains unchanged from my maiden name, used prior to marriage.

List of publications not included in this work

- K. Migkas et al. [including **N. T. Nguyen-Dang**], *Cosmological implications of the anisotropy of ten galaxy cluster scaling relations*, published Astronomy & Astrophysics (A&A) (May 2021), arXiv:2103.13904.
- A. Merloni et al. [including **N. T. Nguyen-Dang**], *The SRG/eROSITA all-sky survey. First X-ray catalogues and data release of the western Galactic hemisphere*, published Astronomy & Astrophysics (A&A) (Feb. 2024), arXiv:2401.17274.
- A. Pandya et al. [including **N. T. Nguyen-Dang**], *Examining the local Universe isotropy with galaxy cluster velocity dispersion scaling relations*, published Astronomy & Astrophysics (A&A) (Nov. 2024), arXiv:2408.00726.
- M. E. Ramos-Ceja et al. [including **N. T. Nguyen-Dang**], *Morphological analysis of the eeHIFLUGCS sample*, to be submitted to Astronomy & Astrophysics (A&A).
- C. Erciyes et al. [including **N. T. Nguyen-Dang**], *AGN-related radio activity in eeHIFLUGCS' BCGs*, to be submitted to Astronomy & Astrophysics (A&A).
- **N. T. Nguyen-Dang** et al., *Constraining the magnetic field at the ongoing forward shock of the supernova remnant HESS J1731-347*, to be submitted to Astronomy & Astrophysics (A&A).

List of Abbreviations

AGN	active galactic nuclei
BCG	brightest cluster galaxy
CCO	central compact object
CMB	cosmic microwave background
CR	Cosmic ray
DSA	diffuse shock acceleration
eV	electronvolt
FoV	Field of view
IC	Inverse Compton
ICM	intracluster medium
ISM	interstellar medium
NIR	near infrared
PSF	point spread function
PWN	Pulsar wind nebula
SED	spectral energy distribution
SN	Supernova
SNR	Supernova remnant
SZ	Sunyaev-Zeldovich
VHE	very high energy
WL	weak lensing

Contents

CHAPTER 1

Introduction

1.1 Multiwavelength study of Galactic Supernova remnants

1.1.1 Supernovae

In short, Supernovae (SNe) are the last scream of a star before finishing its life cycle. They may or may not give birth to a compact object. One thing for sure is that they light up the galaxy in a spectacular way.

The evolutionary path a star follows to its end depends on its initial mass and many other factors. SNe are broadly classified into two types: core-collapse and thermonuclear. For a more detailed discussion on SN classification, readers are referred to e.g., Weiler & Sramek (1988); Filippenko (1997); Vink (2020).

As illustrated in Fig. 1.1, massive stars collapse under their own gravity after exhausting their nuclear fuel, leading to a SN explosion or γ-ray burst. These events can leave behind a compact object, such as a neutron star or a black hole. Core-collapse processes give rise to Type Ib, Ic, and II SNe (see, e.g., Woosley & Janka 2005 and Foglizzo et al. 2015 for comprehensive reviews).

Stars with lower initial masses (up to $8M_{\odot}$), which spend most of their lifetimes on the main sequence as red dwarfs or stars similar to the Sun, eventually evolve into white dwarfs. A white dwarf remains stable due to electron degeneracy pressure counteracting the inward pull of gravity, provided its mass does not exceed the Chandrasekhar limit of $\sim 1.4M_{\odot}$. However, if a white dwarf gains additional mass, for instance, by accreting material from a companion star in a binary system, thermonuclear runaway can occur, triggering a Type Ia SN (Nomoto et al., 1984; Thielemann et al., 1986; Hachisu et al., 1996). In such events, both the white dwarf and its companion are entirely destroyed, leaving no compact object behind.

In both types of SNe, the shock wave from the explosion continues to expand outward and compressing the surrounding interstellar medium (ISM). The interaction between these ingredients triggers various radiation processes, illuminating the space around the explosion and

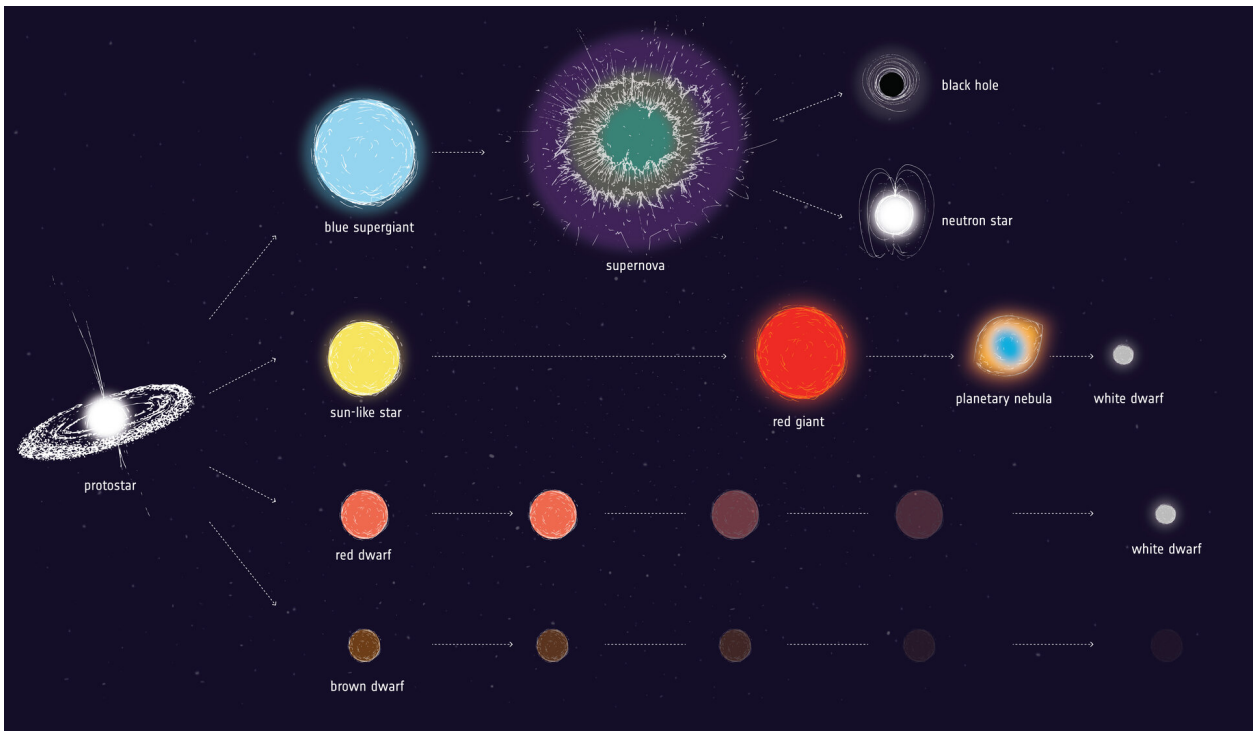

Figure 1.1: Artist impression of stars' life cycle according to its classification on the main sequence. SN type II is illustrated as an explosion after an extremely massive star has exhausted its fuel. Credit: ESA.

forming what is known as a supernova remnant (SNR). Fig. 1.2 presents composite images of two well-known SNRs, Cassiopeia-A and Kepler's, resulting from type II and type Ia SN, respectively.

Additionally, a rare type of SN explosion, known as pair-instability, can occur in supermassive stars ($> 100 M_\odot$). This phenomenon results in the complete destruction of the star, leaving no neutron star or black hole behind (see e.g., Gal-Yam et al., 2009 for an example).

1.1.2 Supernova remnants

SNRs are the magnificent echoes of SN explosions. Far from being inert relics of dead stars, they expand into space, reshaping the dynamic and chemical landscape of the ISM. Over time, they merge seamlessly into the ISM after hundreds of thousands of years.

In contrast to SNe, SNRs are significantly fainter (in optical wavebands) but persist and evolve over much longer timescales. They serve as a critical link between the endpoints of stellar evolution and the broader dynamics of galactic evolution. SNRs provide valuable insights not only into the SN explosion mechanism, the nature of the progenitor star, and the physics of the ISM, but also the nature of cosmic rays (CRs).

For example, X-ray imaging spectroscopy enables mapping the distribution of freshly synthesized elements from the explosion, revealing details of nucleosynthesis in young SNRs. X-ray spectral analysis can uncover properties of the hot plasma in and around SNRs, such as its

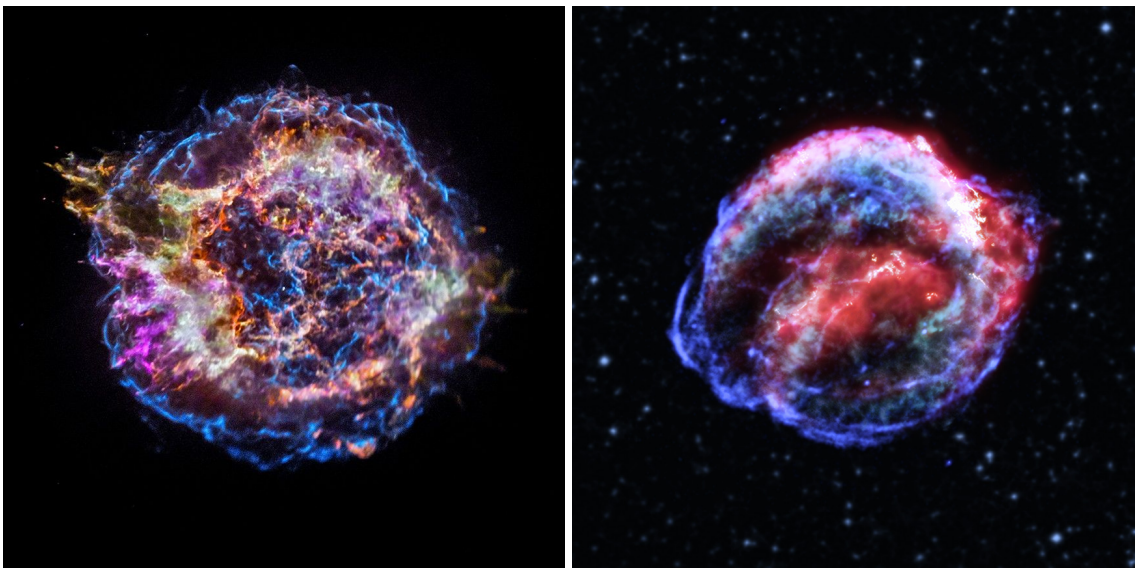

Figure 1.2: *Left:* X-ray images of Cassiopeia A taken by NASA's Chandra X-ray Observatory. Different colors correspond to different chemical elements produced by the SN explosion, the blue color (high energy X-ray) shows the blast wave that ripped through space after the detonation. *Right:* Composite image of Kepler's SNR. Chandra signal in blue indicates the powerful blast wave, while infrared data from NASA's retired Spitzer Space Telescope in red, as well as optical light from Hubble in cyan and yellow, show the debris of the destroyed star. Credit: NASA/CXC/SAO, JPL-Caltech, MSFC, STScI, ESA/CSA, SDSS, ESO.

ionization state and temperature. Furthermore, when the outermost ejecta from the explosion, traveling at thousands of kilometers per second, collide with the ISM, they generate a shock front. This front is a site of extreme heating, compression, and energy transfer, offering a natural laboratory for studying CR production and acceleration. For a more detailed review of fundamental knowledge and research topics related to SNRs, we refer readers to Vink (2012) and Vink (2020).

Shocks

Shocks are regions where the flow characteristics and thermodynamic properties of a fluid change abruptly. A SN explosion injects approximately 10^{51} erg of kinetic energy into the surrounding medium, causing the outer layers of the exploded star's ejecta to move outward at supersonic speeds. As this shock wave propagates through the ISM, it heats and ionizes the gas, forming a shell of shock-heated plasma. Shock-induced processes are crucial to the evolution of SNRs, as well as the production and acceleration of high-energy particles. Further details on how shocks contribute to the generation of relativistic CRs are presented in Sections 1.1.4 and 1.1.5.

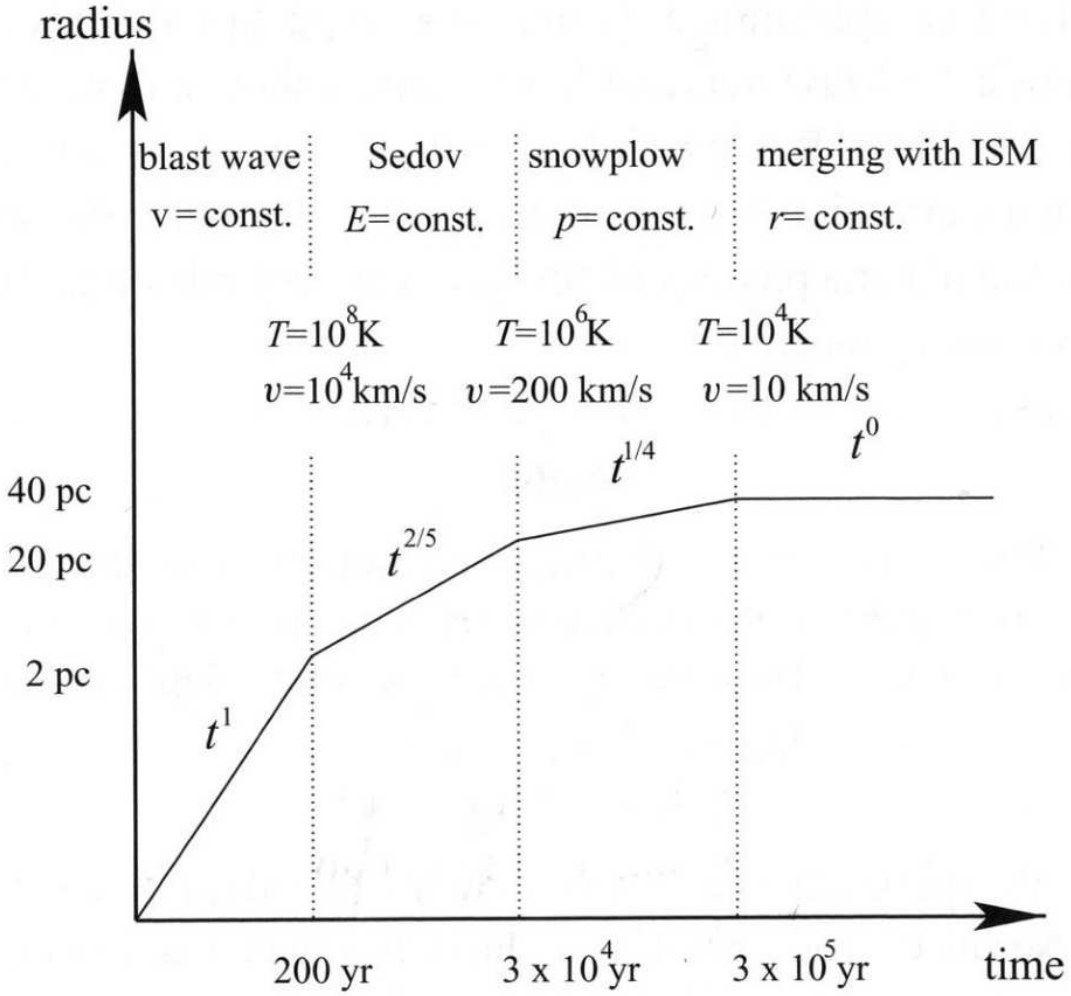

Figure 1.3: SNR's evolutionary phases. From Rosswog & Brüggen (2007).

Evolutionary phases

The evolution of SNRs can be divided into distinct phases, each corresponding to the dominant physical process that governs the dynamics and energy transfer (Vink, 2012 and references therein). Figure 1.3 illustrates the evolutionary phases of SNRs, showing the growth of the remnant's radius as a function of time.

- **Free expansion phase:** This phase begins immediately after the SN explosion and lasts for several hundred years. During this period, the forward shocks expand freely into the ambient medium at a nearly constant speed. Toward the end of this phase, the amount of ISM swept up by the explosion increases, which slows the expansion due to momentum conservation.
- **Adiabatic (Sedov-Taylor) phase:** The expansion speed decreases as the swept-up gas mass becomes comparable to or exceeds the ejecta mass. During this phase, energy loss by radiative cooling is negligible. The expansion is still at supersonic speed. Thus, the gas

is strongly shock-heated, up to millions of Kelvin, emitting thermal bremsstrahlung and line emission at X-ray wavelengths. As the outer ejecta encounter and compress the ISM, the resulting outward pressure starts to generate a reverse shock that propagates inward toward the explosion's center.

- **Radiative (snowplow) phase:** This stage is characterized by the further slowing down of the expansion, although the speed remains larger than $200\,\mathrm{km\,s^{-1}}$. Radiative energy losses now become significant, and cooling processes start to take over. In this phase, the spectra of the SNRs usually show strong line emission in optical and UV wavelengths. The outer, colder, and denser layers of gas are pushed outward by the hot inner layers, with the cold and dense gas accumulating in a manner similar to the action of a snowplow, hence the name.

- **Merging with ISM:** As the expansion slows to a few tens of $\mathrm{km\,s^{-1}}$, the SNR merges into the ISM, enriching the galactic ecosystem, and becomes invisible compared to the surrounding medium.

Emission processes

Simply put, the electromagnetic emission from SNRs originates from two main processes: thermal processes, primarily bremsstrahlung and line emissions, produced by shock-heated gas; and non-thermal processes, driven by highly accelerated particles, including synchrotron radiation, inverse Compton (IC) scattering, and neutral pion decay. Due to the ejecta expelled by the SN explosion, and also potentially by the stellar wind of the progenitor star, the density of SNRs is generally low, ranging from 0.01 $\mathrm{cm^{-3}}$ to 10 $\mathrm{cm^{-3}}$, depending on the evolutionary stage and local ISM conditions (e.g., Kahn, 1980; Leahy & Filipović, 2022). Consequently, the resulting plasma in SNRs is optically thin, allowing emissions to freely escape and carry information about the underlying physical processes to us. Here, we briefly summarize the physics and basic properties of the primary emission from SNRs, while situating them within the broader multiwavelength context of SNR studies. For more detailed discussion, readers are referred to e.g., Vink (2012) and references therein.

It is worth noting that, as an aftermath of a SN explosion, a pulsar wind nebula (PWN) can form inside the SNR. Pulsars are fast-rotating neutron stars that generate strong magnetic fields, propelling relativistic charged particles outward. These energetic particles interact with the surrounding environment and give rise to various emission processes. PWNe share several similarities with SNRs: both are remnants of SNe, capable of ionizing material and emitting radiation observable across radio, X-ray, and γ-ray wavelengths. However, the two are fundamentally distinct in origin and morphology. SNRs result from either the shock waves of a detonation or thermonuclear deflagration, while PWNs are driven by the powerful winds from the central pulsar. Morphologically, SNRs often appear as large, diffuse shells or rings, while PWNe are more

centrally filled and compact. This difference in structure makes PWNe a valuable null hypothesis when using morphology as a criterion for identifying SNRs (see Section 1.1.6).

- **Thermal bremsstrahlung:** When the gas is heated to temperatures between 10^6 and 10^8 Kelvin, highly energetic electrons interact with the ions present in the plasma, producing bremsstrahlung radiation in the X-ray wavelengths. "Bremsstrahlung", which translates from German as "braking radiation," refers to the acceleration or deceleration of electrons under the influence of nearby ions. This process does not require any particle collisions or capture and is therefore also called "free-free" emission. Bremsstrahlung radiation in SNRs is characterized by a soft X-ray spectrum, typically in the range of 1-10 keV. This soft spectrum is defined by the plasma temperature, ionization state and electron density. These factors can be constrained by fitting the SNR spectra to an appropriate emission model, in practice by using software such as `xspec`[1] and `sherpa`[2].

- **Line emissions:** When the gas is heated, atoms are partially or completely ionized, depending on the temperature. Free electrons in the gas can collide with these ions, exciting them by promoting the bound electrons to higher energy states. Shortly after the excitation, the bound electron transitions back to the ground state, emitting radiation that can be observed as line emission in the X-ray spectrum. In addition to collisional excitation, recombination of ions by free electrons in the hot plasma also produces X-ray radiation as ions transition to their ground-state energy levels. Line emissions from atoms such as hydrogen (Hα, Hβ), oxygen (O,III), and sulfur (S,II) occur in the cooler, denser regions of the SNR and can produce radiation in the optical and ultraviolet light ranges.

- **Synchrotron:** Relativistic charged particles emit synchrotron radiation when accelerated in the presence of a magnetic field by gyrating around the magnetic field lines. In a sea of charged particles, electrons (and positrons) radiate synchrotron emission far more efficiently than protons due to their significantly lower mass. Synchrotron radiation is the primary emission mechanism detected in the radio waveband for SNRs (and also, PWNe), the wavebands in which SNRs were traditionally discovered. An electron population accelerated to energies of 10–100 TeV can produce synchrotron radiation that extends into the X-ray regime (1–10 keV) (Reynolds, 1996; Mastichiadis, 1996).

- **Inverse Compton:** When a low-energy photon collides with a relativistic particle, it gains energy through a process known as inverse Compton scattering. In this mechanism, no new photons are created; instead, the initial photons are upscattered to shorter wavelengths. Photons originating from the cosmic microwave background (CMB) or nearby stars can undergo this process when interacting with relativistic electrons in SNRs, producing radiation that can be observed in the TeV regime.

[1] `https://heasarc.gsfc.nasa.gov/xanadu/xspec/`
[2] `https://cxc.cfa.harvard.edu/sherpa/`

The total emitted power of IC radiation in SNRs depends on the energy of relativistic electrons and the energy density of photons,

$$P_{\mathrm{IC}} \propto \gamma^2 u_{\mathrm{photons}}, \tag{1.1}$$

where u_{photons} denotes the energy density of photons and $\gamma = 1/\sqrt{1 - v^2/c^2}$ is the Lorentz factor or relativistic term. As mentioned above, high-speed electrons at the SNR sites are also involved in the synchrotron radiation specifically because of the magnified magnetic field at the shock front. Similarly, the emitted power of the synchrotron radiation is proportional to the square of the electron's relativistic parameter and the energy density of the magnetic field,

$$P_{\mathrm{SYN}} \propto \gamma^2 u_{\mathrm{B}}. \tag{1.2}$$

This implies

$$P_{\mathrm{IC}} \propto \frac{u_{\mathrm{photons}}}{u_{\mathrm{B}}} P_{\mathrm{SYN}} \tag{1.3}$$

or

$$P_{\mathrm{IC}} \propto B^{-2}, \tag{1.4}$$

as the energy density of the magnetic field scales with the square of the magnetic field strength. Suppose the synchrotron radiation observed in X-rays and the IC radiation observed in high-energy γ rays originate from the same population of relativistic electrons. In that case, the relative power between these two emission mechanisms depends on the magnetic field strength and the photon fields. Specifically, if the X-ray flux is measured and the scattering photon population is well constrained, the power emitted by IC radiation becomes inversely proportional to the square of magnetic field strength. This relationship is crucial for modeling the spectral energy distribution (SED) of CRs, particularly because, at GeV-TeV γ-ray energies, the observed emission could also originate from CR protons via pion decay.

- **Pion decay:** The above non-thermal mechanisms (synchrotron and IC) require CR electrons and produce radiation in the radio, X-ray, and high-energy γ-ray wavelengths. In addition to CR electrons, CR protons also act as a source of γ-rays through the process of pion decay. Relativistic protons and atomic nuclei can interact with other less energetic nuclei present in the nearby molecular cloud, leading to the production of charged and neutral pions ($\pi^{+/-}$ and π^0). These neutral pions are unstable and almost immediately decay into high-energy photons, typically at GeV-TeV levels. While CR protons is the most

abundant population of CR, they only radiate (via π^0 decay) in the GeV-TeV wavebands, this is the only regime to detect them.

An effectively amplified magnetic field is required to confine CR protons within the shock and accelerate them to energies of at least 100 TeVThis enables π^0 decay to produce γ-rays in the GeV-TeV range, making the detection of hadronically induced γ-rays from SNRs direct evidence of efficient particle acceleration at these sites.

This brings us to a key question in the field: Which CR population - electrons or protons - is primarily responsible for the observed high-energy γ-rays? γ-ray radiation arising from CR electrons is referred to as leptonic, while that from CR protons is called hadronic. Generally, the VHE γ-ray spectrum from a hadronic scenario shows a flat feature toward the GeV frequency, which connects to a steep spectrum between 100 MeV and 1 GeV, often referred to as the π^0 decay "bump." In contrast, a leptonic γ-ray spectrum typically shows a steepening toward the GeV energy without such break, causing the VHE spectrum to appear more peaked. γ-ray astronomy is particularly important here, as it is the only observational channel through which hadronic CRs, the dominant component of CRs, can be detected. Constraining the origin of VHE γ-rays is one of the key objectives of this thesis.

- **Fluorescence lines:** The X-ray spectra of SNRs may also contain fluorescence lines, emitted by atoms within the ambient cool gas after collisional excitation by low-energy ($\sim$ 100 MeV) CR protons. In particular, the Fe Kα line at 6.4 keV is typically used to study both SNRs and nearby molecular clouds, since Fe is fairly common in the ISM and the line's fluorescence yield is high. It has been detected in a number of SNRs, such as W28, Kes67, Kes69, Kes78, W44 (Nobukawa et al., 2018), as well as in HESS J1534-571 (Saji et al., 2018), which is investigated in this thesis.

1.1.3 Morphology of supernova remnants

SNR's morphologies, shaped by the interplay of stellar winds, SN shocks, and the surrounding medium, tell stories of chaos and creation.

In practice, particularly during the later stages of evolution, the morphology of SNRs is significantly shaped by the conditions of the surrounding ISM. In addition to shell-type SNRs, which are the focus of this thesis, other morphological classes include PWNe (or plerions, typically dominated by strong pulsar wind-induced, centrally filled plasma, see Fig. 1 for an example); and composite SNRs (characterized by a PWN enclosed within a surrounding shell). Young SNRs usually display narrow, bright X-ray filaments (e.g., SN1006, Tycho's, Kepler's), whereas more evolved SNRs appear fainter and more diffuse (e.g., RCW86). This difference can be attributed to the faster cooling of electrons in the presence of a high magnetic field.

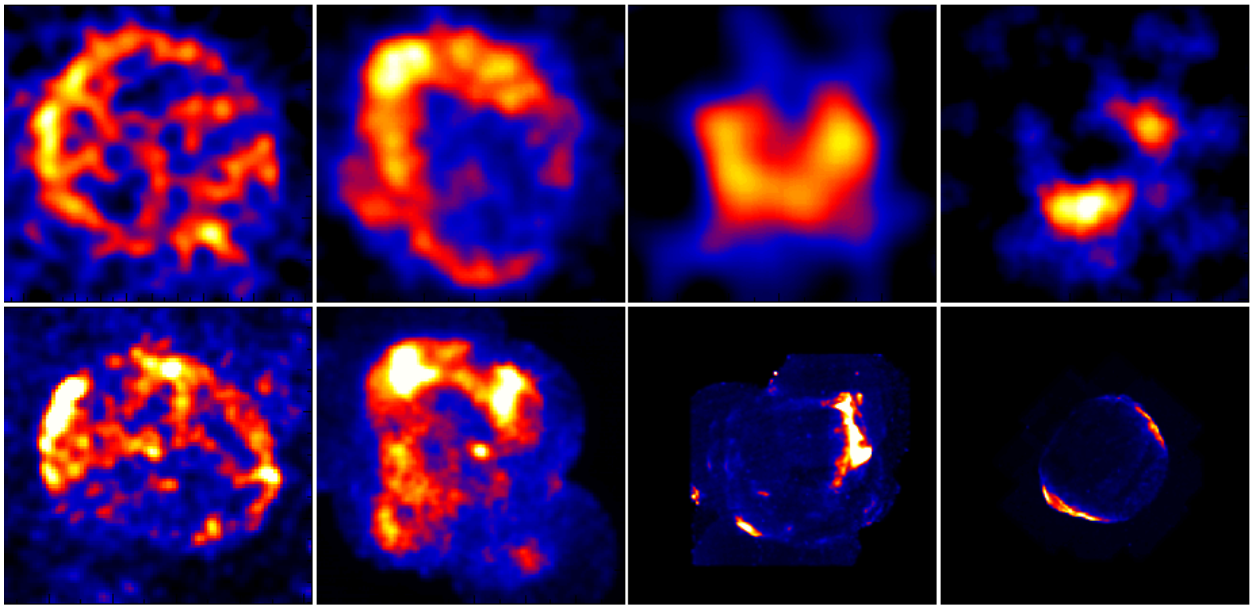

Figure 1.4: *Top:* Young, resolved in TeV, TeV dominated γ-ray emission. *Bottom:* X-ray synchrotron emission, with the apparent correlation to TeV's morphology. Credit: Hinton & Hofmann (2009).

Historically, SNRs were first discovered using ground-based radio telescopes in the mid-20th century, identified by their extended, shell-like structures. These observations provide evidence for the presence of relativistic GeV particles. In the following decades, advances in X-ray astronomy enabled detailed studies of SNRs, including mapping newly synthesized elements, analyzing hot gas, and exploring the interactions between shocks and the ISM. A few decades later, TeV astronomy emerged and began making significant contributions to the field. Ground-based Cherenkov telescopes, such as the High Energy Stereoscopic System (H.E.S.S.) (Aharonian et al., 2004; H.E.S.S. Collaboration et al., 2018c), detected very high-energy (VHE) γ rays originating from SNRs, providing new insights into their energetic processes.

In a simplified one-zone model, where the environment is assumed to be homogeneous and particles are considered to belong to a single population, the radio and X-ray emissions (both originating from synchrotron radiation) exhibit spatial similarity and mark the shock fronts. Indeed, various observations have confirmed this by identifying a special class of synchrotron-dominated X-ray SNRs, including Cassiopeia A, G266.2-1.2 (Vela Jr.), and G347.3 (RX J1713.7-3946) (Fabian et al., 1980; Saha et al., 2021; Maxted et al., 2018b; Lazendic et al., 2004). Likewise, VHE γ-rays (GeV-TeV), if produced via leptonic processes, can show excellent resemblance to the radio and X-ray morphology within the angular resolution achievable in the γ-ray bands (Fig. 1.4). This scenario requires a weak magnetic field (well below $\sim$100 μG, Hillas, 2005) to allow more electron energy to go into IC scattering rather than synchrotron losses, which could challenge the expected picture of efficient particle acceleration. However, if the VHE γ-rays are primarily generated by hadronic CRs, the SNR's morphology in this energy range may differ from that

observed at radio and X-ray wavelengths. Observing potential associated gas (e.g., Maxted et al., 2018a), for instance, could provide additional constraints on the γ-ray production mechanism, as hadronic processes require target material for interactions that lead to π^0 decay. Additionally, complex processes such as CR escape can extend the TeV shell farther from the explosion center than the X-ray shell (e.g., H.E.S.S. Collaboration et al., 2018b). Therefore, analyzing the morphology of SNRs across different wavelengths is crucial not only for studying the SNR's properties but also for understanding the particle acceleration and propagation processes occurring at and around the shocks.

TeV observations with the H.E.S.S. telescope have revealed an intriguing class of objects: strong TeV-emitting SNRs that were previously undetected in X-ray wavelengths. This class of SNRs is particularly valuable for probing CR acceleration at very high energies (VHE). While the detection of X-ray synchrotron emissions from SNRs directly confirms their ability to accelerate CR electrons to TeV energies, SNRs lacking X-ray synchrotron signals yet exhibiting strong TeV emission serve as ideal laboratories for investigating their potential as CR proton accelerators.

1.1.4 Fermi acceleration

Fermi acceleration is nature's way of energizing particles, propelling them to extreme speeds through a cosmic dance with magnetic fields.

In 1949, Enrico Fermi proposed a model for the acceleration mechanism of CRs (Fermi, 1949). The first-order Fermi acceleration, also known as diffuse shock acceleration (DSA), describes how charged particles gain energy by repeatedly crossing a shock front. In contrast, second-order Fermi acceleration involves particles gaining energy through random scattering in turbulent magnetic fields, resulting in a less efficient energy gain. Figure 1.5 illustrates these processes. The turbulence and amplification of magnetic fields in shock environments, such as those found in SNRs, pulsars, and the jets of active galactic nuclei (AGN), play a crucial role in CR acceleration. In particular, the forward shocks of SNRs are considered one of the most promising sites for CR acceleration via DSA (Drury et al., 1994; Hillas, 2005; Berezhko & Völk, 2007; Caprioli et al., 2009).

1.1.5 Cosmic rays and their puzzle

Cosmic rays (and the VHE γ-rays that they produce) are the messengers from the depths of space, traveling across the Universe, carrying the energy of distant astronomical objects.

Cosmic rays...

In 1912, Austrian physicist Victor Hess conducted a pioneering study on atmospheric ionization. Using a series of balloon flights, he measured ionization levels at various altitudes. Contrary to

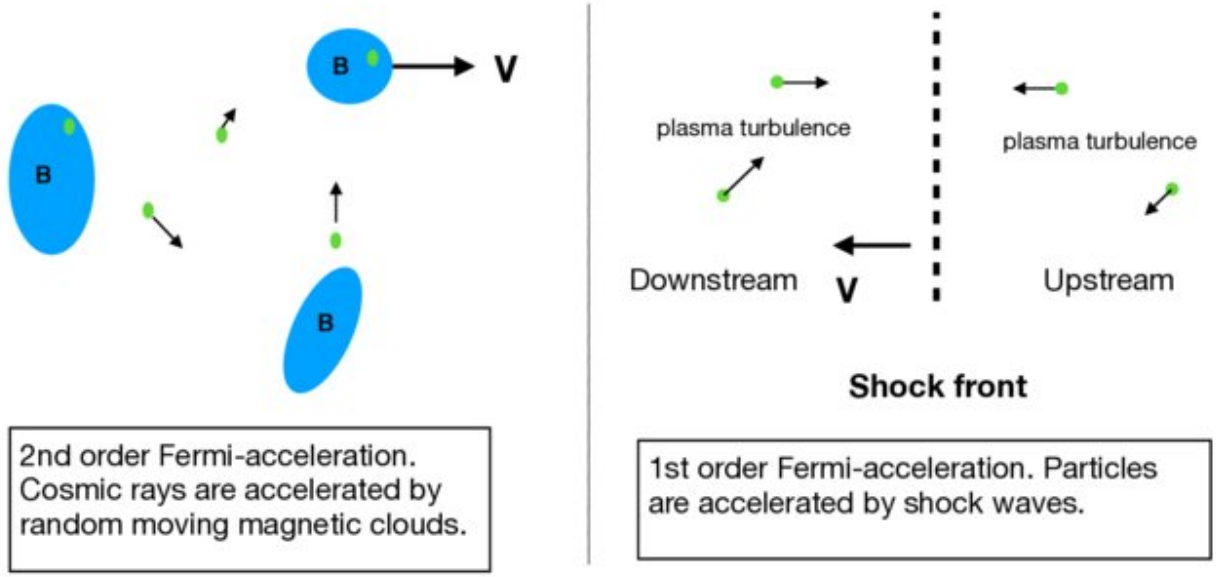

Figure 1.5: Illustration of the first-order (right) and second-order (left) Fermi acceleration. Figure taken from Che & Zank (2019).

the belief at the time that ionization was caused by radioactive elements on Earth, he discovered that ionization levels at an altitude of 5300 meters were three times higher than at sea level. This finding demonstrated that the primary source of ionization must originate from beyond the Earth's atmosphere. This discovery marked the first detection of high-energy particles from space, now known as cosmic rays.[3]

CRs are fast-moving charged particles, primarily composed of protons and ions, which account for 99% of their total composition, with electrons contributing the remaining 1%. The energy of these particles can reach up to 10^{20} eV, and the spectrum of the entire CR population follows a power-law distribution, $F \propto E^{-\Gamma}$ (Fig. 1.6). Carrying substantial energy, primary CRs interact with matter along their paths, producing secondary CRs. For example, when CRs encounter the Earth's atmosphere, they trigger events known as "air showers", which can be detected using ground-based Cherenkov imaging devices such as the H.E.S.S. telescope.

SNRs are widely regarded as the primary engines for the production and acceleration of Galactic CRs, based on their energy input and the efficiency of particle acceleration at their shocks. Considering that the average energy released in a SN explosion is approximately 10^{51} erg, and the SN rate in our galaxy is around 2–3 per century, SNRs would need to channel at least 10% of their explosion energy into CRs to sustain the observed total CR production power of $10^{41}\,\mathrm{erg\,s^{-1}}$.

Looking at Fig. 1.6, there are two interesting features in the CRs' SED. The first is observed at

[3]Victor Hess was awarded the Nobel Prize in 1936 for his discovery of CRs.

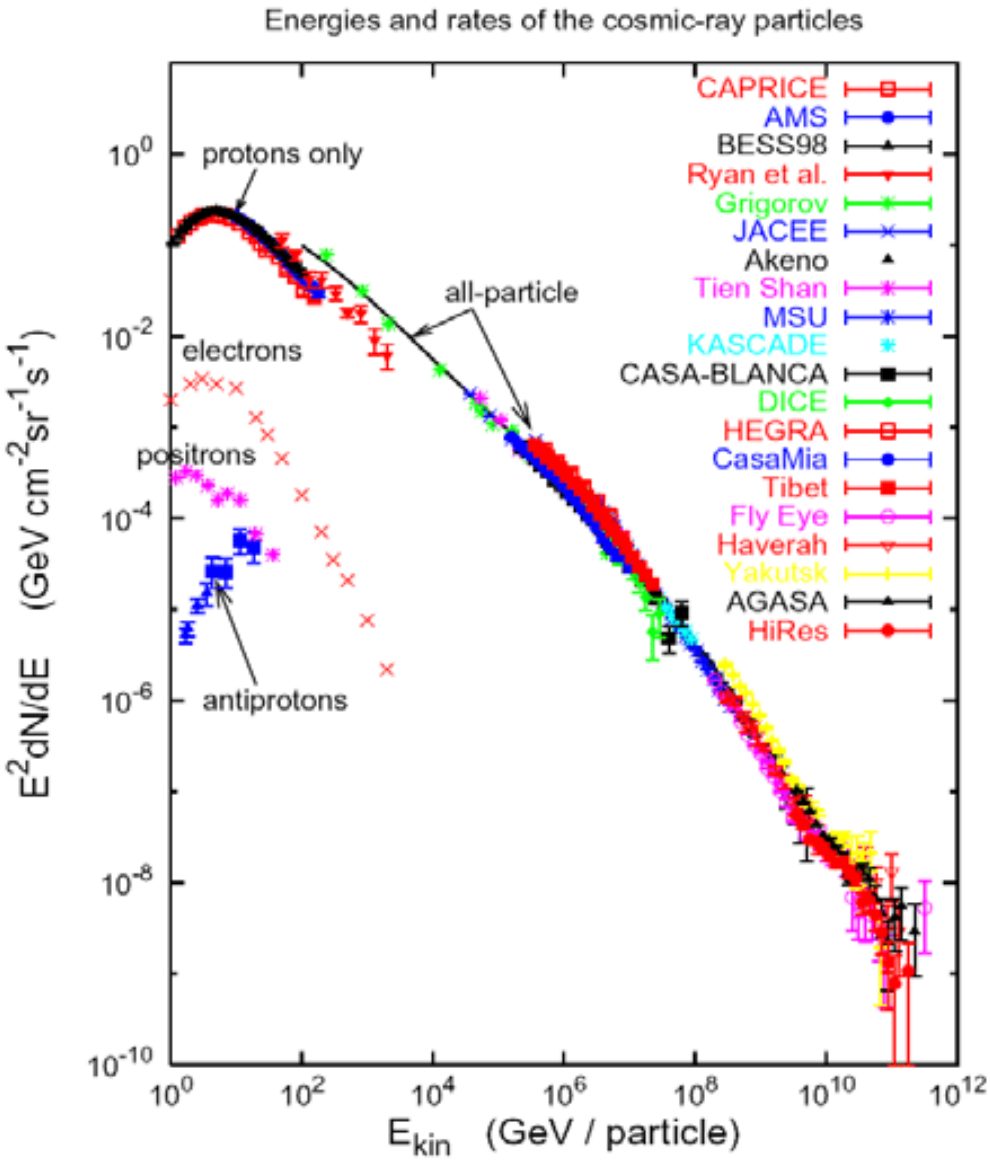

Figure 1.6: The spectrum of CRs. Figure taken from Diehl (2009).

approximately 3 peta electron volt (PeV), characterized by the softening of the power-law index from -2.7 to -3.1. This bend, commonly called the "knee," marks a significant transition (Haungs et al., 2003). The second feature, known as the "ankle", occurs at around 5×10^{18} eV and is identified by a hardening of the spectrum from -3.3 to -2.6 (The Pierre Auger Collaboration et al., 2015). While various theories and observations have been proposed to explain the "knee", such as a transition from Galactic to extragalactic CRs or a shift in CR composition from predominantly protons to heavier nuclei (Peters, 1961; Aglietta et al., 2004; Antoni et al., 2005), the mechanism underlying the "ankle" remains a topic for debate (Unger et al., 2015; Aloisio et al., 2007).

... and their puzzle

How can CRs move so fast the way they do?

CRs have been studied for over a century, yet they remain shrouded in mystery. Why are CRs so energetic? How are they produced and accelerated to such extreme speeds? The highest energy achievable by particles in Earth-based laboratories is 'only' in the TeV range, with the Large Hadron Collider (LHC)[4] holding the current record (Evans & Bryant, 2008). Does the existence of CRs challenge our current understanding of physics and point to the need for new physics?

To explain the observed spectrum up to the "knee" in the CR spectrum, SNRs must act as so-called Galactic PeVatrons, efficiently accelerating protons and nuclei up to PeV energies. However, observational evidence confirming SNRs as PeVatrons is limited (Helder et al., 2012). While some SNRs show γ-ray emission extending to tens of TeV, which supports their role in CR acceleration, no clear evidence for SNRs being PeVatrons has been observed. For recent studies on potential SNR PeVatrons, readers are referred to e.g., Guo & Xin (2024); Albert et al. (2024); Tsuji et al. (2024); Cao et al. (2024). Theoretical work, e.g., by Diesing (2023) suggests that SNRs may be able to accelerate particles to PeV energies under specific conditions, such as when the shock velocity exceeds $\sim 10^4\,\mathrm{km s}^{-1}$ and effective magnetic field amplification occurs due to escaping particles.

Moreover, it is essential to determine the relative energy contributions from relativistic CR protons, nuclei, and electrons, as well as the maximum achievable particle energy, to establish SNRs as the primary engines of Galactic CR acceleration. Given that protons and nuclei account for 99% of the CR composition, SNRs with a hadronic γ-ray spectrum represent a compelling source for investigation. This thesis aims to investigate the origin of γ-ray emission associated with CRs at SNR sites, providing insights into the role of SNRs as CR accelerators, at least up to the energies corresponding to the "knee" in the all-particle CR spectrum.

[4] `https://home.cern/science/accelerators/large-hadron-collider`

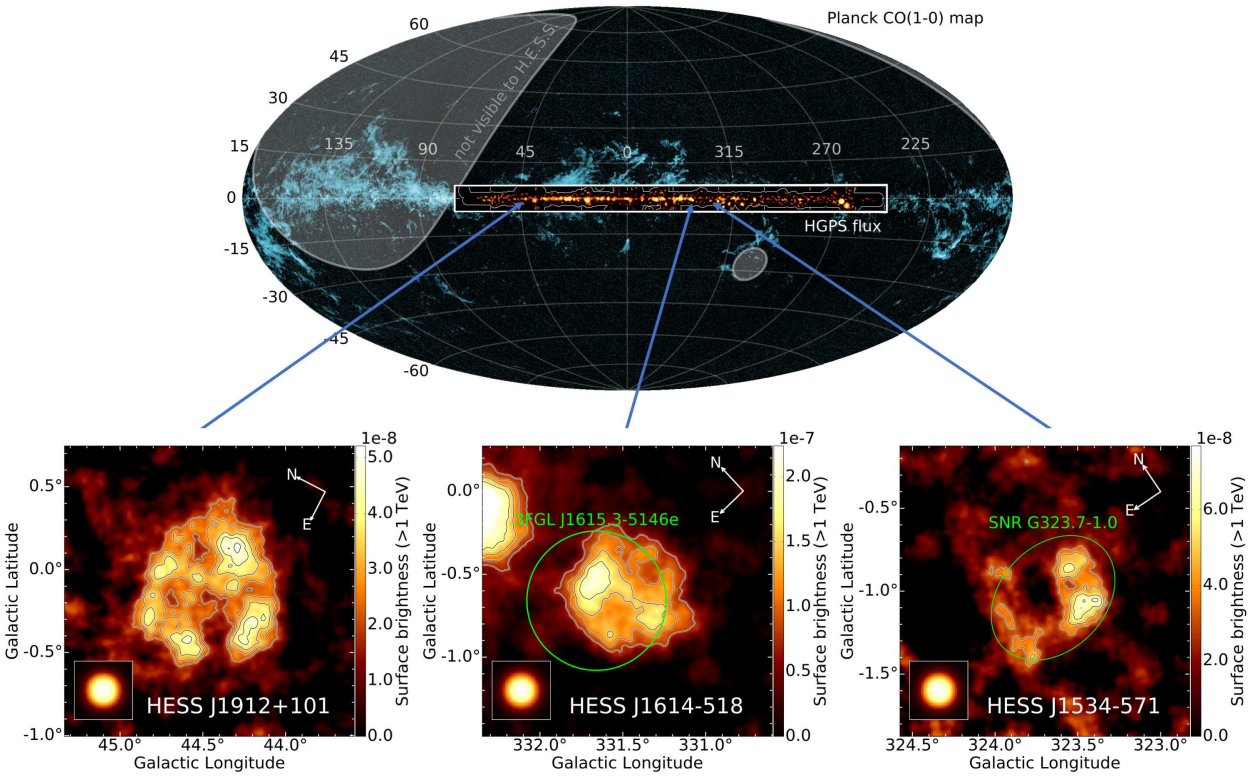

Figure 1.7: Three newly identified SNRs and candidates by the H.E.S.S. Galactic plane survey. Credit: H.E.S.S. Collaboration et al. (2018a).

1.1.6 The H.E.S.S. galactic survey: search for TeV-emitting shell-structured supernova remnants

The H.E.S.S. Collaboration set out to search for new TeV-emitting SNRs. Now, we are on the journey of unveiling their nature, while simultaneously connecting the multiwavelength picture and attempting to answer related scientific questions.

The H.E.S.S. Galactic plane survey aimed to identify TeV-emitting sources, resulting (amongst others) in the selection of three new SNR candidates (Fig. 1.7). This classification was based primarily on their extended, shell-like structures characteristic of (young) SNRs, with the null hypothesis considering a PWN morphology as an alternative scenario (H.E.S.S. Collaboration et al., 2018b).

The search for counterparts of these sources in radio, X-ray and GeV wavelengths were performed. Only HESS J1534-571 had at the time of publication a confirmed radio counterpart, G323.7-1.0, a faint elliptical shell with excellent spatial coincidence with the TeV surface brightness map of HESS J1534-571, as found in the Molonglo Galactic Plane Survey (MGPS; Green et al., 2014). This has confirmed HESS J1534-571 as a SNRs, while the other two remained SNRs candidates. The observed GeV fluxes of HESS J1534-571 and HESS J1614-518 from *Fermi*-LAT are compatible with TeV fluxes, though they do not provide additional constraints for the classification of these sources.

When these three new TeV-selected SNRs and candidates were first identified, no significant X-ray emission was detected from any of the sources. In a magnetic field caused by strong shocks, potentially amplified by CR streaming, non-thermal X-ray radiation (≥ 2 keV) is expected, if the TeV emission originates from relativistic electrons. A possible explanation for this lack of X-rays is analogous to the case of relic TeV PWNe (Kargaltsev et al., 2012; H.E.S.S. Collaboration et al., 2018d; Principe et al., 2020). In relic PWNe, the pulsar has slowed down and no longer actively generates strong winds to inject fresh relativistic particles. Furthermore, the energy-loss timescale for IC scattering being longer than for synchrotron radiation in certain cases can result in a similar pattern. Further discussion on the interplay between synchrotron and IC emissions can be found at e.g., Manolakou et al. (2007); Zacharias (2014); Nalewajko et al. (2018). As a result, TeV γ-rays can still arise from IC scattering by CR electrons, specifically outside of high magnetic field or shock regions, while very high-energy electrons (>10 TeV), required for X-ray synchrotron radiation, have already lost most of their energy via synchrotron cooling and have left the acceleration sites. Furthermore, the weakening of the magnetic field in evolved SNRs further suppresses synchrotron X-ray emission.

In contrast to the pure leptonic origin of CR induced radiation above, and assuming no instrumental limitations, a hadronic origin of the TeV γ-rays offers an alternative explanation for these often called 'dark' TeV accelerators. In this scenario, the TeV emission from evolved SNRs is dominated by π^0 decay resulting from interactions between CR protons and ambient gas (Yamazaki et al., 2006) while emission in other wavebands is so weak that it escapes detection. However, based on the knowledge available at the time of publication, drawing a concrete conclusion about the origin of the TeV γ-rays observed from the three SNRs remains challenging. By presenting these newly identified SNRs and candidates, the search for TeV SNRs conducted by the H.E.S.S collaboration has demonstrated the significant capability of current Imaging Atmospheric Cherenkov Telescope Arrays to uncover new SNRs. Looking forward, the upcoming Cherenkov Telescope Array Observatory (CTAO) will substantially enhance sensitivity, enabling the detection of TeV SNRs across the entire Galaxy.

Table 1.1 summarizes the status of multiwavelength searches for counterparts and constraints of CR acceleration scenarios for the three TeV SNRs and candidates, as of the time of writing this thesis. An asterisk (*) indicates the contributions made specifically by the publications presented in this dissertation.

- **HESS J1912+101** Despite extensive studies aimed at establishing its nature and exploring the underlying physical processes (Puehlhofer et al., 2015; Reich & Sun, 2019; Zeng et al., 2021; Sun et al., 2022; Li et al., 2023), HESS J1912+101 has not yet been definitively identified as a SNR, primarily due to the absence of confirmed radio and X-ray counterparts, and thus it remains an SNR candidate.

- **HESS J1534-571** For the SNR HESS J1534-571, we utilized targeted *XMM-Newton* obser-

vations to further investigate potential non-thermal X-ray emissions. We focused on the remnant shell's brightest region in the TeV map, which had not been covered by Suzaku observations (H.E.S.S. Collaboration et al., 2018a; Saji et al., 2018). An upper limit on the non-thermal X-ray emission was derived, placing a crucial constraint on the SED of CRs accelerated at the SNR. Evidence for interactions between low-energy CR protons ($\sim$ MeV) and nearby cool gas was also found.

- **HESS J1614-518** Our work (Pülhofer et al., 2025) provides the first confirmation of the SNR nature of HESS J1614-518, achieved by identifying its counterparts in both the radio and X-ray regimes. Further properties of the SNR such as a possible associated central compact object and the distance to Earth are also estimated.

	HESS J1912+101	**HESS J1534-571**	**HESS J1614-518**
Radio counterpart	No	Yes	Yes*
GeV counterpart	No	Yes	Yes
X-ray emission	No	No*	Yes*
CR acceleration	Hadronic?	Leptonic?*	Leptonic?*
Classification	SNR candidate	SNR	SNR*

Table 1.1: Summary of multiwavelength studies and CR acceleration constraints of three new SNRs and candidates reported in H.E.S.S. Collaboration et al. (2018a). New results from our work are marked with an asterisk (*).

1.2 Multiwavelength study of galaxy clusters

1.2.1 Current understanding of the Universe

It is believed that we are living in a hierarchical Universe, where structures emerge on the smallest scales, gradually merging and assembling to create larger objects.

According to the Big Bang theory (Lemaitre, 1931; Guth, 1981), the Universe emerged from a singularity, expanding rapidly from an extremely dense and hot state. This theory is essentially a backward extrapolation of the present-day expansion of the Universe, providing a framework for understanding its origins (Postolak, 2024). However, the Big Bang model alone raises several challenges (e.g., Brandenberger, 2010; Peebles, 2022), including the horizon problem and flatness problem, which question why the Universe appears so homogeneous, isotropic, and spatially flat (describable by Euclidean geometry). These issues are addressed by the cosmic inflation theory (Liddle, 1999; Nastase & Skenderis, 2020), which proposes an extremely rapid expansion in the early Universe. The predictions of inflation, particularly regarding the cosmic microwave background (CMB, Planck Collaboration et al., 2020), align well with observational data, reinforcing the standard cosmological model (e.g., Springel et al., 2006; Ferreira & Magueijo, 2008). As a result, the Big Bang theory, with necessary extensions such as inflation, remains widely accepted in modern cosmology (e.g., Chowdhury et al., 2019).

The ΛCDM model (Lambda Cold Dark Matter, Peebles, 1984; Blumenthal et al., 1984; Planck Collaboration et al., 2020) provides a detailed framework for structure formation. In this model, structure formation follows a hierarchical process: smaller gravitationally collapsed objects form first, later merging to create larger structures (e.g., White & Frenk, 1991). As the Universe cooled down, primordial density fluctuations led to the collapse of gas clouds, and the formation of the first stars around 100 million years after the Big Bang (e.g., Nakano, 1981; Bromm et al., 2009; Klessen & Glover, 2023). This marked the end of the cosmic "dark age" (e.g., Rees, 2000; Miralda-Escudé, 2003; Springel & Hernquist, 2003; El Bourakadi & Otalora, 2024). Over time, these small structures merged to form star clusters, galaxies, galaxy groups, and ultimately galaxy clusters.

With advances in astronomical instrumentation and numerical simulations, significant efforts have been devoted to precise measurements of cosmological parameters (e.g., Reiprich & Böhringer, 2002; Vikhlinin et al., 2003; Mantz et al., 2008; Komatsu et al., 2011; Keisler et al., 2011; Burenin & Vikhlinin, 2012). Fig. 1.8 illustrates an example of such measurements, overlaid with different evolution scenarios of the Universe (Knop et al., 2003). As the largest gravitationally collapsed structures, galaxy clusters provide crucial insights into cosmic evolution and large-scale structure formation (e.g., Allen & Mantz, 2019). In particular, their mass function serves as a powerful probe of cosmological parameters (e.g., Starobinsky, 1998; Majumdar & Mohr, 2004). Understanding cluster selection techniques and ensuring the completeness of cluster samples are

key objectives of this thesis, as they directly impact the reliability of cosmological constraints (Grandis et al., 2020; Chiu et al., 2023; Gallo et al., 2024).

1.2.2 Galaxy groups and clusters

Being the largest-scale structures in the Universe, galaxy clusters stand as cosmic archives, preserving the rich history of the Universe's formation and evolution.

Composition

Galaxy clusters are the most massive gravitationally bound structures in the Universe, with typical total masses in the range of $10^{14} - 10^{15} M_{\odot}$. They consist of three primary components: galaxies, the intracluster medium (ICM) filled with hot, diffuse gas, and dark matter, contributing approximately $\sim 5\%$, $\sim 15\%$, and $\sim 80\%$ of the total mass, respectively (e.g., Jones & Forman, 1990; Böhringer, 1994; Makino, 1996). Each component exhibits distinct physical properties and emission mechanisms, making galaxy clusters observable across a broad range of electromagnetic wavelengths, from radio to optical to X-ray.

As dynamic environments, galaxy clusters experience processes such as mergers and active galactic nucleus (AGN) activity, which drive the production of relativistic particles. Similar to SNRs, these energetic phenomena generate shocks, turbulence, and magnetic field amplification, accelerating cosmic ray (CR) electrons and protons (e.g., Brunetti & Jones, 2014; Ruszkowski & Pfrommer, 2023). High-energy particles are expected to produce very high-energy (VHE) γ-ray emission through inverse Compton (IC) scattering of CMB photons or via hadronic interactions leading to π^0 decay (e.g., Brunetti & Jones, 2014). Despite these theoretical predictions, no conclusive detection of VHE γ-rays from galaxy clusters has been made to date. Observations with instruments like *Fermi*-LAT and ground-based imaging atmospheric Cherenkov telescopes (e.g., H.E.S.S., MAGIC, VERITAS) have provided only upper limits on the γ-ray flux from clusters such as Coma and Perseus (e.g., Ackermann et al., 2016; H.E.S.S. Collaboration et al., 2023).

This thesis focuses on studying the global characteristics of galaxy clusters and interpreting the impact of cluster selection techniques based on these properties. Readers interested in the study of astronomical processes related to galaxy clusters can refer to e.g., Norman (2010); Reiprich et al. (2013); Bykov et al. (2015), while those seeking research on cosmology studies using galaxy clusters may refer to e.g., Voit (2005); Allen & Mantz (2019); Pratt et al. (2019); Migkas (2024).

Multiwavelength view of galaxy clusters

The multicomponent nature of galaxy clusters makes them detectable across a wide range of the electromagnetic spectrum. Main techniques for selecting galaxy cluster samples are summarized below:

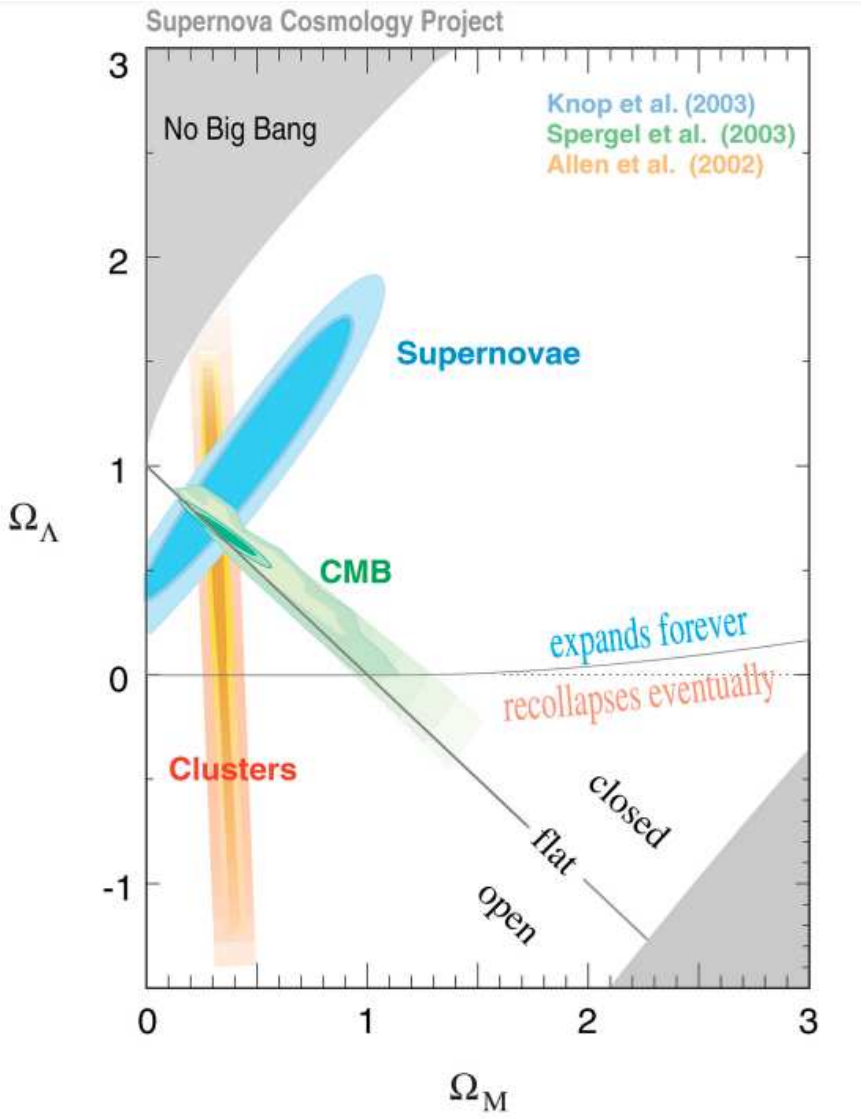

Figure 1.8: Example of cosmological parameters (matter density Ω_m, and dark energy density Ω_Λ) constraints using Type Ia supernovae, CMB data, and early *Chandra* cluster baryon fraction as probes. Credit: `http://supernova.lbl.gov/`, Perlmutter et al., The Supernova Cosmology Project.

- **In optical and near infrared (NIR):** In these wavebands, galaxy clusters are primarily detected through starlight. A key population of galaxies in clusters is the red sequence, which consists of galaxies that exhibit a distinct distribution in the color-magnitude diagram. These galaxies are typically gas-poor, leading to low star formation rates. Since red-sequence galaxies are abundant in clusters, their overdensity serves as a key marker for cluster detection in optical and NIR surveys. Based on this method, optical surveys such as HSC/Subaru can effectively select galaxy clusters. As an observational caveat, the red-sequence technique may lead to an underestimation of certain cluster populations, particularly blue clusters, which are more gas-rich and actively forming stars. Additionally, cluster samples selected in optical wavelengths rely on detecting overdensities along the line of sight using photometric redshifts, making them susceptible to projection effects. Cluster samples built on this technique include the MaxBCG (Koester et al., 2007) and the CAMIRA catalog (Oguri, 2014; Oguri et al., 2018) using the SDSS (Sloan Digital Sky Survey, York et al., 2000) and the Subaru Hyper Suprime-Cam instrument (Subaru HSC, Takada, 2010), respectively.

  Furthermore, in these wavebands, gravitational effect such as weak lensing (WL) can be used to detect clusters, based on the distortion of the appearance of background galaxies due to clusters' large scale extension and deep gravitational well (Zwicky, 1937). Weak lensing-based mass estimates are considered unbiased and robust; however, this method may sometimes result in mis-centering when determining cluster positions. Samples selected via this method are presented in e.g., Ramos-Ceja et al. (2022); Chiu et al. (2024).

- **In X-ray:** The primordial gas can be trapped, ionized, and heated by the deep gravitational well of galaxy clusters (e.g., Gull & Northover, 1975; Loewenstein, 2000; Cho, 2014). This hot, diffuse, and optically thin gas in the ICM emits X-ray radiation primarily through thermal bremsstrahlung (free-free transitions). Additionally, other processes, such as recombination (free-bound transitions) and line emission (bound-bound transitions), contribute to the X-ray flux in the form of emission lines. Figure 1.9 illustrates the X-ray spectrum of galaxy clusters for different plasma temperatures. The hottest plasma, with $k_B T_e = 9\,\mathrm{keV}$ (green), exhibits a stronger bremsstrahlung component and fewer emission lines. In contrast, lower-temperature plasmas ($k_B T_e = 3\,\mathrm{keV}$ and $k_B T_e = 1\,\mathrm{keV}$, shown in red and black, respectively) display more prominent line emission. The typical X-ray luminosity of clusters ranges from $L_X = 10^{43} - 10^{45}\,\mathrm{ergs}^{-1}$, making them among the most extended X-ray sources in the Universe.

  In general, X-ray flux-limited samples tend to favor more relaxed clusters with efficient cooling in their cores, which is called the "cool-core" bias (Pacaud et al., 2007; Hudson et al., 2010; Eckert et al., 2011; Andreon & Moretti, 2011; Xu et al., 2018). Relaxed clusters, which have centrally peaked X-ray profiles and high X-ray flux, are more easily detected by X-ray

telescopes. In contrast, disturbed clusters often exhibit flatter X-ray radial profiles, making them less likely to be identified in X-ray flux-limited surveys. Examples of X-ray selected samples include REFLEX (Böhringer et al., 2004) and HIFLUGCS (Zhang et al., 2011), both of which are based on ROSAT observations (Truemper, 1982).

- **In radio:** The CMB spectrum exhibits a perfect blackbody distribution (Danese & Burigana, 1994). However, CMB photons can be upscattered to higher frequencies by the electrons in the cluster's ICM, resulting in a distortion of the CMB spectrum observed from the cluster's direction. This is known as the (thermal) Sunyaev-Zel'dovich (SZ) effect (Sunyaev & Zeldovich, 1972), which has been used effectively to detect galaxy clusters since 2008 with the South Pole Telescope (SPT, Carlstrom et al., 2011). This detection technique, based on spectral distortion, does not depend on redshift, allowing for the selection of more distant objects compared to X-ray-based methods.

  Cluster samples selected using the SZ effect are typically characterized by a large proportion of massive clusters and extend to high redshifts, offering valuable probes for cosmological studies. The use of SZ cluster samples in comparisons with optical and X-ray selected datasets is crucial, as SZ samples are generally immune to the cool-core bias and projection effects. Such galaxy cluster samples (e.g., Vanderlinde et al., 2010; Ade et al., 2011) have been compiled using the South Pole Telescope (SPT, Carlstrom et al. 2011) and the Planck satellite (Planck Collaboration et al., 2011).

As explained above, each observational technique has its own strengths and weaknesses. Therefore the use of multiwavelength observation to complete the observed cluster population is of great importance.

1.2.3 Morphology and dynamical state of clusters

The deep gravitational wells of galaxy clusters trap the primordial gas, heating it to such extremes that clusters glow beautifully in X-ray light.

Generally speaking, relaxed clusters are assumed to be sufficiently virialized and to maintain hydrostatic equilibrium (e.g., Gull & Northover, 1975). Their X-ray images, which trace the hot gas distribution, exhibit a centrally peaked profile that smoothly declines outward. The brightest cluster galaxy (BCG), formed through galactic cannibalism (e.g., Dubinski, 1998; Katayama et al., 2003; De Lucia & Blaizot, 2007), outshines and outweighs the other cluster members. In relaxed clusters, the central positions observed in different wavelengths, such as the BCG in optical/near infrared and the X-ray peak, are closely aligned. Fig. 1.10 illustrates an example of a relaxed cluster.

On the other hand, clusters undergoing recent mergers tend to display disturbed morphologies in X-ray images. During a merger, the ICMs collide, causing strong shocks and turbulence.

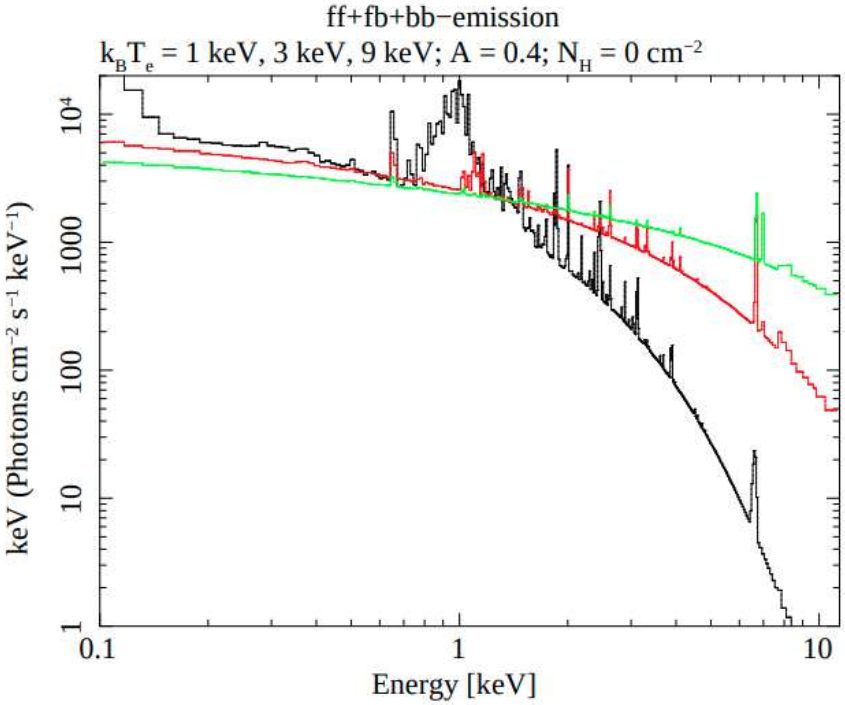

Figure 1.9: Galaxy cluster's spectra including free-free, free-bound, and bound-bound emission as function of gas temperature. The Fe L and Fe K shell line complexes at ~ 1 and ~ 6 keV are noticable. Figure taken from Reiprich et al. (2013).

Figure 1.10: Images of Abell 1835 (z = 0.25) at X-ray, optical, and mm wavelengths, centered at the X-ray peak position, with the same image scale of 5.2 arcminutes on each side. This is an example of a morphologically relaxed cluster. Credits: *Left, X-ray: Chandra* X-ray Observatory/A. Mantz; *Center, Optical:* Canada-France-Hawaii Telescope/A. von der Linden et al.; *Right, SZ:* Sunyaev-Zel'dovich Array/D. Marrone. Figure taken from Allen et al. (2011).

Figure 1.11: Multiwavelength view of six colliding galaxy clusters. In each panel, an optical image from Hubble Space Telescope (Jarzebowski, 1991) is overlaid with X-ray data (magenta) and weak lensing observations (blue). X-ray: NASA/CXC/Ecole Polytechnique Federale de Lausanne, Switzerland/D.Harvey & NASA/CXC/Durham Univ/R.Massey; Optical & Lensing Map: NASA, ESA, D. Harvey (Ecole Polytechnique Federale de Lausanne, Switzerland) and R. Massey (Durham University, UK)

Consequently, the gas content of the interacting clusters is further heated and redistributed. Figure 1.11 presents a gallery of six merging galaxy clusters. As seen in the *Chandra* images (shown in magenta), the ICM appears disrupted and displaced, whereas the collisionless galaxies, observed in the optical band, remain largely unaffected by these violent interactions. Meanwhile, the weak lensing (WL) signal, which traces the total mass (dominated by dark matter) and is shown in blue, exhibits a spatial offset from the hot gas. A more detailed discussion on the subclassification of galaxy cluster morphology can be found in, e.g., Jones et al. (1992).

Assessing a cluster's morphology, which provides insights into its dynamical state, is crucial. As mentioned in Section 1.2.1, galaxy clusters serve as powerful and uniform probes for constraining cosmological parameters, particularly via the cluster mass function. However, if mass estimates suffer from large uncertainties due to mass proxies being sensitive to cluster dynamics, the resulting cosmological constraints will have significant scatter. Therefore, accurately characterizing the dynamical properties of clusters is essential for cosmological studies. Morphological indicators can be used to classify clusters as relaxed or disturbed, based on either the presence of substructures or the properties of the cluster core. Commonly used X-ray morphological indicators include the centroid shift (e.g., Mohr et al., 1995) and the concentration parameter (e.g., Santos et al., 2008; Rasia et al., 2013; Parekh et al., 2015). In this work, we focus on studying the X-ray properties of an optically selected cluster sample, using the BCG – X-ray peak offset as a primary diagnostic of cluster dynamics. In cases where sufficient observational data are not available for all cluster members, simulations can help predict the relaxed fraction of the sample (e.g., Seppi et al., 2023).

1.2.4 The self-similar model and cluster scaling relations

Galaxy clusters mirror each other across scales, like cosmic Russian dolls.

In a hierarchical structure formation scenario, galaxy clusters form through the merging of smaller-scale structures. Both theoretical predictions and observations indicate that clusters exhibit strong internal correlations between their mass and other properties. In other words, clusters can be considered scaled-up or scaled-down versions of each other (see, e.g., Rosati et al., 2002; Voit, 2005; Giodini et al., 2013; Lovisari & Maughan, 2022; Migkas, 2024 for comprehensive reviews). The self-similar model (Kaiser, 1986) describes the scaling relations between cluster observables using power-law functions, derived from the virial theorem under the assumption that clusters are in dynamical equilibrium.

Cluster scaling relations serve as essential tools for both cosmological and astrophysical studies. In a cosmological context, these relations are employed to connect the predicted spatial abundance of massive halos as a function of mass to the observed distribution of galaxy clusters across different wavelengths. This approach enables the use of cluster number counts to constrain cosmological parameters (e.g., Vikhlinin et al., 2009; Henry et al., 2009; Mantz et al., 2010; Rozo

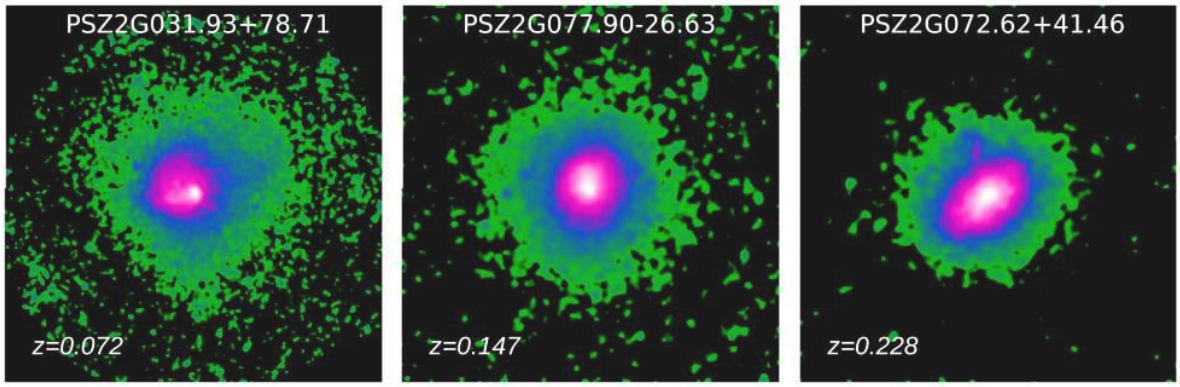

Figure 1.12: Smoothed *XMM-Newton* images of clusters of different mass at different redshift, scaled such that each image is $2.4R_{500}$ on a side. From left to right, cluster masses are $M_{500} \approx 3 \times 10^{14} M_{\odot}$, $M_{500} \approx 5 \times 10^{14} M_{\odot}$ and $M_{500} \approx 11 \times 10^{14} M_{\odot}$, respectively. Figure taken from Lovisari & Maughan (2022), an adaptation from CHEX-MATE Collaboration et al. (2021).

et al., 2010).

In an astrophysical context, scaling relations are particularly effective when non-gravitational processes are not negligible, making them valuable tools for studying the hot gas content of the ICM and the evolution of galaxy clusters (e.g., Evrard & Henry, 1991; Kaiser, 1991; Reiprich & Böhringer, 2002; Rozo et al., 2014). Below, we summarize the most relevant scaling relations for this thesis, with a primary focus on the optical and X-ray properties of clusters. For a more detailed discussion, interested readers are referred to Lovisari & Maughan (2022) and references therein.

The critical density of the Universe at a cluster's redshift is defined as:

$$\rho_c(z) = \frac{3H(z)^2}{8\pi G}. \tag{1.5}$$

In which, $H(z) = E(z)H_0$ is the Hubble parameter, with H_0 denoting the present day Hubble constant, and the redshift evolution term is given by:

$$E(z) = \sqrt{\Omega_{\rm M}(1+z)^3 + \Omega_k(1+z)^2 + \Omega_{\Lambda}}. \tag{1.6}$$

Here, $\Omega_{\rm M}$ and Ω_{Λ} are baryonic matter density and cosmological constant, respectively. The term $\Omega_k = (1 - \Omega_{\rm M} - \Omega_{\Lambda})$ corresponds to the curvature of the Universe. For a flat cosmology, $\Omega_k = 0$. Due to the expansion of the Universe, both the Hubble parameter and the critical density evolve as a function of time, with ρ_c being higher at higher redshifts.

An overdensity radius R_{Δ} is described in relation to the mass M_{Δ} enclosed within a sphere of

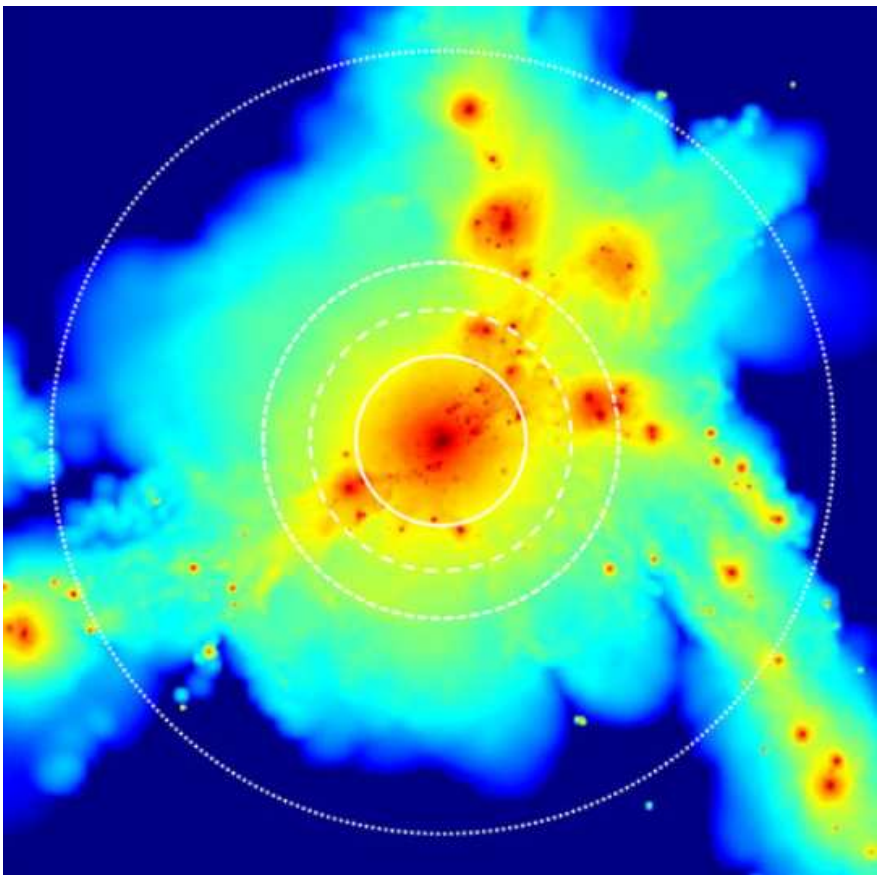

Figure 1.13: X-ray surface brightness in the soft-band (0.5-2.0) keV of simulated galaxy cluster. The white circles denote r_{500}, r_{200}, $r_{\rm vir}$, and $3\,r_{200}$ moving outwards, respectively (adapted from Roncarelli et al., 2006). Figure taken from Reiprich et al. (2013).

R_Δ as follows:

$$\frac{M_\Delta}{\frac{4}{3}\pi R_\Delta^3} = \Delta\rho_c(z). \tag{1.7}$$

In cluster studies using X-ray observations, it is common to adopt $\Delta = 500$ and measure the characteristic radius R_{500}, as this radius is optimal for measuring the ICM properties with current instruments. Fig. 1.12 illustrates the self-similar appearance of galaxy clusters with *XMM-Newton* observations, where the X-ray images are scaled to a size of $2.4R_{500}$. Despite variations in residual background emission, the overall appearance of these clusters remains similar. The properties of galaxy clusters measured within a defined overdensity (as mentioned above, usually R_{500}, though larger radii such as R_{200} are often used in the literature, particularly when studying processes at the cluster outskirts, see Fig. 1.13) are expected to scale with cluster mass following a simple power-law relation. Since the critical density evolves as a function of redshift, using overdensity radii in scaling relations also implies that cluster properties evolve with redshift. Specifically, for a given mass, clusters that formed earlier were denser (see Equation 1.7), and therefore are expected to be hotter and more luminous.

The X-ray luminosity - cluster mass ($L-M$) relation

The bolometric bremsstrahlung luminosity of the ICM is given by:

$$L_{\rm bol} \propto \int \varepsilon {\rm d}V \propto \int \rho_{\rm gas}^2 T_{\rm X}^{1/2} {\rm d}V, \tag{1.8}$$

where $\rho_{\rm gas}$ and V denote the density of the ICM and the volume of the cluster, respectively. Assuming that the ICM is isothermal, such that $T_{\rm X}$ remains constant, we obtain:

$$L_{\rm bol} \propto \rho_{\rm gas}^2 T_{\rm X}^{1/2} R^3. \tag{1.9}$$

Combining this with Equation 1.7, we obtain:

$$L_{\rm bol} \propto E(z)^2 M T^{1/2}. \tag{1.10}$$

If the ICM can be approximated by a single-temperature component $T_{\rm X}$, and if the ionized plasma particles are in virial equilibrium with the cluster's gravitational potential, then the virial theorem gives:

$$T_{\rm X} \propto \frac{M}{R}. \tag{1.11}$$

Substituting R from Equation 1.7, we obtain:

$$T_{\rm X} \propto E(z)^{2/3} M^{2/3}. \tag{1.12}$$

Finally, substituting Equation 1.12 into the bolometric luminosity expression to eliminate $T_{\rm X}$, the self-similar scaling relation for bolometric X-ray luminosity as a function of mass is:

$$\boxed{L_{\rm bol} \propto E(z)^{7/3} M^{4/3}}. \tag{1.13}$$

For soft-band X-ray luminosity (typically in the 0.5–2.0 keV range), the bremsstrahlung emissivity is largely independent of temperature, leading to:

$$L_{\rm soft} \propto E(z)^2 M. \tag{1.14}$$

The X-ray luminosity - temperature ($L-T$) relation

From Equations 1.7 and 1.13, we derive the self-similar scaling relation between bolometric X-ray luminosity and temperature as follows:

$$\boxed{L_{\rm bol} \propto E(z) T^2}. \tag{1.15}$$

For soft-band luminosity, the corresponding relation is:

$$L_{\rm soft} \propto E(z)T^{3/2}. \tag{1.16}$$

However, observational studies have reported steeper slopes for these relations. In particular, the best-fit power-law slope for the $L_{\rm bol} - T$ relation is often found to be around ~ 3, while for $L_{\rm bol} - T$, it is approximately ~ 2.5. This discrepancy suggests that the assumptions of the self-similar model may not be entirely valid.

Furthermore, conflicting results have been reported regarding the redshift evolution of scaling relations. Some studies find agreement with the self-similar evolution (e.g., Maughan, 2007; Pacaud et al., 2007; Bulbul et al., 2019), while others show no significant redshift trend (e.g., Vikhlinin et al., 2009; Chiu et al., 2018; Bahar et al., 2022). Investigating the redshift evolution of scaling relations requires a uniform sample that extends to high redshifts, making this task particularly challenging.

Optical richness - cluster mass ($N - M$) relation

One key aspect of studying cluster scaling relations is the estimation and calibration of various mass proxies. Observations have shown that stellar content related parameters, such as optical richness (N, the number of galaxies of a cluster above the detection threshold), exhibit a strong correlation with cluster mass and can be used as a mass proxy. This provides a complementary approach to other commonly used methods, such as X-ray gas mass estimates. Unlike mass estimation via weak lensing calibration, mass estimates derived from optical richness are relatively inexpensive, requiring only direct imaging of intermediate depth, even for high-redshift clusters. Additionally, this method is effective for low-mass groups, which often contain too few galaxies for a robust dynamical mass measurement.

However, observational studies also indicate that the relation between optical properties and cluster mass exhibits significant scatter, primarily due to the large Poisson noise associated with the small number of galaxy members. Although deriving the $N - M$ relation is not straightforward and does not directly follow from simple physics scaling laws, it is expected that more massive halos host more galaxies. Furthermore, the richness–mass relation is influenced by galaxy formation efficiency and non-gravitational processes such as mergers and tidal stripping of galaxies.

Observations often find that the dependence of optical richness on cluster mass is approximately linear:

$$\boxed{NE(z) \propto ME(z)} \tag{1.17}$$

Such an empirical relation has been reported in various studies (e.g., Rozo & Rykoff, 2014; Oguri,

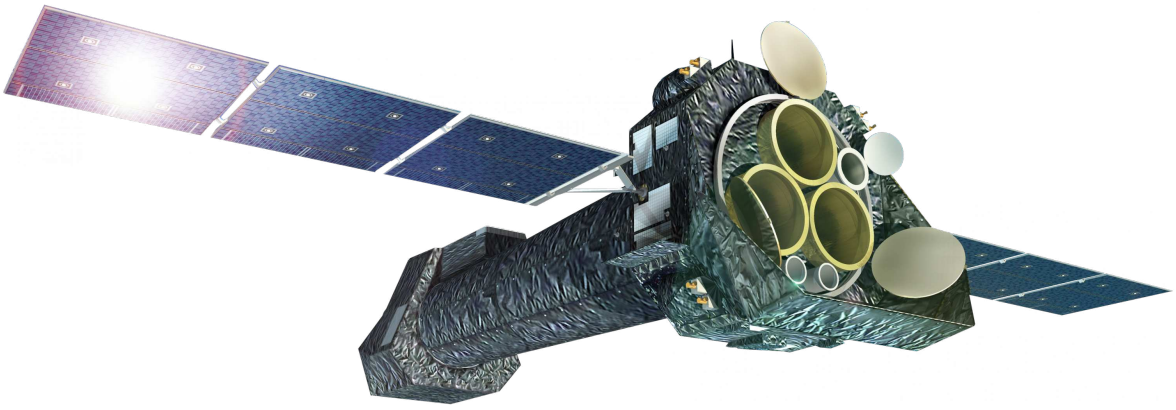

Figure 1.14: Artist impression of *XMM-Newton* satellite in flight. Credit: https://science.nasa.gov/toolkits/spacecraft-icons.

2014; Saro et al., 2015; Murata et al., 2019; Chiu et al., 2020; Bleem et al., 2020; Kiiveri et al., 2021; Grandis et al., 2021).

1.3 Instruments

"O telescope, instrument of knowledge, more precious than any sceptre."
— Johannes Kepler

Using the hot and diffuse plasma generated by SNR shock waves and the gravitational wells of galaxy clusters as primary diagnosis to investigate the objects, the main instruments of this thesis are X-ray telescopes (*XMM-Newton* and SRG/eROSITA). Here we briefly introduce these two main related observatories and place them in the context of the research overview.

1.3.1 *XMM-Newton*

The X-ray Multi-Mirror Mission (*XMM-Newton*) X-ray observatory was launched in 1999 into a high Earth orbit (HEO) and remains operational to this day (Fig. 1.14, Jansen et al., 2001; Schartel et al., 2022). It carries three Wolter type I telescopes and an Optical/UV Monitor (OM). The observatory is equipped with two EPIC MOS cameras and a PN camera, providing high sensitivity and large effective area ($\sim$ 4,250 cm^2 at 1 keV), making it one of the most powerful X-ray observatories. The field of view (FoV) extends to 30 arcminutes, covering an energy range of 0.12-12 keV, which is well-suited for studying hot gas in galaxy clusters, SNRs, and other high-energy astrophysical phenomena. The point spread function (PSF) at 1.5 keV is approximately 17 arcseconds, ensuring good spatial resolution, while its excellent spectral resolution allows for detailed spectroscopic studies.

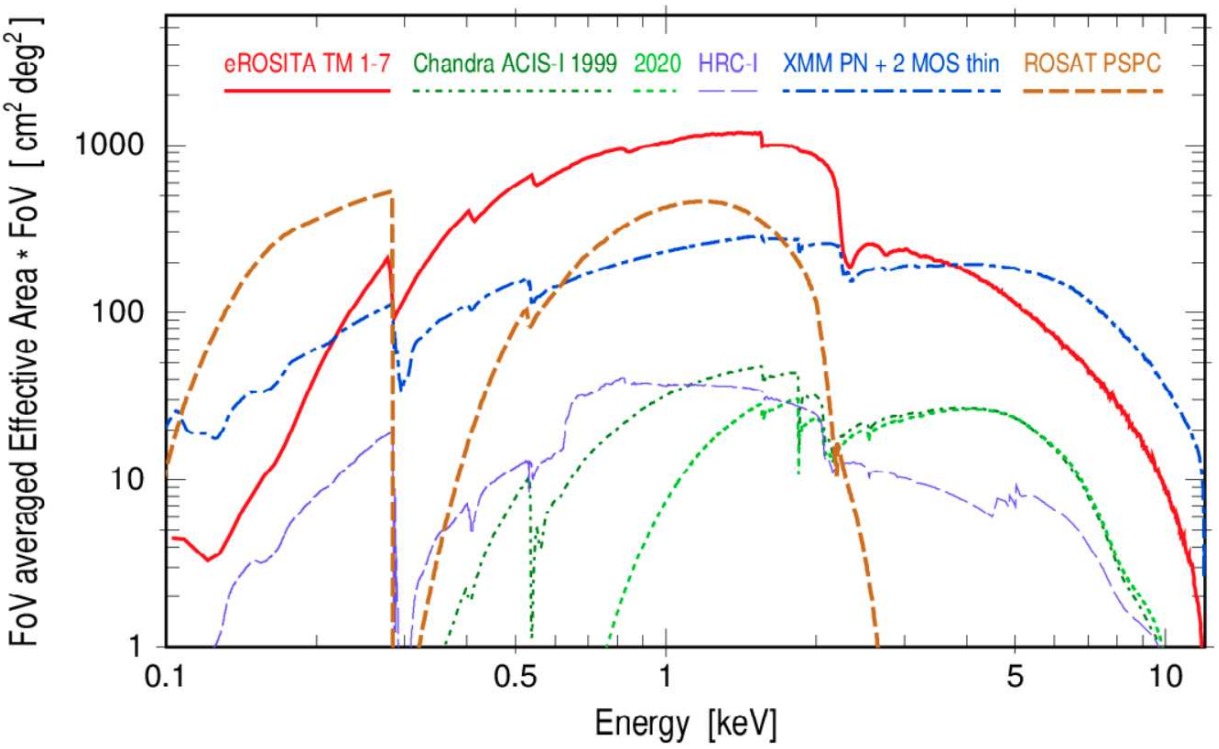

Figure 1.15: On-axis effective areas as a function of energy for various X-ray instruments. Figure taken from Predehl et al. (2021)

Despite *XMM-Newton*'s FoV being comparable to or smaller than typical Galactic SNRs, spectral studies of extended sources can be performed using filter wheel closed (FWC) data to aid background modeling. When the FoV does not fully cover the source, a portion of the observed region can serve as a simultaneous background reference. Observations of Galactic SNRs and extragalactic galaxy clusters generally avoid pile-up effects (which occur when the source is too bright for the detector), but contamination from nearby X-ray-bright sources or transients must be carefully handled. Despite the loss of one CCD and the damage of one CCD in MOS1, *XMM-Newton* remains a reliable instrument for such studies.

In the context of SNR research, *XMM-Newton* has played a key role in identifying new remnants and confirming the SNR nature of TeV-selected sources. Its combination of high sensitivity and spatial resolution enables detailed investigations of shock fronts and the surrounding medium, providing crucial insights into the physics of supernova explosions and their impact on the ISM. For galaxy cluster studies, *XMM-Newton* offers detailed follow-ups of previous X-ray selected cluster samples, such as those from ROSAT-based. Its large FoV enables studies of large-scale cluster environments, including diffuse gas bridges connecting merging clusters (e.g., the Abell 3395/Abell 3391 system, Tümer et al., 2022; Alvarez et al., 2018), providing valuable data on large-scale structure formation and ICM physics.

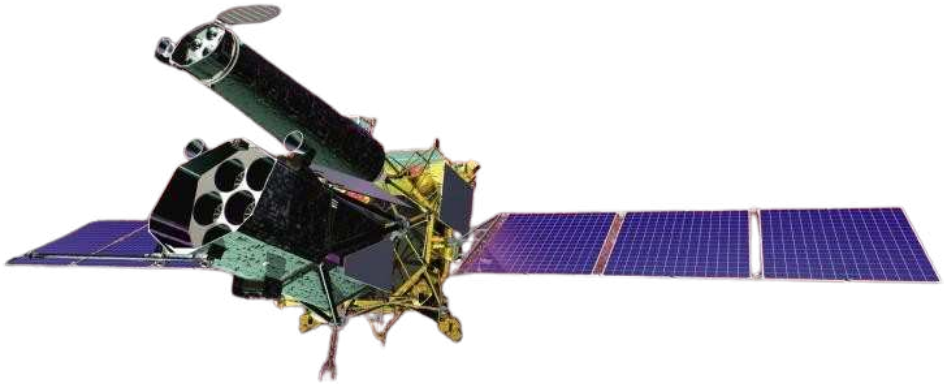

Figure 1.16: Artist impression of the SRG observatory in flight. Credit: `https://iki.cosmos.ru/en/research/missions/spektr-rg`, ©Lavochkin Association.

1.3.2 eROSITA

The extended ROentgen Survey with an Imaging Telescope Array (eROSITA) is the primary X-ray instrument aboard the Russian-German Spektrum-Roentgen-Gamma (SRG) mission (Fig. 1.16, Merloni et al., 2012; Predehl et al., 2021; Merloni et al., 2024). Launched on July 13, 2019, it operates in an orbit around the second Lagrange point (L2). The primary science goals include detecting $\sim$ 100,000 galaxy clusters and groups, $\sim$ millions of AGNs, and various Galactic X-ray sources such as SNRs and X-ray binaries. The German consortium is responsible for the western half of the Galactic hemisphere. The eROSITA Final Equatorial Depth Survey (eFEDS, Liu et al., 2022) was conducted during the calibration and performance verification (Cal-PV) phase as a test field to showcase eROSITA's capabilities. The term 'Final' refers to the dedicated exposure equivalent to eight full scans of the X-ray sky, with an exposure time of approximately $\sim$ 2.2 ks before applying vignetting corrections.

eROSITA operates in the 0.2-10.0 keV energy range in an all-sky survey mode. Its sensitivity in the soft X-ray band (0.5–2.0 keV) is 25 times higher than that of ROSAT (Fig. 1.15). The instrument consists of seven telescope modules (TMs), with TM5 and TM7 lacking optical filters, leading to known light leak issues. The spatial resolution at 1.5 keV is 16 arcseconds (half-energy width, HEW). Each sky tile covers an area of $3.6^\circ \times 3.6^\circ$.

Recent report by Merloni et al. (2024) shows that eROSITA has identified 60% more sources than previously reported in the literature. Although not primarily designed for SNR research, it has demonstrated significant advancements in this field. eROSITA is particularly effective for studying large-scale structures, including galaxy clusters, which would otherwise require extensive observations with telescopes like *XMM-Newton* (Jansen et al., 2001) and *Chandra* (Weisskopf et al., 2000). Example of such improvement with eROSITA observations includes e.g., the Abell 3395/Abell 3391 system (Veronica et al., 2022, 2024). The complex X-ray background is carefully analyzed by the eROSITA team. The combination of large sky coverage and high sensitivity in the soft X-ray band marks a new era in X-ray astronomy.

CHAPTER 2

Objectives and expected outcome of the research

The aim of this dissertation is to explore the Universe in one of the most energetic ranges of the electromagnetic spectrum. On the one hand, the study of SNRs presented in this thesis provides direct view into the most tremendous events of the Universe, offering insights into the physical processes at the particle scale. On the other hand, the study of galaxy clusters contributes to our understanding of the formation and evolution of large-scale structures in the Universe.

2.1 Multiwavelength study of Galactic Supernova remnants

SNRs are believed to be the main source of the observed Galactic CRs. The primary objective of this research is to investigate the physical properties of the shock-heated plasma in SNRs and the role of SNRs as CR accelerating engines. Using multiwavelength observations, particularly in the X-ray and radio domains, this study aims to characterize the morphology and spectral properties of a special class of TeV-emitting SNRs.

The expected outcomes for the SNR HESS J1534-571 and the SNR candidate HESS J1614-518 include:

- **Comprehensive X-ray imaging and spectral analysis:** A detailed study of X-ray data from $XMM-Newton$, *Suzaku*, and eROSITA to characterize the structure, emission processes, and overall morphology of the remnants.
- **Broadband SED modeling and constraints on γ-ray origins:** Integration of the computed X-ray and radio fluxes into the broadband SED observed from the SNRs. Constructed emission models will constrain γ-ray production mechanisms and investigate their connection to particle acceleration processes.

- **Investigation of the 6.4 keV Fe K-α line:** Estimation of the strength of the Fe Kα line to probe interactions between low-energy CR protons and ambient cool gas for HESS J1534-571, shedding light on the surrounding medium's properties, and on the existence of admittedly low energy CRs.
- **Additional insights into SNR properties:** Estimation of key properties for HESS J1534-571 and HESS J1614-518, including potential associations with nearby objects, and distance to Earth.
- **Advancing understanding of SNR physics:** By achieving these objectives, the research aims to advance knowledge of SNR physics, including the mechanisms of particle acceleration and cosmic-ray interactions, contributing to a better understanding of VHE phenomena in the Milky Way.

2.2 Multiwavelength study of galaxy clusters

Galaxy clusters are the largest scale structures in the Universe, located at the nodes of matter concentration within the cosmic web. On the one hand, they serve as vital probes for cosmological research. For example, a cluster sample with high completeness and purity, coupled with a significant fraction of relaxed and virialized members, provides a robust dataset for constraining cosmological parameters through the cluster mass function (e.g., von der Linden et al., 2014; Mantz et al., 2015). On the other hand, dynamically active clusters, such as those undergoing recent mergers or experiencing significant heating from active galactic nucleus (AGN) activity, act as natural laboratories for exploring large-scale gas physics (e.g., Molnar, 2016; Bourne & Sijacki, 2021). Understanding the population of clusters within a given sample is therefore crucial for advancing both cosmological studies and astrophysical research.

The objective of the second part of this dissertation is to study the X-ray properties of optically selected galaxy clusters, with the goal of evaluating the impact of cluster selection methods on their observed properties and the underlying cluster population. Specifically, this research focuses on the CAMIRA optical cluster catalog in the eFEDS footprint (140 deg^2). The expected outcomes for the high richness (Ota et al., 2023) and low richness (Nguyen-Dang et al., submitted 2025) collections of optical CAMIRA clusters in the X-ray eFEDS field include:

- **Systematic identification of brightest cluster galaxies (BCGs) for optical clusters in the eFEDS field:** BCGs, which represent the cluster center in the optical window, will be identified systematically using public optical and infrared databases. Combined with the X-ray peak determined from eROSITA imaging analysis, this will enable morphological diagnostics and an estimation of the fraction of relaxed clusters in the sample.

- **Evaluate the dynamical state of the sample:** Other morphological indicators provided by the eFEDS team are utilized to independently assess the relaxed fraction of the cluster sample.
- **Calculation of X-ray observables and cluster mass:** Key X-ray properties such as luminosity and temperature (the latter is applicable for the high-richness clusters via spectral fitting) are derived. Weak-lensing calibrations will be used to estimate cluster masses.
- **Apply stacking analysis:** For the low richness collection, which consists of $\sim$ 1000 objects, we stack the clusters following similar richness and redshift to improve the statistical robustness.
- **Establish the cluster scaling relations:** Scaling relations are established based on these parameters. A fitting routine taking into account the selection effect is employed to obtain the best-fit of the relations.
- **Comparison with literature:** The properties derived from the CAMIRA clusters will be compared with those from cluster samples selected using alternative methods, such as X-ray or Sunyaev-Zeldovich (SZ) selection. These comparisons permit conclusions on how selection techniques influence sample properties and cluster populations.

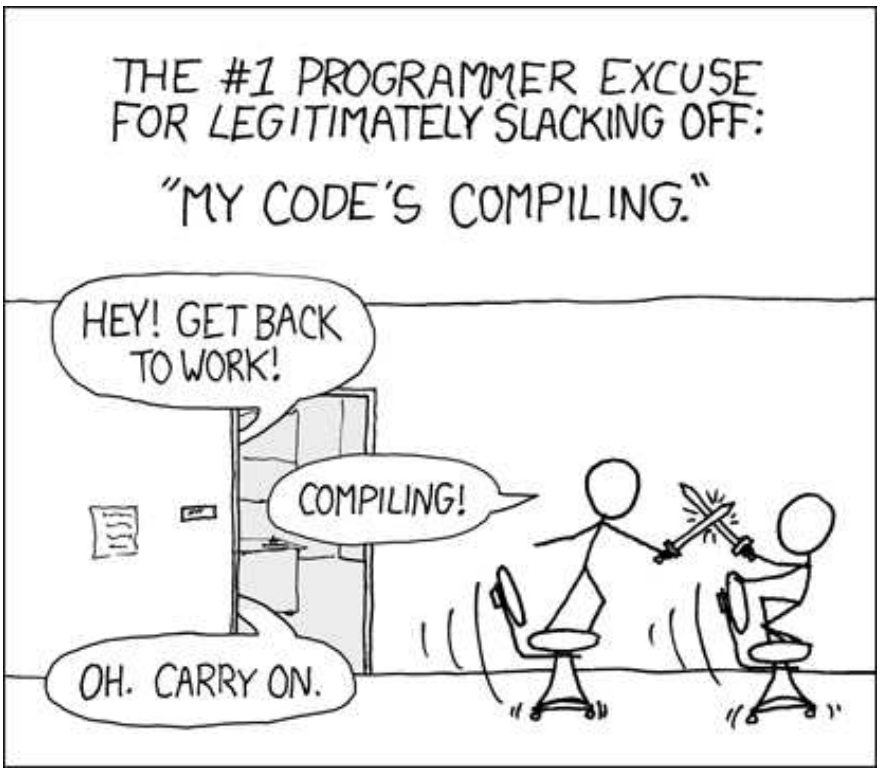

Figure 2.1: Some of the codes and analyses in this work took quite a while to run. This figure captures one of those moments that I truly enjoyed during my doctoral research. Credit: ©`https://xkcd.com/303/`

CHAPTER 3

List of publications

In this chapter, we present the original works that are published and being reviewed for acceptance. Further interpretation of the results will be discussed in Chap. 4.

3.1 Multiwavelength study of Galactic Supernova remnants

3.1.1 *XMM-Newton* observation of the TeV-discovered Supernova remnant HESS J1534-571

Observations and theories indicate that SNRs are responsible for the production and acceleration of Galactic CRs (e.g., Bell et al., 2013; Giuffrida et al., 2022; Abe et al., 2025). While tracing the high energy CRs directly from the source is challenging owing to the potential interactions between these particles and the surrounding medium, it is feasible to track down the radiation produced by the above processes with TeV telescopes. At the same time, X-ray astronomy opens the window to study the highly energetic electrons produced at the SNR via synchrotron (non-thermal emission) as well as the shock-heated plasma component (thermal emission).

We report the results obtained from a joint analysis between *XMM-Newton* and *Suzaku* observatories of the TeV-detected SNR HESS J1534-571. In this work, we use *XMM-Newton* observational data to search for X-ray emissions from the source. A broadband spectral analysis, spanning the radio to TeV domains, was conducted to explore scenarios of CR production and acceleration. No signatures of X-ray synchrotron or thermal emission were detected from the SNR. For the first time, an upper limit of the non-thermal flux is derived in the energy band 2-10 keV for the entire SNR, which places constraints on the relativistic leptonic particle content in the SNR. Furthermore, evidence of a line-like emission is detected at 6.4 keV from localized regions. The result agrees with earlier results obtained with Suzaku from other regions of the object Saji et al. (2018). The emission can be interpreted as the result of interactions between lower energy (at around MeV) CR protons with high gas density regions in and around HESS J1534-571, and thus

potentially be associated with particles accelerated in the SNR.

A&A, 679, A48 (2023)
https://doi.org/10.1051/0004-6361/202346448

Astronomy & Astrophysics

XMM-Newton observation of the TeV-discovered supernova remnant HESS J1534-571

N. T. Nguyen-Dang[1], G. Pühlhofer[1], M. Sasaki[2], A. Bamba[3,4,5], V. Doroshenko[1], and A. Santangelo[1]

[1] Institut für Astronomie und Astrophysik Tübingen (IAAT), Sand 1, 72076 Tübingen, Germany
e-mail: dang-thanh-nhan.nguyen@astro.uni-tuebingen.de
[2] Dr. Karl Remeis Observatory, Erlangen Centre for Astroparticle Physics, Friedrich-Alexander-Universität Erlangen-Nürnberg, Sternwartstraße 7, 96049 Bamberg, Germany
[3] Department of Physics, Graduate School of Science, The University of Tokyo, 7-3-1 Hongo, Bunkyo-ku, Tokyo 113-0033, Japan
[4] Research Center for the Early Universe, Graduate School of Science, The University of Tokyo, 7-3-1 Hongo, Bunkyo-ku, Tokyo 113-0033, Japan
[5] Trans-Scale Quantum Science Institute, The University of Tokyo, 7-3-1 Hongo, Bunkyo-ku, Tokyo 113-0033, Japan

Received 17 March 2023 / Accepted 17 July 2023

ABSTRACT

We report the results obtained from *XMM-Newton* observations of the TeV-detected supernova remnant (SNR) HESS J1534-571. We focus on the nature of the cosmic-ray particle content in the SNR, which is revealed by its γ-ray emission. No signatures of X-ray synchrotron emission were detected from the SNR. This is consistent with earlier results obtained with *Suzaku* from other regions of the object. A joint modeling of the *XMM-Newton* and *Suzaku* spectra yields an upper limit for the total X-ray flux from the SNR area of $\sim 5.62 \times 10^{-13}$ erg cm^{-2} s^{-1} (95% C.I.) in the energy band of 2.0–10.0 keV for an assumed photon index of 2.0. On the other hand, we do find evidence in the *XMM-Newton* data for a line-like emission feature at 6.4 keV from localized regions, again confirming earlier *Suzaku* measurements. We discuss the findings in the context of the origin of the observed γ-ray emission. Although neither hadronic nor leptonic scenarios can be fully ruled out, the observed line emission can be interpreted as the result of interactions between lower-energy ($\sim$ MeV) cosmic-ray protons with high gas-density regions in and around HESS J1534-571, and thus potentially be associated with particles accelerated in the SNR.

Key words. gamma rays: ISM – astroparticle physics – ISM: supernova remnants – cosmic rays – X-rays: individuals: HESS J1534-571

1. Introduction

Supernova remnants (SNRs) are generally considered the most relevant sources of energy input for Galactic cosmic rays (CRs) (Ginzburg & Syrovatskii 1964; Hillas 2005). The main arguments are the required kinetic energy per unit time, and the fact that diffusive shock acceleration (Bell & Lucek 2001; Bell 2004) is a well-established particle acceleration mechanism, in agreement with many observational parameters (Blandford & Eichler 1987; Malkov & Drury 2001; Jones & Ellison 1991). A quantitative probe of this scenario is the electromagnetic emission from the accelerated particles in and around the sources. To specifically probe the high end of the leptonic particle spectra, X-ray synchrotron and TeV γ-ray inverse Compton (IC) emission are the relevant channels (Reynolds 1998). The hadronic component, which is energetically relevant from the CR standpoint, can only be probed in γ-rays (through the π^0 decay process), with the high end of the spectrum at TeV-PeV photon energies (Sturner et al. 1997; Drury et al. 1994).

Young SNRs with ongoing particle acceleration toward the highest energies are key targets for the study of CR acceleration, specifically because the escape of particles upstream of the forward shock plays a strong role in modifying the particle spectrum soon after the shock is slowing down. However, the typically high synchrotron fluxes and the lack of spectra extending to $\sim$100 TeV are the motivation for the preference for a leptonic interpretation of the γ-ray spectra in several cases, despite the need to invoke low magnetic fields in the bulk of the emission regions (well below the $\sim$100 μG levels needed for efficient highest-energy particle acceleration, Hillas 2005). TeV-selected SNRs, which should still be (moderately) young given their TeV dominance and by definition presenting low levels of synchrotron emission, are therefore important targets in view of a potential hadronic dominance of the γ-ray emission, which would permit a direct view of the hadronic energetics of the objects.

This motivates a detailed study of HESS J1534-571 as presented in this paper. HESS J1534-571 is one of only three objects that were classified as SNR candidates after their discovery in TeV γ-rays based on a morphological characterization of new objects discovered in the High Energy Spectroscopic System (H.E.S.S.) Galactic plane survey (H.E.S.S. Collaboration 2018a). From the subsequent identification with the SNR candidate SNR G323.7–1.0 found in archival radio continuum data from the Molonglo Galactic Plane Survey (MGPS; Green et al. 2014), HESS J1534-571 was then classified as a confirmed SNR. No clear X-ray counterpart of the SNR shell has been found so far, with the best limits for the nonthermal X-ray emission obtained with *Suzaku* (Mitsuda et al. 2007) observations of a fraction of the shell, yielding 2.4×10^{-11} erg cm^{-2} s^{-1} in the energy band 2.0–12.0 keV assuming a power-law model of index 2 and scaling to the full SNR area (H.E.S.S. Collaboration 2018a). The object has a diameter of $\sim$0.8° and requires several pointings of current (e.g., the X-ray Multi-Mirror Mission, *XMM-Newton*, Aschenbach et al. 2000) or recent X-ray (e.g., *Suzaku*) satellites

for full coverage. Here, we present results obtained from a ∼25 ks *XMM-Newton* pointing covering the previously unobserved part of the SNR. Similar to the *Suzaku* observations that covered the other parts of the shell, no evidence for X-ray synchrotron emission is found. Using both data sets together, we obtain robust constraints on the X-ray emission from the entire shell for the first time, and we discuss the results in the context of the origin of the observed γ-ray emission from the object.

In addition to synchrotron emission from relativistic electrons and plasma emission (bremsstrahlung and thermally excited fluorescence emission lines), cold gas can also give rise to fluorescence lines in X-ray spectra of SNRs. This process occurs when low-energy CR protons interact with nearby cool gas, where the collisional excitation is then followed by radiative deexcitation. In particular, the fluorescence yield of neutral ion (Fe I) for a deexcitation to K-shell transition is 34%, much higher than other atoms such as neutral silicon at 5% or neutral oxygen at 0.8% (Krause 1979; Kallman et al. 2004; Vink 2012). Due to the high fluorescence yield and the relatively high abundance, the Fe Kα line at 6.4 keV is an important diagnostic channel for studying SNRs and the properties of nearby molecular clouds. Evidence for this line has been widely found for different SNRs, such as W28, Kes67, Kes69, Kes78, and W44 (Nobukawa et al. 2018). Saji et al. (2018) reported the existence of such a line in the *Suzaku* observations of HESS J1534-571 at a 4 σ significance level. We have extended the investigation of this line to the *XMM-Newton* data presented in this work.

A search for a possible gas association of the source conducted by Maxted et al. (2018) using Mopra CO Galactic Plane Survey data (Burton et al. 2013) and the Southern Galactic Plane Survey HI data (McClure-Griffiths et al. 2005) indicated that the SNR might be located inside the Scutum-Crux arm and could stem from a core-collapse event at a kinematic distance of ∼3.5 kpc. In this paper, we adopt this distance estimate.

The paper is organized as follows: in Sect. 2 we describe the *XMM-Newton* observations and the data reduction. In Sect. 3 we describe the obtained results and place them in the context of broadband spectral models describing the emission from assumed nonthermal particle populations. The results are further discussed in Sect. 4 and are placed in the context of the results for other SNRs. We conclude with a summary in Sect. 5.

2. Observations and data reduction

The first attempt to observe HESS J1534-571 with *XMM-Newton* (Lumb et al. 2012) was cancelled due to the outburst of a transient source in the field of view. Close to the geometrical center of HESS J1534-571, a previously unknown X-ray binary (XRB) was discovered with the MAXI/GSC instrument in 2017 (Negoro et al. 2017) and independently with *Swift*/BAT (Kostrzewa-Rutkowska et al. 2017), named MAXI J1535-571. Because the distances are uncertain, an association between the two objects can neither be claimed nor be disputed at the moment. Observationally, when the XRB is in outburst, *XMM-Newton* observations of the SNR shell are impossible because the wings of the point spread function (psf) pollute the entire European Photon Imaging Camera (EPIC) field of view (FoV). Therefore, observations that had been approved for 2017 had to be called off, and we were only able to obtain observations in 2020. The parameters of the *XMM-Newton* observation of HESS J1534-571 are shown in Table 1.

For the data reduction, we used the *XMM SAS* software version 20201028_0905-19.0.0. In particular, the work package *XMM-Newton* Extended Source Analysis Software (XMM-ESAS) was employed. In order to obtain images and spectra of the source, we followed the standard steps as recommended in the XMM-ESAS cookbook[1].

Table 1. *XMM-Newton* and *Suzaku* data.

Observation ID	Dates	Exposure time (ks)	Instruments
		24.07	MOS1
0841440101	2020-Mar.-03	24.51	MOS2
		17.07	PN
508013010	2013-Sep.-08	36.9	XIS0-3
508014010	2013-Sep.-09	36.9	XIS0-3
508015010	2013-Sep.-09	36.9	XIS0-3
508016010	2013-Sep.-10	36.9	XIS0-3

First, the standard reprocessing was applied using the ESAS task *epchain, emchain*. The events were then filtered for soft proton flares, and at the same time, assorted diagnostic files were created using *pn-filter, mos-filter* with the default criteria. The MOS CCDs were operated in full-frame mode. After examining the CCDs for their anomalous states, we excluded CCD 3 and CCD 6 of EPIC MOS1 from the analysis. MOS1 CCD 6 was lost due to the micrometeorite strike in March 2005, and MOS1 CCD 3 was damaged in December 2012. Point sources were listed for later removal from the entire FoV using the task *cheese*, applying a flux threshold at 1×10^{-14} ergs cm^{-2} s^{-1}.

Consequently, spectra, response files, and the model particle background spectra and images were produced with the use of the filter-wheel-closed (FWC) data via the tasks *pn-spectra, mos-spectra*. Finally, tasks *pn_back, mos_back* were run to create quiescent particle background files. The pipeline makes use of the data from unexposed corners of the cameras, FWC data as well as the *ROSAT* All-Sky Survey, in order to estimate the contribution of CRs (Kuntz & Snowden 2008). The spectra were then grouped by the HEASOFT FTOOLS command *grppha*, with 50 counts per bin at least. The coverage areas of each instrument were calculated by the task *proton_scale*. The spectral analysis was carried out with the *xspec* software version 12.11.1b.

The *XMM-Newton* images presented in this work are vignetting corrected, background subtracted, and point-source removed. After the initial screening and filtering, residuals from the soft proton contamination might still be present in the images and spectra. In order to take these soft proton residuals into account in addition to the models that represent the main spectra, we added a power-law model that was not folded with the instrumental effective areas. The best-fit parameters for the soft-proton contamination were used to create soft-proton images that were subtracted from the final images. For each energy band, the images from individual instruments were combined and smoothed adaptively.

For the purpose of producing an image in a narrow band around 6.4 keV covering the entire source, we also reprocessed the archival *Suzaku* data taken of HESS J1534-571. *Suzaku* was pointed toward the northern and eastern part of the source in four dedicated observations of approximately 40 ksec each in 2013 (Saji et al. 2018). We employed the HEASOFT software version 6.24, *Suzaku* reprocessing version 3.0.22.44, and the remote calibration files to ensure that we had access to the most current calibration tools. We filtered bad pixels, excluded the

[1] https://heasarc.gsfc.nasa.gov/docs/xmm/esas/cookbook/xmm-esas.html

data from the chip corners, combined 3×3 and 5×5 modes where possible, and excluded data with an elevation <5 deg above Earth or <20 deg above the sunlit limb of Earth. Additional event filtering was applied for XIS0 due to the area discrimination after the XIS0 anomaly in 2009. For the spectral analysis, the ancillary response files (ARF) and redistribution matrix files (RMF) were created using the tasks *xissimarfgen* and *xisrmfgen*, respectively. For the image production, the non-X-ray background within 300 days from the observation was derived by the task *nxbgen* for background subtraction. A simulated exposure map was also created via the task *xissim* for vignetting correction. The individual images from XIS0, XIS1, and XIS3 were rebinned with 8×8 pixels and combined using *ximage*. For images above 5 keV, only the front-illuminated CCDs XIS0 and XIS3 were used because the signal-to-noise ratio of the back illuminated XIS1 is lower at this energy range. The spectra were extracted from the enhanced regions in the 6.3–6.5 keV narrow-band image that were found both by Saji et al. (2018) and in this work. The NXB spectra were calculated using data within ±300 days from the observation day. Similar to *XMM-Newton*, the *Suzaku* spectral analysis was made using the software *xspec*. For reference, Fig. 1 shows the TeV contours of HESS J1534-571 (H.E.S.S. Collaboration 2018a) and the outer boundary of the radio shell G323.7-1.0 discovered in MGPS data (Green et al. 2014), as well as the EPIC and X-ray Imaging Spectrometer (XIS) FoVs of the *XMM-Newton* pointing and the archival *Suzaku* pointings (Saji et al. 2018), respectively.

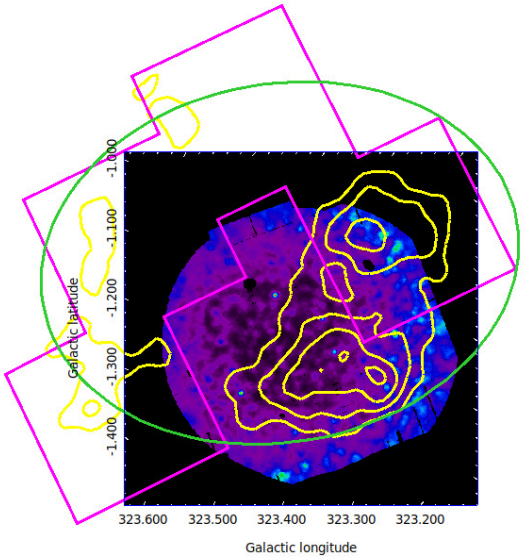

Fig. 1. Adaptively smoothed *XMM-Newton* image in the energy band 2.0–5.0 keV of HESS J1534-571. The green ellipse shows the radio boundary, the magenta region indicates the four *Suzaku* poitings, and the yellow lines represent the TeV surface brightness contour.

3. Results

3.1. X-ray continuum emission

To investigate the potential continuum emission from HESS J1534-571, we produced coadded images from all three *XMM-Newton*-EPIC cameras in two energy bands (the same as were used in Saji et al. 2018), namely a soft band at 0.5–3.0 keV and a hard band at 5.0–8.0 keV. The former is sensitive to putative thermal emission with typical SNR temperatures, and the latter is suited to search for nonthermal (synchrotron) emission. With the radio SNR boundary as a guideline, roughly 85% of the EPIC FoV covers the SNR, and the rest is outside the SNR and can serve as reference and background region. Close inspection of the *XMM-Newton* images shows that no obvious structure is visible that might be associated with the SNR in thermal or in nonthermal emission.

To be able to compare to spectral models of the broadband nonthermal emission of the SNR (see Sect. 3.3), we derived a flux upper limit in the 2.0–10.0 keV band. As on-source region, we used the part of the SNR as defined by the radio boundary that is covered by the EPIC FoV (see Fig. 1). A background spectrum was derived from a source-free (i.e., outside the radio SNR boundary) patch of the FoV. The CCD chips of MOS1 that were available at the time of the observations do not cover the background control region. Therefore, we used the off-source spectrum of MOS2 as the background spectrum for EPIC MOS1 because the sensitivity and calibration of the two MOS cameras are similar. The resulting systematic errors are minor.

We also employed a simultaneous spectral fitting for data from *XMM-Newton* and *Suzaku*. First, test fits for each individual spectrum from each data set (MOS1, MOS2, PN, and 4 *Suzaku* observations) and each telescope (*XMM-Newton* and *Suzaku*) were performed in order to estimate the reasonable range of fit parameters. Then, we carried out a joint fitting to all the source and background data. The background spectra were extracted from the region outside of the radio boundary. We fit all the spectra to the model, which consists of the astrophysical background, and for *XMM-Newton* data an additional, not ARF-folded model for any residual soft proton contamination. We chose the energy range of 1.0–7.0 keV because above 7 keV, the count rate is low. The model for the simultaneous fit is then a collisionally ionized diffuse gas *apec* at a plasma temperature of 0.1 keV to represent the local hot bubble, an absorbed power law *TBabs*pow* with an index of 1.46 for the unresolved cosmic X-ray background, and another absorbed *TBabs*apec* at 0.65 keV for the interstellar medium (ISM). The temperature of the ISM was obtained from earlier test fits and was then fixed. After the best fit was achieved, we fixed the best-fit values and added an absorbed power law *TBabs*pow* model to represent the undetected X-ray source and its total absorption. Because the relevant absorption to the object distance is not known, we adopted the column density through the entire Galaxy estimated by the HEASoft NH FTOOL (HI4PI Collaboration 2016) for the assumed emission component from the SNR. The derived upper limit is therefore a conservative estimate, but the impact is small given the fitted energy range above 2 keV. The data and best-fit models are plotted in Fig. 2. The total models (plotted as solid lines) show the base model without the power-law component, which indicates the upper limit of the synchrotron emission. The spectra of the background control regions are not plotted for better visual presentation.

The power law represents the expected spectral shape of the synchrotron emission in the considered energy range. We adopted two power-law indices: a generic 2.0 value, and a much softer value of 3.0, which corresponds to the average photon index of the model prediction by Araya (2017). Finally, we report the 95% confidence level flux for this additional power-law component and extrapolate into the range 2.0–10.0 keV as the flux upper limit from the covered fraction of the SNR (724.84 arcmin^2 for the *XMM-Newton* FoV and 1214.4 arcmin^2 for *Suzaku* FoV). To be able to compare to model expectations, this limit needs to be extrapolated to the area of the entire SNR defined by the radio region (1521.94 arcmin^2). Assuming that the surface brightness of the SNR is the same (or lower) in the areas that are not covered,

Table 2. Results of the upper-limit estimation.

Region	Radio boundary		TeV peak		*XMM-Newton*	
Index	$\Gamma = 2$	$\Gamma = 3$	$\Gamma = 2$	$\Gamma = 3$	$\Gamma = 2$	$\Gamma = 3$
UL_{2-10}	5.62	4.94	1.03	1.00	2.52	2.27
$\chi^2_{reduced}$	3421/2930	3414/2930	2922/2448	2916/2448	2823/2251	2818/2251

Notes. The upper limit of the flux in the energy range 2.0–10.0 keV is reported in units of $\times 10^{-13}$ erg cm^{-2} s^{-1}. The extraction regions is defined in the text.

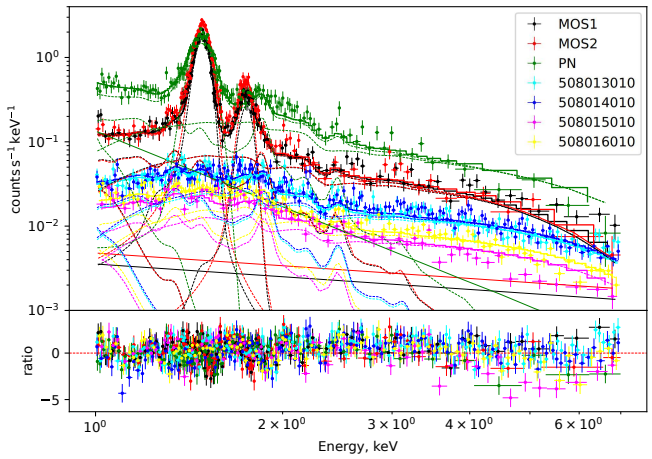

Fig. 2. X-ray spectra of the *XMM-Newton* pointing (MOS1, MOS2, and PN) and the four *Suzaku* pointings in the energy range 1.0–7.0 keV. The upper panel depicts the data and best-fit total model spectrum as well as the individual model components, and the lower panel shows the ratio of each spectrum and the corresponding best-fit model.

a plain area-scaling can be adopted, that is, the relative error on the uncertainty of the zero flux level remains the same. We simply scaled the flux density to the area of the radio boundary. A flux upper limit derived from *XMM-Newton* data alone, representing the flux coming from the SNR's fraction covered by the *XMM-Newton* FoV, is also shown for reference. These two extraction areas are called radio boundary and *XMM-Newton*, respectively (see Table 2).

To test the robustness of the result, we also used a narrower region around the peak significance region of the TeV emission to extract an on-source spectrum because the X-ray emission may trace the gamma-ray emission region better than the entire SNR. This extraction area is referred to as the TeV peak. The derived limits are compared in Table 2. As reference result, we chose the limit obtained for the radio SNR area with an index of 2.0, which yields an upper limit of 5.62×10^{-13} erg cm^{-2} s^{-1} at a 95% confidence level. To place this number in context, the expected flux in a model by Araya (2017) is 2.7×10^{-14} erg cm^{-2} s^{-1} in the 2.0–10.0 keV energy band. The expectation critically depends on the adopted energy cutoff of the electron spectrum population, which was constrained in a leptonic model by fitting to the GeV-TeV (and radio) data from the source. Further comparisons to synchrotron and broadband model expectations are discussed in Sect. 3.3.

3.2. 6.4 keV line emission

Triggered by the report by Saji et al. (2018), we also created an image in the narrow band around 6.3–6.5 keV. The authors reported evidence for line emission at 6.4 keV in the four *Suzaku* pointings on HESS J1534-571 at a statistical significance of $\sim 4\sigma$.

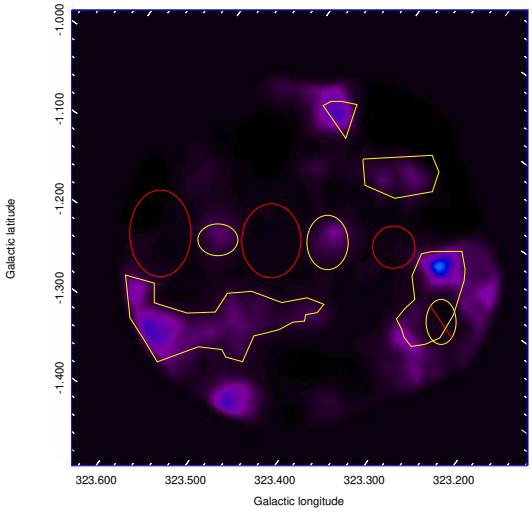

Fig. 3. Adaptively smoothed MOS1-MOS2-PN combined *XMM-Newton* image in the energy band 6.3–6.5 keV of HESS J1534-571. The enhanced and reference regions of MOS1 are depicted with yellow and red boundaries, respectively. The regions differ slightly for different cameras due to their CCD geometry.

The corresponding narrow-band *XMM-Newton* image also shows evidence for localized emission from the area of the SNR. We chose on-source extraction regions based on the enhancements in the image, and reference background regions (Fig. 3). The coadded on- and off-source spectra are shown in Fig. 4 in an energy band between 6.3 and 6.5 keV.

Galactic ridge (Galactic ridge X-ray emission, GRXE; Yamauchi et al. 2016) is expected to be seen from the direction of HESS J1534-571 because the SNR resides in the Galactic plane. These are unresolved X-ray emission lines along the Galactic plane, namely the neutral iron Fe I Kα, Fe XXV Kα, Fe XXVI Kα, and Fe I Kβ centered at 6.4 keV, 6.68 keV, 6.97 keV, and 7.06 keV, respectively. The stacked spectrum from MOS1 and MOS2 data shows that the Fe Kα line emission 6.68 keV from the GRXE is visible in both on-source and off-source spectra at the same level. The Fe XXVI Kα line is also detected at 6.97 keV. The enhancement in the image clearly corresponds to a line-like feature at 6.4 keV, which can be identified with Fe Kα emission, and which is not seen in the reference region. We fit the spectra in the range 5.5–7.5 keV to a power-law component and four Gaussian lines representing the GRXE (Fig. 4).

Similar to Saji et al. (2018), we fixed the Gaussian width of the line 6.68 keV at 23 eV (Koyama et al. 2007) and linked the normalization of the line 7.06 keV as 0.125 times that of the 6.4 keV line (Kaastra & Mewe 1993). The best-fit parameters are shown in Table 3. We ran MCMC simulations to calculate the probability that the 6.4 keV line could stem from background fluctuations. To do this, 1.000 spectra in the energy range of interest were simulated. We found that the 6.4 keV emission is significant at the $\sim 3\sigma$ confidence level and contains the signal from interactions of CRs with cold gas, as well as a small contribution (not significantly detected in the reference region) from the GRXE. Because the extraction regions had to be chosen based on the low-significance image, this is a pre-trial significance. However, taking the significances from the *Suzaku* and the *XMM-Newton* results together, we consider the results summarized above as a sufficient motivation for further investigation of this feature. Because the conversion factor from count rates into flux in this band is very similar between the used *XMM-Newton* and *Suzaku*

Table 3. Best-fit parameters of the spectra analysis of the 6.4 keV clumps.

Parameters	Enhanced region	Reference region
Energy (keV)	6.4 (fixed)	6.4 (fixed)
σ (keV)	0 (fixed)	0 (fixed)
Normalization$^{(a)}$	$1.892^{+1.017}_{-0.959}$	<0.679
Equivalent width$^{(b)}$	549	212
Energy (keV)	6.68 (fixed)	6.68 (fixed)
σ (keV)	0.023 (fixed)	0.023 (fixed)
Normalization	$1.096^{+1.121}_{-0.811}$	$0.762^{+0.785}_{-0.628}$
Equivalent width	275	504
Energy (keV)	6.97 (fixed)	6.97 (fixed)
σ (keV)	0 (fixed)	0 (fixed)
Normalization	$0.157^{+1.352}_{-0.106}$	<0.578
Equivalent width	224	172

Notes. Errors and upper limits are given at 90% C.L. $^{(a)}$Photon flux in units of 10^{-5} photons cm^{-2} s^{-1}, $^{(b)}$keV at a 95% significance level.

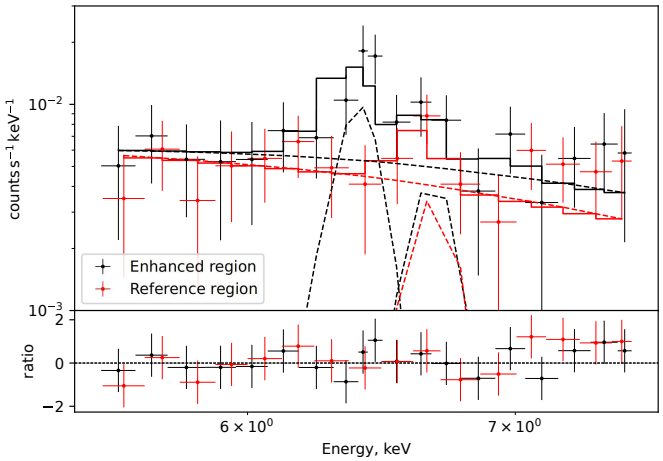

Fig. 4. MOS1+MOS2 stacked spectra and the best-fit model of the 6.4 keV enhanced region (black) and of the reference region (red).

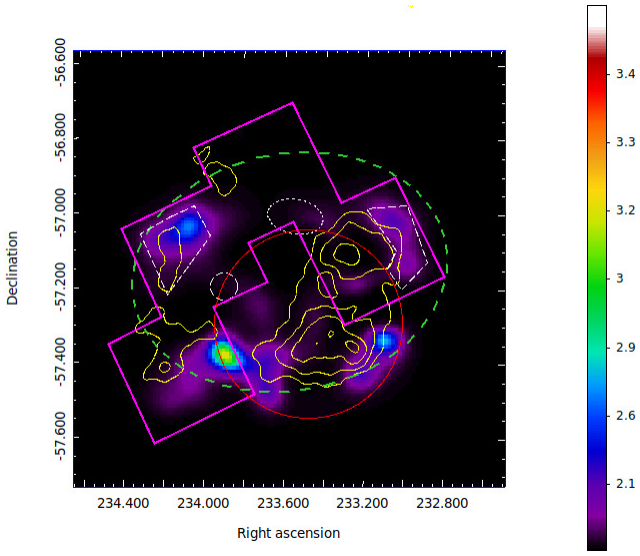

Fig. 5. Combined *XMM-Newton* and *Suzaku* image of HESS-J1534-571 in 6.3–6.5 keV in units of counts per second. The red circle shows the *XMM-Newton* field of view, the green ellipse indicates the *Molonglo* radio boundary, the yellow contour follows the TeV profile, and the magenta region shows the four pointings of the *Suzaku* observations. The dashed white regions denote the enhancement regions found by Saji et al. (2018). A point source in the Suzaku southern pointing has been removed. A similarity between the bright clumps in this narrow energy band and the TeV profile is apparent.

detectors (MOS1+2 and XIS0+3, respectively), we combined the count maps of these two instruments to show the morphology of the enhanced Fe Kα line emission across the complete SNR. Figure 5 shows a mosaic of *XMM-Newton* and *Suzaku* pointings in the 6.3–6.5 keV band, with the radio boundary and the TeV emission overlaid as contours. A visual comparison to the *Suzaku* map in Saji et al. (2018) reveals overall similar enhancement positions and shapes, despite the limited significance of individual features. Small deviations may be attributed to differences in handling of the area discrimination for the XIS0 chip (lower fluxes in the small dashed circle and ellipse regions in Fig. 5) and in the creation of the exposure map. In the southern *Suzaku* pointing, the difference (apparently higher flux) might be attributed to a different zero suppression in the image, after the necessary point-source subtraction.

3.3. Broadband SED of HESS J1534-571

With the robust X-ray upper limit of the entire SNR obtained in this work, we investigated whether the relativistic particle distribution in the SNR can be further constrained through its expected emission. Radio data at 843 MHz come from MGPS, and the flux point needs to be treated as a lower limit because certain angular scales may be missed. Sources with a diameter larger than 25 arcmin are not entirely covered by the radio telescope (Green et al. 2014). The GeV spectrum obtained with Fermi-LAT was taken from Araya (2017). The TeV data from H.E.S.S. were taken from H.E.S.S. Collaboration (2018a). To convert the integral upper limit obtained from the X-ray data into a value suitable for the (differential) SEDs shown in Figs. 6 and 7, we performed a spectral joint fitting of *XMM-Newton* and *Suzaku* in the range 2.0–7.0 keV and extrapolated to 2.0–10.0 keV (Sect. 3.1). The *naima*[2] (Zabalza 2015) package was used to simulate the nonthermal radiation from assumed relativistic particle populations. All models presented here are static one-zone models, in which homogeneous distributions of particles and of target fields relevant for the emission are maintained.

In Fig. 6, we show the result from a leptonic model in which the entire emission across all wavebands is dominated by leptonic emission, electron synchrotron at radio to X-ray frequencies, and IC emission in the GeV to TeV band. The photon fields that are upscattered by the relativistic electrons are the cosmic microwave background (CMB), near-infrared (NIR) stellar emission, and far-infrared (FIR) dust, which can be described by a blackbody distribution. For the NIR field, 3000 K and 0.4 eV cm^{-3} were adopted (Shibata et al. 2010; Vernetto & Lipari 2016), and for the FIR field, we used 20 K and 0.8 eV cm^{-3} (Araya 2017). The distance to the SNR was set to 3.5 kpc, adopting the association with the Galactic arm Scutum-Crux (Maxted et al. 2018). Because an unbroken power law was adopted for the particle population, the adopted magnetic field needed to be lower than 10 μG in order not to undershoot the radio lower limit and overshoot the γ-ray data. ∼10 μG would be required in simple shock-compression scenarios, and this value was also found by

[2] https://naima.readthedocs.io/en/latest/api-mcmc.html

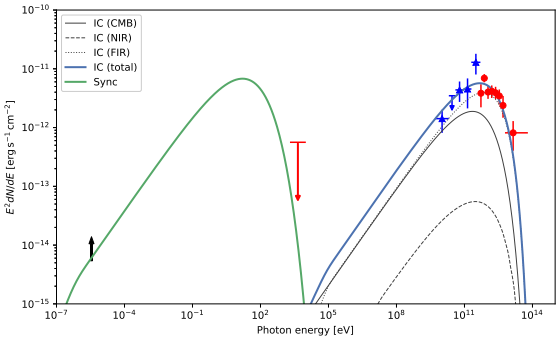

Fig. 6. Spectral energy distribution of HESS J1534-571. The *Fermi*-LAT data (Araya 2017) are plotted as blue tirangles. The red circles are H.E.S.S. TeV flux points (H.E.S.S. Collaboration 2018a). The black arrow shows the lower limit of the flux detected in radio (Green et al. 2014). The red arrow illustrates the estimated upper limit in the 2.0–10.0 keV band. The leptonic model described in the text is also plotted.

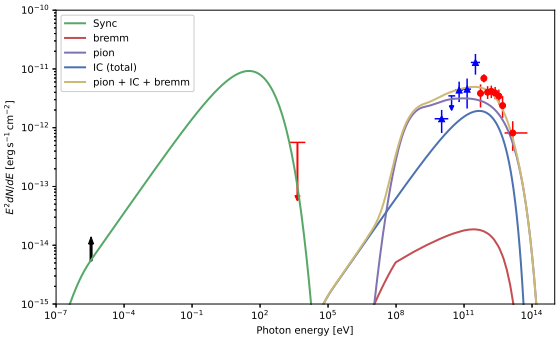

Fig. 7. Data points are same as in Fig. 6, here compared to the hadronic model described in the text.

Ferriere (2009), for example, even for the diffuse intercloud medium. Here, we adopted 6 μG (Araya 2017). To match the γ-ray spectral shape, a particle cutoff energy at 7 TeV and a spectral index of 1.9 were chosen. The gas density was assumed to be low so that bremsstrahlung could be ignored; it is usually assumed that if Bremsstrahlung plays a significant role in the γ-ray range, corresponding line emission in the X-ray band should be visible. This model satisfies all data, including the upper limit derived in X-rays.

Triggered by the low required magnetic field in the leptonic model, which speaks against recent TeV particle acceleration, and by the Fe Kα-indications of lower-energy protons in the SNR, we also attempted to fit a hadronic emission model to the broadband data. Here, the leptonic population was only constrained by the radio to X-ray band, except for the magnetic field. In this case, we used 12 μG in order to follow the radio lower limit and at the same time reduce the contribution of IC emission in the very high energy range. Canonically, the proton particle distribution is described with a power law with an energy index of 2.0 (in the test-particle approach of a Fermi-accelerated spectrum), or softer when particle escape is relevant, for instance. We show a model with an index of 2.0 and a cutoff energy at 60 TeV in Fig. 7. The input for the synchrotron and IC radiation were the same as for the leptonic model. The hadronic model requires the energy of the accelerated protons to be no more than a few 10^{50} erg (Aharonian & Atoyan 1999). We assumed two different values of the ISM density at 0.5 cm^{-3} and 1 cm^{-3} (Fig. 7), which correspond to the total energy of the protons at 3.3×10^{50} erg and 1.6×10^{50} erg, respectively. These densities could be viable in a scenario in which the emission occurs in molecular clouds or in gas shells created by the progenitor wind. At this level of target gas density, the contribution of bremsstrahlung emission is negligible.

4. Discussion

A pure leptonic model describes all available data from HESS J1534-571 well. The model is very similar to the one proposed by Araya (2017). Because of the relatively low energy of the particle spectral cutoff and the large size of the remnant, which leads to a sensitivity in the X-ray band that is lower by some orders of magnitude compared to typical point-source sensitivities, the X-ray limit obtained in this work is not sufficient to challenge a pure leptonic model. The low deduced magnetic field implies that the bulk of emission occurs outside of shock-acceleration regions. This is reminiscent of relic TeV pulsar wind nebulae, which also have no morphologically matching counterpart in X-rays (Kargaltsev et al. 2012; H.E.S.S. Collaboration 2018b). The fact that no X-ray synchrotron emission is detected even from the actual accelerating sites (possibly at the forward shock as outlined by the radio remnant) can be explained by shocks that have meanwhile slowed down, which implies that the corresponding high-energy end of the synchrotron spectrum has shifted to lower energies to which X-ray satellite observations are not sensitive (Vink 2012). Alternatively, the flux level at these sites could be too low for the current detectors because of the large angular extension of the source.

The alternative, hadronic scenario for the γ-ray emission matches the available γ-ray data less well in the simple test-particle and one-zone form as presented in Fig. 7. It might require modifications. The γ-ray spectral shape is reminiscent of the shape of RX J1713.7-3946 (Muraishi et al. 2000). For this SNR, motivated by the excellent morphological match between TeV emission and gas tracers (Sect. 3.2), a scenario has been proposed in which the energy-dependent penetration depth of CR protons into dense clumpy molecular clouds leads to a strong modification of the spatially integrated γ-ray spectrum (Aharonian et al. 2006; Gabici & Aharonian 2014). Because the highest-energy protons "see" denser material, the emission is boosted, which leads to a steepening of the spectrum below the cutoff energy. A spectrum like this would match the observed γ-ray data from HESS J1534-571 qualitatively better. This scenario would imply that the MeV/GeV emission would differ from the TeV emission spatially, which cannot be probed with the currently available γ-ray data from Fermi-LAT. However, if the Fe Kα emission tentatively detected from HESS J1534-571 is taken as a tracer of low-energy CRs, then the apparent morphology seen in Fig. 5 is agrees with expectations qualitatively. The Fe Kα-emission is on the scale of the SNR size following the TeV emission, but on smaller angular scales, the agreement appears to be poor. Moreover, this hadronic scenario would imply dense molecular clumps in spatial correspondence to the TeV emission, and indeed, Maxted et al. (2018) have identified molecular clumps like this in CO emission, following the TeV emission morphology on the scale of the full SNR. However, given the low statistical significance of individual morphological features both in the TeV and the X-ray band, any firm conclusion needs to be corroborated by future more sensitive observations.

If the Fe Kα line at 6.4 keV indeed stems from CR protons interacting with gas material (at typical particle energies of 100 MeV), a correlation between the GeV luminosity and the 6.4 keV line luminosity would be expected, not only on smaller

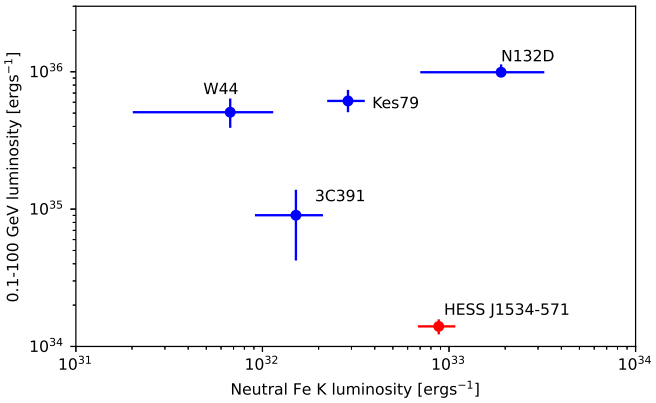

Fig. 8. Relation of the Fe Kα line emission luminosity and the luminosity in the range of 0.1–100 GeV γ-ray detection. The red data point shows HESS J1534-571 (Fe Kα: this work, GeV: Araya 2017), and the blue points represent N132D, Kes79, W44, and 3C391 (Bamba et al. 2018; Acero et al. 2016; Sato et al. 2016).

morphological scales in an individual SNR, but also on average for all SNRs for which the γ-ray emission is suspected to be of hadronic nature. Figure 8 shows such a correlation plot, in which we compare the data from HESS J1534-571 to numbers from other SNRs (taken from Bamba et al. 2018). To derive the line luminosity for HESS J1534-571, we simply added the line fluxes from *XMM-Newton* ($1.9 \pm 1.0 \times 10^{-5}$ photons cm^{-2} s^{-1}, see Table 3) and from *Suzaku* ($4.0 \pm 0.9 \times 10^{-5}$ photons cm^{-2} s^{-1} derived from the enhanced regions in our analysis) because the corresponding extraction areas overlap very little. The statistical uncertainties of the Fe line luminosities were calculated from the respective photon flux errors at the 90% confidence level (Bamba et al. 2018; Auchettl et al. 2014). The statistical uncertainties of the GeV luminosities were derived from the Fermi-LAT analysis of each SNR (W44, Abdollahi et al. 2022; Kes 79, Auchettl et al. 2014; N132D, Bamba et al. 2018; 3C391, Castro & Slane 2010; HESS J1534-571, Araya 2017). We again adopted the distance of 3.5 kpc following the Scutum-Crux arm gas association in Maxted et al. (2018) for HESS J1534-571. The figure shows, however, that no clear conclusion can be drawn for HESS J1534-571 from this comparison at this point in time. While the Fe Kα luminosity is similar to that of the other SNRs, the GeV luminosity is substantially lower. A corresponding lack of dense molecular clouds in the environment may also limit the intensity of the 6.4 keV line. If confirmed, this would indicate a different physical mechanism for the production of the Fe Kα line emission.

5. Conclusion

For the first time, a TeV-emitting SNR has been shown to not exhibit a clear X-ray continuum counterpart at the current X-ray satellite sensitivity. This is a quite robust statement because the *XMM-Newton* and *Suzaku* observations together cover ~85% of the radio shell.

The γ-ray data of HESS J1534-571 can be explained in a leptonic emission scenario, with a magnetic field that indicates that the γ-ray emitting electrons have propagated away from their acceleration sites, similar to relic TeV pulsar wind nebula scenarios. A hadronic emission scenario can be constructed under the assumption that the spectrum is modified by energy-dependent penetration of the accelerated protons into dense and clumpy gas material. This scenario also avoids a potential conflict with the lack of thermal X-ray emission from the SNR. We find evidence for Fe Kα emission from localized regions in the SNR, confirming earlier findings of Saji et al. (2018). Whether this emission is caused by interactions of low-energy CRs in the SNR and thus could support a hadronic nature of the γ-ray emission requires further investigations with more sensitive next-generation instruments.

Acknowledgement. We thank the anonymous referee and editor for the valuable comments and suggestions. We acknowledge support from the Deutsches Zentrum für Luft- und Raumfahrt (DLR) through DLR-PT grant FKZ 50 OR 1914. This work is based on observations obtained with *XMM-Newton*, an ESA science mission with instruments and contributions directly funded by ESA Member States and NASA. This research has also made use of data obtained from the *Suzaku* satellite, a collaborative mission between the space agencies of Japan (JAXA) and the USA (NASA).

References

Abdollahi, S., Acero, F., Baldini, L., et al. 2022, ApJS, 260, 53
Acero, F., Ackermann, M., Ajello, M., et al. 2016, ApJS, 224, 8
Aharonian, F. A., & Atoyan, A. M. 1999, A&A, 351, 330
Aharonian, F., Akhperjanian, A. G., Bazer-Bachi, A. R., et al. 2006, A&A, 449, 223
Araya, M. 2017, ApJ, 843, 12
Aschenbach, B., Briel, U. G., Haberl, F., et al. 2000, SPIE Conf. Ser., 4012, 731
Auchettl, K., Slane, P., & Castro, D. 2014, ApJ, 783, 32
Bamba, A., Ohira, Y., Yamazaki, R., et al. 2018, ApJ, 854, 71
Bell, A. R. 2004, MNRAS, 353, 550
Bell, A. R., & Lucek, S. G. 2001, MNRAS, 321, 433
Blandford, R., & Eichler, D. 1987, Phys. Rep., 154, 1
Burton, M. G., Braiding, C., Glueck, C., et al. 2013, PASA, 30, e044
Castro, D., & Slane, P. 2010, ApJ, 717, 372
Drury, L. O., Aharonian, F. A., & Voelk, H. J. 1994, A&A, 287, 959
Ferriere, K. 2009, A&A, 505, 1183
Gabici, S., & Aharonian, F. A. 2014, MNRAS, 445, L70
Ginzburg, V. L., & Syrovatskii, S. I. 1964, The Origin of Cosmic Rays (New York: Macmillan)
Green, A., Reeves, S., & Murphy, T. 2014, PASA, 31
H.E.S.S. Collaboration (Abdalla, H., et al.) 2018a, A&A, 612, A8
H.E.S.S. Collaboration (Abdalla, H., et al.) 2018b, A&A, 612, A2
HI4PI Collaboration (Ben Bekhti, N., et al.) 2016, A&A, 594, A116
Hillas, A. M. 2005, J. Phys. G Nucl. Phys., 31, R95
Jones, F. C., & Ellison, D. C. 1991, Space Sci. Rev., 58, 259
Kaastra, J. S., & Mewe, R. 1993, A&AS, 97, 443
Kallman, T., Palmeri, P., Bautista, M., Mendoza, C., & Krolik, J. 2004, ApJS, 155, 675
Kargaltsev, O., Pavlov, G. G., & Durant, M. 2012, in Electromagnetic Radiation from Pulsars and Magnetars, eds. W. Lewandowski, O. Maron, & J. Kijak, Astronomical Society of the Pacific Conference Series, 466, 167
Kostrzewa-Rutkowska, Z., Lopez, K. M., Jonker, P. G., et al. 2017, ATel, 11007, 1
Koyama, K., Hyodo, Y., Inui, T., et al. 2007, PASJ, 59, 245
Krause, M. O. 1979, J. Phys. Chem. Ref. Data, 8, 307
Kuntz, K., & Snowden, S. 2008, A&A, 478, 575
Lumb, D. H., Schartel, N., & Jansen, F. A. 2012, Opt. Eng., 51, 011009
Malkov, M. A., & Drury, L. O. 2001, Rep. Progr. Phys., 64, 429
Maxted, N. I., Braiding, C., Wong, G. F., et al. 2018, MNRAS, 480, 134
McClure-Griffiths, N. M., Dickey, J. M., Gaensler, B. M., et al. 2005, ApJS, 158, 178
Mitsuda, K., Bautz, M., Inoue, H., et al. 2007, PASJ, 59, S1
Muraishi, H., Tanimori, T., Yanagita, S., et al. 2000, A&A, 354, A57
Negoro, H., Ishikawa, M., Ueno, S., et al. 2017, ATel, 10699, 1
Nobukawa, K. K., Nobukawa, M., Koyama, K., et al. 2018, ApJ, 854, 87
Reynolds, S. P. 1998, ApJ, 493, 375
Saji, S., Matsumoto, H., Nobukawa, M., et al. 2018, PASJ, 70, 23
Sato, T., Koyama, K., Lee, S.-H., & Takahashi, T. 2016, PASJ, 68, S8
Shibata, T., Ishikawa, T., & Sekiguchi, S. 2010, APJ, 727, 38
Sturner, S. J., Skibo, J. G., Dermer, C. D., & Mattox, J. R. 1997, ApJ, 490, 619
Vernetto, S., & Lipari, P. 2016, Phys. Rev. D, 94, 063009
Vink, J. 2012, A&ARv, 20, 49
Yamauchi, S., Nobukawa, K. K., Nobukawa, M., Uchiyama, H., & Koyama, K. 2016, PASJ, 68, 59
Zabalza, V. 2015, in International Cosmic Ray Conference, 34, 922

3.1.2 Identification of HESS J1614-518 as Supernova remnant using GLEAM and eROSITA survey data

As mentioned in Section 1.1.6, HESS J1614-518 was initially classified as an SNR candidate upon its discovery due to the lack of confirmed counterparts in the radio and X-ray wavebands. Here, we present evidence in both radio and X-ray regimes that, for the first time, confirm the SNR nature of HESS J1614-518, establishing it as an SNR. Furthermore, we conduct an extensive study of its characteristics, including the potential association with a central compact object (CCO) and its distance. Additionally, we found that the SED of CRs from this SNR does not contradict to a leptonicγ-ray origin. This finding aligns with the purely non-thermal X-ray spectrum of the source, suggesting that HESS J1614-518 effectively accelerates cosmic-ray electrons to TeV energies.

Astronomy & Astrophysics manuscript no. output
June 10, 2024

Identification of HESS J1614-518 as Supernova remnant using GLEAM and eROSITA survey data

G. Pühlhofer[1], M. Michailidis[1⋆], N. T. Nguyen-Dang[1], A. Santangelo[1], M. Sasaki[2], W. Becker[3], G. Ponti[3]

[1] Institut für Astronomie und Astrophysik Tübingen (IAAT), Sand 1, 72076 Tübingen, Germany
e-mail: gerd.puehlhofer@uni-tuebingen.de
[2] Universität Erlangen/Nürnberg, Dr.-Remeis-Sternwarte, Sternwartstraße 7, D-96049, Bamberg, Germany or ECAP Erlangen
[3] Max-Planck-Institut für extraterrestritche Physik, Giessenbachstrasse, 85748 Garching, Germany

To be submitted

ABSTRACT

We report new soft X-ray and radio continuum observations of the TeV-emitting supernova remnant (SNR) candidate HESS J1614-518, using eROSITA and MWA data. Radio continuum data were retrieved from the GLEAM survey, X-ray data from the first four completed full-sky eRASS surveys. An object displaying a shell-type morphology is discovered in GLEAM data, matching the TeV source position and morphology. An X-ray counterpart is discovered in eRASS data above ~ 1.3 keV, in good agreement with the radio and TeV sources, above a softer and more extended X-ray component which is likely unrelated to the object. The findings confirm the SNR nature of HESS J1614-518. A combined GeV-TeV γ-ray spectrum, using updated data from Fermi-LAT, displays a peak structure that is compatible with Inverse Compton emission from relativistic electrons in a standard one-zone emission scenario.

Key words. supernova remnants (Individual object: HESS J1614-518) — multiwavelength study — cosmic rays: acceleration

1. Introduction

Galactic supernova remnants are predominantly discovered in the radio continuum band, and to a smaller extent in the X-ray domain. A discovery of an SNR in the gamma-ray domain might be interpreted as an indication of a strong hadronic component of the relativistic particles responsible for the gamma-ray emission, given that relativistic hadrons only radiate at gamma-ray energies, above the energy threshold for π^0-production. In recent years, several TeV sources along the Galactic plane have been discovered, the nature of which could not be immediately clarified. In particular, the H.E.S.S. Galactic plane survey (HGPS) has yielded a considerable number of unidentified sources. From statistical considerations and also from the center-filled morphology of these sources, it is likely that many of those objects are pulsar wind nebulae (PWNe). Only a small number of HGPS sources was suggested to be SNR candidates, based on the shell-type appearance of the TeV sources (H.E.S.S. Collaboration et al. 2018). Amongst those sources, HESS J1614-518 stood out at the time of discovery because of a comparatively luminous counterpart in the Fermi-LAT band showing a hard spectrum below 1 TeV with a differential photon index of $\sim$2 (H.E.S.S. Collaboration et al. 2018). Such a spectral shape was indicative of a standard hadronic emission spectrum from a relativistic hadronic particle population currently being accelerated by diffusive shock acceleration.

Convincing counterparts to HESS J1614-518 with matching morphology in energy bands below the gamma-ray regime have not been reported yet in the literature. The source has a diameter of $\sim 0.8^\circ$ and is located in the Galactic Plane, which both complicates the identification of counterparts. A tentative detection of extended X-ray emission in the 3-7 keV band with XMM-Newton from a North-Eastern portion of the object was reported in H.E.S.S. Collaboration et al. (2018). We report here the discovery of a radio-continuum emitting shell in morphological agreement with the TeV shell, as well as extended X-ray emission from the object that is consistent with the TeV morphology. While a spectral index of the radio emission cannot be determined because of the sparseness of the radio data, the combination of the gamma-ray, radio and X-ray information firmly classifies the source as a SNR. We also readdress the GeV-TeV spectrum in view of the fact that more Fermi-LAT data and updated analysis methods have become available (de Palma et al. 2019; Guo & Xin 2021).

The paper is organized as follows: In section 2, the observations and the reduction of the X-ray data from the eROSITA survey is described. We also present updated GeV results using the full Fermi-LAT data set available to date. To obtain a clear identification of the different counterparts, in section 3 we perform a quantitative comparison of the TeV, radio, and X-ray morphologies of the sources. In section 4 we put the measured fluxes into context of broadband spectral models describing the emission from assumed nonthermal particle populations. In section 5, we discuss the distance to HESS J1614-465 in view of the obtained results. All results are further discussed in section 6 and are put into context of data from other SNRs. We conclude with a summary in section 7.

2. Observations and data reduction

The TeV data (sky map and energy spectrum of the entire source) used in this paper have been obtained with the H.E.S.S. telescopes and are retrieved from H.E.S.S. Collaboration et al. (2018), with an energy threshold of 1 TeV for the sky maps and a 0.3 TeV spectral energy threshold. The radio continuum sky

⋆ Corresponding author, e-mail: michailidis@astro.uni-tuebingen.de

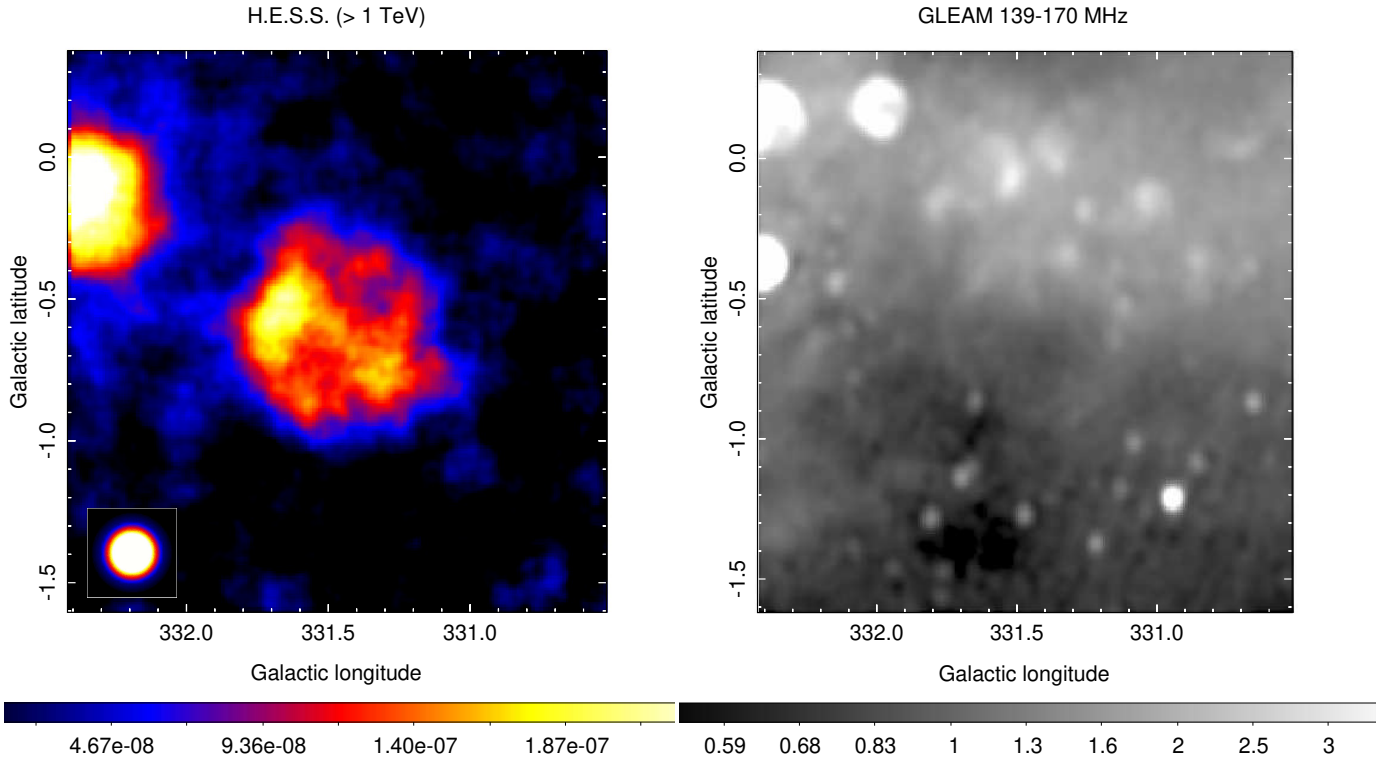

Fig. 1. Left panel: TeV surface brightness map of HESS J1614-518, expressed in units of counts/[$m^2 \cdot s \cdot deg^2$] above 1 TeV (H.E.S.S. Collaboration et al. 2018). The image (pixel size $\sim 36''$) is correlated with a circle with a radius of 0.1 deg, and was additionally convolved with a Gaussian with $\sigma = 36''$ to remove statistically not significant features, similar to what was done in (H.E.S.S. Collaboration et al. 2018). Right panel: GLEAM radio continuum intensity map at the 139-170 MHz frequency range, in units of Jy beam^{-1}. The beam size is $3.299' \times 3.018'$, no further smoothing was applied to the image (whose pixel size is $\sim 34''$).

map (139-170 MHz) is taken from the publicly available GaLactic and Extragalactic All-sky MWA survey (GLEAM)[1], a survey of the entire radio sky south of declination 30° at the frequency range between 72 and 231 MHz (Wayth et al. 2015; Hurley-Walker et al. 2017; For et al. 2018; Hurley-Walker et al. 2019b). The remnant is visible on all five discrete GLEAM radio continuum maps, 72-103 MHz, 103-139 MHz, 139-170 MHz, 170-201 MHz, and 200-230 MHz that provide nearly contiguous coverage. For display purposes and further morphology analysis, we selected the frequency band 139-170 MHz where the remnant is best visible and appears to have a well-defined shell structure. A GLEAM RGB cube, formed as R:72-103 MHz, G:103-134 MHz, B:139-170 MHz, was also employed aiming at discriminating the shell-type morphology of the remnant from nearby HII regions and extracting the remnant's flux density. The TeV and radio sky maps are shown in Fig. 1, left and right panel, respectively.

X-ray sky maps and spectrum are derived from the first four surveys of the eROSITA all-sky survey, making use of a single sky tile of square shape and a size of $3.6° \times 3.6°$ (ObsID 242141, named after a unique six-digit configuration: the first three digits correspond to Right Ascension (RA) and the last three to Declination (Dec) of the tile center). The X-ray analysis is described in section 2.1. GeV γ-ray sky maps, above 10 GeV, and the spectrum of the source in the 1-800 GeV energy band are derived from publicly available Fermi-LAT data; the analysis is described in section 2.2.

[1] `https://www.mwatelescope.org/science/galactic-science/gleam/`

2.1. eROSITA data analysis

eROSITA is a wide-field X-ray instrument consisting of seven co-aligned individual telescopes, which is hosted on the spacecraft Spectrum-X-Gamma (Merloni et al. 2012; Sunyaev et al. 2021; Predehl et al. 2021). The instrument covers an energy range of 0.2-10 keV. In the initial survey phase, which started in 2019, the satellite is steered to cover the entire sky every six months. For the presented results, data from four surveys, eRASS:4, have been analyzed. Pipeline version c020 was adopted and data processing was carried out using the `evtool` and `srctool` tasks of version `eSASSusers_201009` of (Brunner et al. 2022) of eSASS (eROSITA Standard Analysis Software).

2.1.1. Image analysis

Data analysis was performed using a single sky tile, with ObsID: 242141. The data reduction process involves deleting all events flagged as corrupt either individually or as part of a corrupt frame, retaining all four of the recognized legal patterns (`pattern=15`), and identifying and repairing disordered GTIs. For the image production, events from all 7 telescopes, TM1-7, were used. The left panel of Fig. 2 shows a $4.2° \times 4.2°$ sky area around HESS J1614-518, using a broad energy range from 0.2-5.0 keV. A $60'$ extraction radius was used to filter out all point sources above 3σ detection significance. Additionally, the bright sources RCW 103 (an SNR) and 4U 1608-52 (a Low Mass X-ray Binary, LMXB) as well as the SNR Kes 32 are masked for clarity. The binary is visible in eRASS2 and eRASS4, while it was found in off-state during eRASS1 and eRASS3.

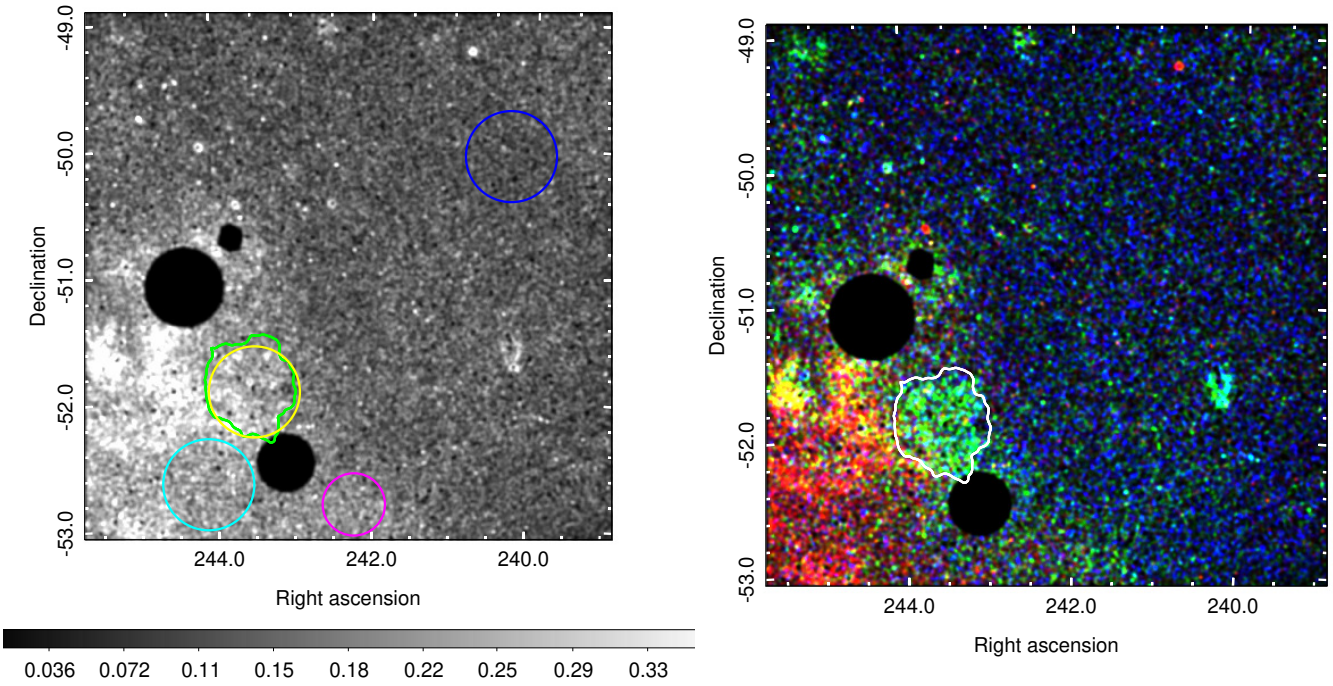

Fig. 2. eRASS:4 intensity sky maps of the area around HESS J1614-518. At the left panel, the full energy band 0.2-5.0 keV is shown with a linear grey-scale. At the right panel, an RGB representation (R: 0.2-1.3 keV, G: 1.3-2.5 keV, B: 2.5-5.0 keV) with a squared color palette is used, to enhance the visibility of distinct structures. The images are plotted in units of counts/pixel with a pixel size of 10″, and are convolved with a $\sigma = 45''$ Gaussian. The green (left panel) and white (right panel) contours mark the 5 σ significance TeV extent of HESS J1614-518 as measured with H.E.S.S. (H.E.S.S. Collaboration et al. 2018). Point sources are filtered out, and the LMXB 4U 1608-52 as well as the SNRs RCW 103 and Kes 32 are masked. At the left panel, additionally, the four spectral extraction regions used for the analysis are shown. The yellow circle denotes the on-source region with position and extension corresponding to the radio GLEAM centroid as defined in Tab. 2. Blue and cyan circles represent the selected background control regions, while the magenta circle represents a region adjacent to the cyan-schemed region which was used to validate the quality of the background model.

This sky map is overall dominated by diffuse extended emission, which is mainly confined to below 1.3 keV. The emission from HESS J1614-518 only becomes apparent when filtering out this soft emission. The right panel of Fig. 2 shows an RGB representation of the map (R: 0.2-1.3 keV, G: 1.3-2.5 keV, and B: 2.5-5.0 keV), where the X-ray emission coincident with the TeV source becomes clearly apparent. The range of the medium energy band was optimized using the energy spectrum extracted from the HESS J1614-518 region as discussed below. At the left panel of Fig. 3, the same sky field is shown after restriction to the energy range 1.3-2.5 keV, clearly demonstrating that the emission is confined inside the outer 5σ TeV emission significance contour detected with H.E.S.S. (H.E.S.S. Collaboration et al. 2018). There is also no extension of this diffuse emission region into the LMXB area. To illustrate this, at the right panel of Fig. 3 the shown data set was restricted to the first eRASS survey, during which the LMXB was in an off state, and the mask is omitted.

2.1.2. Spectral analysis

To derive an energy spectrum from the TeV source region, events were selected from a circular region with radius 0.4° around the position RA=243.510°, Dec=-51.919°. Position and extension correspond to the TeV centroid as reported in H.E.S.S. Collaboration et al. (2018) and to a radius that encompasses both the TeV emission and the radio shell (see section 3), respectively. A systematic uncertainty check was also performed by extracting the spectrum from the radio and X-ray best fit regions. No significant variation was found in the parameters of the spectral fits. Events from five telescopes, TM1, TM2, TM3, TM4, and TM6 were used for the spectrum extraction, while TM5 and TM7 event data were omitted since the latter telescopes suffer from light leaks discovered at early stages during the commissioning phase of eROSITA, specifically due to sun-light reaching the CCD by-passing the filter wheel as the consequence of the lack of Aluminium (Al) on-chip optical filters on those telescopes. As a precaution against possible contamination of our signal, and thus of the derived spectrum, by point sources that fall within the region of interest, we applied a similar filter to the one used in Fig. 2, setting a 60′ extraction radius in order to exclude all point sources detected with a 3σ significance or higher. One of the point sources stands out because it is located just 1′ away from the geometrical center of both the TeV and radio shell-type emission, called XMMU J161406.0-515225. As of now, this source has not been considered as a CCO (central compact object) candidate, because it has been classified as an X-ray emitting star (Lin et al. 2012) after the detection of an optical counterpart reported in Landi et al. (2006). However, the possibility of an unresolved binary (cf., e.g., the CCO and its stellar binary companion in the SNR HESS J1731-347, Doroshenko et al. 2016) cannot be excluded.

An estimate of the astrophysical background which is representative for the source region is hampered by the diffuse, uneven emission in the surrounding area, which is considered to stem from diffuse emission from the Galactic Plane along

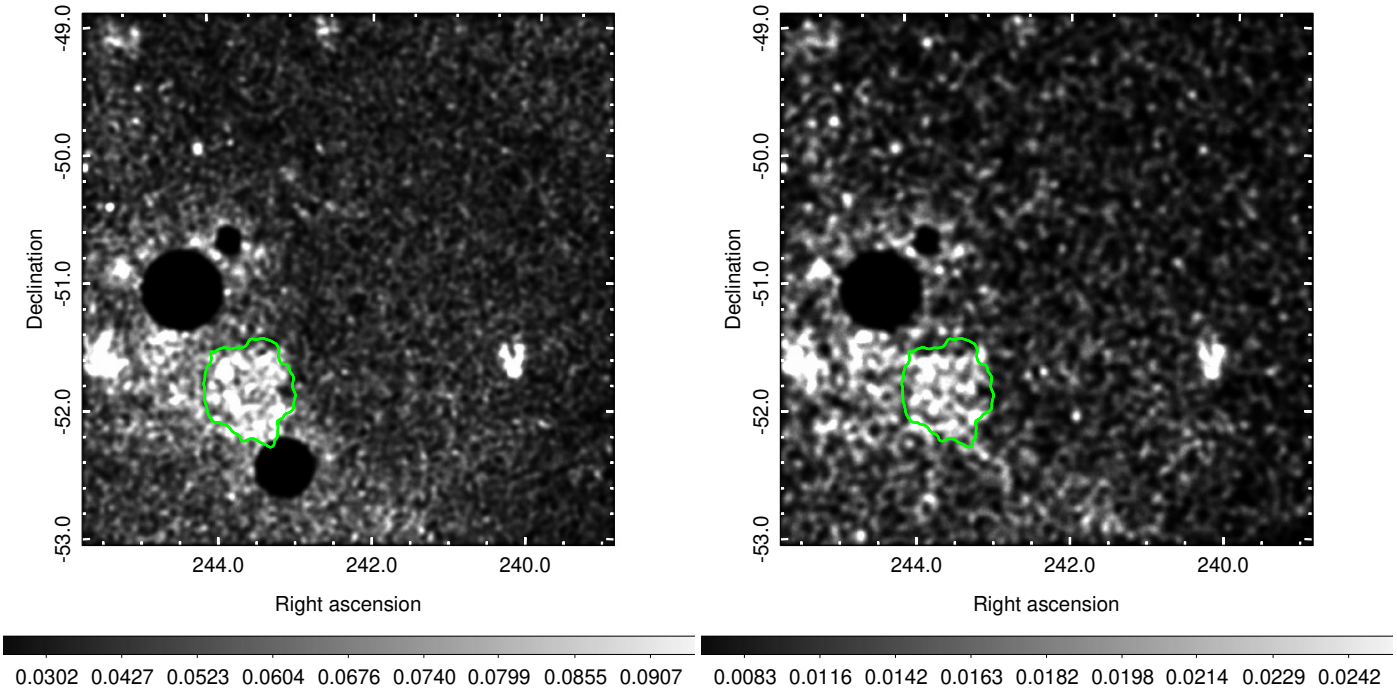

Fig. 3. eRASS intensity sky maps of the area around HESS J1614-518, restricted to the 1.3-2.5 keV energy band in which the emission from HESS J1614-518 is concentrated. A squared color distribution is used on both panels. The images are plotted in units of counts/pixel with a pixel size of $10''$, and are convolved with a $\sigma = 75''$ and $\sigma = 100''$ Gaussian for the left and right panels, respectively. Point sources are filtered out, and the LMXB 4U 1608-52 (only left panel) as well as the SNRs RCW 103 and Kes 32 are masked. The green contour marks the 5 σ significance TeV extent of HESS J1614-518 as measured with H.E.S.S. (H.E.S.S. Collaboration et al. 2018). At the left panel, the entire eRASS:4 data set is shown. To illustrate that the emission from HESS J1614-518 is fully confined inside the TeV contour also towards the LMXB position, at the right panel the data set is restricted to eRASS:1 during which the LMXB was in a low state and is not masked in the image.

with emission from unresolved sources. Two nearby circular regions, which are of same size as the source extraction region and are free of apparent strong sources, were chosen to estimate the background at the source position (see left panel of Fig. 2). The blue-schemed region has been chosen to be free of diffuse foreground and/or background emissions except for the astrophysical background, whose components are described below. Contrary to that, the cyan-schemed region has been chosen such that it is likely fully dominated by the diffuse foreground and/or background of the softer extended X-ray emission detected at and around HESS J1614-518, in the energy range below ~ 1.3 keV, but free of what we believe are unrelated X-ray excesses detected in the surrounding area of HESS J1614-518. These two control regions, when appropriately combined (details see below), yeald a spectrum that matches the source region's spectrum in the energy range < 1.3 keV, i.e. outside of the energy range where emission from HESS J1614-518 appears visible.

The contribution of the soft diffuse foreground and/or background emission component that the cyan region displays at energies > 1.3 keV is very relevant to correctly model the X-ray excess emission originating from the region of interest, since it exhibits strong emission lines in the 1.3-2.5 keV energy range, even though those appear less significant compared to the emission at softer X-rays. We validated the quality of the background model by additionally extracting the spectrum from an adjacent region as shown on the left panel of Fig. 2 with a magenta circle. This region was chosen as the best available additional control region with visually similar background properties, i.e. free of X-ray sources but dominated by the apparent diffuse foreground and/or background emission. Indeed, the same strong emission lines in the 1.3-2.5 keV energy band are present as in the cyan-circled background, so the features are not specific to the cyan-circled control region (i.e., the same background model, as introduced below, has been successfully applied to the magenta-colored background control region).

The background emission is modeled with the following components: the instrumental or particle background arising

Table 1. Best-fit parameters of the HESS J1614-518 X-ray spectrum.

Region	Background (Cyan)		On source (Yellow)		
Model	vapec+vapec		pow	vapec	vapec
$kT_{(keV)}$	$0.25^{+0.01}_{-0.01}$	$0.63^{+0.05}_{-0.05}$		$1.13^{+0.12}_{-0.07}$	$0.96^{+0.06}_{-0.06}$
Γ			$1.79^{+0.38}_{-0.32}$		
$N_{H(10^{22}cm^{-2})}$	$0.09^{+0.03}_{-0.03}$	$0.98^{+0.12}_{-0.11}$	$0.82^{+0.32}_{-0.22}$	$2.47^{+0.14}_{-0.15}$	$3.00^{+0.19}_{-0.17}$
Ne	$3.21^{+0.86}_{-0.82}$	$1.78^{+0.46}_{-0.41}$	N.A		
Mg			N.A		$0.27^{+0.26}_{-0.24}$
Al		$4.52^{+1.83}_{-1.64}$	N.A		
Si			N.A		$0.20^{+0.12}_{-0.10}$
S		$4.56^{+1.99}_{-1.68}$	N.A		$0.04^{+0.26}_{-0.04}$
χ^2/dof	1.01		1.11	1.28	1.15

Notes. Best-fit parameters are reported along with 1σ errors. Where not defined otherwise, elemental abundances are set to Wilms (Wilms et al. 2000).

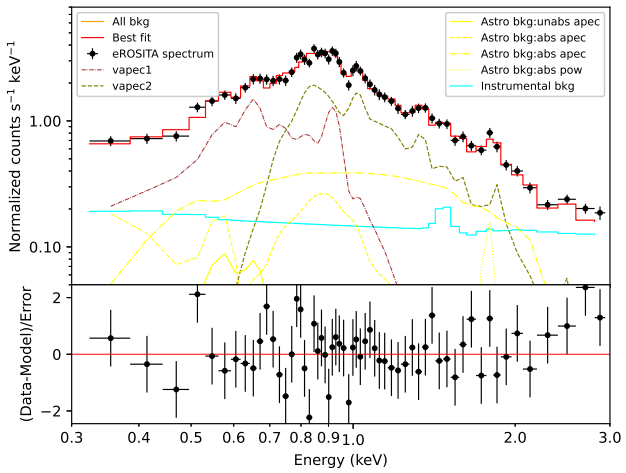

Fig. 4. Energy spectrum in the 0.3-3.0 keV energy band extracted from the cyan background control region (see Fig. 2), using eRASS:4 data obtained from TM1-4 and TM6. For visual purposes, adjacent bins are combined until they have a significant detection above 10σ, and a minimum number of 30 counts per bin was applied. The spectrum is modeled with a two-temperature plasma model representing the diffuse foreground and/or background emission component (represented in brown and olive colors). Yellow spectra represent the instrumental background.

from the production of particle secondaries when cosmic-rays interact with the spacecraft and the detector shield (in xspec notation `gaussian + expfac(bkn2pow + powerlaw + powerlaw) + powerlaw + gaussian + gaussian + gaussian+ gaussian + gaussian + gaussian`), the Local Hot Bubble (LHB) originating from the low-temperature plasma which encircles the Galactic neighborhood (expressed in terms of a non-absorbed `apec`), the Galactic Halo (GH) (well-modeled by a two-temperature absorbed plasma `apec+apec`), and the Cosmic X-ray Background (CXB) accounting for the combined emission of unresolved AGN (described by a single absorbed `powerlaw` component). The diffuse foreground and/or background emission component described above is well modeled by a two-temperature plasma model with temperatures of 0.25 keV and 0.63 keV, respectively (`vapec+vapec`), as shown in Fig. 4. Whether that diffuse X-ray emission component should be attributed to foreground and/or background emission is not clear, as indicated by the spectral analysis results (see Tab. 1). The cooler plasma is certainly located in front of HESS J1614-518, given its low absorption column density obtained from the best fit of the source spectrum. The location of the hotter plasma (whether in the foreground, in the background, or coincident with the source) cannot be constrained from the absorption. A similar discussion of that soft X-ray emission component dominating the complex region at and around Kes 32, which is located just 1° to the North of HESS J1614-518, is reported in Vink (2004).

For the on-source fit, given the limited effective area of eROSITA above $\sim$3 keV, no statistically significant excess counts are detected above that energy from the source region, therefore the fit was a priori restricted to < 3.0 keV. We note that there are hints of diffuse X-ray emission in the eRASS:4 spectrum above 3.0 keV, primarily in the 3.0-6.0 keV energy range weak emission from a population of non-thermal particles could be present. But above 3.0 keV the background becomes dominant (as shown on the right-hand panel of Fig. 5), and we lack a sufficient amount of data (low statistics) to exploit and conduct a detailed spectral analysis in those harder energy ranges. Nevertheless, these hints are consistent to what was reported in H.E.S.S. Collaboration et al. (2018) (i.e., a hard diffuse emission component in the 3.0-7.0 keV energy band) when exploiting XMM-Newton data from the location of HESS J1614-518.

The lower energy threshold was set to 0.3 keV, given that the background model fits the data in the blue and cyan background control regions in the 0.3-3.0 keV energy band with high precision ($\chi^2/d.o.f = 1.01$, see Tab. 1 and Fig. 4). In fact, restricting the fit range to > 1.3 keV would impact the results reported below (e.g. the fitted power-law index would change from ~ 1.8 to ~ 0.9), because of the narrow fit energy range. Since we are confident in the background model below 1.3 keV, we decided to include that energy range in the fits.

The source spectrum is derived with a simultaneous (xspec Ver. 12.12.1 (Dorman et al. 2003)) fit of on-source and background region, using both reference background regions (cyan and blue circles, see above) to determine the background in the on-source region. As introduced above, the blue-colored circular region is well modeled when employing all four aforementioned background components (of astrophysical and instrumental origin), whereas the cyan background control region requires two additional vapec components We determine the thermal plasma temperatures and the photon indices of the astrophysical and instrumental background components from the blue background control region. Those values are then frozen when fitting the cyan background control region. Finally, the on-source (yellow) and cyan (for background) regions are simultaneously fitted, keeping fixed the plasma temperature, elemental abundances, and photon indices (i.e., all spectral components of the cyan background control region except the normalizations). As additional source component, either a non-thermal or a thermal component is then used. C-statistics (Cash 1979) were applied in the fitting procedure to take the low-number statistics into account. To model the Galactic absorption $N_{\rm H}$ towards the source, the `TBABS` absorption model with Wilms abundances (Wilms et al. 2000) was used.

The source was modeled either with a power-law representing synchrotron emission from relativistic electrons, or with an apec model representing hot plasma composed of collisionally ionized diffuse gas (Foster et al. 2012). The power-law fit ($\chi^2/dof = 1.11$) yields a photon index of $\Gamma = 1.79^{+0.38}_{-0.32}$ and an absorption column density of $N_{\rm H} = 0.82^{+0.32}_{-0.22} \times 10^{22}{\rm cm}^{-3}$, and is shown in Fig. 5. The apec fit ($\chi^2/dof = 1.28$) yields a temperature $kT = 1.13^{+0.12}_{-0.07}$ keV with $N_{\rm H} = 2.47^{+0.14}_{-0.15} \times 10^{22}{\rm cm}^{-3}$, as shown on the left panel of Fig. 6. The hot plasma model goodness of fit can be significantly improved to an only marginally worse fit ($\chi^2/dof = 1.15$) compared to the power-law model, when permitting extremely low plasma emission lines. In particular, Magnesium (Mg), Sulfur (S), and Silicon (Si) then need to be strongly sub-solar, as shown in Tab. 1. The obtained temperature and absorption column density in this case are $kT = 0.96^{+0.06}_{-0.06}$ keV and $N_{\rm H} = 3.0^{+0.19}_{-0.17} \times 10^{22}{\rm cm}^{-3}$, respectively, the fit is shown on the right panel of Fig. 6.

Given the limited statistics (excess of $\sim$ 1200 counts in the 1.3-2.5 keV energy range, depending on the selected background control region), the narrow energy band, and the contamination from the larger-scale diffuse emission, from purely statistical arguments neither of the two physical models can be clearly favoured. However, three arguments strongly favour the power-law interpretation. Firstly, the low elemental abundances

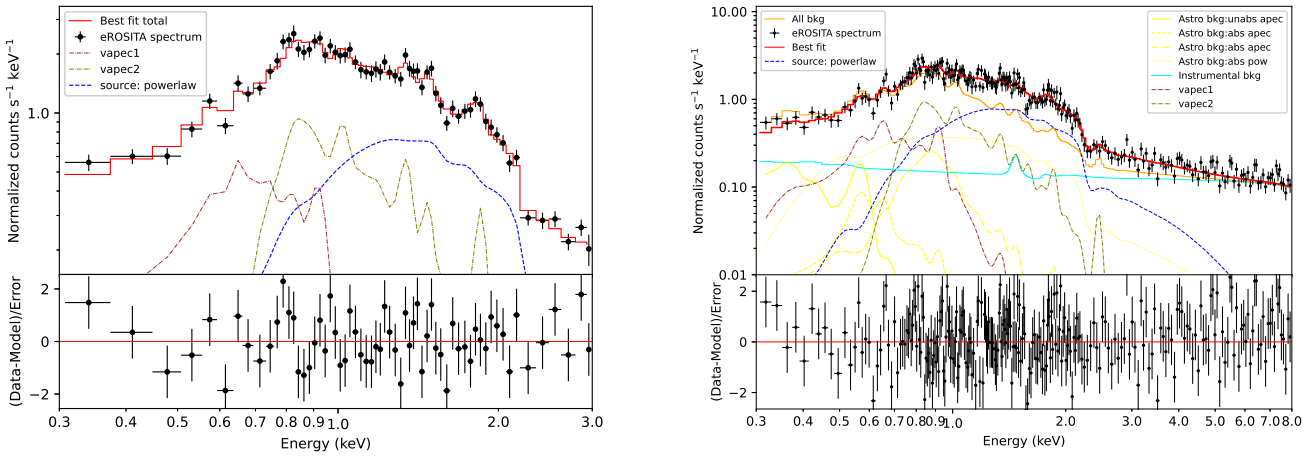

Fig. 5. Left panel: Energy spectrum in the 0.3-3.0 keV energy band obtained from the on-source region (yellow circle in Fig. 2), using eRASS:4 data obtained from TM1-4 and TM6. For visual purposes only, adjacent bins are combined until they have a significant detection at least as large as 10σ, a minimum number of 30 counts per bin was set. HESS J1614-518 energy spectrum is best described by a simple power law indicated with the blue dashed line. The brown and olive dash-dotted lines represent the two plasma temperature model of the diffuse foreground and/or background emission component that dominates at softer X-rays as shown in Fig. 4. Right panel: The same energy spectrum is shown, but raw (no further re-binning than the initial 30 counts per bin has been applied) in the broader 0.3-8.0 keV energy band and with all components contributing to the total emission displayed in detail. The orange line stands for the sum of all background components i.e., instrumental (cyan color), astrophysical (yellow color), and diffuse foreground and/or background (brown and olive colors) detected at and around HESS J1614-518, revealing the overall contribution of the source to the total spectrum.

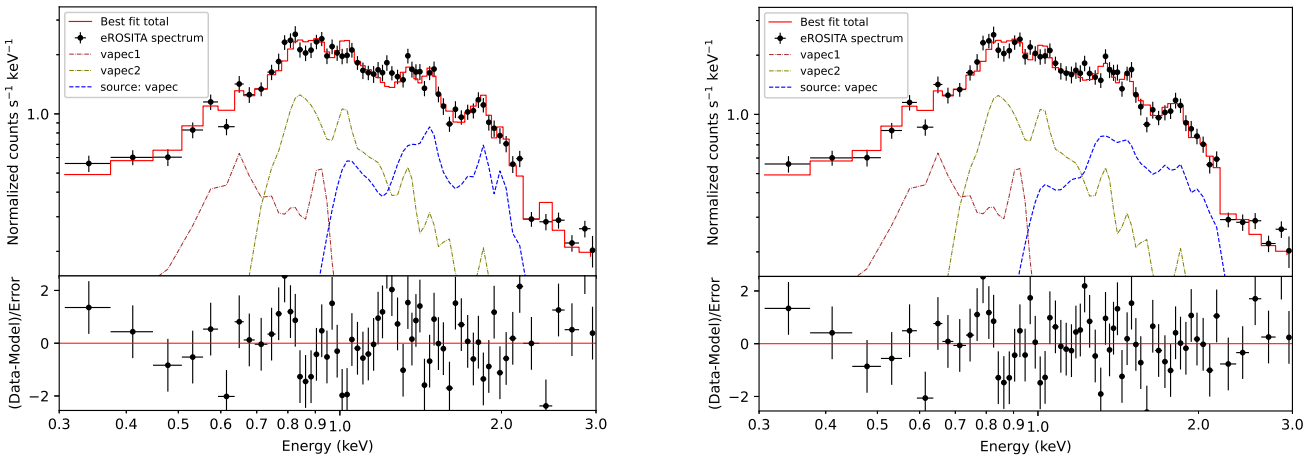

Fig. 6. Left panel: The same energy spectrum as Fig. 5 is shown. A single temperature plasma (vapec) model with abundances set to Wilms (Wilms et al. 2000) is used, instead of a power law, to model the emission from HESS J1614-518. Right panel: The same energy spectrum as Fig. 5 is shown. A single temperature plasma (vapec) model with strongly suppressed Mg, S, and Si emission lines is shown. The rest of the elemental abundances are set to Wilms (Wilms et al. 2000) values.

required for a good thermal fit are untypical for SNR plasmas (adopting the identification of the source as SNR as argued in this paper). Secondly, when attempting to fit the spectrum up to 8 keV (i.e., include that faint diffuse emission above 3.0 keV as mentioned above) an unreasonably high plasma temperature of the scale of 10 keV would be required to describe the spectrum. Keeping the plasma temperature fixed to what is obtained from the spectral fit in the 0.3-3.0 keV energy range ($kT \sim 1.0$ keV, as shown in Tab. 1), positive residuals become apparent in the 3.0-7.0 keV energy band indicating the existence of a weak population of non-thermal particles which cannot be well-modeled by thermal plasma models. And thirdly, when extrapolating the spectrum – after restriction to the extraction region used to derive the XMM-Newton result mentioned in the introduction – into the 3-7 keV range, the power-law is consistent (within the uncertainties of the power-law index) with the flux derived with XMM-Newton in that energy range, while the apec model falls short of it (by a factor of 0.78 [0.67-0.89]). Therefore, we claim that the power-law interpretation is favoured, and conclude that the flux derived with eROSITA from the entire source is likely a measure of its synchrotron emission.

2.2. Fermi-LAT data analysis

Based on four years of Fermi-LAT data (3FGL, LAT Collaboration 2015), Acero et al. (2015) have derived a GeV spectrum from HESS J1614-518. This result was used in H.E.S.S. Collaboration et al. (2018) to produce a GeV-TeV spectrum of the source, which showed a rather hard ($\Gamma \sim 2$) spectrum below 1 TeV indicative of a hadronic emission spectrum, and a softening at higher energies. To improve the LAT spectrum, we have used data until January 2023 (in total $\sim$ 14.5 years) and have derived an updated sky map above 10 GeV and an updated spectrum above 1 GeV.

To this end, we analyzed Pass 8 Fermi-LAT data (P8R3) using the `fermitools` Ver. 2.0.8 standard analysis software, selecting a region of 40° size centered on the remnant's TeV coordinates (see Tab. 2), Source event class and type were selected so that front and back interactions (evclass=128, evtype=3) are included in the data sets. A maximum zenith angle of 90° was used for the data selection. To secure a good sampling of the Fermi-LAT Point Spread Functions (PSF), we set an angular bin size of 0.05°. The Fermi-LAT background was modeled by including the Galactic diffuse component (`gll_iem_v07.fits`), the isotropic diffuse component (`iso_P8R3_SOURCE_V3_v1.txt`), and all sources present in the Fermi-LAT 12 year point source catalog (4FGL-DR3). We chose to let the normalization of all sources within 5° of the center of the region of interest (ROI) free, and fixed the remaining parameters to default catalog values. A maximum likelihood analysis, described in Mattox et al. (1996), was employed to maximize the probability of the model fitting the data. The 4FGL-DR3 extended GeV source 4FGL J1615.3-5146e that is associated with the remnant appears with different spectral parameters than the 3FGL source in Acero et al. (2015), with a Log-Parabola spectrum being favoured over a simple power law. Therefore we tested both models in the following.

We perform a series of binned analysis procedures for extended Fermi-LAT sources. Both residual count map and Test Statistic (TS) maps were constructed to assess the morphology of the gamma-ray emission. The detection significance calculation is based on the maximum likelihood Test Statistic (TS). The process of TS map creation is contingent on a simulated point source which is moved through the grid obtaining the maximum likelihood fit at each position of the grid $2\Delta\ln(\text{likelihood})$. On the left panel of Fig. 7, the Fermi-LAT Test Statistic (TS) skymap above 10 GeV is shown. The right panel of the same figure illustrates the residual count map above 10 GeV, from the exact same position of the sky.

Four distinct approaches were employed for the production of the GeV SED of the source of interest. Initially, we adopted the default 4FG-DR3 spatial disk model of the remnant, Ra=243.83°, Dec=-51.78°, and Radius=0.42°, which favors a reconstructed source position that is somewhat shifted to the North-East (by $\sim 0.3°$) in comparison to the radio and TeV best-fit position of the remnant. This discrepancy is also visible in the obtained GeV skymaps of Fig. 7. We then moderately modified the parameters of this default spatial disk model by changing its center and size according to the best-fit TeV (H.E.S.S. Collaboration et al. 2018) and radio centroids as obtained from this work, respectively, and re-ran the spectral analysis. The two models derived when moderately modifying the spatial disk parameter to match those of the TeV and radio centroids are consistent with the default spatial disk Fermi/LAT model, while the resulting difference in flux and spectrum is negligible. Finally, for consistency purposes between the GeV and TeV data, a shell-type structure as defined in H.E.S.S. Collaboration et al. (2018) was also adopted as a spatial template, to evaluate whether the GeV emission is also consistent with a shell-type emisssion pattern as observed in the TeV range. As expected by the obtained morphology of the source at GeV energies, the TS value for a shell-like spatial template is slightly lower than that for a disk template (~ 280 vs ~ 320), however it is statistically similarly acceptable, and motivated by the TeV result it is a viable physics model of the source also in the GeV band. The GeV flux derived with a shell model is only $\sim 7\%$ lower than that derived with a disk-like template. Thus, the GeV spectrum derived with the disk model can also be used to estimate the spectrum under a shell hypothesis, for example when describing the γ-ray SED with a one-zone model.

For the spectral fitting procedure, the normalizations of all 4FGL-DR3 sources included in the model within 5° distance from the analysis (source of interest) center, as well as the normalizations of the Galactic diffuse and isotropic background were let to vary. A Log-Parabola describes the GeV spectrum of HESS J1614-518 better than a power-law (a result which is also supported by the derived spectral plots of all 4FGL-DR3 sources[2]). To derive spectral data points, the data are divided into five equally-spaced (in log-space) bins. The resulting SED in the 1-800 GeV energy band is shown in the right panel of Fig. 8, together with the H.E.S.S. data, revealing a substantially steeper spectrum than what was previously reported when using 4 years of Fermi-LAT data (3FGL).

The result is largely insensitive to the adopted spectral model (best-fit log-parabola or best-fit power-law) used to construct the SED. In particular, as explicitly stated in the 12 year Fermi/LAT source catalog[2] sources are modeled as a Log-Parabola if statistically significant curvature is detected (according to `Signif_Curve task`), or as a simple powerlaw otherwise. Overall, we conclude that this discrepancy between published and updated results arises as a combination of the additional years of Fermi/LAT data employed in this work and the updated model used in the 4FGL-DR3 data to model the Galactic diffuse component and the isotropic diffuse component (`gll_iem_v07.fits` and `iso_P8R3_SOURCE_V3_v1.txt` Fermi/LAT files respectively).

Fermi-LAT analysis results reported in this work are consistent with those obtained by Guo & Xin (2021) who analyzed $\sim$ 12 years of Fermi-LAT data in a similar effort to refine the morphology of the GeV emission, and broadly consistent in terms of spectral shape with the obtained spectral plots (and corresponding spectral models) of 4FGL-DR3 sources[2].

2.3. GLEAM data analysis

For this work, we used publicly available GLEAM radio continuum data, which were extracted using the GLEAM's team cutout server into 3° raw cutouts. However, the first release of GLEAM radio data (Wayth et al. 2015) covers the extragalactic sky minus the Galactic Plane (for the most part) and since HESS J1614-518 is located on the Galactic plane, although raw intensity maps from the location of our source of interest are available, no further analysis products have been publicly released. This prevents us from cleaning the images and/or performing a detailed radio spectral analysis of the remnant. However, since the publicly available image products have pixels in units of Jy/beam, they can be used for rough flux estimates.

[2] `https://fermi.gsfc.nasa.gov/ssc/data/access/lat/12yr_catalog/`

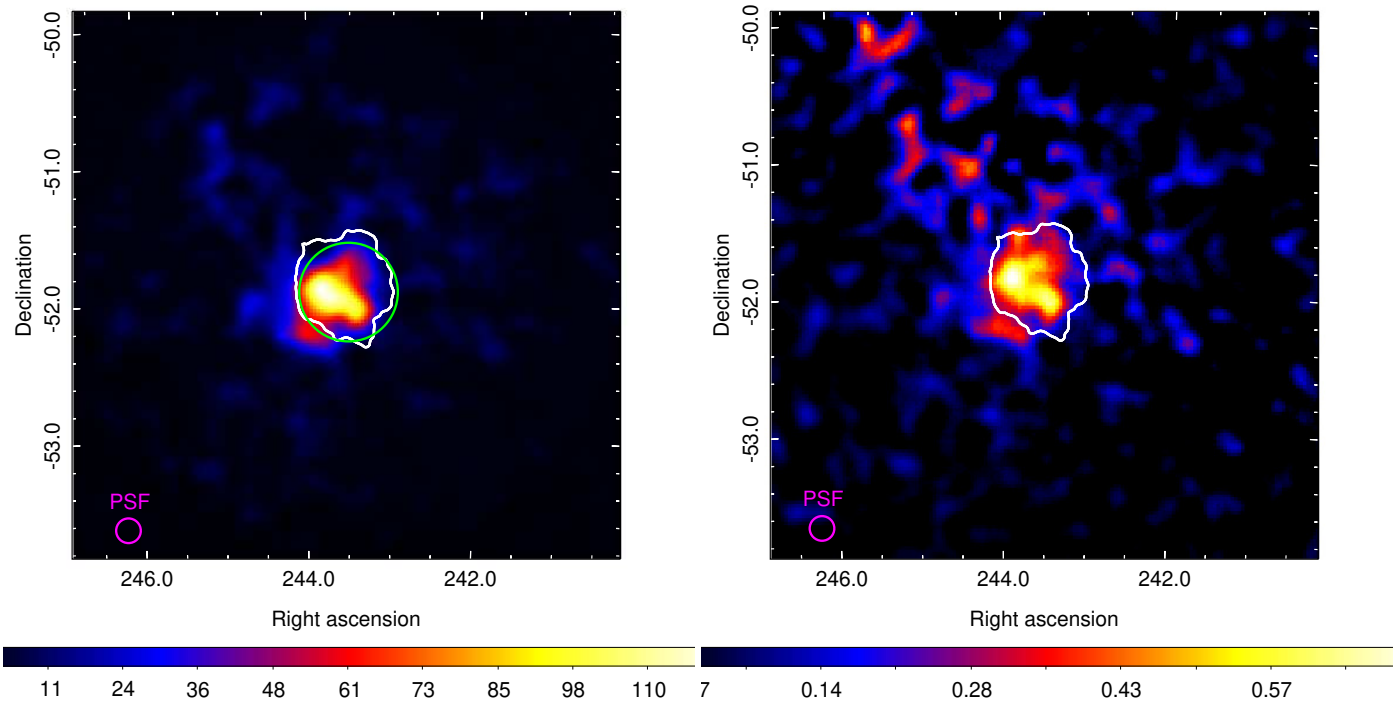

Fig. 7. Left panel: $4^\circ \times 4^\circ$ Fermi-LAT TS map above 10 GeV, centered at the best fit coordinates of the TeV emission according to Tab. 2. The best fit position and size of the counterpart from the GLEAM survey data is illustrated as green circle. The image, which has a $90''$ pixel size, is convolved with a $\sigma = 2.25'$ Gaussian. Right panel: Fermi-LAT residual count map above 10 GeV from the same portion of the sky. The image, which has a $90''$ pixel size, is convolved with a $\sigma = 3.75'$ Gaussian. The white contour marks the 5 σ significance extent of the TeV source as detected with H.E.S.S. (H.E.S.S. Collaboration et al. 2018). The magenta circle represents the 68% containment size of the PSF at the energy threshold of the sky maps (10 GeV), no smoothing applied. *To be checked: Ideally, the PSF representation would be an inset with the same color scale as the actual source.*

As a zero-order attempt, a flux can be derived from the entire on-source region. Taking into account the central frequency (155 MHz) of the 139-170 MHz wide-frequency band used for the construction of the right-hand panel radio continuum image of Fig. 1, the exact size and shape of the beam at that particular declination of the remnant's position, and considering as an extraction region the best radio fit as obtained in sec. 3 and reported in Tab. 2 and a nearby background extraction region of the same size and shape, a source flux can be obtained by simply subtracting the derived background flux from the on-source flux making use of the following mathematical formula for the total flux calculation:

$$\text{Total flux}[\text{erg}/\text{cm}^2/\text{s}] = 10^{-23} \times \text{Total flux}[\text{Jy}/\text{beam}] \times (\text{pixelarea}[(^\circ)^2] \times \text{central frequency}[\text{Hz}]/\text{beamvolume}[(^\circ)^2]) \quad (1)$$

Beamvolume is defined as:

$$\text{beamvolume} = \frac{\pi \times \phi \times \theta}{4 \times ln2} \quad (2)$$

where ϕ and θ represent the Full Width Half Maximum (FWHM) of the semi-major and semi-minor axis of the beam in deg (an elliptical beam of $\sim 0.055^\circ \times 0.05^\circ$ size is obtained at the remnant's location, as mentioned in the caption of Fig. 1). However, the such-derived result is unstable and not trustworthy (negative flux values, obtained results depend heavily on the selection of the background region), given that the source is located in a highly contaminated region.

A more sophisticated approach in terms of selection of the proper on-source and background regions is therefore necessary. We adopted a similar approach as the one used in the Hurley-Walker et al. (2019a). Here, the `POLYGON_FLUX`[3] software was employed, providing an interactive view of either a single band GLEAM radio continuum image or of the GLEAM RGB cube. In Fig. 9 we show the obtained RGB cube that we inspected in this work for the optimal selection of the on-source and background control regions. The aforementioned image provides a wide frequency coverage of the region of interest, allowing us to distinguish candidate remnants from HII regions, since the latter appear as optically thick structures in dark blue color in the images, due to radio synchrotron absorption. Those dark blue HII regions mainly positioned at the North-Western side of the remnant prevent the detection of the radio synchrotron shell of the remnant when looking at higher frequencies (e.g., at 1.4 GHZ, 873 MHz with the Australian Telescope Compact Array (ATCA) as discussed in H.E.S.S. Collaboration et al. (2018)) where most of the emission seems to be associated with the surrounding HII regions rather than being attributed to the remnant. The proper selection of the flux extraction regions is achieved by inspecting the GLEAM RGB cube and drawing a polygon region that contains the area that the SNR extends over (without including those parts where the remnant overlaps with nearby HII regions - an identical cut to the North-Western parts of the remnant as in sec. 3, where we study the morphology of the remnant, was applied), and additionally disentangling which parts of the annulus surrounding the polygon are representative of the background by excluding polygonal regions which are likely contaminated with HII regions or emission originating from unre-

[3] `https://github.com/nhurleywalker/polygon-flux`

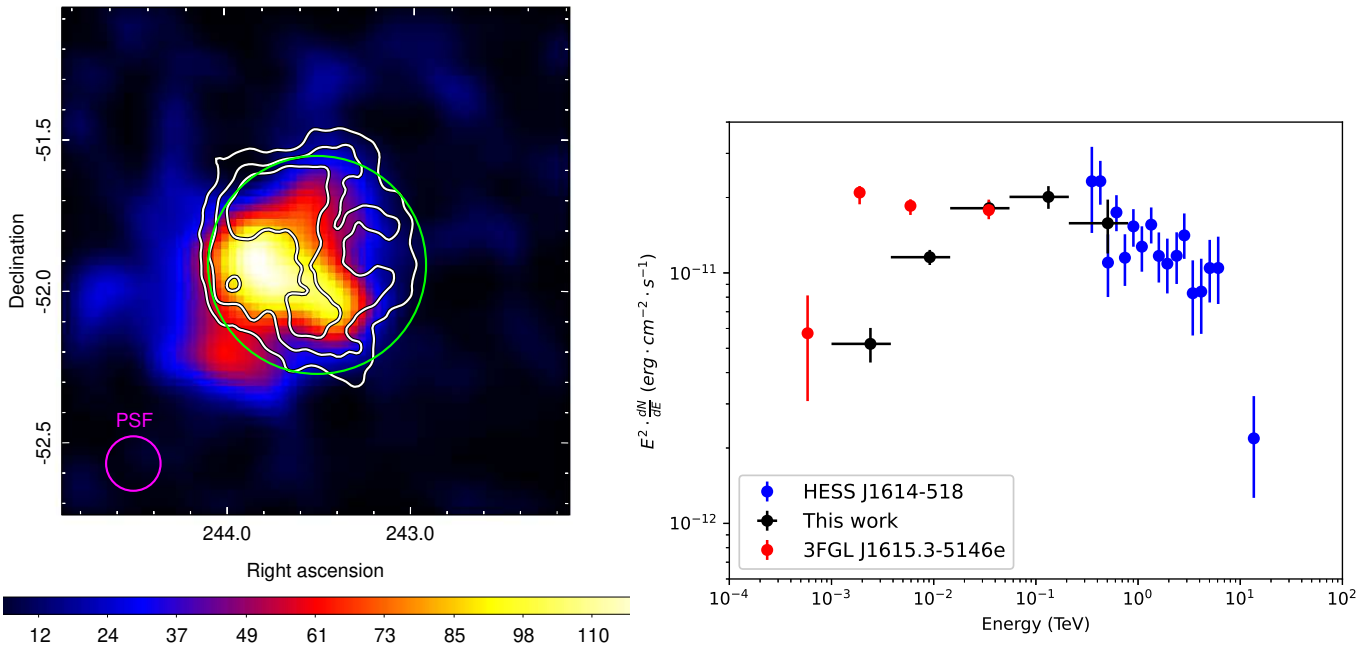

Fig. 8. Left panel: $1.7^\circ \times 1.7^\circ$ Fermi-LAT TS map >10 GeV centered at the best fit coordinates of the TeV emission according to Tab. 2. The white contours mark the 5, 7, 9, 11 σ significance of the source as detected with H.E.S.S. (H.E.S.S. Collaboration et al. 2018). The best fit position of the radio GLEAM survey data is illustrated in green. The image, of 90″ pixel size, is convolved with a $\sigma = 2.25'$ Gaussian. The magenta thick circle represents the 68% containment PSF size, applied at the 10 GeV energy threshold used for the construction of the TS map. Right panel: HESS J1614-518 γ-ray SED. Black dots correspond to the Fermi-LAT spectrum in the 1-800 GeV band. Red and blue dots correspond to the 3FGL GeV spectrum from Acero et al. (2015) and to the H.E.S.S. TeV spectrum from H.E.S.S. Collaboration et al. (2018), respectively.

lated objects. On the right panel of Fig. 9, the selected polygons are displayed. Further explanation of the individual polygons can be found in the caption of the corresponding figure. We calculated the total flux inside the white polygon (on-source region) and the yellow polygonal region (background control region). We then extrapolated these values to the total area of the SNR as computed from the best radio fit in sec. 3 and subtracted the background flux from the on-source value to derive the source flux. The derived flux is $0.31^{+0.19}_{-0.14} \times 10^{-13}$erg/cm^2/s at 155 MHz. $0.13^{+0.08}_{-0.06} \times 10^{-13}$erg/cm^2/s at 88 MHz, $0.23^{+0.15}_{-0.10} \times 10^{-13}$erg/cm^2/s at 118 MHz, and $0.29^{+0.18}_{-0.12} \times 10^{-13}$erg/cm^2/s at 200 MHz. Flux errors were estimated by taking into account errors in the beam size at each individual frequency, errors in the surface brightness calculation when inspecting the reconstructed GLEAM maps by `SAOIMAGE DS9` (i.e., adding up the surface brightness values of each pixel), and errors from the radio morphology study when extrapolating the selected on-source and background regions to the obtained best-fit size and shape of the remnant. The latter error dominates the total error values by a wide margin.

Table 2. Best-fit parameters of HESS J1614-518 observation to a 2D shell model, using H.E.S.S., GLEAM, and eROSITA images.

Data	Parameter (degree)	Best-fit value	Lower bound	Upper bound
TeV	R.A.	243.54	-0.01	+0.01
	Dec.	-51.87	-0.01	+0.01
	R_{in}	0.18	-0.02	+0.02
	R_{out}	0.42	-0.01	+0.01
Radio	R.A.	243.51	-0.02	+0.10
	Dec.	-51.92	-0.04	+0.04
	R_{in}	0.25	-0.03	+0.05
	R_{out}	0.36	-0.09	+0.10
X-rays	R.A.	243.61	-0.01	+0.01
	Dec.	-51.94	-0.02	+0.01
	R_{in}	0.18	-0.01	+0.01
	R_{out}	0.45	-0.01	+0.02

Notes. The values for the TeV data were taken from H.E.S.S. Collaboration et al. (2018). In this work, we treat the parameters derived in the latter work as representative for our analysis, i.e., the position of the centroids is fixed to the TeV centroid.

3. Morphological results

The TeV morphology has been identified in H.E.S.S. Collaboration et al. (2018) as shell-type. The morphology can satisfactorily be described by a thick spherical shell, with homogeneous emission inside the thick shell, which is projected onto the sky (see Tab. 2 for the fit parameters). From the image (Fig. 1) and the radial profile (see Fig. A.1 in H.E.S.S. Collaboration et al. (2018)), respectively, it seems in addition that – even if statistics is limited – there is no full azimuthal symmetry, and some emission might emerge from inside the shell.

The GLEAM (radio continuum emission at 0.139-0.17 GHz) survey data towards the area in which HESS J1614-518 is located exhibit extended diffuse emission likely associated with the Galactic plane as well as nearby HII regions. Nevertheless, a shell-type emission structure co-located with HESS J1614-518 is clearly visible. Given the position and sizes of the TeV and radio sources, it is likely that the emissions stem from the same

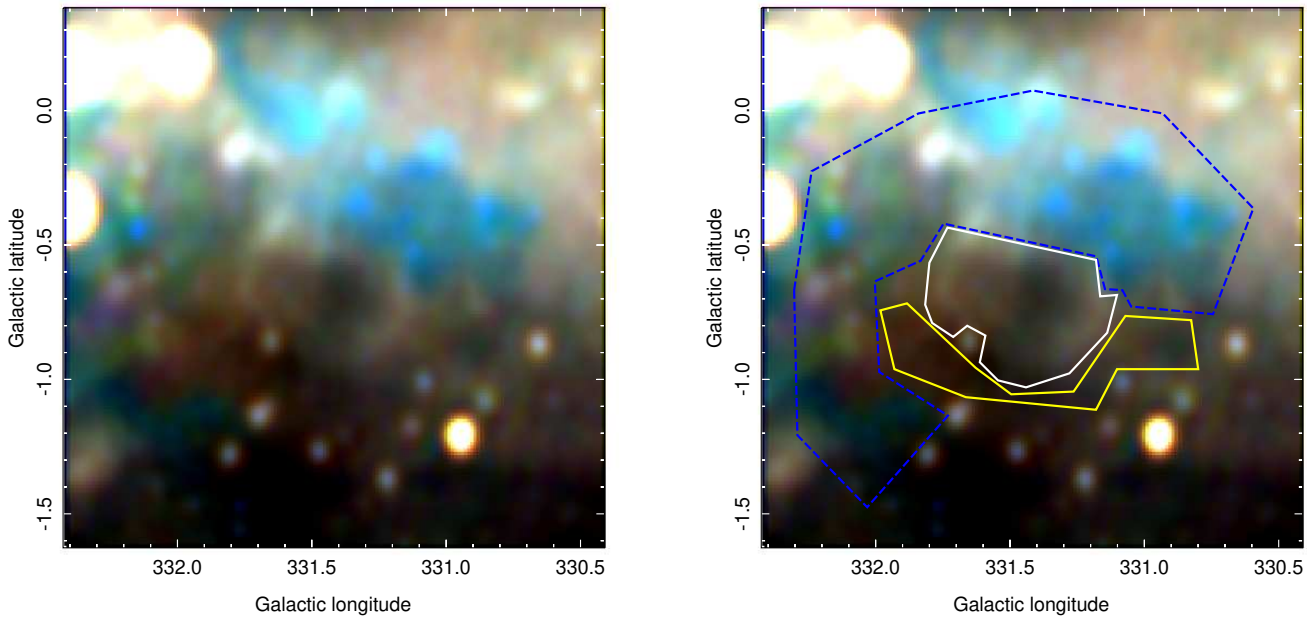

Fig. 9. The two panels show the GLEAM RGB cube with color-to-energy correspondence as follows: R:72-103 MHz, G:103-134 MHz, and B:139-170 MHz. Although the images depict a complex background region, HESS J1614-518 is clearly discernible as an elliptical shape in white color at the center of the image. The remnant is surrounded by HII regions which become apparent in dark blue colors since they become optically thick absorbing radio synchrotron emission at lower frequency bands. The right panel indicates the flux computation method used in this work. The white polygon encapsulates the region that the SNR extends over, the blue-dashed line corresponds to contaminated regions that are not representative of the background, whereas the yellow region indicates the background control region.

astrophysical object, despite the high source density towards the Galactic plane. To quantify the agreement, we applied the same source model to the GLEAM data as was used for the TeV shell. Since there is no available template for the diffuse extended emission, we excluded the strongest contaminated area from the fitting procedure (see Fig. 10). The fit model is a homogeneous spherical 3D shell projected onto a 2D plane and is described by the following equation:

$$\varepsilon = \mathrm{A} \times \frac{2}{3}\pi(R_{\mathrm{out}}^3 - R_{\mathrm{in}}^3) \begin{cases} \sqrt{R_{out}^2 - r^2} - \sqrt{R_{in}^2 - R^2},\ R < R_{in} \\ \sqrt{R_{out}^2 - R^2},\ R_{in} < R < R_{out} \\ 0,\ \text{otherwise} \end{cases} \tag{3}$$

Here, R_{in} and R_{out} are the inner and outer radius of the shell, respectively. R denotes the distance from the point of interest to the center of the shell. The amplitude A indicates the relative strength of emission from the shell compare to the background. Fitting is performed using the *Sherpa*[4] environment. First, a model of a flat background is fit to the data. Once the background level is obtained, we add the main component that describes the emission from the SNR candidate. The above shell model is folded with the point spread function (PSF) of the corresponding instrument and multiplied with the exposure map before being fit to the data. We assume a Gaussian PSF with the FWHM interpreted from the primary beam size of the MWA of 2.4 arcmin (Wayth et al. 2015). This PSF assumption is also consistent with the average PSF calculated by Hurley-Walker et al. (2019b). Fit parameters are the center of the homogeneous shell, inner radius and the thickness of the shell. For the center coordinates of the emitting shell, we first fix them to the best-fit values of the TeV shell morphology, and later allow them to vary. The resulting fit parameters are given in Tab. 2. The source centroids of the radio and the TeV sources are within errors identical, confirming the cross-identification of the two sources. As also expected from the image, the shell width of the radio source is smaller with an outer radius of 0.36^{o}, see also the comparison of the radial profiles in Fig. 11. Given the available data, we nevertheless conclude that there is strong evidence that the radio shell seen in GLEAM data and the TeV shell-type source HESS J1614-518 are from the same astrophysical object.

The X-ray emission seen from the direction of HESS J1614-518 is apparently more center-filled than the radio shell (Fig. 3). We fit the same 2D shell model to the eRASS:4 image in the energy range 1.31-3.10 keV, where the X-ray emission is most visible. Similar to the radio image fitting, a single Gaussian profile is also used as the PSF of eROSITA survey, where the FWHM is the half energy width (HEW) at 15 arcsec (Predehl et al. 2021). Here, we mask the data coming from the bright point source toward the southern part of the SNR candidate. We also restricted the fitting area as a circular region closely surrounding HESS J1614-518, which does not include the source HESS J1616-508 (Fig. 10). Best-fit results for the X-ray morphology investigation are shown in Tab. 2.

As can be seen from the residual image (Fig. 10), the shell model does not model the entire X-ray emission from the source. To quantify whether a shell description is warranted by the data, we adopted the procedure introduced in H.E.S.S. Collaboration et al. (2018) and compared the shell fit result to a result from a

[4] https://cxc.cfa.harvard.edu/sherpa/

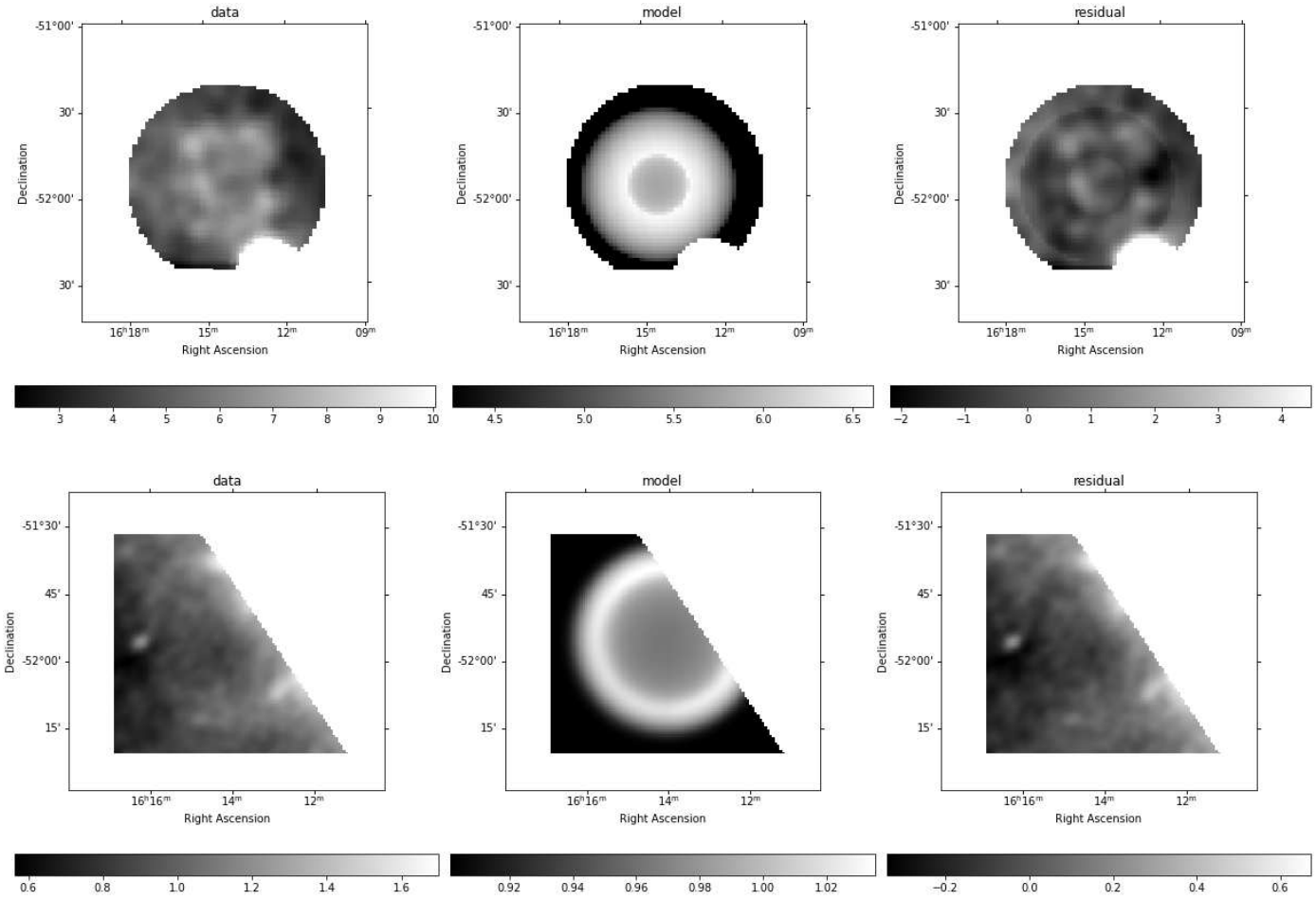

Fig. 10. Upper panel, left to right: Data, best-fit model, and residual images when fitting the eROSITA image of HESS J1614-518 to a 2D shell model. The image used for the morphology study is in the energy range 1.31-3.10 keV, binned with 8 × 8 pixels (1 pixel corresponds to 10") and smoothed with a Gaussian kernel of $\sigma = 2$ bins. The bright source towards the southwest direction is excluded from the fitting procedure. Lower panel: Similarly, the best-fit results for morphology study of the radio shell based on GLEAM data are shown. Note that the maxima and minima of the color scales differ between the images for the purpose of visual inspection. This approach however exaggerates the significance of the residuals.

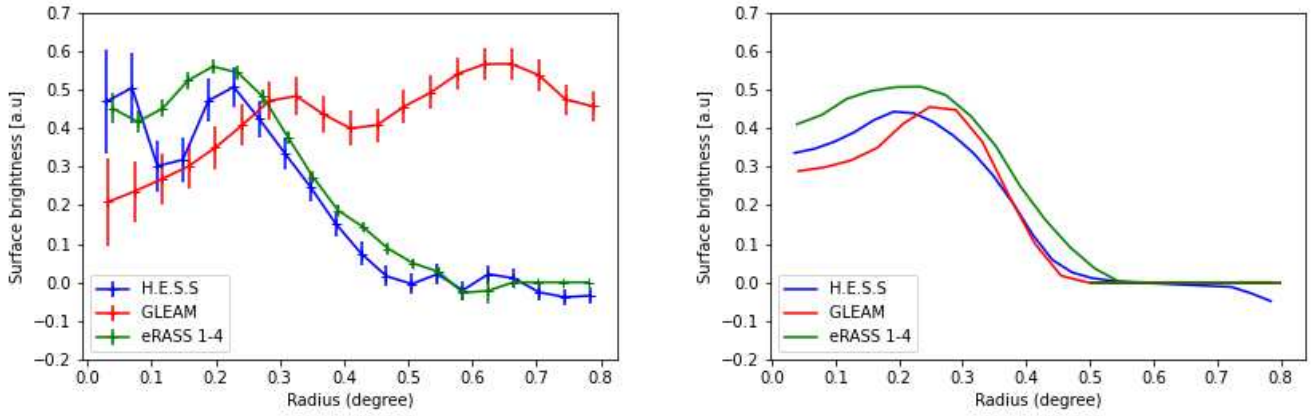

Fig. 11. Left panel: Radial emission profile of HESS J1614-518. Data from the H.E.S.S Galactic survey, GLEAM and eRASS:4 are plotted in blue, red and green points, respectively. All surface brightnesses are extracted from concentric annuli around the TeV best-fit shell center (H.E.S.S. Collaboration et al. 2018). All profiles were normalized to an arbitrary unit for better visualization of the shell structure. The increase of the surface brightness of the radio data beyond $\sim 0.4°$ is attributed to the contamination towards the northwest direction. Right panel: Radial profiles are computed from 2D shell models fitted to H.E.S.S, GLEAM, and eRASS:4 data depicted in the left panel. Similar to the left panel, these profiles originate from annular extraction areas centered at the TeV emission center. Only the 2D shell models are plotted here, disregarding the central peak in the TeV image and the contamination in the radio image.

Gaussian as null hypothesis description. The *Akaike Information Criterion* (AIC) is used to quantify the improvement of the fit with the shell model H_1 to the Gaussian hypothesis H_0, since the two models are non-nested meaning they can not be cross-transformed continuously. First we calculate the AIC value for each best fit model:

$$\mathrm{AIC} = 2k - 2\ln \mathscr{L}_{ML} \tag{4}$$

where $\mathscr{L}_{ML}$ is the log likelihood of the best-fit model, and k are the degrees of freedom. Then we estimate the likelihood of the improvement of H_1 to the best-fit null hypothesis H_0:

$$\mathscr{L}_{\mathrm{AIC,H_0}} = \mathrm{C\dot{e}xp}(-\frac{\mathrm{AIC,H_0} - \mathrm{AIC,H_1}}{2}) \tag{5}$$

where C is set to unity. The computed $\mathscr{L}_{\mathrm{AIC,H_0}}$ of the shell model for the X-ray data is 1.67×10^{-5}. We argue that the setting is similar to the one used in (H.E.S.S. Collaboration et al. 2018), where the interpretation of $\mathscr{L}_{\mathrm{AIC,H_0}}$ as a null-hypothesis probability (with $C = 1$) was verified with simulations. The derived value therefore confirms that the shell-hypothesis is warranted by the X-ray data with sufficient degree of certainty. For the radio data, the shell interpretation is much clearer already by eye, which is confirmed by an extremely low $\mathscr{L}_{\mathrm{AIC,H_0}}$ when the same test is applied to the radio data. *To be checked: The null hypothesis* $\mathrm{H_0}$ *is the Gaussian (the best-fit Gaussian, in fact), whereas the shell model is the tested hypothesis* $\mathrm{H_1}$. *Make sure this is clear.*

From the best-fit model depicted in Fig. 10, it is evident that the 2D shell effectively represents the data. While the best-fit centers agree within the margin of errors, the X-ray shell appears to be more diffuse and wider compared to the radio shell (see Table. 2). On the other hand, from the Fermi-LAT analysis, the residual count map above 10 GeV appears as a spatial disk with some extended wings toward the south-west and south-east directions of the SNR (see Fig. 7, section 2.2). This is also the case for other TeV-selected SNRs such as HESS J1534-571 (Araya 2017), HESS J1731-347 and SN 1006 (Condon et al. 2017). It is worth mentioning that the GeV disks of the above TeV SNRs reside relatively well within the TeV shell and show the most detection significance near the TeV peak, whilst the GeV disk of HESS J1614-518 presents a anti-correlation to the TeV profile.

4. Broadband spectral results

Table 3. The required energy budget for protons in different scenarios.

Target density ($\mathrm{cm^{-3}}$)	1		10	
Distance (kpc)	3.5	5.5	3.5	5.5
$W_\mathrm{p}^\mathrm{tot}$ ($\times 10^{51}$ erg)	0.63	1.13	0.06	0.11

To construct a broadband spectral energy distribution from HESS J1614-518, we used archival TeV data H.E.S.S. Collaboration et al. (2018) as well as the GeV, X-ray, and radio continuum GLEAM spectra derived in this work. For the GLEAM data, as mentioned in sec. 2.3, we must treat the obtained flux results with caution, mainly due to high contamination at and around the remnant's location.

The SED is plotted in Fig. 12. To construct expected model SEDs in a leptonic scenario (GeV-TeV emission from Inverse Compton scattering of relativistic electrons) and in a hadronic scenario (GeV-TeV emission from π^0-decay following interactions of relativistic protons with gas), the *naima*[5] (Zabalza 2015) package is employed.

A pure leptonic emission model is also plotted in Fig. 12. The emission modeling package *naima* was used to calculate the flux coming from different processes, assuming a simple one-zone model with a exponential cutoff power-law particle distribution. The particle cutoff energy is at 5 TeV and the spectral index is 1.8. Constrained by the radio and X-ray flux, the magnetic field is estimated to be 25 μG. The IC scattering of high energy CR electrons are considered from three target photon fields, namely the FIR photon fields from heated dust, the NIR photon fields from stellar emission and the cosmic microwave background (CMB). The temperature and energy density of the FIR and NIR fields are calculated based on the relation in Shibata et al. (2011) assuming a distance of 5.5 kpc. The values are 2500 K and 1.42 eV $\mathrm{cm^{-3}}$ for the FIR and 30 K and 0.74 eV $\mathrm{cm^{-3}}$ for the NIR photon fields, respectively. These values are consistent with the estimation of the absorption of the very high energy gamma rays in the Milky Way (Vernetto & Lipari 2016). The required total energy in the CR electrons for the distance 5.5 kpc is 5.29 x 10^{48} erg, approximately 0.5% of the typical kinetic energy released in a supernova explosion. At a distance of 3.5 kpc, the electron energy is roughly half of the above value. This leptonic energy is of the same order as other SNRs such as RCW 86 (H. E. S. S. Collaboration et al. 2018).

To be able to compare with the hadronic dominant gamma rays production at VHE range, we also constructed a combination leptonic + hadronic model as following. The protons particle distribution follows a powerlaw of index 1.7 with cut-off energy at 30 TeV. The gamma rays at GeV-TeV are assumed to be the products of π^0-decay following the interaction between CR protons and nearby gas with typical average target density of 1 $\mathrm{cm^{-3}}$. In order to reproduce the data points from Fermi - LAT (this work) and H.E.S.S. (H.E.S.S. Collaboration et al. 2018), the required total energy of protons is 1.13 $\times 10^{51}$erg, which exceeds the typical total kinetic energy of supernovae. For the π^0-decay to take over the gamma rays production at GeV-TeV range, the energy injected in electrons has to be lower, in this example 1.27 $\times 10^{48}$erg. Consequently, the magnetic field strength needs to have higher value at 50 μG. In addition to the typical value of target gas density, a denser environment, e.g. a molecular cloud, at 10 $\mathrm{cm^{-3}}$ is also considered. Table 3 summarizes the total energy content of protons for different target densities and distance to the SNR.

The contamination towards the North-West direction of the source (Fig. 9) in the radio image could indicate the presence of molecular clouds nearby the source. However, the fact that the GeV emission comes from the opposite part of the SNR implies that the GeV gamma rays is not likely to stem from hadronic interaction of CRs and nearby cold gas. Furthermore, the total energy of protons required to reproduce the gamma ray spectrum at the GeV-TeV range is unrealistic because it is of order of the SNR's total kinetic energy. Analysis of other TeV emitting SNRs, e.g. RX J1713.7-3946 (Aharonian et al. 2006b; Fukui et al. 2012), RX J0852.0-4622 (Fukui et al. 2017) and HESS J1731-347 (Fukuda et al. 2014) predict that the total CR protons energy for a hadronic scenario of gamma rays is around $\sim 10^{49}$ erg. Therefore, the observed gamma rays are not likely to originate from hadronic induced processes.

[5] https://naima.readthedocs.io/en/latest/

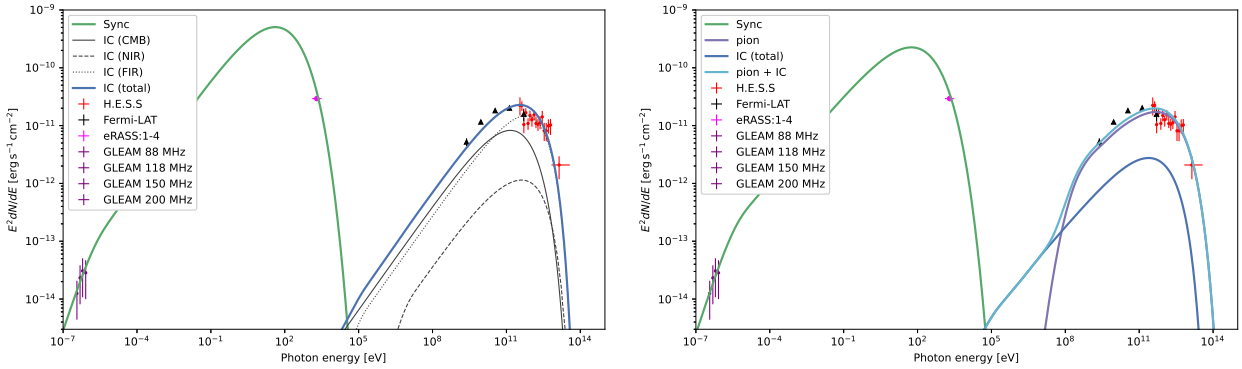

Fig. 12. Broadband SED of HESS J1614-518. Left: A pure leptonic origin of cosmic rays interaction is plotted. The IC emission at very high energy is fitted to the data points from *Fermi*-LAT and H.E.S.S. The synchrotron flux is constrained with eRASS:1-4 data (this work) and radio (GLEAM survey). Right: A leptonic + hadronic model of gamma rays production is also presented.

5. Distance to HESS J1614-465, age, and pulsar association

In the last two decades, distance measurements have been attempted on the remnant. When assumed that the remnant's progenitor star was part of the Pismis open cluster, which is positioned in the remnant's center vicinity, a 1.0 ± 0.4 kpc distance can be derived (Piatti et al. 2000). A similar distance is also obtained from HI void line velocity measurements (Sagittarius-Carina spiral arm) (H.E.S.S. Collaboration et al. 2018). On the other hand, considering a potential association of the remnant with the XMMU J161406.0-515225 point source (Sakai et al. 2011) and the diffuse Suzaku Src A (Matsumoto et al. 2008), both located close to the center of the remnant, a rough distance scale of 10 kpc is derived based on the derived absorption column values. It is noteworthy that Matsumoto et al. (2008) spectral analysis of Src A extended source gave acceptable results for both an absorbed powerlaw (of $\Gamma = 1.73$ and $N_H = 1.21 \times 10^{22}$cm^{-2} - results highly consistent with what we obtained in this work in terms of power law index and consistent within uncertainties in terms of absorption column density) and an apec model, however, the apec model provided an uncomfortably large temperature of ~ 10 keV and thus they adopted the non-thermal powerlaw model for the rest of their analysis. Finally, a distance of 5.5 kpc - compatible with the Norma-Cygnus spiral arm has been considered (H.E.S.S. Collaboration et al. 2018).

In this work, we made use of the remnant's derived best-fit absorption column density to provide more insight into its distance estimation, since all distance measurements reported to date come from potential remnant's associations and not from the object itself. In more detail, a $N_h = 0.82^{+0.32}_{-0.22} \times 10^{22}$cm^{-2} arises as the best fit from the X-ray spectral fitting process. Taking into consideration the latest statistical relation between the observed absorption in X-rays with extinction/mean color excess (Foight et al. 2016):

$$\begin{aligned} N_H/E_{B-V} &= 8.9 \times 10^{21}\ \mathrm{cm}^{-2} \cdot \mathrm{mag}^{-1} \\ N_H[cm^{-2}/A_v] &= 2.87(\pm 0.12) \times 10^{21} \end{aligned} \quad (6)$$

one obtains an extinction range as follows: $A_v = 2.86^{+1.23}_{-0.88}$mag. Comparing the derived extinction to GAIA/2MASS data sets (Lallement et al. 2019) one places the remnant well above 3.5 kpc, as shown on the left panel of Fig. 13. However, when employing the latest data sets (Lallement et al. 2022) as provided by G-Tomo app-EXPLORE[6] significantly lower distances are favored towards the direction of the remnant, as shown on the right panel of Fig. 13. In particular, comparing the obtained extinction values to Lallement et al. (2022) data sets a distance range of $3.51^{+1.76}_{-0.88}$ kpc is derived as shown on the right panel of Fig. 13 in black, with the best-fit absorption column density value corresponding to a 3.51 kpc distance and thus likely placing the remnant at the Scutum-Crux spiral arm. The above results suggest that a potential association of the remnant with the Pismis open cluster and HI void (1.2-1.5 kpc), which would place the remnant at the Sagittarius-Carina spiral arm is highly unlikely. Similarly, a potential association of the remnant with the XMMU J161406.0-515225 point source and the diffuse Suzaku Src A which would place the remnant at a distance of the scale of 10 kpc is also highly unlikely. However, such an association with the aforementioned X-ray sources cannot be excluded given that the distance measurements of the latest were performed based on the absorption column density obtained from the X-ray spectral fitting and thus carrying large uncertainties. Finally, an association of the remnant with the Norma-Cygnus spiral arm (at ~ 5.5kpc distance) cannot be excluded. If one uses the derived best-fit absorption column density considering that the X-ray emission is of thermal nature, then an extinction lower threshold of 8.0 mag is derived; potentially placing the remnant at a distance well above 6 kpc which is highly unlikely.

A potential association with Pismis 22 could provide constraints on the remnant's age, given that the open cluster age is estimated to be $\sim 40 \pm 15$ Myrs (Piatti et al. 2000). However, the distance computation that we performed in this work disfavors such an association. In light of the new X-ray data, one can now employ the evolutionary models of SNR as provided in Leahy & Williams (2017) to derive an age estimate. Assuming a distance of 3.51 kpc one derives a 44 pc linear diameter for the remnant (using the 0.36° remnant's angular radius, as estimated from the GLEAM radio data). Adopting the default inputs, except for the local ISM number density which is computed to be $n_H = 0.76^{+0.65}_{-0.39}$ cm^{-3} (for $N_H = 0.82^{+0.32}_{-0.22}$ 10^{22}cm^{-2} and a distance of $3.51^{+1.76}_{-0.88}$ kpc as derived above), and assuming an explosion energy of 10^{51} erg, one obtains a remnant's age of $3.9^{+2.35}_{-1.4}$ 10^4 yrs.

All the estimates reported above are provided for an adopted distance of ~ 3.5 kpc. Nevertheless, the later estimates are based on empirical relations. Such empirical relations carry substan-

[6] https://explore-platform.eu/

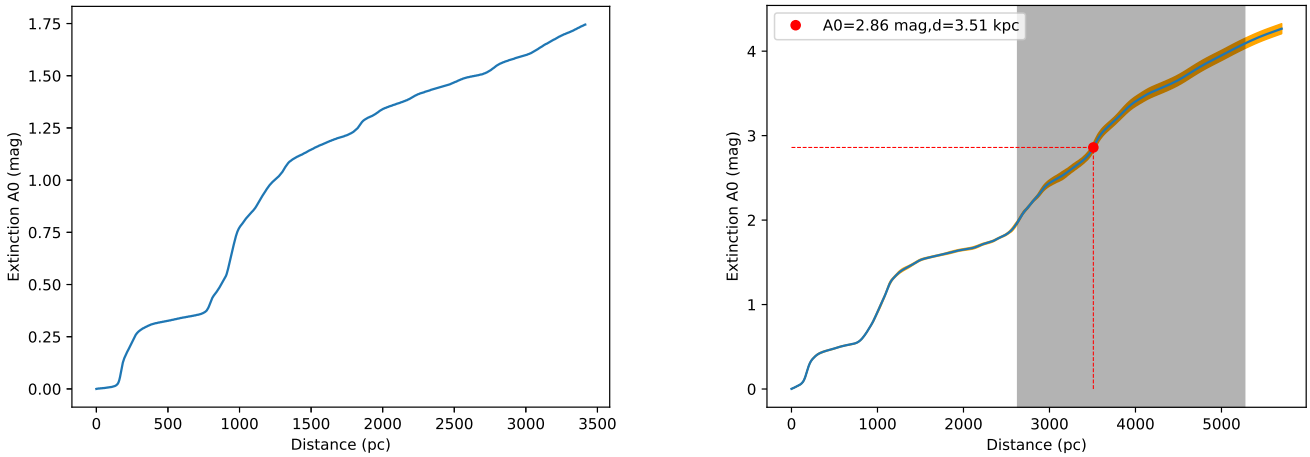

Fig. 13. One-dimensional cumulative extinction as a function of the distance. Left panel: The GAIA/2MASS tool: `https://astro.acri-st.fr/gaia_dev/` is employed, which provides extinction data sets up to 3.5 kpc (Lallement et al. 2019). Right panel: The G-Tomo app created by EXPLORE based on GAIA eDR3 and 2MASS data: `https://explore-platform.eu/` is employed, which provides updated extinction data sets extended up to 5.5 kpc (Lallement et al. 2022).

Table 4. Pulsars within 2° the remnant's center.

Pulsar	Ang. sep. (°)	DM $\mathrm{pc \cdot cm^{-3}}$	D_1 kpc	D_2 kpc	Age kyr	Power ($\dot{E}$) 10^{34} erg $\cdot$ s^{-1}	v_{transv} km $\cdot$ s^{-1}
J1613-5211	0.27	360.1	4.72(6.42)	-	377	0.79	57.68
J1615-5137 (4FGL_J1615.3-5136)	0.36	–	(< 4.10)[a]	-	267	7.3	< 95 ($80.8^{+39.3}_{-20.3}$)[b]
J1614-5048 (4FGL_J1614.5-5047)	1.12	582.4	5.15(7.94)	–	7.42	160	13265
J1617-5055	1.14	467.0	4.74(6.82)	-	8.13	1600	11342
J1616-5017	1.68	194.0	3.48(4.67)	-	167	1.6	597.4

Notes. The table is splitted in two halves: the upper half contains the first three pulsars which lie within the remnant's extension. The rest of the pulsars that lie well outside the remnant's structure are displayed in the lower half of the table. The first and second columns give the pulsar's name and angular separation from the remnant's center (as defined in this work using on the radio GLEAM data). The third column gives the Dispersion Measure. The fourth and fifth columns give the pulsar's distance from Earth based on DM measurements and potential associations, respectively. The values within parenthesis correspond to older distance estimates based on the NE2001 electron density model (Cordes & Lazio 2002). Since 2017, YMW16 is considered the default model for DM-based distance calculations (Yao et al. 2017). The sixth column corresponds to the pulsar's spin-down age. The seventh column presents the pulsar's spin down power. The eighth column displays the transverse velocity required for each pulsar to move from the remnant's center to its present location.

[a] Upper limit distance reported in de Palma et al. (2019)
[b] Computed transverse velocity assuming the remnant's distance of $3.51^{+1.76}_{-0.88}$ kpc

tial scatter. Thus, an alternative scenario with a somewhat larger distance proposed in the literature is examined. Assuming a 5.5 kpc distance (consistent with the derived distance in this work within uncertainties), as reported in H.E.S.S. Collaboration et al. (2018), one computes a 69 pc linear diameter for the remnant by adopting the 0.36° remnant's angular radius, as estimated from the GLEAM radio data. Following a series of identical calculations, as for the case of a 3.5 kpc distance, one derives a local ISM number density of $n_{\mathrm{H}} = 0.48^{+0.19}_{-0.13}$ cm^{-3}, which yields a $1.11^{+0.34}_{-0.24}$ 10^5 yrs age for the remnant according to Leahy & Williams (2017) SNR evolutionary models. However, H.E.S.S. Collaboration et al. (2018) derived local density values of the order of $n_{\mathrm{H}} = 17 - 110$ cm^{-3} from atomic (HI) and molecular (H2) gas distribution data at a distance of 5.5 kpc. Such high values are reasonable if the SNR is indeed located within a spiral arm. Adopting a $n_{\mathrm{H}} = 10$ cm^{-3} as a possible value for a homogeneous density at a distance of 3.5 kpc we obtain a ~ 3.2 10^5 yrs upper limit age for the remnant. It is noteworthy that a 69 pc SNR size (as derived by assuming a distance of 5.5 kpc) cannot line up with the evolutionary SNR solutions when such high local density values $n_{\mathrm{H}} = 17 - 110$ cm^{-3} are considered unless one assumes a higher explosion energy. Assuming the broadly adopted explosion energy of 10^{51} erg, the remnant is expected to have a linear size < 41 pc for $n_{\mathrm{H}} = 17$ cm^{-3} and < 22 pc for $n_{\mathrm{H}} = 110$ cm^{-3} since it expands at a much denser medium. This means that a significantly smaller distance than 5.5 kpc would be required to explain such high local density values given its angular size. In the latter case, the corresponding ages cannot exceed $< 4.4 \times 10^5$ yrs and $< 2.2 \times 10^5$ yrs, respectively. For a remnant of 0.36° angular radius to be located at a distance of 5.5 kpc, a moderately increased explosion energy, $> 4 \times 10^{51}$ erg for $n_{\mathrm{H}} = 17$ cm^{-3}, and a significantly increased explosion energy, $> 4 \times 10^{52}$ erg for $n_{\mathrm{H}} = 110$ cm^{-3}, would be required.

Twenty-one pulsars fall within 2° angular extension from the remnant's radio centroid. Among the twenty-one nearby pulsars, only five have ages that could be compatible with the remnant's young age. The rest are considerably older, $> 5 \times 10^5$ yrs (the majority of which have ages well above 10^6 yrs). The main prop-

erties of the latter five candidates, from the ATNF pulsar catalog[7] (Manchester et al. 2005) together with their computed transverse velocities (using the remnant's center as a starting point and taking into account each pulsar's spin-down age), are summarized in Tab. 4. Among the latter five pulsars, we singled out three, J1613-5211, J1615-5137 (4FGL J1615.3-5136) and J1616-5017, as the most probable candidates since for J1614-5048 and J1617-5055 (which is considered to be associated with HESS J1616-508) the estimated transverse velocity that would be required to reach theirs present location, assuming the remnant's center as a starting point, forbids an association with the remnant. A newly discovered gamma-ray pulsar (it was not included in the 3FGL catalog (Acero et al. 2015), however, it is as of recently part of the 4FGL point source Fermi-LAT catalog under the name 4FGL J1615.3-5136 and its detection and main properties are discussed in more detail in de Palma et al. (2019)), which is considered to be associated with the J1615-5137 radio pulsar, stands out mainly due to its energetics (it exhibits the highest spin down power (7.3×10^{34} erg $\cdot$ s^{-1}, as shown in Tab. 4) among the three candidates), distance from the remnant's center, and computed transverse velocity. We note that since there is no distance estimate for the latter gamma-ray emitting pulsar (except for an upper limit estimate of 4.1 kpc reported in de Palma et al. (2019) which results to a $v_{\rm transv} = 94.3$ km/s), assuming a $3.51^{+1.76}_{-0.88}$ kpc distance (derived remnant's distance), one obtains a $80.8^{+39.3}_{-20.3}$ km/s transverse velocity. It is noteworthy that a potential association with any of the aforementioned pulsars disfavors the extreme close (1.5 kpc distance, related to Pismis 22) and extreme distant (10 kpc) distance estimates/scenarios reported in the literature and is well aligned with the $3.51^{+1.76}_{-0.88}$ kpc remnant's distance reported in this work.

6. Discussion

To be revised: The counterparts of HESS J1614-518 found in the radio continuum and in the X-ray band clearly classify HESS J1614-518 as an SNR. We find that the X-ray emission does not stem from hot gas, but rather from accelerated electrons to TeV energies (synchrotron). This result is compatible with the earlier indication for a non-thermal X-ray component reported in H.E.S.S. Collaboration et al. (2018) by using XMM-Newton data, even though the XMM-Newton results are subject to large systematic uncertainties. The good spatial coincidence of the X-ray, GeV, and TeV emission further supports the results obtained from the modeling of the multiwavelength SED of the SNR, so to say a preference on the leptonic scenario for the origin of gamma ray emission mainly due to the unrealistic total energy of protons required to reconstruct the GeV-TeV spectrum of the remnant, since the same population of accelerated TeV electrons is expected to emit in X-rays through synchrotron and in gamma-rays through inverse Compton. Such a result is also in line with the latest tendency, even if not universally confirmed, that the absence of a non-thermal component in the X-ray spectrum of Galactic SNRs is accompanied by the detection of gamma-ray emission of hadronic origin, while non-thermal X-rays are usually accompanied by leptonically induced gamma-rays (Michailidis et al. 2024a,b; Khabibullin et al. 2024; Guo & Liu 2024). On the other hand, because the electron particle energies emitting radio synchrotron and TeV inverse Compton emission are very different, different morphologies are viable even in a leptonic TeV scenario. Different outcomes are equally feasible in a hadronic setting. Overall, a good spatial correlation of the emission from this SNR is observed across the entire EM spectrum.

In light of the new X-ray data, the distance estimate provided in this work favors a distance of 3.5 kpc for this remnant waning extremely small and large distances of 1 kpc and 10 kpc, respectively, as discussed in the literature by uncertain associations of the remnant with objects that appear spatially coincident with the SNR by chance (refer to sec. 5 for a detailed discussion concerning potential associations). Nevertheless, a 5.5 kpc distance, suggested by H.E.S.S. Collaboration et al. (2018), cannot be ruled out since it is consistent with the derived distance in this study within uncertainties. Despite the fact that we are not able to distinguish between a thermonuclear and a core-collapse origin for a remnant with the information that the present data provide, based on reasonable section criteria, we identified J1613-5211, J1615-5137 (4FGL J1615.3-5136) and J1616-5017 pulsars as the most likely candidates for being associated with the remnant, if the latter is not of type Ia progenitor origin. The association of the remnant with any of these pulsars would also support the idea that the remnant is located at 3.5 kpc. This work emphasizes the importance of multiwavelength studies of Galactic SNR to determine their nature and key properties.

7. Conclusion

To be revised: HESS J1614-518 was originally discovered by H.E.S.S. and reported in Aharonian et al. (2006a). Rowell et al. (2008) reported on a closer look at the HESS J1614-518 source, which has so far been unidentified, suggesting a potential X-ray counterpart as well as a possible link with Pismis 22 open cluster, which happens to lie at the same location. HESS J1614-518 was eventually classified as a supernova remnant candidate purely based on morphological criteria, namely its shell-like appearance in the TeV energy band, only after a comprehensive study of H.E.S.S. Galactic Plane Survey (HGPS) carried out by H.E.S.S. Collaboration et al. (2018). HESS J1614-518 has likely not been discovered in earlier X-ray surveys like the ROSAT all-sky survey because of its extension, mild surface brightness, and contamination with large-scale diffuse emission. A putative detection of X-rays from a small portion of the source without permitting retrieval of any conclusive results was reported using XMM-Newton data (H.E.S.S. Collaboration et al. 2018) largely due to large systematic errors caused by significant stray light impact caused by adjacent strong X-ray emitters (e.g., RCW 103 SNR and 4U 1608-52 LMXB). The detection of significant X-ray emission from HESS J1614-518 using eRASS data demonstrates the potential of exploiting eROSITA's sensitivity even in survey phase to detect X-ray emission from non-thermal SNRs in the Galactic Plane when guided by information from higher and lower energy bands. The X-ray emission has a shell-type appearance, it conforms to the TeV morphology at all 4 sides of the remnant and is strictly contained within the outermost 5σ significance contour detected by H.E.S.S. as depicted in all eRASS images. On top of the detection of HESS J1614-518 X-ray counterpart we report on the additional detection of its radio counterpart utilizing one-year of GLEAM radio data from the source location, thus confirming the SNR nature of the source. A well-defined shell spatially coincident with both the TeV and X-ray extension of the source becomes clearly apparent in the 139-170 MHz radio band, though the sparseness of the data does not allow us to further inspect the radio emission aside from the total flux calculation of the radio synchrotron emission originating from the remnant, which is based on a detail inspection of the radio emission and its nature at and around the remnant of

[7] https://www.atnf.csiro.au/research/pulsar/psrcat/

interest. In particular, we inspected the GLEAM RGB cube that permits us to discriminate between thermal radio (HII regions) and radio synchrotron emission (remnant candidates) thus allowing us to properly select the on-source and background control regions for the calculation of the remnant's flux density, which found to be of the order of 0.31×10^{-13}erg/cm^2/s.

The spectral analysis performed at and around HESS J1614-518 confirms the presence of a soft diffuse foreground and/or background emission component mainly confined below 1.3 keV, which plays a key role though on determining the source spectrum due to the strong emission lines that exhibits in the 1.3-2.5 keV energy range. That soft diffuse component, which has also been reported to be present in Vink (2004) when analyzing the adjacent Kes 32 SNR with Chandra data, can be well described by a two-temperature plasma which we believe to stem from a combination of the diffuse Galactic Plane emission and emission from unresolved sources from the region of interest. The emission from the source itself can be best described by a simple absorbed power law of $\Gamma = 1.79^{+0.67}_{-0.51}$, confirming the non-thermal nature of the remnant indicated by XMM-Newton spectral analysis > 3.0 keV in H.E.S.S. Collaboration et al. (2018) and been broadly consistent with the best-fit spectral parameters of the diffuse Suzaku Src A (Matsumoto et al. 2008) which is likely associated with the remnant. However, a single temperature plasma with strongly suppressed Mg, S, and Si emission lines cannot be excluded due to the limited statistical quality of data.

Exploiting 10.5 additional years of Fermi-LAT data we managed to refine the morphology of the GeV emission from the location of HESS J1614-518 and successfully confirm it as HESS J1614-518 counterpart providing both an updated TS sky map and a residual count map from the location of the source of interest. The updated spectrum in the 1-800 GeV energy band reveals a much steeper spectrum, described best by a LogParabola, in comparison to the relatively hard spectrum below 1 TeV as reported in Acero et al. (2015); H.E.S.S. Collaboration et al. (2018), and thus waning strong indications for hadronic origin production of gamma-rays from the source.

Despite not being at the prime focus of this paper we report on the detection of diffuse X-ray emission from the location of the adjacent, hitherto unidentified, HESS J1616-508 TeV emitter. The diffuse emission is partially overlapping with both RCW103 and Kes 32 but of different origin as its spatial morphology indicates. However, the poor statistic does not allow us to distinguish between a PWN or SNR scenario for the origin of the emission.

The obtained N_H values from the X-ray spectral analysis of the remnant result in a remnant's distance of $3.51^{+1.76}_{-0.88}$ kpc by means of optical extinction data. A physical SNR size of 44 pc in X-rays is then derived under the assumption of the above distance estimate. A $3.9^{+2.35}_{-1.4} \times 10^4$ yrs age estimate is obtained using the SNR model calculator reported by Leahy & Williams (2017). Among the twenty-one pulsars positioned at and in the near vicinity of the remnant's extension (within 2° from its radio center), we singled out three as the most compelling candidates based on age and transverse velocity measurements. Among the latter three, J1615-5137 (which as of recently been identified as a gamma-ray pulsar 4FGL J1615.3-5136) stands out due to its angular separation from the remnant's center and its high energetics.

Acknowledgements

MM and GP acknowledge support from the Deutsche Forschungsgemeinschaft through grant PU 308/2-1.

This work is based on data from eROSITA, the soft X-ray instrument aboard SRG, a joint Russian-German science mission supported by the Russian Space Agency (Roskosmos), in the interests of the Russian Academy of Sciences represented by its Space Research Institute (IKI), and the Deutsches Zentrum für Luft- und Raumfahrt (DLR). The SRG spacecraft was built by Lavochkin Association (NPOL) and its subcontractors, and is operated by NPOL with support from the Max Planck Institute for Extraterrestrial Physics (MPE).

The development and construction of the eROSITA X-ray instrument was led by MPE, with contributions from the Dr. Karl Remeis Observatory Bamberg & ECAP (FAU Erlangen-Nuernberg), the University of Hamburg Observatory, the Leibniz Institute for Astrophysics Potsdam (AIP), and the Institute for Astronomy and Astrophysics of the University of Tübingen, with the support of DLR and the Max Planck Society. The Argelander Institute for Astronomy of the University of Bonn and the Ludwig Maximilians Universität Munich also participated in the science preparation for eROSITA. The eROSITA data shown here were processed using the eSASS/NRTA software system developed by the German eROSITA consortium.

We thank the EXPLORE team which provided us access to the G-TOMO tool of the EXPLORE platform `https://explore-platform.eu/` allowing us to exploit updated GAIA/2MASS data. We thank Denys Malyshev, Victor Doroshenko and Lorenzo Ducci for fruitful discussions as well as the anonymous referee for his significant comments that help improving this manuscript to its current finalized version...

References

Acero, F., Ackermann, M., Ajello, M., et al. 2015, ApJS, 218, 23
Aharonian, F., Akhperjanian, A. G., Bazer-Bachi, A. R., et al. 2006a, ApJ, 636, 777
Aharonian, F., Akhperjanian, A. G., Bazer-Bachi, A. R., et al. 2006b, A&A, 449, 223
Araya, M. 2017, ApJ, 843, 12
Brunner, H., Liu, T., Lamer, G., et al. 2022, A&A, 661, A1
Cash, W. 1979, ApJ, 228, 939
Condon, B., Lemoine-Goumard, M., Acero, F., & Katagiri, H. 2017, ApJ, 851, 100
Cordes, J. M. & Lazio, T. J. W. 2002, arXiv e-prints, astro
de Palma, F., Clark, C., & Di Venere, L. 2019, in International Cosmic Ray Conference, Vol. 36, 36th International Cosmic Ray Conference (ICRC2019), 560
Dorman, B., Arnaud, K. A., & Gordon, C. A. 2003, in AAS/High Energy Astrophysics Division, Vol. 7, AAS/High Energy Astrophysics Division #7, 22.10
Foight, D. R., Güver, T., Özel, F., & Slane, P. O. 2016, ApJ, 826, 66
For, B. Q., Staveley-Smith, L., Hurley-Walker, N., et al. 2018, MNRAS, 480, 2743
Foster, A. R., Ji, L., Smith, R. K., & Brickhouse, N. S. 2012, ApJ, 756, 128
Fukuda, T., Yoshiike, S., Sano, H., et al. 2014, ApJ, 788, 94
Fukui, Y., Sano, H., Sato, J., et al. 2017, ApJ, 850, 71
Fukui, Y., Sano, H., Sato, J., et al. 2012, ApJ, 746, 82
Guo, X. & Liu, X. 2024, A&A
Guo, X.-L. & Xin, Y.-L. 2021, in Proc. 37th International Cosmic Ray Conference (ICRC 2021), Vol. PoS(ICRC2021)629 (PoS-SISSA), 6
H. E. S. S. Collaboration, Abramowski, A., Aharonian, F., et al. 2018, A&A, 612, A4
H.E.S.S. Collaboration, Abdalla, H., Abramowski, A., et al. 2018, A&A, 612, A8
Hurley-Walker, N., Callingham, J. R., Hancock, P. J., et al. 2017, MNRAS, 464, 1146
Hurley-Walker, N., Gaensler, B. M., Leahy, D. A., et al. 2019a, PASA, 36, e048
Hurley-Walker, N., Hancock, P. J., Franzen, T. M. O., et al. 2019b, PASA, 36, e047
Khabibullin, I. I., Churazov, E. M., Chugai, N. N., et al. 2024, arXiv e-prints, arXiv:2401.17261
Lallement, R., Babusiaux, C., Vergely, J. L., et al. 2019, A&A, 625, A135
Lallement, R., Vergely, J. L., Babusiaux, C., & Cox, N. L. J. 2022, A&A, 661, A147
Landi, R., Bassani, L., Malizia, A., et al. 2006, The Astrophysical Journal, 651, 190
LAT Collaboration. 2015, Fermi Large Area Telescope Third Source Catalog
Leahy, D. A. & Williams, J. E. 2017, The Astronomical Journal, 153, 239
Lin, D., Webb, N. A., & Barret, D. 2012, The Astrophysical Journal, 756, 27
Manchester, R. N., Hobbs, G. B., Teoh, A., & Hobbs, M. 2005, AJ, 129, 1993
Matsumoto, H., Uchiyama, H., Sawada, M., et al. 2008, Publications of the Astronomical Society of Japan, 60, S163
Mattox, J. R., Bertsch, D. L., Chiang, J., et al. 1996, ApJ, 461, 396
Merloni, A., Predehl, P., Becker, W., et al. 2012, arXiv e-prints, arXiv:1209.3114
Michailidis, M., Pühlhofer, G., Becker, W., et al. 2024a, arXiv e-prints, arXiv:2401.17312
Michailidis, M., Pühlhofer, G., Santangelo, A., Becker, W., & Sasaki, M. 2024b, arXiv e-prints, arXiv:2401.17311
Piatti, A. E., Clariá, J. J., & Bica, E. 2000, A&A, 360, 529
Predehl, P., Andritschke, R., Arefiev, V., et al. 2021, A&A, 647, A1
Rowell, G., Horns, D., Fukui, Y., & Moriguchi, Y. 2008, in American Institute of Physics Conference Series, Vol. 1085, American Institute of Physics Conference Series, ed. F. A. Aharonian, W. Hofmann, & F. Rieger, 241–244
Sakai, M., Yajima, Y., & Matsumoto, H. 2011, PASJ, 63, S879
Shibata, T., Ishikawa, T., & Sekiguchi, S. 2011, ApJ, 727, 38
Sunyaev, R., Arefiev, V., Babyshkin, V., et al. 2021, A&A, 656, A132
Vernetto, S. & Lipari, P. 2016, Phys. Rev. D, 94, 063009
Vink, J. 2004, ApJ, 604, 693
Wayth, R. B., Lenc, E., Bell, M. E., et al. 2015, PASA, 32, e025
Wilms, J., Allen, A., & McCray, R. 2000, ApJ, 542, 914
Yao, J. M., Manchester, R. N., & Wang, N. 2017, ApJ, 835, 29
Zabalza, V. 2015, in International Cosmic Ray Conference, Vol. 34, 34th International Cosmic Ray Conference (ICRC2015), 922

3.2 Multiwavelength study of galaxy clusters

3.2.1 The eROSITA Final Equatorial-Depth Survey (eFEDS): X-ray properties of Subaru's optically selected clusters

Galaxy clusters are one of the most powerful tools to study cosmological models, e.g. via constraints on the cosmological parameters by the evolution of the cluster mass function. However, it is necessary to understand the dynamical status and the mass-observable scaling relations of the cluster sample when employing them in cosmology.

In this work, we conducted a systematic X-ray analysis of 43 high-richness clusters from the CAMIRA catalog, which have counterparts in the eFEDS field. We identified the brightest cluster galaxy (BCG) using the optical and far-infrared databases and used the offset between these optical centers and the X-ray peak, together with the gas concentration parameter, and the number of galaxy-density peaks to evaluate the dynamical status of the clusters. We found the fraction of relaxed clusters of this sample to be smaller than that of the X-ray selected cluster samples. We also presented the $L-T$ and $L-M$ scaling relations, which are consistent with the predictions of the self-similar model although shallower than that of other X-ray samples. In conclusion, our study suggests that the average X-ray properties of the optical clusters are likely to be different from those observed in the X-ray samples.

A&A 669, A110 (2023)
https://doi.org/10.1051/0004-6361/202244260

Astronomy & Astrophysics

The eROSITA Final Equatorial-Depth Survey (eFEDS)

X-ray properties of Subaru's optically selected clusters

N. Ota[1,2], N. T. Nguyen-Dang[3], I. Mitsuishi[4], M. Oguri[5,6,7], M. Klein[8], N. Okabe[9,10,11], M. E. Ramos-Ceja[12], T. H. Reiprich[1], F. Pacaud[1], E. Bulbul[12], M. Brüggen[13], A. Liu[12], K. Migkas[1], I. Chiu[14,15,16], V. Ghirardini[12], S. Grandis[8], Y.-T. Lin[16], H. Miyatake[7,17], S. Miyazaki[18,19], and J. S. Sanders[12]

(Affiliations can be found after the references)

Received 13 June 2022 / Accepted 10 November 2022

ABSTRACT

Context. We present the results of a systematic X-ray analysis of optically rich galaxy clusters detected by the Subaru Hyper Suprime-Cam (HSC) survey in the eROSITA Final Equatorial-Depth Survey (eFEDS) field.

Aims. Through a joint analysis of the SRG (Spectrum Roentgen Gamma)/eROSITA and Subaru/HSC surveys, we aim to investigate the dynamical status of the optically selected clusters and to derive the cluster scaling relations.

Methods. The sample consists of 43 optically selected galaxy clusters with a richness >40 in the redshift range of 0.16–0.89. We systematically analyzed the X-ray images and emission spectra using the eROSITA data. We identified the brightest cluster galaxy (BCG) using the optical and far-infrared databases. We evaluated the cluster's dynamical status by measuring three quantities: offset between the X-ray peak and BCG position, the gas concentration parameter, and the number of galaxy-density peaks. We investigated the luminosity–temperature and mass–luminosity relations based on eROSITA X-ray spectra and HSC weak-lensing data analyses.

Results. Based on these three measurements, we estimated the fraction of relaxed clusters to be $2(< 39)\%$, which is smaller than that of the X-ray-selected cluster samples. After correcting for a selection bias due to the richness cut, we obtained a shallow $L{-}T$ slope of 2.1 ± 0.5, which is consistent with the predictions of the self-similar model and the baseline model incorporating a mass–concentration relation. The $L{-}M$ slope of 1.5 ± 0.3 is in agreement with the above-cited theoretical models as well as the data on the shear-selected clusters in the eFEDs field.

Conclusions. Our analysis of high-richness optical clusters yields a small fraction of relaxed clusters and a shallow slope for the luminosity–temperature relation. This suggests that the average X-ray properties of the optical clusters are likely to be different from those observed in the X-ray samples. Thus, the joint eROSITA and HSC observations are a powerful tool in extending the analysis to a larger sample and understanding the selection effect with a view to establish cluster scaling relations.

Key words. galaxies: clusters: intracluster medium – intergalactic medium – X-rays: galaxies: clusters

1. Introduction

One of the most powerful constraints on current cosmological models comes from observations of how the galaxy cluster population evolves over time. The redshift evolution of the cluster mass function, particularly in the number of high-mass clusters, is sensitive to cosmological parameters (Allen et al. 2011). This makes observations of massive clusters in the distant universe vital. In particular, understanding the mass-observable scaling relations of these clusters is crucial to facilitating their use in cosmology (Giodini et al. 2013). However, measurements at higher redshifts pose a considerable challenge due to the small sample size and difficulties in accounting for selection bias (Pratt et al. 2019), along with the overall need for deep observations.

A combination of eROSITA and HSC observations has given us the unique opportunity to conduct a systematic study of optically selected clusters. The extended ROentgen Survey with an Imaging Telescope Array (eROSITA) on board the Spectrum-Roentgen-Gamma (SRG) satellite performed scanning X-ray observations of the $140\,\mathrm{deg}^2$ eROSITA Final Equatorial-Depth Survey field (the eFEDS field), during the performance verification phase (Predehl et al. 2021). The eFEDS survey has improved X-ray data uniformity of optically selected clusters; the vignetted, average exposure time is 1.3 ks in the 0.5–2 keV band (Brunner et al. 2022). On the other hand, the Hyper Suprime-Cam (HSC; Miyazaki et al. 2018) Subaru Strategic Program (SSP) is a wide-field optical imaging survey (Aihara et al. 2018a,b, 2022; Tanaka et al. 2018; Bosch et al. 2018), which has a significant overlap with the eFEDS survey. From the HSC-SSP dataset, Oguri et al. (2018) constructed a cluster catalog using the red-sequence cluster finding algorithm, CAMIRA (Oguri 2014). The catalog contains about 20 000 clusters at $0.1 < z < 1.3$ with richness $N > 15$. The cluster mass–richness relation is carefully calibrated using weak-lensing analysis (Okabe et al. 2019; Murata et al. 2019). Therefore, by a joint analysis of the two surveys, the scaling relations and their dependence on cluster dynamical status can be studied over a wide range of redshifts and masses.

Recent X-ray follow-up observations of optically selected clusters have reported that the X-ray properties of the optical clusters are marginally different from those observed in the X-ray samples. Willis et al. (2021) compared the XXL and CAMIRA catalogs, finding that 71/150 XXL clusters (67/270 CAMIRA clusters) are matched to the location of a CAMIRA cluster (an XXL cluster). Of the unmatched CAMIRA clusters, the stacked *XMM-Newton* data yielded a low, flat surface–brightness distribution, which is unlikely to follow the conventional β-model (Cavaliere & Fusco-Femiano 1976). From the *XMM-Newton* data analysis of 37 CAMIRA clusters, Ota et al. (2020) found a small fraction of relaxed clusters compared to

Table 1. Cross-matching of optical and X-ray cluster catalogs.

$\hat{N}_{\rm mem}$	CAMIRA	eFEDS	Fraction (%)
15–20	524	27	5
20–30	335	62	19
30–40	97	50	52
>40	41	32	78
Total	997	171	17

X-ray cluster samples suggesting that the optical cluster sample covers a larger range of the cluster morphologies. They also derived the luminosity–temperature relation and found that the slope is marginally shallower than those of X-ray-selected samples and consistent with the self-similar model prediction of 2 (Kaiser 1986). To obtain more conclusive results, we aim to improve the measurement accuracy and sample uniformity.

In this paper, we study the dynamical status and scaling relations for a subsample of high-richness, optically selected clusters in the eFEDS field. This paper is structured as follows. Sections 2 and 3 present the sample selection and optical analyses of the brightest cluster galaxies and weak-lensing mass, respectively. Section 4 describes the X-ray measurements of the cluster centroid and spectral properties. Section 5 derives the centroid offset and the relations between mass and X-ray observables. Section 6 presents a discussion of the implication of our results.

The cosmological parameters used throughout this paper are $\Omega_{\rm m} = 0.3$, $\Omega_\Lambda = 0.7$ and $h = 0.7$. We use the abundance table from Asplund et al. (2009) in the X-ray spectral modeling. The quoted errors represent the 1σ statistical uncertainties, unless stated otherwise.

2. Sample

We selected a sample of optically selected clusters based on the CAMIRA S20a v2 cluster catalog, an updated version of the HSC CAMIRA cluster catalog presented in Oguri et al. (2018). Among the 21,250 optical clusters discovered in the Subaru HSC survey fields, 997 objects with richness $N > 15$ and redshift $0.10 < z < 1.34$ lie in the eFEDS field. The richness range $N > 15$ ($N > 40$) corresponds to the cluster mass $M_{500} \gtrsim 5\times10^{13}\,M_\odot$ ($M_{500} \gtrsim 2\times10^{14}\,M_\odot$) at $z > 0.1$ (Okabe et al. 2019). We cross-matched the CAMIRA catalog with the eFEDS X-ray cluster catalog (Liu et al. 2022) to find 211 optical clusters that have at least one spatially-extended X-ray source within the scale radius R_{500} from the optical centers and the redshift difference of $|\Delta z| < 0.02$. Here, R_{500} was estimated from the mass–richness relation (Okabe et al. 2019) and the cluster richness (Oguri et al. 2018). Table 1 summarizes the result of the cross-matching of two catalogs.

In general, the X-ray detectability tends to be lower for lower richness and higher redshift; however, the observed fraction of 17% is lower than expected from the known cluster mass-observable relations (Okabe et al. 2019) and eROSITA's sensitivity, when assuming the typical β-model brightness distribution of regular clusters (Ota & Mitsuda 2004). This result can be attributed to multiple factors such as a large fraction of irregular clusters with low surface brightness (Ota et al. 2020), the BCG miscentering effect (Oguri et al. 2018), and misclassification as point sources (Bulbul et al. 2022), thus requiring further investigation.

To study the optical clusters' dynamical status and scaling relations based on the eROSITA analysis of individual objects, we focus on high-richness clusters with $N > 40$ and $0.16 < z < 0.89$ in this paper. We note that there were 41 clusters with $N > 40$ in the CAMIRA catalog (Table 1); however, since several CAMIRA clusters have two galaxy-density peaks separated by $\gtrsim R_{500}$, we treat them as two individual clusters in the following analysis. There are seven clusters identified in this way: HSC J085621+014649, HSC J085629+014157, HSC J092050+024514, HSC J092246+034241, HSC J093512+004738, HSC J093501+005415, and HSC J093523+023222. Their optical properties were obtained by the forced run of the CAMIRA optical cluster finder (Klein et al. 2022; Oguri et al. 2018). This yields a sample size of 43. Table 2 gives the sample list. Figure 1 shows examples of HSC images with superposed X-ray contours. A statistical analysis of the whole cluster sample will be presented in a separate paper.

3. Optical data analysis

3.1. BCG identification

The CAMIRA algorithm (Oguri 2014) first calculates the probability of each galaxy in the field being on the red sequence. Consequently, the galaxy clusters are defined as the overdensity of this type of galaxy population. At the same time, the selection method also returns the brightest cluster galaxy's (BCG) position for each cluster. This cluster's optical center is the position of the most luminous red-sequence galaxy close to the galaxy density peak. However, ultra-bright BCGs may not be correctly identified as BCGs because they are saturated in the HSC images, and the color estimates tend to be inaccurate. These reasons suggest that an additional confirmation of the BCG's position is necessary.

To determine the BCGs of all the clusters, we used the optical/NIR data from SDSS (York et al. 2000), Pan-STARRS (Kaiser et al. 2002, 2010), 2MASS (Skrutskie et al. 2006), and WISE (Wright et al. 2010). Each survey has a different sensitivity and filter response. In particular, SDSS has an i-band saturation level of 14 mag for point sources, which is brighter than the 18 mag of the HSC. In fact, for nearly half of the clusters, the brightest galaxies exceeded the HSC's saturation level and were re-identified in the following way. We searched for the brightest galaxy that locates within an R_{500} radius from the cluster's optical center, which is taken from the CAMIRA catalog. For the optical data, we used the r-band magnitudes to determine the brightest galaxy, whilst the K_s band and W_1 values were used in the IR regime. The redshifts of the galaxies were either taken from the SDSS catalog or the NASA/IPAC Extragalactic Database (NED)[1]. The redshift constraints of the BCGs search is $\Delta z = |z_{\rm galaxy} - z_{\rm cluster}| = 0.01 \times (1 + z_{\rm cluster})$ for the spectroscopic redshifts and $\Delta z = 0.02 \times (1 + z_{\rm cluster})$ for the photometric ones, respectively. Here, we considered uncertainties of redshift measurements and redshift tolerance of $3\sigma/c \sim 0.01$ for the typical velocity dispersion of rich clusters, $\sigma \sim 1000\,{\rm km\,s^{-1}}$ (Fadda et al. 1996).

Two additional corrections have been made before the photometric data are used for the BCGs search. First, we corrected for the galactic extinction, using the Schlegel map (Schlegel et al. 1998), assuming an extinction law (Fitzpatrick 1999) with $R_V = 3.1$. Second, appropriate K-correction methods are applied to obtain the magnitudes as in the rest frames of

[1] https://ned.ipac.caltech.edu/

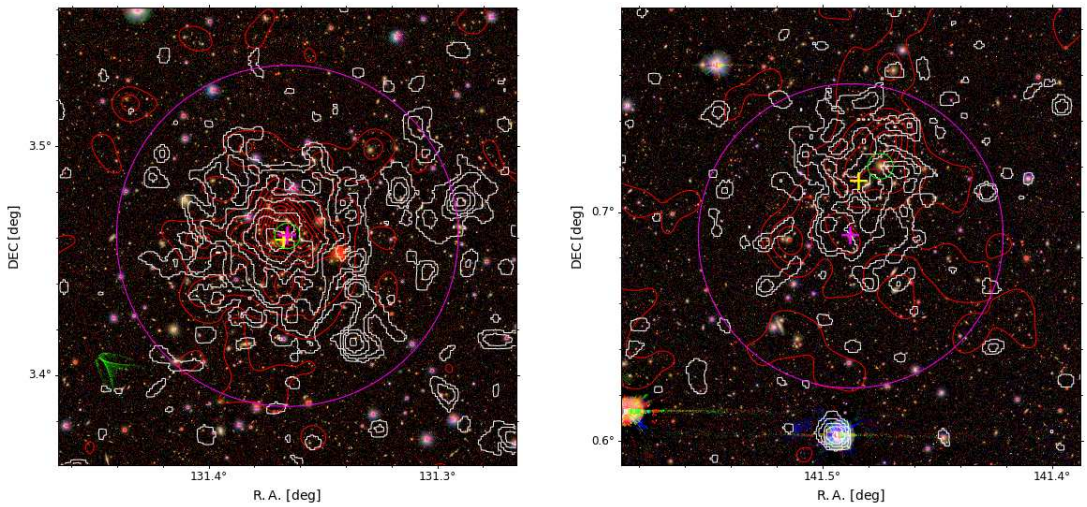

Fig. 1. Examples of Subaru riz-composite images of the optically selected clusters with overlaid the eROSITA X-ray intensity maps, HSC J084528+032739 (*left*) and HSC J092557+004122 (*right*). The red contours are linearly spaced by half of the average height of galaxy density maps over all CAMIRA clusters at the same redshift. The white contours for X-ray emission are ten levels logarithmically spaced from [10−1000] cts s^{-1} deg^{-2}. In each panel, the X-ray centroid and the initial CAMIRA coordinates are marked by the yellow and pink cross, respectively. The green circle denotes the position of the confirmed BCG. The magenta circle indicates R_{500}.

individual galaxies. We used the K-correction code version 2012 (Chilingarian et al. 2010; Chilingarian & Zolotukhin 2012) for the SDSS, Pan-STARRS, and 2MASS data because this method performs well with bright sources and does not require the compulsory input of multiple filter bands. However, this method does not provide the coefficients for WISE filters; therefore, we applied the K-correction code from Blanton & Roweis (2007) on the WISE photometric data instead.

Finally, we assessed the BCG search result through a careful visual inspection. In the case that multiple BCG candidates are suggested for one cluster, we assigned the BCG to the elliptical galaxy with a more extended envelope. If the search from different surveys returns different BCGs, we gave more weight to the BCG results from the optical observations. There were two cases (HSC J091843+021231 and HSC J092041+024660), where we needed to check the information of the obvious BCG candidates manually. These were the seemingly best choices but were not selected by the BCG finding program. Indeed, these galaxies do not have photometric imprints in any of the aforementioned surveys. We found the redshift of these visible BCG candidates on NED and their brightness in GAMA (Wright et al. 2016). We thus confirmed that they are the BCGs of their host clusters because they also follow the spatial and redshift constraints.

3.2. Weak-lensing mass measurement

Next, we describe weak-lensing (WL) analyses for the CAMIRA clusters in the eFEDS field. We used the latest shape catalog and the weak-lensing mass calibration from the three-year HSC data (S19A; Li et al. 2022). The galaxy shapes are measured by the re-Gaussianization method (Hirata & Seljak 2003) implemented in the HSC pipeline (see details in Mandelbaum et al. 2018a,b). The same shape catalog is used in the WL mass measurements for the eFEDS clusters (Chiu et al. 2022). We adopted the full-color and full-depth criteria for precise shape measurements and photometric redshift estimations.

The dimensional, reduced tangential shear, $\Delta\Sigma_+$, is computed by averaging the tangential component of a galaxy ellipticity $e_+ = -(e_1 \cos 2\varphi + e_2 \sin 2\varphi)$ where φ is the angle measured in sky coordinates from the RA direction to the line between the source galaxy and the lens. The formulation is specified by:

$$\Delta\Sigma_+(R_k) = \frac{\sum_i e_{+,i} w_i \langle \Sigma_{\rm cr}(z_{\rm l}, z_{{\rm s},i})^{-1} \rangle^{-1}}{2\mathcal{R}(R_k)(1 + K(R_k)) \sum_i w_i}, \quad (1)$$

(e.g., Miyaoka et al. 2018; Medezinski et al. 2018a; Okabe et al. 2019, 2021; Miyatake et al. 2019; Murata et al. 2019; Umetsu et al. 2020; Chiu et al. 2022). Here, the subscripts, i and k, denote the ith galaxy located in the kth radial bin, and $z_{\rm l}$ and $z_{\rm s}$ are the cluster and source redshift, respectively. The inverse of the mean critical surface mass density, $\langle \Sigma_{\rm cr}(z_{\rm l}, z_{\rm s})^{-1} \rangle$, is calculated by weighting the critical surface mass density, $\Sigma_{\rm cr} = c^2 D_{\rm s} / 4\pi G D_{\rm l} D_{\rm ls}$, by the probability function of the photometric redshift, $P(z)$:

$$\langle \Sigma_{\rm cr}(z_{\rm l}, z_{\rm s})^{-1} \rangle = \frac{\int_{z_{\rm l}}^{\infty} \Sigma_{\rm cr}^{-1}(z_{\rm l}, z_{\rm s}) P(z_{\rm s}) {\rm d}z_{\rm s}}{\int_0^{\infty} P(z_{\rm s}) {\rm d}z_{\rm s}}. \quad (2)$$

Here, $D_{\rm l}$, $D_{\rm s}$, and $D_{\rm ls}$ are the angular diameter distances from the observer to the cluster, to the sources, and from the lens to the sources, respectively. The photometric redshift is estimated by the machine learning method (MLZ; Carrasco Kind & Brunner 2014) calibrated with spectroscopic data (Nishizawa et al. 2020). The dimensional weighting function is expressed as

$$w = \frac{1}{e_{\rm rms}^2 + \sigma_{\rm e}^2} \langle \Sigma_{\rm cr}^{-1} \rangle^2, \quad (3)$$

where $e_{\rm rms}$ and $\sigma_{\rm e}$ are the root mean square of intrinsic ellipticity and the measurement error per component (e_α; $\alpha = 1$ or 2), respectively. The shear responsivity, $\mathcal{R}$, and the calibration factor, K, are obtained by $\mathcal{R} = 1 - \sum_{ij} w_{i,j} e_{{\rm rms},i}^2 / \sum_{ij} w_{i,j}$ and $K = \sum_{ij} m_i w_{i,j} / \sum_{ij} w_{i,j}$, with the multiplicative shear calibration factor m (Mandelbaum et al. 2018a,b), respectively. We also conservatively subtracted an additional, negligible offset term for calibration. The radius position, R_k, is defined by the weighted harmonic mean (Okabe & Smith 2016). We selected background

Table 2. Sample list.

Cluster	z	$\hat{N}_{\rm mem}$ [a]	R_{500} (Mpc/″)	BCG position RA, Dec (deg)	X-ray centroid RA, Dec (deg)	X-ray peak RA, Dec (deg)	$D_{\rm XC}$ [b] (kpc)	$D_{\rm XP}$ [c] (kpc)
HSC J083655+025855	0.189	42.5	0.852/269	129.2144, 3.0004	129.2141, 2.9992	129.2163, 2.9988	13	27 (27,37)
HSC J083932−014128	0.255	45.7	0.866/217	129.8891, −1.6791	129.8844, −1.6831	129.8916, −1.6790	87	35 (30,35)
HSC J084222+013826	0.418	75.8	1.050/188	130.5912, 1.6406	130.5975, 1.6463	130.5919, 1.6385	167	44 (44,657)
HSC J084245−000936	0.420	48.5	0.848/152	130.6896, −0.1601	130.6991, −0.1635	130.7021, −0.1411	202	453 (453,453)
HSC J084435+031020	0.735	40.9	0.709/ 96	131.1453, 3.1723	131.1449, 3.1697	131.1443, 3.1703	68	57 (48,75)
HSC J084441+021656	0.649	71.3	0.949/135	131.1710, 2.2823	131.1582, 2.2847	131.1743, 2.2833	325	84 (65,94)
HSC J084502+012631	0.415	40.5	0.779/141	131.2596, 1.4420	131.2592, 1.4554	131.2533, 1.4626	265	426 (238,426)
HSC J084528+032739	0.320	103.6	1.255/268	131.3657, 3.4608	131.3675, 3.4589	131.3691, 3.4588	44	65 (65,69)
HSC J084548+020640	0.582	44.8	0.777/116	131.4498, 2.1054	131.4508, 2.1130	131.4619, 2.1203	181	454 (421,454)
HSC J084656+013836	0.597	41.1	0.743/110	131.7340, 1.6432	131.7481, 1.6482	131.7306, 1.6670	359	575 (575,644)
HSC J084824+041206	0.873	60.1	0.816/104	132.0988, 4.2017	132.0949, 4.2020	132.0995, 4.2023	107	25 (8,33)
HSC J084939−005121	0.616	53.4	0.836/122	132.4136, −0.8560	132.4156, −0.8572	132.4165, −0.8583	57	91 (91,97)
HSC J085019+020011	0.419	44.8	0.817/146	132.5635, 2.0099	132.5762, 1.9969	132.5776, 2.0078	362	283 (275,284)
HSC J085056−000931	0.890	44.4	0.703/ 89	132.7330, −0.1586	132.7328, −0.1586	132.7301, −0.1605	4	96 (86,103)
HSC J085232+002551	0.280	46.6	0.868/203	133.1256, 0.4205	133.1255, 0.4085	133.1270, 0.4066	183	213 (213,213)
HSC J085741+031135	0.188	73.6	1.108/351	134.4751, 3.1764	134.4669, 3.1810	134.4642, 3.1797	105	128 (125,128)
HSC J090143−014019	0.302	49.6	0.888/197	135.3779, −1.6548	135.3775, −1.6602	135.3715, −1.6685	87	242 (88,441)
HSC J090330−013622	0.440	50.8	0.862/150	135.8756, −1.6062	135.8718, −1.6070	135.8570, −1.6010	81	395 (389,395)
HSC J090451+033310	0.807	50.6	0.768/100	136.2176, 3.5537	136.2229, 3.5593	136.2183, 3.5606	207	189 (178,246)
HSC J090541+013226	0.636	40.4	0.727/105	136.4216, 1.5406	136.4212, 1.5366	136.4150, 1.5191	99	555 (26,555)
HSC J090754+005732	0.693	47.5	0.772/107	136.9765, 0.9590	136.9794, 0.9589	136.9765, 0.9561	74	72 (72,212)
HSC J090914−001220	0.305	50.7	0.897/198	137.3074, −0.2056	137.3120, −0.2067	137.3002, −0.2079	77	122 (122,122)
HSC J090917−010134	0.823	49.9	0.758/98	137.3190, −1.0261	137.3137, −1.0191	137.3168, −1.0188	239	205 (198,216)
HSC J091352−004535	0.264	49.1	0.893/218	138.4674, −0.7597	138.4687, −0.7580	138.4775, −0.7622	31	151 (147,151)
HSC J091606−002338	0.297	113.9	1.322/297	139.0385, −0.4045	139.0466, −0.3970	139.0427, −0.3974	176	131 (131,131)
HSC J091843+021231	0.268	57.6	0.964/233	139.7092, 2.2009	139.7056, 2.2142	139.7055, 2.2014	204	54 (54,60)
HSC J092024+013444	0.698	44.3	0.746/103	140.0981, 1.5788	140.0974, 1.5783	140.0990, 1.5784	21	27 (26,43)
HSC J092121+031713	0.345	95.4	1.198/243	140.3380, 3.2870	140.3392, 3.2891	140.3417, 3.2948	42	152 (152,152)
HSC J092211+034641	0.252	65.9	1.032/261	140.5319, 3.7663	140.5369, 3.7667	140.5467, 3.7763	71	252 (243,257)
HSC J092557+004122	0.260	57.8	0.967/239	141.4748, 0.7199	141.4845, 0.7133	141.4919, 0.7071	169	310 (310,310)
HSC J092847+005132	0.310	41.4	0.813/177	142.1952, 0.8587	142.2048, 0.8775	142.2499, 0.8913	345	1043 (540,1043)
HSC J092942+022843	0.537	43.6	0.778/121	142.4255, 2.5061	142.4232, 2.4956	142.4344, 2.5122	243	246 (75,246)
HSC J093025+021726	0.532	66.0	0.949/149	142.5929, 2.3068	142.6030, 2.2916	142.6045, 2.2907	414	450 (450,456)
HSC J093049−003651	0.310	43.4	0.832/181	142.7055, −0.6159	142.7052, −0.6197	142.7051, −0.6175	62	27 (27,369)
HSC J093431−002308	0.342	45.5	0.842/172	143.6300, −0.3855	143.6353, −0.3870	143.6196, −0.3844	96	183 (183,184)
HSC J094025+022840	0.164	66.4	1.062/377	145.1024, 2.4776	145.1188, 2.4822	145.1902, 2.4350	171	985 (520,985)
HSC J085621+014649	0.769	44.1	0.728/97	134.0858, 1.7804	134.0865, 1.7794	134.0886, 1.7810	34	77 (42,77)
HSC J085629+014157	0.692	42.6	0.733/102	134.1288, 1.7105	134.1294, 1.7077	134.1136, 1.7099	74	389 (388,389)
HSC J092050+024514	0.284	47.5	0.875/203	140.2071, 2.7539	140.2084, 2.7565	140.2067, 2.7506	45	50 (50,50)
HSC J092246+034241	0.257	55.3	0.948/236	140.6929, 3.7113	140.6893, 3.7079	140.6911, 3.7151	71	60 (58,133)
HSC J093512+004738	0.352	96.2	1.200/240	143.8018, 0.7939	143.8069, 0.7977	143.8083, 0.8010	112	172 (172,177)
HSC J093501+005415	0.374	53.9	0.905/174	143.7528, 0.9041	143.7553, 0.9036	143.7591, 0.9030	46	117 (109,117)
HSC J093523+023222	0.513	84.5	1.074/172	143.8439, 2.5569	143.8414, 2.5451	143.8383, 2.5436	267	321 (321,329)

Notes. [a]Richneess. [b]Centroid offset. [c]Peak offset. The error range estimated by changing the smoothing scale of the X-ray image is given in the parenthesis (see Sects. 4.2 and 5.2).

galaxies behind each cluster using the photometric selection (p-cut) following Medezinski et al. (2018b):

$$\int_{z_l+0.2}^{\infty} P(z)\mathrm{d}z > p_{\rm cut}, \tag{4}$$

where we allowed for a 2% contamination level with $p_{\rm cut} = 0.98$.

In order to measure individual cluster masses, we used the NFW profile (Navarro et al. 1996, 1997). The three-dimensional mass density profile of the NFW profile is expressed as

$$\rho_{\rm NFW}(r) = \frac{\rho_{\rm s}}{(r/r_{\rm s})(1+r/r_{\rm s})^2}, \tag{5}$$

where $r_{\rm s}$ is the scale radius and $\rho_{\rm s}$ is the central density parameter. The NFW model is also specified by the spherical mass, $M_\Delta = 4\pi\Delta\rho_{\rm cr}r_\Delta^3/3$, and the halo concentration, $c_\Delta = r_\Delta/r_{\rm s}$. Here, r_Δ is the overdensity radius. We treat M_Δ and c_Δ as free parameters and adopt $\Delta = 500$. We computed the model of the dimensional, reduced tangential shear, $f_{\rm model}$, at the projected radius R by integrating the mass density profile along the line of sight (Okabe et al. 2019; Umetsu 2020);

$$f_{\rm model}(R) = \frac{\bar{\Sigma}(<R) - \Sigma(R)}{1 - \mathcal{L}_z\Sigma(R)}, \tag{6}$$

where $\Sigma(R)$ is the local surface mass density at R, $\bar{\Sigma}(<R)$ is the average surface mass density within R, and $\mathcal{L}_z = \sum_i\langle\Sigma_{{\rm cr},i}^{-1}\rangle w_i / \sum_i w_i$. We chose the X-ray-defined centers and adopt an adaptive radial-bin choice (Okabe & Smith 2016) for cluster mass estimation.

The log-likelihood of the weak-lensing analysis is expressed as

$$-2\ln\mathcal{L}_{\rm WL} = \ln(\det(C_{km})) + \sum_{k,m}(\Delta\Sigma_{+,k} - f_{\rm model}(R_k))C_{km}^{-1}(\Delta\Sigma_{+,m} - f_{\rm model}(R_m)), \tag{7}$$

where k and m denote the kth and mth radial bins. We considered three components in the covariance matrix $C = C_g + C_{\rm s} + C_{\rm LSS}$;

Table 3. Results of X-ray spectral analysis and lensing mass measurements.

Cluster	$N_{\rm H}$ (10^{20} cm^{-2})	kT [(a)] (keV)	$L_{\rm X}$ [(b)] (10^{44} erg s^{-1})	M_{500} [(c)] (10^{14} $M_\odot$)
HSC J083655+025855	3.54	$2.39^{+0.36}_{-0.28}$	$1.31^{+0.09}_{-0.08}$	$4.57^{+1.70}_{-1.43}$
HSC J083932−014128	3.09	$3.71^{+0.71}_{-0.55}$	$3.73^{+0.30}_{-0.26}$	–
HSC J084222+013826	5.52	$1.95^{+0.48}_{-0.35}$	$2.55^{+0.25}_{-0.25}$	$9.28^{+3.05}_{-2.57}$
HSC J084245−000936	3.33	$3.34^{+3.04}_{-1.17}$	$1.33^{+0.41}_{-0.24}$	$5.66^{+2.51}_{-2.00}$
HSC J084435+031020	3.71	$2.37^{+1.21}_{-0.53}$	$3.43^{+0.53}_{-0.44}$	$7.27^{+9.67}_{-7.26}$
HSC J084441+021656	5.17	$2.42^{+0.66}_{-0.45}$	$5.98^{+0.60}_{-0.55}$	$15.92^{+18.92}_{-9.18}$
HSC J084502+012631	4.58	$4.37^{+3.40}_{-1.54}$	$2.18^{+0.57}_{-0.37}$	$2.67^{+1.63}_{-1.25}$
HSC J084528+032739	3.63	$7.72^{+3.52}_{-1.43}$	$8.69^{+1.18}_{-0.75}$	$5.32^{+1.64}_{-1.37}$
HSC J084548+020640	4.82	3.69(fix)	$1.45^{+0.30}_{-0.28}$	$2.69^{+3.16}_{-2.26}$
HSC J084656+013836	4.20	3.54(fix)	$0.44^{+0.22}_{-0.21}$	$5.22^{+4.78}_{-2.83}$
HSC J084824+041206	4.12	$4.09^{+3.58}_{-1.44}$	$6.15^{+1.67}_{-0.94}$	–
HSC J084939−005121	2.60	$6.29^{+10.99}_{-2.96}$	$5.02^{+2.17}_{-1.20}$	$2.81^{+3.33}_{-2.87}$
HSC J085019+020011	3.24	$2.76^{+4.47}_{-1.12}$	$0.89^{+0.41}_{-0.20}$	$1.68^{+1.52}_{-1.27}$
HSC J085056−000931	3.21	$1.44^{+0.57}_{-0.24}$	$3.25^{+0.69}_{-0.61}$	$7.37^{+15.94}_{-10.67}$
HSC J085232+002551	4.13	$2.67^{+1.27}_{-0.64}$	$1.11^{+0.20}_{-0.14}$	$2.69^{+1.17}_{-0.91}$
HSC J085741+031135	4.15	$5.94^{+1.30}_{-0.88}$	$5.25^{+0.43}_{-0.35}$	$3.21^{+1.57}_{-1.29}$
HSC J090143−014019	2.28	$5.39^{+2.37}_{-1.31}$	$5.00^{+0.81}_{-0.58}$	–
HSC J090330−013622	2.26	$5.00^{+7.49}_{-1.90}$	$3.37^{+1.43}_{-0.62}$	–
HSC J090451+033310	3.60	$5.06^{+4.35}_{-1.69}$	$6.51^{+1.80}_{-1.00}$	–
HSC J090541+013226	4.01	$3.88^{+2.90}_{-1.56}$	$2.90^{+0.72}_{-0.53}$	–
HSC J090754+005732	3.39	3.80 (fix)	$3.14^{+0.43}_{-0.41}$	$0.16^{+3.12}_{-2.04}$
HSC J090914−001220	3.00	$3.22^{+0.97}_{-0.77}$	$1.82^{+0.23}_{-0.20}$	$1.99^{+1.32}_{-0.93}$
HSC J090917−010134	2.84	$2.98^{+1.61}_{-0.72}$	$5.93^{+0.99}_{-0.70}$	–
HSC J091352−004535	3.20	$2.21^{+0.84}_{-0.44}$	$0.85^{+0.12}_{-0.10}$	$3.50^{+1.17}_{-1.00}$
HSC J091606−002338	3.20	$4.39^{+1.10}_{-0.79}$	$5.40^{+0.56}_{-0.45}$	$8.65^{+3.26}_{-2.52}$
HSC J091843+021231	2.74	$2.57^{+0.49}_{-0.34}$	$2.12^{+0.17}_{-0.15}$	$2.80^{+1.47}_{-1.09}$
HSC J092024+013444	2.90	$2.95^{+0.70}_{-0.43}$	$10.09^{+0.82}_{-0.66}$	$10.84^{+8.61}_{-6.84}$
HSC J092121+031713	3.87	$6.19^{+1.52}_{-1.09}$	$10.38^{+0.96}_{-0.82}$	$5.12^{+1.69}_{-1.37}$
HSC J092211+034641	3.98	$5.33^{+1.34}_{-1.06}$	$4.53^{+0.45}_{-0.41}$	$3.82^{+1.52}_{-1.27}$
HSC J092557+004122	3.43	$3.25^{+1.27}_{-0.90}$	$1.09^{+0.17}_{-0.15}$	$2.03^{+1.26}_{-0.98}$
HSC J092847+005132	4.27	$1.74^{+0.57}_{-0.27}$	$0.46^{+0.08}_{-0.07}$	$1.08^{+1.04}_{-0.86}$
HSC J092942+022843	4.85	$3.53^{+4.22}_{-1.35}$	$1.69^{+0.61}_{-0.33}$	$1.86^{+1.95}_{-1.38}$
HSC J093025+021726	5.06	$6.98^{+12.14}_{-1.97}$	$8.27^{+3.30}_{-1.09}$	$5.11^{+3.40}_{-2.45}$
HSC J093049−003651	3.09	$2.43^{+0.73}_{-0.40}$	$1.16^{+0.15}_{-0.11}$	$3.21^{+1.42}_{-1.19}$
HSC J093431−002308	3.15	$2.78^{+1.23}_{-0.66}$	$1.59^{+0.26}_{-0.19}$	$9.13^{+4.05}_{-2.83}$
HSC J094025+022840	3.72	$2.18^{+1.29}_{-0.52}$	$1.31^{+0.30}_{-0.21}$	$7.10^{+2.21}_{-1.75}$
HSC J085621+014649	3.87	$4.49^{+1.60}_{-0.91}$	$15.93^{+2.06}_{-1.42}$	–
HSC J085629+014157	3.97	$3.21^{+1.06}_{-0.69}$	$6.62^{+0.78}_{-0.65}$	$1.46^{+4.00}_{-3.20}$
HSC J092050+024514	3.50	$3.05^{+0.56}_{-0.42}$	$2.84^{+0.22}_{-0.19}$	$2.84^{+2.65}_{-1.38}$
HSC J092246+034241	3.93	$1.61^{+0.38}_{-0.25}$	$0.42^{+0.06}_{-0.06}$	$1.13^{+0.93}_{-0.78}$
HSC J093512+004738	4.34	$5.90^{+1.77}_{-1.12}$	$10.40^{+1.15}_{-0.89}$	$12.39^{+3.74}_{-2.89}$
HSC J093501+005415	4.46	$3.12^{+1.07}_{-0.61}$	$2.73^{+0.36}_{-0.26}$	$3.16^{+1.52}_{-1.38}$
HSC J093523+023222	3.43	$3.95^{+0.78}_{-0.56}$	$14.71^{+1.13}_{-0.92}$	$5.41^{+3.50}_{-3.50}$

Notes. [(a)]Gas temperature. [(b)]Bolometric luminosity within the scale radius R_{500}. [(c)]Weak-lensing mass within R_{500}.

the shape noise C_g, the errors of the source redshifts, $C_{\rm s}$ and the uncorrelated large-scale structure (LSS), $C_{\rm LSS}$, of which the elements are correlated with each other (Schneider et al. 1998; Hoekstra 2003). The details of calculations are described in Sect. 3 of Okabe & Smith (2016). We measured WL masses in 38 out of the 43 CAMIRA clusters that satisfy the full-color

and full-depth conditions (Table 3). The signal-to-noise ratios, $S/N = (\Delta\Sigma_{+,k} C^{-1}_{km} \Delta\Sigma_{+,m})^{1/2}$, of individual clusters were small; $S/N < 2$ for 3, $2 \leq S/N < 4$ for 20, and $4 < S/N$ for 17 clusters, resulting in uncertainties in M_{500}. Here, for consistency with other X-ray observables, the center coordinates in the WL measurements were assumed to be equal to the X-ray centroids.

We also carried out the NFW model fitting with a free central position using two-dimensional shear pattern (Oguri et al. 2010; Okabe et al. 2011). The log-likelihood is expressed as

$$-2 \ln \mathcal{L}_{\rm WL} = \sum_{\alpha,\beta=1}^{2} \sum_{k,m} \left[\Delta\Sigma_{\alpha,k} - f_{{\rm model},\alpha}(\boldsymbol{R}_k)\right] \boldsymbol{C}^{-1}_{\alpha\beta,km} \times \left[\Delta\Sigma_{\beta,m} - f_{{\rm model},\beta}(\boldsymbol{R}_m)\right] + \ln(\det(C_{\alpha\beta,km})). \quad (8)$$

Here, the subscripts α and β denote each shear component. We used the box size of $1\farcm5 \times 1\farcm5$ for the shear pattern. We constrained the central positions for 23 clusters with good posterior distributions and compared them with X-ray centers, CAMIRA centers, and galaxy map peaks (Sect. 5.1).

4. X-ray data analysis

4.1. Data reduction

The eFEDs data of seven telescope modules (TMs) were reduced in a standard manner by using the eROSITA Standard Analysis Software System (eSASS) version `eSASSusers_201009` (Brunner et al. 2022). We extracted cleaned event files by applying a flag to reject bad events and selecting all valid patterns, namely single, double, triple, and quadruple events. The point sources were removed by referring to the main eFEDS X-ray source catalog[2] (Brunner et al. 2022). We checked that the faint sources with low detection likelihood in the supplemental eFEDS catalog do not affect our X-ray analysis.

4.2. Centroid and peak determination

We extracted the X-ray image of each cluster from merged event files of seven TMs in the 0.5–2 keV band and corrected them for exposure and vignetting. The pixel size is $1\farcs5$. The X-ray centroid was determined from the mean of the photon distribution within a circle of radius R_{500} using the algorithm described in Ota et al. (2020); starting with the BCG coordinates, we iterated the centroid search until its position converged within $1''$. The X-ray peak within R_{500} was measured using the 0.5–2 keV image smoothed with a $\sigma = 3$ (pixels) Gaussian function. We note that we calculated the two-dimensional (2D) PSF image of the survey mode at each cluster coordinates using `ermldet` in the eSASS package and confirmed that it is almost symmetric and does not affect the present measurement.

4.3. Spectral analysis

To measure the gas temperature and bolometric luminosity, we extracted the spectra from a circular region of a radius R_{500} centered on the X-ray centroid. Here, it is reasonable to assume that the cluster center is represented by the X-ray centroid (Sect. 5.1, Fig. 2). The TM1,2,3,4,6/TM5,7 spectra in the 0.3–10 keV/1–10 keV band were simultaneously fit using `XSPEC 12.1.1`. For TM5 and TM7, the energies below 1 keV were excluded due to the light-leak contamination (Predehl et al. 2021). The spectral model consists of cluster emission and background components. For the cluster component, we assumed the APEC thin-thermal plasma model (Smith et al. 2001; Foster et al. 2012), with the Galactic absorption model `tbabs` (Wilms et al. 2000). The redshift and metal abundance were fixed at the optical value (Table 2) and 0.3 solar, respectively. The hydrogen column density $N_{\rm H}$ in the `tbabs` model was fixed at a value taken from Willingale et al. (2013). For the background components, the Galactic emission and cosmic X-ray background were determined by fitting an annulus with inner and outer radii of 2.5 and 4 Mpc from the cluster. The instrumental background was estimated based on the filter wheel closed (FWC) data[3]. Table 3 lists the resultant gas temperature, kT, and bolometric luminosity, $L_{\rm X}$. We note that for three clusters (HSC J084548+020640, HSC J084656+01383, and HSC J090754+005732), we fixed kT at a value expected from the N–T relation (Oguri et al. 2018) and the richness due to the large statistical uncertainty.

Table 4. Median values of centroid offset and peak offset.

$D_{\rm XC}$ (kpc)	$D_{\rm XC}$ (R_{500})	$D_{\rm XP}$ (kpc)	$D_{\rm XP}$ (R_{500})	Fraction [(a)]
100	0.10	152	0.14	2(< 16)%

Notes. [(a)]Fraction of relaxed clusters based on the BCG-X-ray peak offset (Sect. 5.2).

5. Results

5.1. Centroid offsets

We calculated the spatial separation from the cluster's X-ray centroid to the BCG's position and report it as the BCG-and-X-ray centroid offset, $D_{\rm XC}$. In addition, we estimate the distance between the cluster's X-ray peak to its BCG $D_{\rm XP}$. Figure 3 demonstrates the distributions of $D_{\rm XC}$ and $D_{\rm XP}$ for 43 clusters in our sample. The median values of these offsets in the unit of kpc and R_{500} are shown in Table 4.

Next, we compare the projected distance between 2D weak-lensing mass and three kinds of cluster centers, namely X-ray centroid, galaxy map peak, and the CAMIRA coordinates for 23 clusters. We estimated the statistical errors of the probability distributions by the bootstrap resampling method. As shown in Fig. 2, all the histograms are well described by double Gaussian distributions:

$$p(r) = f_{\rm cen} p_1(r) + (1 - f_{\rm cen}) p_2(r), \quad (9)$$

where $p_i(r) = (r/\sigma_i^2) \exp\left[-r^2/2\sigma_i^2\right]$ and $f_{\rm cen}$ is the fraction of the central component (Oguri et al. 2010, 2018). The first standard deviation, σ_1, for the X-ray centroid is smaller than those of the CAMIRA and galaxy ones, suggesting that the X-ray centroids are closer to the WL mass centers. Although the values of σ_1 for the CAMIRA centers are the largest and the histogram is slightly skewed from the double Gaussian distributions, the amplitude of the CAMIRA centers at $r \lesssim 60$ kpc is comparable to that of the X-ray centers. Although the value of σ_1 for the galaxy peak is the second smallest among the first components of the three centers, the amplitude at $r \lesssim 100$ kpc is ~60–70% of the others. The second standard deviation, σ_2, of the galaxy peak is the smallest among the three centers.

[2] https://erosita.mpe.mpg.de/edr/eROSITAObservations/Catalogues/

[3] The FWC spectral model version 1.0 (https://erosita.mpe.mpg.de/edr/eROSITAObservations/EDRFWC/)

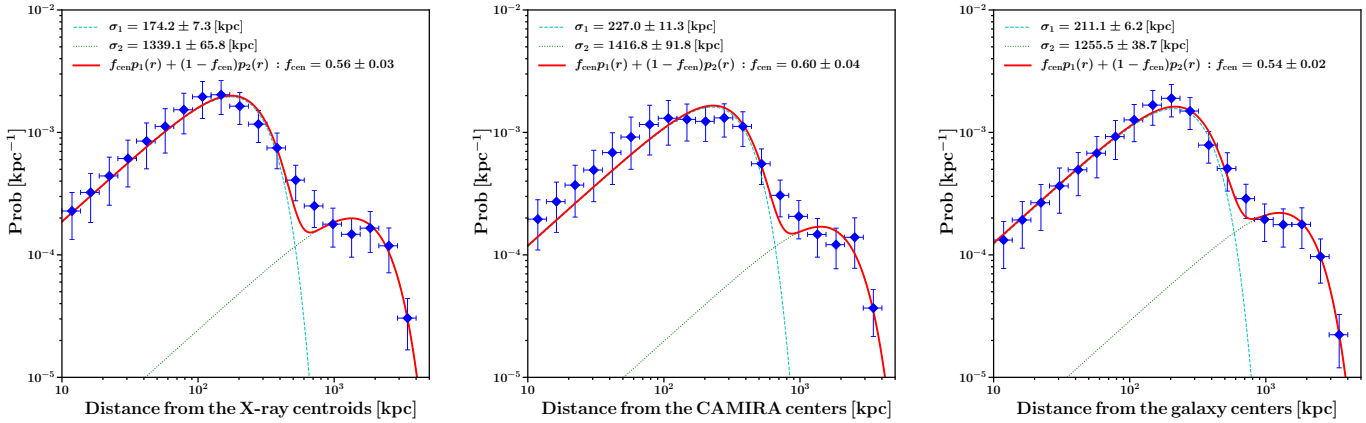

Fig. 2. Histograms of the projected distance between 2D weak-lensing mass center and X-ray centroid (*left*), CAMIRA center (*middle*), galaxy map peak (*right*) for 23 CAMIRA clusters. The error bars indicate the statistical uncertainties. The best-fit model (red) consisting of the first and second Gaussian components is indicated by the cyan dashed, and green dotted curves, respectively.

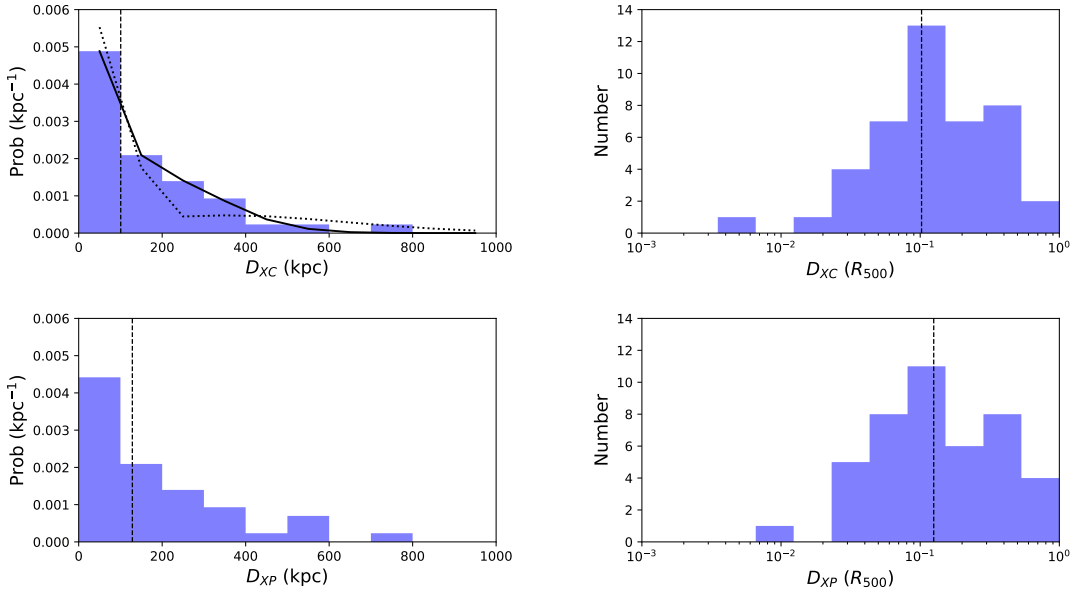

Fig. 3. Distributions of centroid offset (*upper panels*) and peak offset (*lower panels*) in units of kpc (*left panels*) and R_{500} (*right panels*). In each panel, the dashed line indicates the median. In the upper-left panel, the solid and dotted curves show the best-fit double-Gaussian models for the present sample and the positional offset between the CAMIRA and XXL clusters (Oguri et al. 2018), respectively.

5.2. Morphological classification

In this subsection, we use three different methods to classify the morphology of galaxy clusters: (i) BCG-X-ray offset, (ii) concentration parameter, and (iii) galaxy peak-finding method.

First, the BCG-X-ray offset: We divided the clusters into two groups following the criteria used in Sanderson et al. (2009), namely, "relaxed" clusters with a small peak offset ($D_{\rm XP} < 0.02R_{500}$) and "disturbed" clusters with a large offset ($D_{\rm XP} > 0.02R_{500}$). There is only one cluster that posseses a small offset of $D_{\rm XP} \leq 0.02R_{500}$, which corresponds to a very small fraction of relaxed clusters $2.3 \pm 2.2\,(^{+0.0}_{-2.3})\%$ or <5%. Here, the statistical and systematic errors are calculated via the bootstrap resampling method and by varying the smoothing scales between 2 and 4 pixels, respectively.

The accuracy of the X-ray peak position depends on the statistical quality of the X-ray observations, which broadly varies among clusters. In fact, based on the *XMM-Newton* observations of the CAMIRA clusters, Ota et al. (2020) reported that the clusters with low photon statistics tend to show larger centroid and peak offsets. We thus calculated the standard error of the peak offset $\delta D_{\rm XP}$ based on a comparison of X-ray images of each cluster with different smoothing scales ($\sigma = 2, 3, 4$ pixels). As a result, $\delta D_{\rm XP}$ ranges from 0% to 55 % (the mean is 5%), which is smaller than that of the *XMM-Newton* study (Ota et al. 2020).

At high redshifts, however, $0.02R_{500}$ is comparable to the accuracy of the attitude determination (Predehl et al. 2021). With regard to how much the results would change based on the threshold, when we set the threshold value to $0.05R_{500}$, the percentage of relaxed clusters was 9%. This example suggests that the systematic uncertainty of the relaxed fraction is not negligible. Accordingly, we assigned the typical positional accuracy of 4.″7 (Brunner et al. 2022) to the systematic error of $D_{\rm XP}$. This increases the number (or fraction) of relaxed clusters that fall in $D_{\rm XP} \leq 0.02R_{500}$ to 7 (or 16%). Consequently, we estimate the fraction of relaxed clusters as 2(<16)% from the BCG-X-ray offset (Table 4).

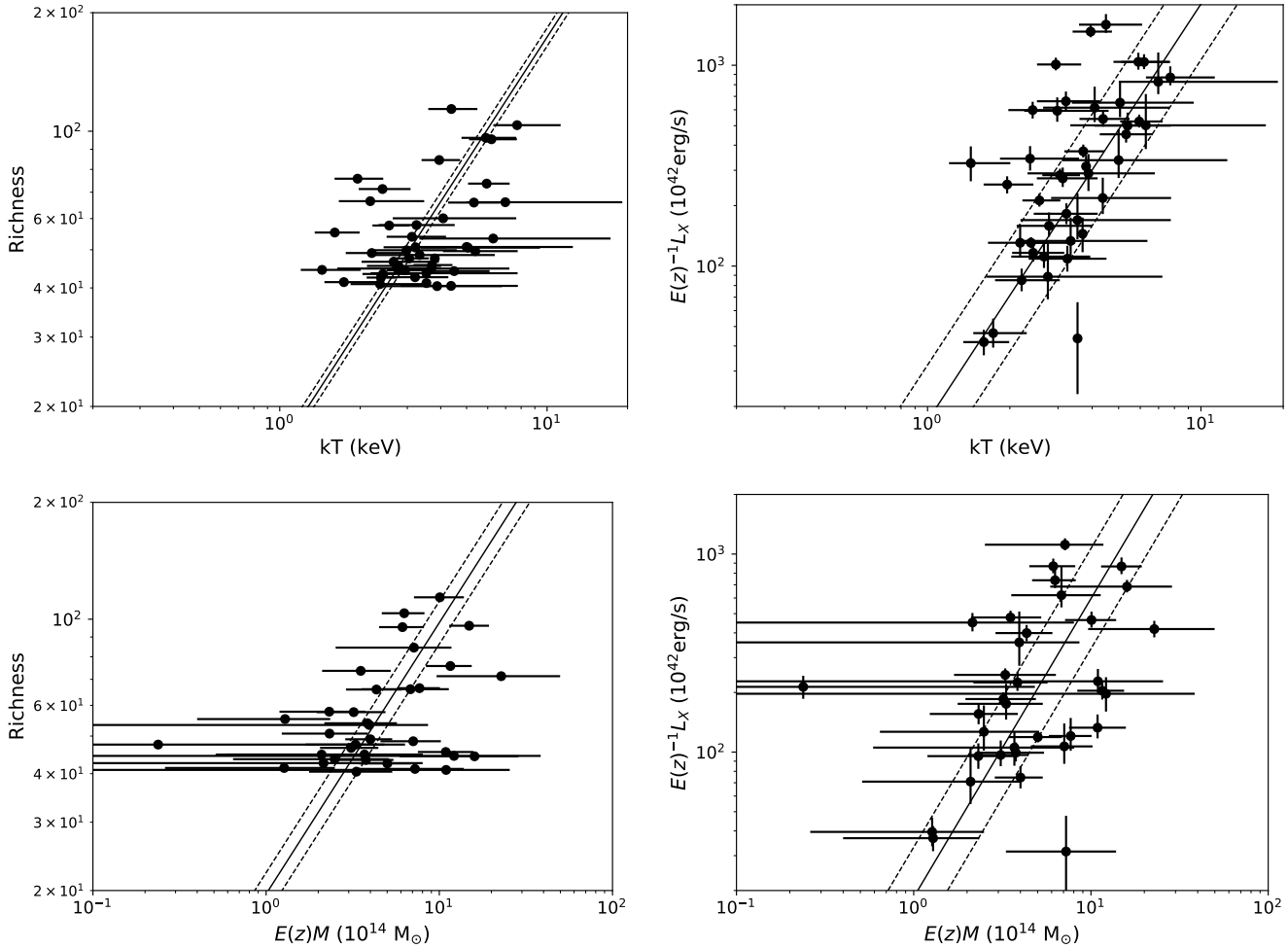

Fig. 4. Scaling relations of the high-richness, optically selected clusters (circles). In the upper panels, the simultaneous fit of $T-N$ and $T-L$ relations are shown. In the lower panels, $M-N$ and $M-L$ relations are shown. In each panel, the best-fit power-law model and the 1σ uncertainty around the mean relation are indicated with the solid and dashed lines, respectively.

We should note that this modest fraction of relaxed clusters is potentially impacted by other effects. First, the selection of the BCG itself faces undeniable obstacles. The lack of redshift information and the use of photometric redshifts with large errors could lead to a poor choice of BCG. In some cases, the true BCG may not be detected due to being overbright for the optical instruments.

Second, there is the concentration parameter: if we refer to the concentration parameter of the X-ray surface brightness, $C_{\mathrm{SB},R_{500}}$, and apply $C_{\mathrm{SB},R_{500}} > 0.37$ to identify relaxed clusters (Lovisari et al. 2017), the fraction of relaxed clusters is estimated as 39% for 33 optical clusters with X-ray counterparts in the eFEDS catalog within R_{500} from the X-ray centroid and $\Delta z < 0.02$. Here, $C_{\mathrm{SB},R_{500}}$ is defined as $C_{\mathrm{SB},R_{500}} = S_B(< 0.1R_{500})/S_B(< R_{500})$ (Maughan et al. 2012) and we quoted the value measured by Ghirardini et al. (2022), based on the X-ray morphological study of the eFEDS clusters. Because all ten unmatched clusters are disturbed clusters, according to the BCG–X-ray offset measurements, we consider the above estimate to be an upper limit on the relaxed fraction.

Third, the galaxy peak-finding method: Since our optically selected sample covers a wide range of morphologies, we expect a large percentage of merging clusters. These complex systems could be classified using the peak-finding method (Okabe et al. 2019). Thus, we also checked the fraction of merging clusters by finding peaks of member-galaxy distribution (Ramos-Ceja et al. 2022). The threshold corresponds to the peak height of the richness $N = 15$ at each redshift. In the eFEDS field, the fraction of clusters with single over multiple peaks is 27/73% for the high-richness CAMIRA clusters, while the fraction of single over multiple peaks is 83/17% for the eFEDS clusters.

To be conservative, we quote the results from three kinds of measurements and estimate the relaxed fraction of our sample to be 2(<39)%.

5.3. Scaling relations

To derive the temperature- and mass-observable relations of the high-richness clusters, we fit the data to the power-law model (Eq. (10)) via the Bayesian regression method (Kelly 2007):

$$\log y = a + b \log x. \tag{10}$$

The quantities a, b, and the intrinsic scatter are treated as free parameters. According to the self-similar model and Hubble's law, $E(z) = [\Omega_M(1+z)^3 + \Omega_\Lambda]^{1/2}$ describes the redshift evolution of the scaling relation. The luminosity of the cluster in the hydrostatic equilibrium follows $E(z)^{-1}L \propto T^2$ and $E(z)^{-1}L \propto [E(z)M]^{4/3}$. In Fig. 4, we corrected the redshift evolution by applying the self-similar model and plotted $E(z)^{-1}L$ against T or

Table 5. Best-fit scaling relations of the optically selected clusters obtained from three types of fitting codes.

	Kelly			1D HiBRECS			2D HiBRECS		
Relation	a	b	σ	a	b	σ	a	b	σ
$N-T$	1.44 ± 0.10	0.61 ± 0.21	0.095	1.19 ± 0.02	1.05 (fix)	0.24	1.07 ± 0.04	1.05 (fix)	0.30 (fix)
$E(z)^{-1}L-T$	1.38 ± 0.24	1.87 ± 0.45	0.28	1.48 ± 0.21	1.70 ± 0.40	0.63	1.23 ± 0.28	2.08 ± 0.46	0.63
$N-E(z)M$	1.43 ± 0.19	0.45 ± 0.24	0.10	1.22 ± 0.03	0.70 (fix)	0.25	1.29 ± 0.06	0.70 (fix)	0.16
$E(z)^{-1}L-E(z)M$	1.44 ± 0.32	1.22 ± 0.43	0.32	1.50 ± 0.29	1.27 ± 0.25	0.65	1.24 ± 0.25	1.52 ± 0.34	0.65
$N-T$	–	–	–	–	–	–	1.07 ± 0.03	1.05 (fix)	0.30 (fix)
$L-T$	1.45 ± 0.27	1.94 ± 0.50	0.31	1.57 ± 0.24	1.72 ± 0.44	0.68	1.41 ± 0.30	1.97 ± 0.50	0.70
$N-M$	1.36 ± 0.22	0.61 ± 0.33	0.094	1.31 ± 0.03	0.70 (fix)	0.11	1.24 ± 0.08	0.70 (fix)	0.27
$L-M$	1.56 ± 0.34	1.33 ± 0.49	0.33	1.62 ± 0.30	1.24 ± 0.45	0.72	1.39 ± 0.32	1.58 ± 0.44	0.64

Notes. T, L, M are in the units of keV, 10^{42} erg s^{-1}, $10^{14}\,M_\odot$, respectively. The best-fit values of a, b in Eq. (10), and the intrinsic scatter of y are listed. The results with and without $E(z)$-correction are shown in 1–4 and 5–8 rows, respectively. The 2D HiBRECS code takes into account the correction for the selection bias and mass calibration, but the other two codes do not (Sects. 5.3 and 6.2).

$E(z)M$ since no clear consensus has been reached on the evolution of the scaling relations (Giodini et al. 2013). Table 5 lists the best-fit parameters for the $N-T$ and $L-T$ relations of 43 clusters and the $N-M$ and $L-M$ relations for 38 clusters with the weak-lensing measurements (Sect. 3.2). The correlation coefficient is 0.62–0.70 for the four relations.

As described in Akino et al. (2022), a multi-variate analysis is needed to properly correct the selection bias and the dilution effect and incorporate the weak-lensing mass calibration. Thus, to correct for the selection bias due to the richness cut of $N > 40$, we simultaneously fit two kinds of relations, $N-T$ and $L-T$ or $N-M$ and $L-M$, by the hierarchical Bayesian regression method (HiBRECS; Akino et al. 2022; Fig. 4). Because the slopes of $N-T$ and $N-M$ were not well constrained due to the large data scatter, we fixed them at 1.05 and 0.70, respectively, that were deduced from the best-fit mass-richness relation (Okabe et al. 2019). We also assumed the intrinsic scatter of the weak-lensing mass to be $\ln \sigma_M = -1.54$ (Umetsu et al. 2020). Table 5 summarizes the best-fit scaling relations obtained from three types of fitting codes.

From Table 5, we find that the fitting results with the Kelly and 1D HiBRECS codes agree well. The Kelly code gave a marginally shallower $N-T$ slope of 0.61 ± 0.21, as compared to the expectation from $M \propto T^{3/2}$ and $M \propto N^{1.4}$ (Okabe et al. 2019). In the present analysis, the impact of selection bias correction was small; the 1D and 2D HiBRECS analyses gave consistent results within the error bars. Therefore, in Sect. 6, we quote the above results based on the 2D HiBRECS code, which can properly handle the bias correction and the mass calibration.

6. Discussion

6.1. BCG–X-ray offset and cluster dynamical status

As mentioned in Sect. 5, only $2(<16)\%$ clusters out of our cluster sample possess a small X-ray peak offset $D_{\rm XC} \le 0.02R_{500}$. Compared with the previous *XMM-Newton* measurements of 17 optical clusters with $N > 20$, $29 \pm 11(\pm 13)\%$ (Ota et al. 2020), the two results agree within the errors.

Rossetti et al. (2016) investigated the dynamical states of 132 galaxy clusters of a Sunyaev–Zel'dovich (SZ) selected a sample at a median redshift of $z = 0.16$ to find that $52 \pm 4\%$ of the sample has $D_{\rm XP} \le 0.02R_{500}$. The SZ selection method tends to pick out dynamically-active systems, which leads to a relatively lower percentage of small peak shift. On the other hand, the relaxed ratio is higher in the X-ray selected sample, at ≈74%, indicating that clusters collected in an X-ray flux-limited survey are subject to the cool-core bias. This accounts for a large fraction of X-ray bright, hence, dynamically relaxed clusters with a small peak shift. In addition, Migkas et al. (2021) found that approximately 44% of the X-ray flux-limited eeHIFLUGCS sample have a small peak shift of $D_{\rm XP} < 0.02R_{500}$. Therefore, our sample's relaxed fraction is considerably small compared to the above SZ and X-ray samples. We note that Ghirardini et al. (2022) reported that the eFEDS-selected cluster sample is not biased toward cool-core clusters, but that it does contain a similar fraction of cool-cores as SZ surveys.

As shown in the upper-left panel of Fig. 3, we assessed the distribution of the centroid offset by the double Gaussian model (Eq. (9)) since there is a tail toward large $D_{\rm XC}$. The fitting yields $\sigma_1 = 28 \pm 2$ kpc, $\sigma_2 = 95 \pm 6$ kpc, and $f_{\rm cen} = 0.46 \pm 0.04$. In comparison with the positional offset between the CAMIRA and XXL clusters (Oguri et al. 2018), the present sample has a marginally smaller fraction of well-centered clusters and a lower tail component.

Pasini et al. (2022) showed that BCGs with radio-loud active galactic nucleus (AGN) are more likely to lie close to the cluster center than radio-quiet BCGs and that the relations between the AGN and the intracluster medium (ICM) hold regardless of the dynamical state of the cluster (see also Pasini et al. 2020).

6.2. Scaling relations

In what follows, we discuss the $L-T$ and $L-M$ relations based on a comparison with previous observations and theoretical models. The $L-T$ relation shows a large intrinsic scatter of $\sigma_{L|T} = 0.63$, as noted by the previous X-ray studies (e.g., Ota et al. 2006; Pratt et al. 2009). The observed $L-T$ slope of 2.08 ± 0.46 agrees with 2.2 ± 0.6 (± 0.2) derived from the *XMM-Newton* observations of the CAMIRA clusters (Ota et al. 2020). In contrast, a steeper slope of ∼3 has been reported by many X-ray observations in the past (Giodini et al. 2013). From the analysis of 265 eFEDS clusters, Bahar et al. (2022) obtained the best-fit $L_{\rm bol}-T$ slope of $3.01^{+0.13}_{-0.12}$, suggesting a strong deviation from the self-similar model, $L \propto T^2$. Because of the small fraction of relaxed clusters, we consider the present measurement is less affected by the cool-core emission.

The scatter of $L-M$ relation is comparably large, $\sigma_{L|M} = 0.65$, which confirms previous reports (e.g., Pratt et al. 2009). The $L-M$ slope of 1.52 ± 0.34 is consistent with 1.51 ± 0.09

derived for 232 clusters at $z = 0.05-1.46$ based on a compilation of 14 published X-ray data sets (Reichert et al. 2011). The best-fit $L-M$ relation of the present optical sample also agrees with the result on 25 shear-selected clusters in the eFEDS field (Ramos-Ceja et al. 2022) and the luminosity–mass-and-redshift relation of the eFEDS cluster sample with the HSC weak-lensing mass calibration (Chiu et al. 2022) within the measurement errors though the fitting functions are not exactly the same.

Finally, we discuss the interpretation of our results by referring to the baseline scaling relations. The self-similar model (Kaiser 1986) predicts simple relations between X-ray properties of ICM and mass in the absence of baryonic physics such as AGN feedback and radiative cooling. Moreover, these baseline relations were derived without considering the fact that less massive clusters tend to be more concentrated and have higher characteristic densities in the hierarchical structure formation in a CDM universe (Navarro et al. 1997). On the other hand, Fujita & Aung (2019) constructed the new baseline luminosity–temperature and mass relations by considering the mass–concentration relationship. This is again the case when additional physics, such as feedback and radiative cooling, do not work. They showed that the baseline relations should be shallower than the conventional self-similar model and follow $L \propto T^{1.6-1.8}$ and $L \propto M^{1.1-1.2}$. They also suggested that the $L-T$ relation of high-mass clusters should be close to the baseline model because the feedback from stars and AGN is less effective.

To carry out a comparison with their model, we derived the scaling relations without $E(z)$-correction in the same manner as in Fujita & Aung (2019). From rows 5–8 of Table 5, the fitted slopes of $L-T$ and $L-M$ relations agree with the baseline models within the 1σ errors. Here, the baseline relations show little difference between merging and non-merging clusters (Fig. 3 of Fujita & Aung 2019), while disturbed clusters dominate our sample. The nature of the fundamental plane can explain the above trend because the $L-T$ relation is close to the edge-on view of the fundamental plane and the clusters do not substantially deviate from the thin plane, even during a merging process (Fujita et al. 2018). Therefore, the small $L-T$ slope observed in the high-richness massive clusters agrees with the prediction of the revised baseline model by Fujita & Aung (2019). We plan to extend the analysis using the eROSITA and HSC surveys to test the shallow scaling relations.

7. Summary

Based on a joint analysis of the eROSITA/eFEDS and Subaru/HSC surveys, we studied the X-ray properties of 43 optically selected clusters with a high richness of >40 at $0.16 < z < 0.89$. Our major findings are as follows:

1. We studied the cluster dynamical status by the X-ray–BCG offset and the gas concentration parameter and measured the morphology of member-galaxy distributions by the peak-finding method. As a result, we estimated the fraction of relaxed clusters to be 2(<39)%, which is smaller than that of the X-ray-selected cluster samples.
2. We performed the X-ray spectral analysis and weak-lensing mass measurement, deriving the scaling relations using the hierarchical Bayesian regression method. The luminosity–temperature relation is shallow; the slope is consistent with the predictions of the self-similar model and the baseline model incorporating the mass–concentration relation. The luminosity–mass relation also agrees with the two theoretical models cited in this work as well as what has been observed for the shear-selected clusters in the eFEDS field within the measurement errors.

Our joint eROSITA and HSC study showed that the average X-ray properties of high-richness clusters are likely to be different from those found in the X-ray cluster samples. To improve the sample size, we plan to incorporate more than 900 objects with $15 < N < 40$ (Table 2) and extend the analysis to the eROSITA all-sky survey (eRASS) data that overlap with the HSC footprint. These works enable us to study the mass-observable relations and the redshift evolution of the optical clusters. Furthermore, comparisons with the X-ray and shear-selected samples will improve our knowledge about the selection effect and cluster evolution.

Acknowledgements. This work is based on data from eROSITA, the soft X-ray instrument aboard SRG, a joint Russian-German science mission supported by the Russian Space Agency (Roskosmos), in the interests of the Russian Academy of Sciences represented by its Space Research Institute (IKI), and the Deutsches Zentrum für Luft- und Raumfahrt (DLR). The SRG spacecraft was built by Lavochkin Association (NPOL) and its subcontractors, and is operated by NPOL with support from the Max Planck Institute for Extraterrestrial Physics (MPE). The development and construction of the eROSITA X-ray instrument was led by MPE, with contributions from the Dr. Karl Remeis Observatory Bamberg & ECAP (FAU Erlangen-Nuernberg), the University of Hamburg Observatory, the Leibniz Institute for Astrophysics Potsdam (AIP), and the Institute for Astronomy and Astrophysics of the University of Tübingen, with the support of DLR and the Max Planck Society. The Argelander Institute for Astronomy of the University of Bonn and the Ludwig Maximilians Universität Munich also participated in the science preparation for eROSITA. The eROSITA data shown here were processed using the eSASS/NRTA software system developed by the German eROSITA consortium. The Hyper Suprime-Cam (HSC) collaboration includes the astronomical communities of Japan and Taiwan, and Princeton University. The HSC instrumentation and software were developed by the National Astronomical Observatory of Japan (NAOJ), the Kavli Institute for the Physics and Mathematics of the Universe (Kavli IPMU), the University of Tokyo, the High Energy Accelerator Research Organization (KEK), the Academia Sinica Institute for Astronomy and Astrophysics in Taiwan (ASIAA), and Princeton University. Funding was contributed by the FIRST program from Japanese Cabinet Office, the Ministry of Education, Culture, Sports, Science and Technology (MEXT), the Japan Society for the Promotion of Science (JSPS), Japan Science and Technology Agency (JST), the Toray Science Foundation, NAOJ, Kavli IPMU, KEK, ASIAA, and Princeton University. We thank Y. Fujita for valuable discussions and the anonymous referee for comments. This work was supported in part by the Fund for the Promotion of Joint International Research, JSPS KAKENHI Grant Number 16KK0101, 20K04027(NO), 20H05856, 20H00181, 19KK0076, 22H01260 (MO).

References

Aihara, H., Arimoto, N., Armstrong, R., et al. 2018a, PASJ, 70, S4
Aihara, H., Armstrong, R., Bickerton, S., et al. 2018b, PASJ, 70, S8
Aihara, H., AlSayyad, Y., Ando, M., et al. 2022, PASJ, 74, 247
Akino, D., Eckert, D., Okabe, N., et al. 2022, PASJ, 74, 175
Allen, S. W., Evrard, A. E., & Mantz, A. B. 2011, ARA&A, 49, 409
Asplund, M., Grevesse, N., Sauval, A. J., & Scott, P. 2009, ARA&A, 47, 481
Bahar, Y. E., Bulbul, E., Clerc, N., et al. 2022, A&A, 661, A7
Blanton, M. R., & Roweis, S. 2007, AJ, 133, 734
Bosch, J., Armstrong, R., Bickerton, S., et al. 2018, PASJ, 70, S5
Brunner, H., Liu, T., Lamer, G., et al. 2022, A&A, 661, A1
Bulbul, E., Liu, A., Pasini, T., et al. 2022, A&A, 661, A10
Carrasco Kind, M., & Brunner, R. J. 2014, MNRAS, 438, 3409
Cavaliere, A., & Fusco-Femiano, R. 1976, A&A, 500, 95
Chilingarian, I. V., Melchior, A.-L., & Zolotukhin, I. Y. 2010, MNRAS, 405, 1409
Chilingarian, I. V., & Zolotukhin, I. Y. 2012, MNRAS, 419, 1727
Chiu, I. N., Ghirardini, V., Liu, A., et al. 2022, A&A, 661, A11
Fadda, D., Girardi, M., Giuricin, G., Mardirossian, F., & Mezzetti, M. 1996, ApJ, 473, 670
Fitzpatrick, E. L. 1999, PASP, 111, 63
Foster, A. R., Ji, L., Smith, R. K., & Brickhouse, N. S. 2012, ApJ, 756, 128
Fujita, Y., & Aung, H. 2019, ApJ, 875, 26
Fujita, Y., Umetsu, K., Rasia, E., et al. 2018, ApJ, 857, 118

Giodini, S., Lovisari, L., Pointecouteau, E., et al. 2013, Space Sci. Rev., 177, 247
Ghirardini, V., Bahar, Y. E., Bulbul, E., et al. 2022, A&A, 661, A12
Hirata, C., & Seljak, U. 2003, MNRAS, 343, 459
Hoekstra, H. 2003, MNRAS, 339, 1155
Kaiser, N. 1986, MNRAS, 222, 323
Kaiser, N., Aussel, H., Burke, B. E., et al. 2002, in Survey and Other Telescope Technologies and Discoveries, eds. J. A. Tyson, & S. Wolff, SPIE Conf. Ser., 4836, 154
Kaiser, N., Burgett, W., Chambers, K., et al. 2010, in Ground-based and Airborne Telescopes III, eds. L. M. Stepp, R. Gilmozzi, & H. J. Hall, SPIE Conf. Ser., 7733, 77330E
Kelly, B. C. 2007, ApJ, 665, 1489
Klein, M., Oguri, M., Mohr, J. J., et al. 2022, A&A, 661, A4
Li, X., Miyatake, H., Luo, W., et al. 2022, PASJ, 74, 421
Liu, A., Bulbul, E., Ghirardini, V., et al. 2022, A&A, 661, A2
Lovisari, L., Forman, W. R., Jones, C., et al. 2017, ApJ, 846, 51
Mandelbaum, R., Lanusse, F., Leauthaud, A., et al. 2018a, MNRAS, 481, 3170
Mandelbaum, R., Miyatake, H., Hamana, T., et al. 2018b, PASJ, 70, S25
Maughan, B. J., Giles, P. A., Randall, S. W., Jones, C., & Forman, W. R. 2012, MNRAS, 421, 1583
Medezinski, E., Battaglia, N., Umetsu, K., et al. 2018a, PASJ, 70, S28
Medezinski, E., Oguri, M., Nishizawa, A. J., et al. 2018b, PASJ, 70, 30
Migkas, K., Pacaud, F., Schellenberger, G., et al. 2021, A&A, 649, A151
Miyaoka, K., Okabe, N., Kitaguchi, T., et al. 2018, PASJ, 70, S22
Miyatake, H., Battaglia, N., Hilton, M., et al. 2019, ApJ, 875, 63
Miyazaki, S., Komiyama, Y., Kawanomoto, S., et al. 2018, PASJ, 70, S1
Murata, R., Oguri, M., Nishimichi, T., et al. 2019, PASJ, 71, 107
Navarro, J. F., Frenk, C. S., & White, S. D. M. 1996, ApJ, 462, 563
Navarro, J. F., Frenk, C. S., & White, S. D. M. 1997, ApJ, 490, 493
Nishizawa, A. J., Hsieh, B. C., Tanaka, M., & Takata, T. 2020, ArXiv e-prints [arXiv:2003.01511]
Oguri, M. 2014, MNRAS, 444, 147
Oguri, M., Takada, M., Okabe, N., & Smith, G. P. 2010, MNRAS, 405, 2215
Oguri, M., Lin, Y.-T., Lin, S.-C., et al. 2018, PASJ, 70, S20
Okabe, N., & Smith, G. P. 2016, MNRAS, 461, 3794
Okabe, N., Bourdin, H., Mazzotta, P., & Maurogordato, S. 2011, ApJ, 741, 116
Okabe, N., Oguri, M., Akamatsu, H., et al. 2019, PASJ, 71, 79
Okabe, N., Dicker, S., Eckert, D., et al. 2021, MNRAS, 501, 1701
Ota, N., & Mitsuda, K. 2004, A&A, 428, 757
Ota, N., Kitayama, T., Masai, K., & Mitsuda, K. 2006, ApJ, 640, 673
Ota, N., Mitsuishi, I., Babazaki, Y., et al. 2020, PASJ, 72, 1
Pasini, T., Brüggen, M., de Gasperin, F., et al. 2020, MNRAS, 497, 2163
Pasini, T., Brüggen, M., Hoang, D. N., et al. 2022, A&A, 661, A13
Pratt, G. W., Croston, J. H., Arnaud, M., & Böhringer, H. 2009, A&A, 498, 361
Pratt, G. W., Arnaud, M., Biviano, A., et al. 2019, Space Sci. Rev., 215, 25
Predehl, P., Andritschke, R., Arefiev, V., et al. 2021, A&A, 647, A1
Ramos-Ceja, M. E., Oguri, M., Miyazaki, S., et al. 2022, A&A, 661, A14
Reichert, A., Böhringer, H., Fassbender, R., & Mühlegger, M. 2011, A&A, 535, A4
Rossetti, M., Gastaldello, F., Ferioli, G., et al. 2016, MNRAS, 457, 4515
Sanderson, A. J. R., Edge, A. C., & Smith, G. P. 2009, MNRAS, 398, 1698
Schlegel, D. J., Finkbeiner, D. P., & Davis, M. 1998, ApJ, 500, 525
Schneider, P., van Waerbeke, L., Jain, B., & Kruse, G. 1998, MNRAS, 296, 873
Skrutskie, M. F., Cutri, R. M., Stiening, R., et al. 2006, AJ, 131, 1163
Smith, R. K., Brickhouse, N. S., Liedahl, D. A., & Raymond, J. C. 2001, ApJ, 556, L91
Tanaka, M., Coupon, J., Hsieh, B.-C., et al. 2018, PASJ, 70, S9
Umetsu, K. 2020, A&ARv, 28, 7
Umetsu, K., Sereno, M., Lieu, M., et al. 2020, ApJ, 890, 148
Willingale, R., Starling, R. L. C., Beardmore, A. P., Tanvir, N. R., & O'Brien, P. T. 2013, MNRAS, 431, 394
Willis, J. P., Oguri, M., Ramos-Ceja, M. E., et al. 2021, MNRAS, 503, 5624
Wilms, J., Allen, A., & McCray, R. 2000, ApJ, 542, 914
Wright, E. L., Eisenhardt, P. R. M., Mainzer, A. K., et al. 2010, AJ, 140, 1868
Wright, A. H., Robotham, A. S. G., Bourne, N., et al. 2016, MNRAS, 460, 765
York, D. G., Adelman, J., Anderson, John E., J., , et al. 2000, AJ, 120, 1579

[1] Argelander-Institut für Astronomie (AIfA), Universität Bonn, Auf dem Hügel 71, 53121 Bonn, Germany
e-mail: naomi@astro.uni-bonn.de
[2] Department of Physics, Nara Women's University, Kitauoyanishi-machi, Nara 630-8506, Japan
[3] Institut für Astronomie und Astrophysik Tübingen (IAAT), Universität Tübingen, Sand 1, 72076 Tübingen, Germany
[4] Graduate School of Science, Division of Particle and Astrophysical Science, Nagoya University, Furo-cho, Chikusa-ku, Nagoya, Aichi 464-8602, Japan
[5] Center for Frontier Science, Chiba University, 1-33 Yayoi-cho, Inage-ku, Chiba 263-8522, Japan
[6] Department of Physics, Graduate School of Science, Chiba University, 1-33 Yayoi-Cho, Inage-Ku, Chiba 263-8522, Japan
[7] Kavli Institute for the Physics and Mathematics of the Universe (Kavli IPMU, WPI), University of Tokyo, Chiba 277-8582, Japan
[8] Faculty of Physics, Ludwig-Maximilians-Universität, Scheinerstr. 1, 81679 Munich, Germany
[9] Physics Program, Graduate School of Advanced Science and Engineering, Hiroshima University, 1-3-1 Kagamiyama, Higashi-Hiroshima, Hiroshima 739-8526, Japan
[10] Hiroshima Astrophysical Science Center, Hiroshima University, 1-3-1 Kagamiyama, Higashi-Hiroshima, Hiroshima 739-8526, Japan
[11] Core Research for Energetic Universe, Hiroshima University, 1-3-1, Kagamiyama, Higashi-Hiroshima, Hiroshima 739-8526, Japan
[12] Max Planck Institute for Extraterrestrial Physics, Giessenbachstrasse 1, 85748 Garching, Germany
[13] University of Hamburg, Hamburger Sternwarte, Gojenbergsweg 112, 21029 Hamburg, Germany
[14] Tsung-Dao Lee Institute, and Key Laboratory for Particle Physics, Astrophysics and Cosmology, Ministry of Education, Shanghai Jiao Tong University, Shanghai 200240, PR China
[15] Department of Astronomy, School of Physics and Astronomy, and Shanghai Key Laboratory for Particle Physics and Cosmology, Shanghai Jiao Tong University, Shanghai 200240, PR China
[16] Academia Sinica Institute of Astronomy and Astrophysics (ASIAA), 11F of AS/NTU Astronomy-Mathematics Building, No.1, Sec. 4, Roosevelt Rd, Taipei 10617, Taiwan
[17] Kobayashi-Maskawa Institute for the Origin of Particles and the Universe (KMI), Nagoya University, Nagoya 464-8602, Japan
[18] National Astronomical Observatory of Japan, 2-21-1 Osawa, Mitaka, Tokyo 181-8588, Japan
[19] SOKENDAI (The Graduate University for Advanced Studies), Mitaka, Tokyo 181-8588, Japan

3.2.2 The eROSITA Final Equatorial-Depth Survey (eFEDS): X-ray stacking analysis of Subaru's optically selected clusters spanning low richness regime

We extend the work presented in Section 3.2.1 to a larger sample of approximately 1,000 galaxy clusters spanning a broader range of mass and richness. Due to the low photon counts for most clusters, we employ a stacking technique to enhance statistical robustness. The findings from this analysis are consistent with and strengthen our previous study, which indicate that (i) the relaxed fraction of galaxy clusters in the optically selected sample is lower than in X-ray- or SZ-selected samples, and (ii) the average X-ray properties, including scaling relations and radial profiles, of the optical sample differ from those of X-ray-selected samples.

Leveraging a large and uniform optical dataset combined with X-ray observations from the state-of-the-art eROSITA observatory, this study enables robust conclusions on the impact of cluster selection methods, offering new insights into the complex interplay between optical and X-ray properties of galaxy clusters.

Astronomy & Astrophysics manuscript no. output
January 22, 2025

The eROSITA Final Equatorial-Depth Survey (eFEDS)

X-ray stacking analysis of Subaru's optically selected clusters spanning low richness regime

N. T. Nguyen-Dang[1], N. Ota[2,3], N. Okabe[4,5,6], M. Oguri[7,8,9], I. Mitsuishi[10], T. H. Reiprich[2], F. Pacaud[2], E. Bulbul[11], J. S. Sanders[11], M. Brüggen[12], A. Liu[11], Y. Tsujita[3], I. Chiu[13,14,15], V. Ghirardini[11], S. Grandis[16], M. Klein[16], Y.-T. Lin[15], K. Migkas[17,18], H. Miyatake[9,19], S. Miyazaki[20,21], and M. E. Ramos-Ceja[11]

(Affiliations can be found after the references)

Received September 15, 1996; accepted March 16, 1997

ABSTRACT

Context. This is the second paper in a series exploring the X-ray properties of galaxy clusters optically selected by the Subaru Hyper Suprime-Cam (HSC) survey, utilizing the SRG/eROSITA Final Equatorial-Depth Survey (eFEDS) dataset.
Aims. We aim to analyze the dynamical state of the cluster sample, establish scaling relations between observable properties and mass, and examine X-ray radial profiles.
Methods. Our sample includes 997 optical clusters with richness > 15 and redshifts $0.1 < z < 1.3$. We identify the brightest cluster galaxy (BCG) and assess dynamical states via the BCG–X-ray peak offset. Stacking techniques are employed to investigate the bolometric luminosity-mass ($L-M$) and richness-mass ($N-M$) relations, accounting for selection effects and redshift evolution. Clusters with and without X-ray counterparts in the eFEDS catalog are compared using scaling relations and radial profiles.
Results. The relaxed fraction is < 14%, slightly lower than in X-ray flux-limited samples but consistent with optically selected catalogs. The best-fit $L-M$ slope ($1.67^{+0.18}_{-0.15}$) is consistent with our previous study but steeper than the self-similar prediction. The $N-M$ slope ($0.878^{+0.099}_{-0.079}$) aligns with self-similarity and other observations. We find a negative redshift evolution in the $N-M$ relation, while the $L-M$ relation shows no significant trend with redshift. Clusters with X-ray counterparts exhibit a steeper $L-M$ slope, higher central surface brightness, and more peaked profiles compared to those without X-ray detections.
Conclusions. Our findings support theoretical models and recent observations, showing noticeable differences in the X-ray properties of optically selected clusters compared to those of X-ray flux-limited samples. This work extends scaling relation studies to low-mass and low-luminosity regimes, leveraging deep eROSITA X-ray and Subaru optical surveys.

Key words. Galaxies: clusters: intracluster medium; intergalactic medium; X-rays: galaxies: clusters

1. Introduction

Galaxy clusters play a crucial role in cosmological research, since at various stages of their formation and evolution, they mirror the corresponding conditions of the Universe (see e.g., Pierre 2022 for a recent review). At the same time, galaxy clusters serve as laboratories for large-scale physics. Constructing comprehensive cluster samples is essential for these studies, typically involving selection criteria based on observable properties in specific wavebands, ranging from sub-millimeter to X-ray. In optical surveys, clusters can be identified through overdensities in the red-sequence galaxy population (Rozo & Rykoff 2014; Oguri 2014; Maturi et al. 2019; Vakili et al. 2023). Weak lensing (WL) shear surveys detect clusters by observing distortions of the images of background galaxies caused by the gravitational potential wells of foreground clusters (Miyazaki et al. 2018; Oguri et al. 2021; Chen et al. 2024; Chiu et al. 2024). Meanwhile, X-ray surveys reveal clusters (Böhringer et al. 2001; Schellenberger & Reiprich 2017; Xu et al. 2022) via the optically thin bremsstrahlung emission from the hot intracluster medium (ICM).

Observations show that cluster samples obtained from different selection methods differ from each other on average properties (Ota et al. 2020, 2023; Willis et al. 2021). Generally speaking, X-ray flux limited samples are reported to exhibit a cool-core bias, primarily selecting a significant fraction of massive clusters with relaxed morphologies due to their intense X-ray emissions (Pacaud et al. 2007; Hudson et al. 2010; Andreon & Moretti 2011; Eckert et al. 2011; Xu et al. 2018). Consequently, these X-ray samples tend to include a higher number of massive and/or relaxed clusters. Since the first X-ray all sky survey was conducted by the ROSAT satellite in 1990 (Truemper 1993; Ebeling et al. 1998, 2010; Böhringer et al. 2017), the science community has witnessed great effort to provide deeper and more detailed X-ray surveys such as the XXL sample performed by the XMM-Newton satellite (Jansen et al. 2001; Adami et al. 2018), the CDF-S sample conducted by the Chandra X-ray observatory (Finoguenov et al. 2015), and culminating recently in eROSITA (Predehl et al. 2021; Liu et al. 2022b). The excellent effective area at soft energy range of eROSITA makes it possible to collect a highly complete X-ray sample, including objects up to redshifts $z \sim 1.5$ and down to cluster mass $M_{500} \sim 10^{13} M_{\odot}$. In contrast to X-ray flux selected ones, optically identified cluster samples are unaffected by the cool-core bias and can present a higher abundance of low-mass objects as well as those having more complex morphologies. At the same time, optical clusters have been compiled from numerous surveys, including SDSS, Legacy, and HSC (Rykoff et al. 2014; Zou et al. 2021; Oguri 2014). These samples have signif-

icantly contributed to constraining cosmological models using cluster abundance (Planck Collaboration et al. 2016; Chiu et al. 2023; Ghirardini et al. 2024; Bocquet et al. 2024) or using angular power spectrum of clusters (Fonseca et al. 2019; Lau et al. 2024). Furthermore, they facilitate investigations into the effects of cluster selection methods. Willis et al. (2021) studied the impact of cluster selection effects using the XXL X-ray sample and the CAMIRA sample observed by the Subaru HSC. The authors note that the discrepancies between the two samples fall within the known selection effects, which can be attributed to a combination of the morphological search criteria employed by the XXL pipeline and the properties of the XMM point spread function (PSF).

Galaxy clusters represent the endpoint of structure formation, being the largest gravitationally collapsed objects in the Universe. They are believed to form through the gravitational collapse of matter and grow by merging with smaller structures within a cold dark matter framework (e.g., Kravtsov & Borgani 2012). Virialized clusters are typically morphologically relaxed, characterized by centrally concentrated mass distributions, smooth X-ray profiles, and minimal substructures. In contrast, clusters undergoing recent mergers appear morphologically disturbed. Assessing cluster morphology, which reflects the cluster's dynamical state, is essential for interpreting results from cosmology and cluster physics investigations based on the sample.

The formation and evolution scenario of galaxy clusters can be characterized by the tight connections between cluster observables across different mass scales. Self-similar models (Kaiser 1986), derived from the virial theorem and based on the assumption that galaxy clusters are in hydrostatic equilibrium, are widely used to describe observed scaling relations. However, non-gravitational processes such as AGN feedback, radiative cooling, recent mergers, and galactic winds can cause observed scaling relations to deviate from self-similar predictions. For instance, the slopes for the X-ray temperature and luminosity relative to mass relations are often reported at a higher value than self-similarity (Pratt et al. 2009; Molham et al. 2020). Interested readers are referred to Giodini et al. (2013) for a review on cluster scaling relations. In addition, cluster scaling relations of samples with a wide range of redshifts provide an excellent test for the redshift evolution of the baryonic content in the Universe. Recent studies have yielded contradictory reports on the redshift evolution of cluster scaling relations; some show significant redshift trends (Maughan 2007; Pacaud et al. 2007; Bulbul et al. 2019), while others reveal no such trends (Vikhlinin et al. 2009; Chiu et al. 2018; Bahar et al. 2022a). This indicates a need for deeper surveys and larger samples to draw conclusive insights on this topic. For a comprehensive discussion, refer to e.g., Reichert et al. (2011), which provides a detailed study of scaling evolution using a combination of 14 published data sets.

As mentioned above, the eROSITA X-ray observatory has been offering the most recent all sky survey for astronomical research. eROSITA, aboard the Spectrum-Roentgen-Gamma (SRG) mission (Predehl et al. 2021; Sunyaev et al. 2021), delivers highly uniform X-ray follow-ups for optical samples. The eROSITA Final Equatorial-Depth Survey (eFEDS) was conducted during the calibration and performance verification phase of eROSITA to forecast the capabilities of the full survey once it reaches its final depth of eight scans (Brunner et al. 2022). This 140 deg^2 mini-survey is strategically aligned with other deep optical surveys (SDSS, Legacy, HSC) for optical confirmation and weak-lensing mass calculations. Meanwhile, the Subaru HSC continuously provides optical cluster samples alongside accurate weak-lensing calibrated masses for relevant studies (Oguri et al. 2018; Miyazaki et al. 2018), aiding the investigations utilizing eROSITA cluster samples (Liu et al. 2022a; Bulbul et al. 2022a).

We continue the ongoing investigations by using the X-ray data obtained from the eFEDS survey to study the CAMIRA optical clusters. The use of CAMIRA clusters improves the sample uniformity and allows direct, meaningful comparison between the X-ray detected and undetected sub-samples. The final-depth survey X-ray data from eFEDS expands the investigation to a lower mass range and deeper redshift compared to recent X-ray databases. Furthermore, the stacking analysis is employed to refine the count statistics. Therefore, the joint analysis of these two data sets allows us to address the following two main questions: **1/** How do X-ray detected clusters differ from solely optically detected ones? and **2/** How are the observables-to-mass relations of our cluster sample described? We attempt to answer these questions by analyzing the dynamical status of the sample, the observable-to-mass scaling relations and the X-ray surface brightness profiles of the stacked clusters.

The structure of the paper is as follows. Section 2 describes the sample construction. Section 3 presents the X-ray analysis, including the determination of X-ray peaks, the calculation of stacked X-ray luminosity, and the estimation of X-ray radial profiles. Section 4 shows the optical analysis, in particular the BCG identification and WL mass calibration. Section 5 derives the X-ray involved properties of the sample, namely the morphological status, observables-mass scaling relations, and X-ray surface brightness. Section 6 discusses the results of this work. Finally, Section 7 summarizes the main findings of this paper.

In this paper, we assume a flat ΛCDM cosmology with $\Omega_{\rm m} = 0.3$, $\Omega_\Lambda = 0.7$ and $h = 0.7$. We use the abundance table from Asplund et al. (2009) in the X-ray spectral modeling. The errors correspond to 68% unless noted differently.

2. Sample

Out of the 21,250 optically selected galaxy clusters in the CAMIRA galaxy cluster catalog S20A v2 (Oguri et al. 2018), we selected 997 objects located in the eFEDS field. The richness range is $15 < N < 114$, and the redshift range is $0.10 < z < 1.34$ (Fig. 1). Table 1 shows the first ten clusters in the sample list.

While Ota et al. (2023) dealt only with the 43 objects with high richness ($N > 40$), we include all 997 objects. This significantly improves the sample size for the X-ray follow-up of optically selected galaxy clusters compared to previous studies, allowing for a systematic investigation of galaxy clusters across a wider mass range.

Additionally, there is a tendency for higher richness clusters to have a higher X-ray detection rate. In fact, 171 objects, accounting for 17% of the total, have been detected in X-rays and registered in the eFEDS catalog (Liu et al. 2022a). Similar to our previous work (Ota et al. 2023), we identified X-ray counterparts for the optical clusters by searching for a spatially-extended X-ray source within the characteristic radius R_{500}[1] from the CAMIRA center, which satisfies the redshift condition of $|\Delta z| < 0.02$. This redshift deviation is set to be at the order of the typical uncertainty of photometric redshift (e.g., Takey et al. 2013). Most objects are X-ray faint, making it difficult to accurately determine the X-ray center. Therefore, unless otherwise specified, the BCG coordinates from the CAMIRA catalog are used as the cluster center coordinates.

[1] The radius within which the average density is 500 times of the critical density of the Universe at the considered redshift

Table 1. Sample list. Here we show an example of 10 CAMIRA clusters, the full table can be accessed online.

Cluster	z	$\hat{N}_{\rm mem}{}^{a}$	R_{500} (Mpc/″)	BCG position RA, Dec (deg)	BCG z	X-ray peak RA, Dec (deg)	$D_{\rm XP}{}^{b}$ (kpc)
HSC J083151+031637	1.224	16.6	0.403/ 48	127.9634, 3.2769	1.224 ± 0.000	127.9566, 3.2681	333 (244,333)
HSC J083303+024433	0.187	30.1	0.725/ 231	128.2617, 2.7425	0.184 ± 0.000	128.2834, 2.7710	405 (294,404)
HSC J083317–003730	0.417	18.1	0.534/ 96	128.3223, -0.6250	0.413 ± 0.026	128.3349, -0.6079	420 (419,419)
HSC J083321+033847	0.773	24.9	0.559/ 75	128.3369, 3.6465	0.747 ± 0.000	128.3408, 3.6549	249 (180,253)
HSC J083322+031634	0.826	22.8	0.527/ 69	128.3366, 3.2902	0.737 ± 0.106	128.3411, 3.2826	239 (229,239)
HSC J083322–011142	0.289	28.7	0.689/ 158	128.3414, -1.1949	0.292 ± 0.012	128.3438, -1.1522	669 (554,669)
HSC J083326+002545	0.794	18.2	0.479/ 63	128.3428, 0.4299	0.923 ± 0.106	128.3423, 0.4310	33 (15,579)
HSC J083338+033453	0.951	18.9	0.464/ 58	128.4085, 3.5813	0.951 ± 0.000	128.4032, 3.5764	205 (196,204)
HSC J083339–011229	1.068	22.7	0.489/ 59	128.4140, -1.2081	1.068 ± 0.000	128.4173, -1.2074	100 (88,439)
HSC J083351+004427	0.380	20.2	0.568/ 109	128.4363, 0.7391	0.388 ± 0.000	128.4464, 0.7435	207 (206,206)

Notes. [(a)] Richness. [(b)] Peak offset. The error range estimated by changing the smoothing scale of the X-ray image is given in parentheses (see Sects. 3.2 and 5.1).

3. X-ray data analysis

3.1. Data reduction

We reduced the eFEDs data of seven telescope modules (TMs) by using version `eSASSusers_201009` (Brunner et al. 2022) of the eROSITA Standard Analysis Software System (eSASS). This is analogous to Ota et al. (2023). We extracted cleaned event files and removed point sources by referring to the main eFEDS X-ray source catalog[2] (Brunner et al. 2022).

3.2. X-ray peak determination

We measured the X-ray peak position within a radius of R_{500} in the X-ray image to quantify the BCG-X-ray peak offset as a morphological indicator. Here, we extracted the 0.5-2.0 keV band image from the merged event files of seven TMs (1 image pixel = 1″.5) and corrected for exposure and vignetting. We then smoothed the image by applying a Gaussian filter with $\sigma = 3$ pixels. We consider the systematic uncertainty due to the finite pixel size, astrometry, and the telescope response (See sec 5.1 for details). As pointed out in our previous study (Ota et al. 2023), the two-dimensional survey PSF image at each cluster position is approximately symmetric and does not affect the calculation of the X-ray peak.

3.3. Stacking analysis of X-ray luminosity

We define the cluster source and background regions by drawing a circle of radius R_{500} around the center of the CAMIRA cluster coordinates (Section 2) and the surrounding annulus with inner and outer radii 2.5 and 4.0 Mpc, respectively. Similar to our previous work (Ota et al. 2023), we calculated R_{500} by using the mass-richness relation (Okabe et al. 2019) and the cluster richness taken from the CAMIRA catalog (Oguri et al. 2018). Since most objects have low photon statistics, we estimate the bolometric (0.01-30.0 keV) X-ray luminosity from the observed count rates instead of performing individual spectral fitting. Here, we calculate the bolometric luminosity focusing on the energy range where most cluster emission occurs. Specifically, $L_{\rm bol} = (L_{\rm model}/C_{\rm model})C_{\rm obs}$, where $C_{\rm obs}$ is the observed count rate in the 0.5–2 keV band and $(L_{\rm model}/C_{\rm model})$ is the conversion factor calculated from the APEC thin-thermal emission model (Smith et al. 2001; Foster et al. 2012) and the metal abundance of 0.3 solar, corrected for the Galactic absorption PHABS model (Balucinska-Church & McCammon 1992). The response files are generated at the position of each cluster using the eROSITA `srctool`. We estimated the gas temperature by the richness-temperature relation of the optically selected clusters (Oguri et al. 2018).

Furthermore, we employ a stacking analysis to enhance the statistical significance, allowing for a more robust study of the sample's scaling relations. We divide the clusters into groups of similar redshift and richness, such that each group has more than 500 counts and consists of at least two members. For simplicity, we begin by separating the sample into 3 classes of redshift, namely "low", "mid" and "high", where the redshift ranges are $z < 0.4$, $0.4 \leq z < 0.8$ and $z \geq 0.8$, respectively. In terms of richness, the initial separation is $15 \leq N < 20$, $20 \leq N < 25$, $25 \leq N < 30$, $30 \leq N < 35$, $35 \leq N < 40$ and finally $N \geq 40$. We then collect clusters within each initial bin to form groups following the above conditions. If the total count of all the objects in an initial bin does not pass the count threshold, it will be grouped with an adjacent initial bin. Fig. 1 illustrates the resulting 27 stacked groups. Finally, we calculate the weighted averages of bolometric X-ray luminosity, optical richness, and WL mass for the stacked objects, using the signal-to-noise ratio of the weak lensing estimates (See Section 4.2) as weights. For each cluster, the optical richness is obtained from the sample construction process (refer to Oguri 2014; Oguri et al. 2018), while the weak-lensing (WL) mass is estimated using the method described in Section 4.2.

3.4. Stacking analysis of X-ray surface brightness

As mentioned in Sect. 2, approximately 80% of the sample has no X-ray counterpart in the eFEDS cluster catalog (Liu et al. 2022a). Based on the presence of X-ray counterparts in the eFEDS cluster catalog (see Section 2), we divide the present sample into X-ray-detected and undetected clusters to study the stacked brightness distributions. We further defined nine subgroups by dividing the richness and redshift into three ranges each: $15 \leq N < 25$, $25 \leq N < 40$, $40 \leq N < 60$, and $0.1 \leq z < 0.3$, $0.3 \leq z < 0.6$, $0.6 \leq z < 1.2$.

In order to average the X-ray surface brightness of objects at different distances, we defined the range of radii of the annuli in physical units and derived the X-ray counts in the 0.5–

[2] `https://erosita.mpe.mpg.de/edr/eROSITAObservations/Catalogues/`

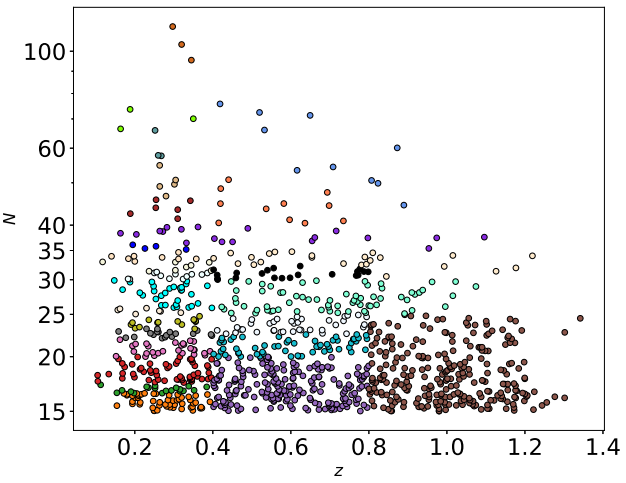

Fig. 1. Clusters are stacked following bins of similar redshift and richness. Each stacked group is indicated by a different color. See text for more details.

2 keV band for each annulus. The center of the annular regions was set to the cluster coordinates from the CAMIRA catalog. Next, we summed up the photon counts for each subsample defined above to derive the stacked surface-brightness profiles. The background was estimated from the surrounding area of the clusters in the same manner as Sect. 3.3 and subtracted, followed by exposure correction.

We then fitted the stacked brightness profiles of the subgroups to the following one-dimensional β-model (Cavaliere & Fusco-Femiano 1978),

$$I_{(r)} = I_0 \times \left(1 + \left(\frac{x}{r_c}\right)^2\right)^{-3\beta+0.5}, \quad (1)$$

where r_c and β represent the core radius and the slope parameter, respectively.

To account for the telescope response, the model is convolved with the instrumental point-spread function (PSF). We calculated the PSF for each subgroup by first applying the `ermldet` tool to each individual cluster and then averaging across the subgroup. Next, we produced one-dimensional (1D) profiles of the stacked PSFs. Finally, we estimated the analytical solution for the 1D PSF profiles by fitting them to a double Gaussian function. The model accurately reproduces the PSF profiles within a 10% deviation. Since the PSF model's emission rapidly declines beyond 40 arcsec, we limit the fitting range up to this radius to improve statistical accuracy. Although the eROSITA PSF wings extend beyond this range, their effect on our surface brightness analysis is negligible. Because of large uncertainties in some cases, the fit does not always converge. Hence, we fix the slope of the beta model at $\beta = 2/3$ in order to make a more straightforward comparison.

4. Optical data analysis

4.1. BCG identification

The CAMIRA cluster finding algorithm searches for clusters based on the overdensity of red sequence galaxies (Oguri 2014). In this method, for each galaxy, the likelihood of being a red sequence is calculated as a function of redshift. This is achieved by fitting the galaxy's spectral energy distribution to the stellar population synthesis of Bruzual & Charlot (2003). Once a cluster candidate is determined based on the constructed richness map, its redshift and richness are calculated. In the next step, its BCG is identified as the most massive, red sequence galaxy that is close to the cluster center. The algorithm begins by choosing an initial BCG candidate, and in each following iteration replaces the peak position with that of the candidate, estimates the cluster redshift, and calculates a new candidate based on these. Convergence is achieved when the BCG candidate position's change from one iteration to the next becomes negligible. This implementation provides a homogeneous red sequence BCG catalogue, however, blue BCGs and/or overly bright BCGs may not be classified via this algorithm, since the saturation in one of the filter bands may affect its red sequence likelihood (Oguri 2014; Oguri et al. 2018). Therefore, we employ an independent pipeline to reidentify the BCGs for our sample.

Similar to our previous work (Ota et al. 2023), we utilize the newest data releases from the current optical and infrared surveys, namely SDSS DR18 (York et al. 2000), Pan-STARRS DR1 (Kaiser et al. 2002, 2010), 2MASS (Skrutskie et al. 2006) and WISE (Wright et al. 2010) to search for the BCGs. The study of 43 high richness clusters (Ota et al. 2023) has shown that nearly half of brightest galaxies in the high richness sample exceeded the HSC's saturation level and therefore were not assigned as BCGs. These clusters then got updated BCGs from e.g., the SDSS survey because the saturation threshold of SDSS is higher than that of HSC at the same filter band. In this work, we update the redshift constraint of the BCG as following:

$$\frac{\Delta z}{1+z} = \frac{|z_{\rm cl} - z_{\rm BCG}|}{1+z_{\rm cl}} \leq 0.02, \quad (2)$$

where $z_{\rm cl}$ is the photometric redshifts of clusters (Oguri 2014), $z_{\rm BCG}$ is the redshifts of the BCG candidates. In our previous study of 43 high richness clusters (Ota et al. 2023), we limited the offset to $\Delta z/(1+z) \leq 0.01$ for galaxies with spectroscopic redshifts, as their small errors make this threshold appropriate for capturing galaxies within a velocity dispersion of 3000 km s^{-1} around the cluster redshift (e.g., Carlberg et al. 1996). Photometric redshifts, however, typically have larger uncertainties, requiring a broader offset constraint of 0.02. Since the cluster redshifts are photometric, in this work we uniformly applied the maximum redshift offset of 0.02 to all galaxies.

For 229 CAMIRA clusters, there is no available photometric data and/or redshift from the optical - NIR surveys used in our search. For these cases, we adopt the BCG position from the original CAMIRA catalog (see Sec. 2).

Finally, all newly identified BCGs are carefully inspected case by case. When multiple candidates are found at similar brightness, additional criteria such as having an elliptical appearance with wider extended envelopes and being selected as BCG in the optical wavebands are applied. Galaxies with photometric data being overestimated due to point source contamination and cosmic ray saturation are excluded. We then classify the BCG results with flags indicating different levels of quality. **Flag 1** is assigned to typical giant elliptical BCGs that outshine the rest of their host cluster. **Flag 2** indicates that the host cluster appears as a multi-peaked system, and the BCG is one of the brightest galaxies. This implies a likely, but less dominant BCG than Flag 1. **Flag 3** represents cases where the BCG result is hard to be evaluated by visual inspection. Possible reasons for this include inadequacy of input photometric and redshift information or a lack of clear evidence of the selected BCG being the most prominent galaxy of the clusters. **Flag 4** means that the BCG position

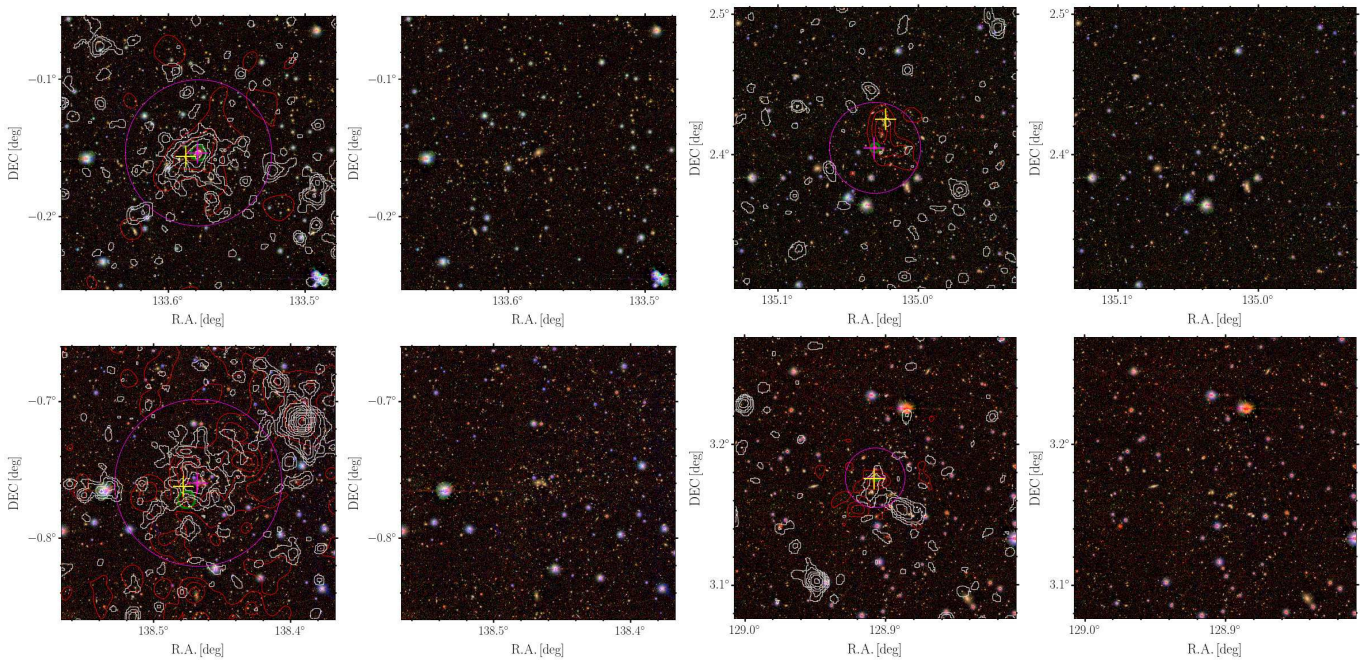

Fig. 2. Example pairs of BCG quality flags. *Top left*: Flag 1, *top right*: Flag 2, *bottom left*: Flag 3, *bottom right*: Flag 4. For each example, a pair of figures with (*left*) and without (*right*) contour maps and labels similar to Fig. 5 are plotted for better visual comparison.

is taken as the cluster center from the CAMIRA original catalog due to the lack of input data for our independent BCG search. In general, these BCG quality flags indicate the confidence of the BCG result solely based on visual impression, rather than on the morphology of the cluster. Fig. 2 illustrates the BCG quality flags. That is, flag 2 implies a cluster with several brightest galaxies at similar brightness, but does not necessarily mean that the cluster in question has multiple sub-structures. The impact of using the BCG positions found by the new method described in this section, rather than those from the original CAMIRA algorithm, will be discussed in section 5.1. Finally, we estimate that the fraction of BCGs that are identical in this work and in the original CAMIRA catalog (within 3 arcsec) to be about 70%. Fig. 3 shows the bimodal distribution of the angular offset between these two BCG results, where the left peak represents the confirmed CAMIRA BCGs and the right peak corresponds to the reidentifed BCGs.

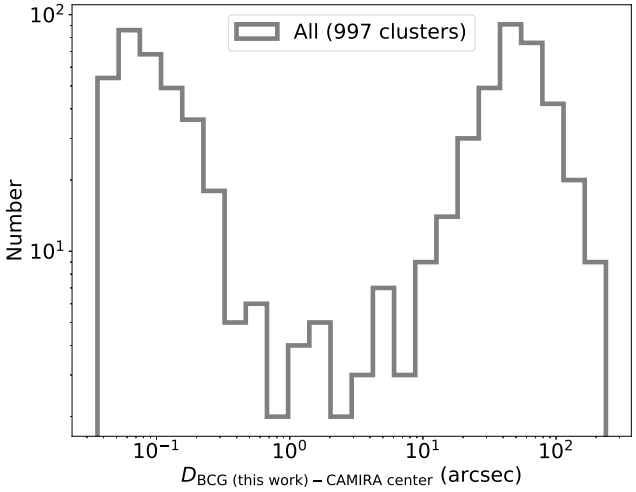

Fig. 3. Distribution of the angular separation between the BCG positions (this work) and the original CAMIRA cluster centers.

4.2. Weak-lensing mass measurement

We use the HSC-Y3 shape catalogue measured by a method of Point Spread Function (PSF) correction which is known as re-Gaussianization (Hirata & Seljak 2003; Mandelbaum et al. 2018; Li et al. 2022). To achieve both precise shape measurement and photometric redshift estimation, we use only galaxies satisfying the full-colour and full-depth condition (see Okabe et al. 2019 for details). The main systematics of cluster WL analysis is background selection (e.g., Okabe & Smith 2016). We follow Medezinski et al. (2018) to securely select background galaxies with the following condition

$$\int_{z_l+0.1} P(z)dz > 0.98, \tag{3}$$

where z_l is a cluster redshift and $P(z)$ is the probability of the photometric redshift (Tanaka et al. 2018; Nishizawa et al. 2020) from the machine learning method (MLZ; Carrasco Kind & Brunner 2014).

We compute the stacked profile of the reduced tangential shear $\langle\Delta\Sigma_+\rangle$ for a subsample of CAMIRA clusters, as follows,

$$\langle\Delta\Sigma_+(r_k)\rangle = \frac{1}{2\mathcal{R}_k(1+K_k)} \frac{\sum_i \sum_j e_{+,j} w_{ij} \langle\Sigma_{\rm cr}(z_{l,i}, z_{s,j})^{-1}\rangle^{-1}}{\sum_i \sum_j w_{ij}}, \tag{4}$$

where j-th galaxy in a given k-th radial bin centering the i-th cluster, e_+ is the tangential ellipticity ($e_+ = -(e_1 \cos 2\varphi + e_2 \sin 2\varphi)$, w_{ij} is the weighting function, $\langle\Sigma_{\rm cr}(z_{l,i}, z_{s,j})^{-1}\rangle$ is the inverse of the mean critical surface mass density, $\mathcal{R}$ is the shear responsivity, and K is the calibration factor. The weighting function is computed by

$$w_{ij} = \frac{1}{e^2_{\rm rms,j} + \sigma^2_{e,j}} \langle\Sigma_{\rm cr}(z_{l,i}, z_{s,j})^{-1}\rangle^2. \tag{5}$$

where $e_{\rm rms}$ and σ_e are the root mean square of intrinsic ellipticity and the measurement error per component (α = 1 or 2), respectively. Given the i-th cluster and the j-th background galaxy, the surface mass density is computed by

$$\Sigma_{\rm cr}(z_{l,i}, z_{s,j}) = \frac{c^2 D_A(z_{s,i})}{4\pi G D_A(z_{l,i}) D_A(z_{l,i}, z_{s,j})} \tag{6}$$

where D_A is the angular diameter distance. The inverse of the mean critical surface mass density is described by

$$\langle \Sigma_{\rm cr}(z_{l,i}, z_{s,j})^{-1} \rangle = \frac{\int_{z_{l,i}}^{\infty} \Sigma_{\rm cr}^{-1}(z_{l,i}, z_{s,j}) P(z_{s,j}) dz_{s,j}}{\int_0^{\infty} P(z_{s,j}) dz_{s,j}}. \tag{7}$$

where $P(z)$ is the probability function. The shear responsivity is expressed as

$$\mathcal{R} = 1 - \frac{\sum_i \sum_j e_{{\rm rms},j}^2 w_{ij}}{\sum_i \sum_j w_{ij}}, \tag{8}$$

The calibration factor, K, is computed by

$$K = \frac{\sum_i \sum_j m_j w_{ij}}{\sum_i \sum_j w_{ij}}. \tag{9}$$

where m is a multiplicative calibration bias to describe the relation between the input and output shear component, defined by STEP (Shear TEsting Programme) simulations (Heymans et al. 2006; Massey et al. 2007). Here, m is measured on individual galaxies (Li et al. 2022) using GREAT3-like simulations (Mandelbaum et al. 2017). Since the shape galaxies are not uniformly distributed but masked around bright stars, the weighted harmonic mean (Okabe & Smith 2016) is adapted as the representative radial position

$$r_k = \frac{\sum_i \sum_j w_j}{\sum_i \sum_j r_j^{-1} w_j}. \tag{10}$$

We compute $\langle \Delta\Sigma_+ \rangle$ in the range of $100-3000\, h_{70}^{-1}$kpc with $N_{\rm bin}$ = 6.

To measure the average masses, we adopt a spherical NFW profile (Navarro et al. 1996) specified by

$$\rho_{\rm NFW}(r) = \frac{\rho_s}{(r/r_s)(1 + r/r_s)^2}, \tag{11}$$

where r_s is the scale radius and ρ_s is the central density parameter. The two parameters can be converted to the spherical mass, M_Δ, and the halo concentration, $c_\Delta = r_\Delta / r_s$, where r_Δ is the radius inside which the average mass density is Δ times the critical mass density at the cluster redshift, $\rho_{\rm cr}(z)$. The spherical mass within r_Δ is defined by

$$M_\Delta = \frac{4}{3}\pi \Delta \rho_{\rm cr} r_\Delta^3. \tag{12}$$

We consider a mis-centering effect in the mass modeling.

$$\begin{aligned} f_{\rm model}(r) &= f_{\rm cen} f_{\rm NFW}(r) + (1 - f_{\rm cen}) \int_0^{\infty} P(r') f_{\rm NFW}^{\rm mis}(r, r') dr', \\ f_{\rm NFW}(r) &= \Delta\bar{\Sigma}_+(r)\,(1 + \mathcal{L}_z \Sigma(r))\,, \qquad (13) \\ P(r) &= \frac{r}{\sigma^2} \exp\left[-\frac{r^2}{2\sigma^2}\right]. \qquad (14) \end{aligned}$$

To maintain linearity, the reduced shear profile of the NFW model, $f_{\rm NFW}$, is expanded by the differential surface mass density and the local surface mass density Σ weighted with $\mathcal{L}_z = \sum_i \sum_j \langle \Sigma_{\rm cr}(z_{l,i}, z_{s,j})^{-1} \rangle w_{ij} / \sum_i \sum_j w_{ij}$. $\Delta\bar{\Sigma}_+$ and $\Sigma(r)$ are the differential surface mass density and the local surface mass density, respectively. $f_{\rm NFW}^{\rm mis}$ is the reduced tangential shear profile with mis-centering effect. The dimensional surface mass density is computed by

$$\Sigma^{\rm mis}(r, r') = \frac{1}{2\pi} \int_0^{2\pi} d\theta \Sigma(r^2 + r'^2 - 2rr' \cos\theta). \tag{15}$$

(Yang et al. 2006). We assume that lensing signals are composed of two components; the first term is the case where the CAMIRA center coincides with the true center with a probability $f_{\rm cen}$, and the second term is the case that the CAMIRA center is offset from the true center with a Gaussian distribution of which scale parameter (standard error) is specified by σ.

The log-likelihood is expressed as

$$\begin{aligned} -2 \ln \mathcal{L} &= \ln(\det(C_{nm})) + \\ &\sum_{n,m} (\Delta\Sigma_{+,n} - f_{\rm model}(r_n)) C_{nm}^{-1} (\Delta\Sigma_{+,m} - f_{\rm model}(r_m)), \end{aligned} \tag{16}$$

where the covariance matrix, C, is composed of the uncorrelated large-scale structure (LSS), $C_{\rm LSS}$, along the line-of-sight (Schneider et al. 1998), the shape noise C_g and the error of photometric redshift C_s. Here, $C_{\rm LSS}$ is proportional to the inverse of the number of clusters in the subsamples. We adopt the Markov chain Monte Carlo (MCMC). In the MCMC run, we introduce parameters of WL mass $M_{200}^{\rm WL}$, $f_{\rm mis}$, and σ where $|f_{\rm mis}| = 1 - f_{\rm cen}$ is a mis-centering probability. We assume the mass concentration relation of Bhattacharya et al. (2013) and that the mass and concentration for the central and offset components are common. Since the mis-centering probabilities in some clusters are very close to zero, we use an absolute value of $f_{\rm mis}$ to avoid the boundary of 0 in the modeling. We use a flat prior $\ln(0.05) < \ln M_{200} < \ln(50)$ and $-1 < f_{\rm mis} < 1$. Since the scale parameter cannot be constrained, we use a Gaussian prior 0.3475 ± 0.060 Mpc based on Okabe et al. (2025). They constrained a scale parameter between galaxy map peaks and NFW-determined centers by two-dimensional shear pattern, $0.3475^{+0.0282}_{-0.0304}$ Mpc. We use the 2 sigma uncertainty as the prior. We convert the resulting $M_{200}^{\rm WL}$ to $M_{500}^{\rm WL}$.

In the scaling relation analysis, we also compute the ensemble average of X-ray luminosity and cluster richness over the subsamples. To fairly compare with the WL masses, we introduce a lensing-related weight to compute these baryonic quantities, as follows

$$w_{{\rm lens},i} = \frac{\sum_j w_{ij}}{\sum_i \sum_j w_{ij}}. \tag{17}$$

5. Results

5.1. Dynamical status

We compute the positional offset between the BCG and the X-ray peak (see Sec. 3.2) to quantify the dynamical properties of the sample. Fig. 4 depicts the distribution of the BCG - X-ray peak offsets $D_{\rm XP}$ both in units of kpc and as a ratio of R_{500}. Our previous study of the high richness group of the CAMIRA clusters in the eFEDS field (Ota et al. 2023) showed that the median values of $D_{\rm XP}$ are 152 kpc and 0.14 R_{500}. Compared to these numbers, the median values of $D_{\rm XP}$ of our sample are larger,

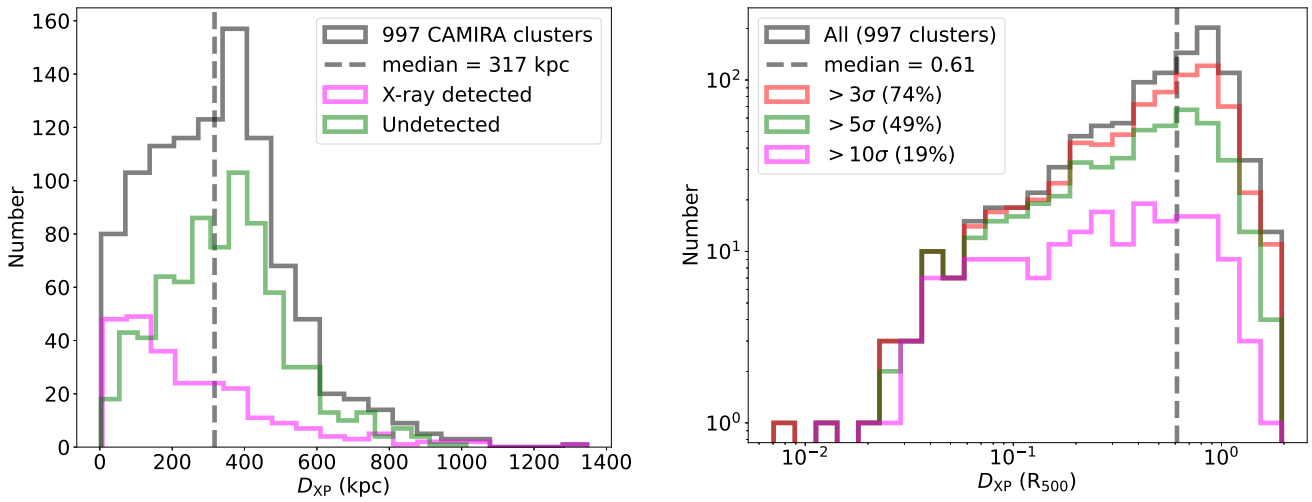

Fig. 4. Distribution of the BCG - X-ray peak offset in units of kpc (*left*) and of R_{500} (*right*). In each panel, the median value is indicated by the gray vertical line. BCG offset of sub-samples with respect to clusters with and without X-ray counterparts (left) and to different level of X-ray detection significance (right) are also plotted.

namely 317 kpc and 0.61 R_{500}. Similarly, our D_{XP} is significantly larger than the optical-to-X-ray center offset of $92.6^{+44.3}_{-35.1}$ kpc found by Seppi et al. (2023) for eFEDS clusters. However, it is important to note that their eFEDS sub-sample applied a richness cut at 20, higher than the threshold used in our sample. This higher richness cut reduces the X-ray center's positional uncertainty to less than 100 kpc. Therefore, the larger offset observed in our sample can be attributed to the higher uncertainties in measuring X-ray positions.

We applied the commonly used criteria of Sanderson et al. (2009) to classify each cluster's dynamical status based on the D_{XP} value. That is, clusters with $D_{XP} \leq 0.02R_{500}$ belong to the "relaxed" category and clusters with $D_{XP} > 0.02R_{500}$ belong to the "disturbed" category (Fig. 5). Only 2 out of 997 clusters are classified as relaxed using this definition. Due to the large uncertainty in the measurements, it is important to carefully estimate both statistical and systematic errors. We estimate statistical error through bootstrap resampling and calculate systematic error by applying smoothing scales of 2, 3, and 4 pixels. Finally, we consider the instrumental errors to estimate the upper limit of the relaxed fraction. As mentioned in Ota et al. (2023), the systematic error due to the instruments' positional error is not negligible. Here, we use the mean positional uncertainty of 4″.7 (Brunner et al. 2022) for eFEDS point sources as instrumental error. However, for extended sources, the positional uncertainty could be higher, therefore we add another source of error that stems from the smoothing routine itself. Since the D_{XP} value is reported with a smoothing scale of $\sigma = 3$ pixels, we adopt the full width at half maximum size as the corresponding uncertainty, which translates to 10″.6.

To evaluate the impact of the BCG choice on the resultant D_{XP}, we consider the D_{XP} for different BCG definitions: either taken from the original CAMIRA catalog (BCG with quality flag 4), or from the result in this work (BCG of flag 1-3), or combined from both BCG sets (whole sample). Table 2 summarizes the result of the relaxed fraction calculation. The fraction of relaxed clusters in the whole sample is $0.2 \pm 0.1^{+0.2}_{-0.0} < 13.6\%$. The first value indicates the relaxed fraction, the second and third values refer to the statistical and systematic uncertainties. The last number show the upper limit of the relaxed fraction due to instrument's pointing accuracy and the finite smoothing scale. Although the relaxed threshold of $0.02R_{500}$ is commonly used to identify a cluster's dynamical status, a different threshold of $0.05R_{500}$ is usually adopted for samples with a large X-ray centroid error (e.g., Lavoie et al. 2016). If this criterium is applied to our sample, the relaxed fraction becomes $2.2 \pm 0.5^{+0.4}_{-0.4} < 15.4\%$. The upper limits of the relaxed fraction in both cases do not differ much from each other, which indicates that the inclusion of the instrumental uncertainty was reasonable. At the same time, utilizing BCGs identified from different algorithms does not affect the final relaxed fraction of the whole sample. Therefore, we can safely say that the relaxed fraction is <14% based on the BCG offset. On the other hand, this limit slightly increases to 16% when only the Flag 1 and Flag 2 BCGs are considered. This demonstrates that the newly identified BCGs are sufficiently well selected.

Furthermore, we investigate the relaxed fraction for the X-ray detected and X-ray undetected sub-groups. The definition of this classification is described in Section 2. As can be seen in Table 2, the X-ray detected clusters have a higher relaxed fraction (<34%) compared to the X-ray undetected clusters (<9%) if all BCGs are used. The left panel of Fig. 4 shows that the X-ray detected clusters are distributed mostly near the small BCG offset end while the X-ray undetected clusters spread more towards larger offsets. The same tendency holds true if only one source of BCGs is considered. This again implies that clusters detected in X-ray observations are more likely to have regular morphology and relaxed dynamics. On the other hand, the low statistics may give rise to higher X-ray uncertainty for X-ray undetected clusters as shown in the right panel of Fig. 4. Here, we plot the distribution of D_{XP} for different levels of X-ray detection significance, which is simply defined by the ratio of the observed X-ray counts to its standard error (see Section 3.3). As a result, the group of clusters with at least 3σ significance contributes to most of the large BCG offset range, while the collection of clusters that are detected at more than 10σ significance has a higher probability to present smaller BCG offsets.

Although the BCG - X-ray peak offset results show large uncertainties, especially due to the X-ray peak measurement, it is still feasible to use D_{XP} to interpret the dynamical state of

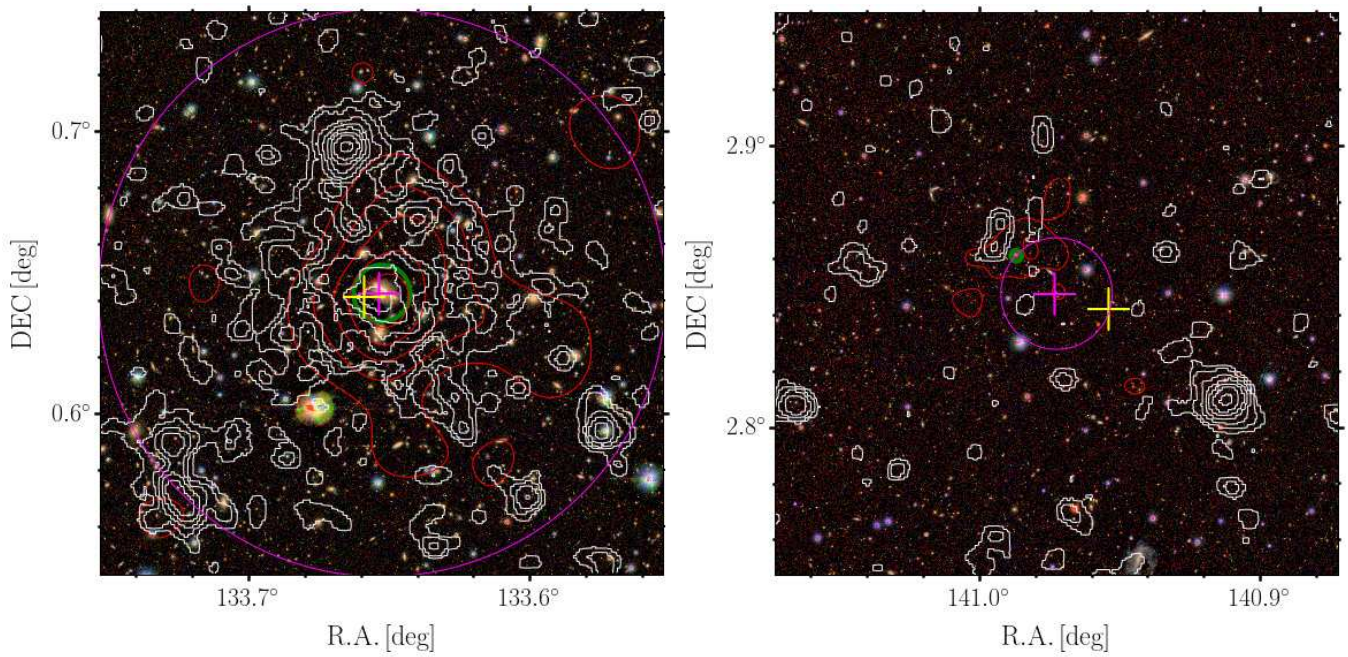

Fig. 5. Examples of relaxed (*left*) and disturbed (*right*) CAMIRA optical clusters in the eFEDS field. HSC *riz* composite images are centered on the original CAMIRA cluster position (pink cross). Galaxy density contours and X-ray maps are plotted in red and white, respectively. The X-ray peaks of the eFEDS image smoothed with a Gaussian of $\sigma = 3$ pixels are marked by the yellow cross, the BCG positions by the green circle. The magenta circles enclose the characteristic radius R_{500}.

clusters. Seppi et al. (2023) reported a correlation between the optical - X-ray center offset to other morphological indicators (e.g., photometry parameter APHOT and the offset parameter predicted by N-body simulation) using eFEDS clusters. When they applied the same relaxed threshold as in Ota et al. (2023) for the selection of 87 clusters in a well-controlled sub-sample of eFEDS, the resulting relaxed fraction is comparable to the value reported in Ota et al. (2023). On the one hand, this shows the consistency among different methods of measuring the dynamical states for different eFEDS sub-samples. On the other hand, these values imply that the eFEDS sub-samples do not exhibit preference for relaxed clusters, which was also concluded by previous works (Brunner et al. 2022; Ghirardini et al. 2022a).

5.2. Scaling relations

5.2.1. Self-similar models

Scaling relations are computed based on the assumption that gravitation is the only force that governs the formation and evolution of large scale structures. The bolometric X-ray luminosity - mass and the richness - mass relations are

$$L \propto M^{4/3} \tag{18}$$

and

$$N \propto M. \tag{19}$$

According to Hubble's law (Hubble 1929), the Universe is expanding, implying that the critical density was higher at earlier times. Consequently, scaling relations between cluster observables and mass must account for this change in density at different redshift. This redshift trend can be described by the cosmological factor based on the Hubble parameter $E(z) = H(z)/H_0 = [\Omega_M(1+z)^3 + \Omega_\Lambda]^{0.5}$. The scaling relations in this case are described as following

$$LE(z)^{-1} \propto [ME(z)]^{4/3} \tag{20}$$

and

$$NE(z) \propto ME(z). \tag{21}$$

In this section, we fit the scaling relations to a power-law model with various assumptions regarding the redshift dependence of the observables. We define the fitting function as following

$$\ln\left(\frac{\boldsymbol{y}}{\boldsymbol{y}_p}\right) = \boldsymbol{a} + (\boldsymbol{b} + \boldsymbol{d}\ln(ev))\ln\left(\frac{x}{x_p}\right) + \boldsymbol{c}\ln(ev), \tag{22}$$

where $x = M_{500}^{\rm true}E(z)$ and $\boldsymbol{y} = \{M_{500}^{\rm WL}E(z), LE(z)^{-1}, NE(z)\}$ with the true mass $M_{500}^{\rm true}$ and the WL mass $M_{500}^{\rm WL}$. The pivot parameters are $x_p = E(z_{\rm ref})10^{14}h_{70}^{-1}M_\odot$ and $\boldsymbol{y}_p = \{E(z_{\rm ref})10^{14}h_{70}^{-1}M_\odot, E(z_{\rm ref})^{-1}10^{42}\,{\rm ergs}^{-1}, E(z_{\rm ref})\}$, respectively. The vector regression parameters of $\boldsymbol{a}$, $\boldsymbol{b}$, $\boldsymbol{c}$ and $\boldsymbol{d}$ are the normalization, the power-law slope, the redshift dependent parameter in the normalization, and the redshift dependence parameter in the mass dependent parameter, respectively. The evolution term is defined as $ev = E(z)/(E(z_{\rm ref}))$. We calculate the pivot redshift for our sample by averaging the redshift with the WL weight, which yields $z_{\rm ref} = 0.35$. We consider two cases: (1) we fix $\boldsymbol{c} = 0$ and $\boldsymbol{d} = 0$, (2) we treat $\boldsymbol{c}$ and $\boldsymbol{d}$ as free parameters. When we do not include $E(z)$ in the observables of x and $\boldsymbol{y}$, we consistently remove $E(z_{\rm ref})$ from the pivot parameters. The log-normal intrinsic scatter of the luminosity and the richesss are assumed to be independent of the redshift because they cannot be constrained. We fix the WL mass calibration parameters obtained by Appendix A.

We employ the hierarchical Bayesian regression for clusters with selection (Akino et al. 2022, Okabe et al. 2025, see also

Table 2. Relaxed fraction of the X-ray detected groups, X-ray undetected groups and the whole sample. See text for more details.

	X-ray detected		X-ray undetected		All	
	Relaxed fraction	Total	Relaxed fraction	Total	Relaxed fraction	Total
BCG[a]	$0 \pm 0^{+0}_{-0} < 100\%$	3	$0 \pm 0^{+0}_{-0} < 11\%$	226	$0 \pm 0^{+0}_{-0} < 12\%$	229
BCG[b]	$0 \pm 0^{+2}_{-0} < 33\%$	168	$0 \pm 0^{+0}_{-0} < 9\%$	600	$0 \pm 0^{+0}_{-0} < 14\%$	768
All BCG	$0 \pm 0^{+2}_{-0} < 34\%$	171	$0 \pm 0^{+0}_{-0} < 9\%$	826	$0 \pm 0^{+0}_{-0} < 14\%$	997

[a] original CAMIRA center.
[b] this work.

Notes. For each relaxed fraction, the first value is the relaxed fraction derived from the relax threshold adapted from Sanderson et al. (2009) ($D_{\rm XP} < 0.02R_{500}$). The second error is the statistical uncertainty estimated by bootstrap resampling, the third error comes from the variation of the X-ray peak when smoothing the X-ray image with different Gaussian width σ at 2, 3 and 4 pixels. Finally, the last term indicates the upper limit of the relaxed fraction, which was calculated from the positional accuracy of the instruments.

Sereno 2016, Sereno et al. 2020). Since we applied a richness cut at $N > 15$ when compiling the sample, it is important to address this selection bias. This method can take into account both selection and dilution biases and compute the scaling relations with respect to the cluster's true mass. We found no significant redshift-dependent trend of the mass population, which is similar to the findings of Chiu et al. (2022). Using HSC data, they studied the relations of X-ray observables to mass and redshift of eFEDS galaxy groups and clusters. The best-fit results are summarized in Table 3 and illustrated in Fig. 6. Using the SIXTE simulator (Dauser et al. 2019), we performed simulated eFEDS observations of the same sample and analyzed them using the same method, thereby validating the reliability of the derived scaling relations.

First of all, based on the Akaike Information Criterion (AIC) and Bayesian Information Criterion (BIC), fixing the redshift evolution parameters to 0 in the $ME - NE - LE^{-1}$ scaling relation results in a better fit compared to the free redshift evolution (rows 1 - 4 of Table 3). This is consistent with the fact that when the correction term $E(z)$ is not included, the model with free redshift evolution is better (rows 5 - 8 of Table 3). However, since the errors of parameters $\boldsymbol{c}$ and $\boldsymbol{d}$ are large, other results agree with no redshift evolution in the $ME - NE - LE^{-1}$ scaling relation. Therefore, we will quote the values of the fixed evolution models of $LE(z)^{-1} - ME(z)$ and $NE(z) - ME(z)$ (hereafter $L - M$ and $N - M$ unless stated otherwise) as the best-fit scaling relations obtained from this work.

Secondly, we compare our results to our previous work. Ota et al. (2023) carried out the scaling relation analysis for individual CAMIRA clusters with richness $N > 40$ in the eFEDS field. They assumed a WL mass calibration at a single redshift of $z = 0.25$. Here, we introduced a redshift-dependent WL mass calibration and repeated the analysis. The resulting scaling relations with the true masses at $z = 0.35$ are shown in Figure 7. The richness for a given mass for this work is higher than that for Ota et al. (2023). The orange line is the result from the the first eROSITA All Sky Survey (eRASS1; Bulbul et al. 2024, Merloni et al. 2024, Okabe et al. 2025) X-ray-selected clusters using the CAMIRA richness (Okabe et al. 2025). The two baselines agree well with each other. The baseline for this work is consistent with those for the previous studies within errors. Our WL mass estimates incorporated a probability function to describe the mis-centering effect into the modelling. Okabe et al. (2019) did not assume mis-centering effect in the stacked WL analysis and estimated based on single NFW model. We also computed the WL mass assuming no mis-centering effect, and found that the resulting baseline agrees with that of Okabe et al. (2019). We also note that $\sim 94\%$ and $\sim 75\%$ of clusters at $z < 0.4$ and $0.2 < z < 0.4$ have non-zero fractions of the mis-center component, and their averages, $\langle f_{\rm mis} \rangle = 0.58 \pm 0.04$ and 0.30 ± 0.08, are high, respectively. Therefore, the mis-centering effect is important in the stacked WL analysis for the optically-selected clusters. As for the $L - M$ relation, the normalization of the luminosity is slightly higher than that of Ota et al. (2023), in which correction for mis-centering effect was not included. From the analogy from the $N - M$ relation, the shift is partially caused by lower values in our mass but not all offsets can be explained by that. Figure 8 shows a tight correlation between stacked richness and luminosity. The two baselines at $N \gtrsim 40$ overlapped with each other, while the baseline (Ota et al. 2023) at $N < 40$ is higher than our result though they agree within 1σ uncertainty. The same overlapping is also shown in the $L - M$ relation at true mass $M^{\rm true}_{500} \gtrsim 2 - 3 \times 10^{14} h_{70}^{-1} M_\odot$, which corresponds to richness at around $N \gtrsim 40 - 50$. A detailed comparison of our findings with relevant literature is provided in Section 6.2.1.

5.2.2. X-ray detected and undetected sub-groups

Clusters with and without X-ray counterparts may exhibit distinct behaviors in the $L - M$ relation, reflecting differences in underlying physical processes and selection effects. In this section, we investigate the $L - M$ and $N - M$ scaling relations of CAMIRA clusters with respect to their X-ray detectability in the eFEDS field.

We divide our sample into two categories: X-ray detected and X-ray undetected, corresponding to having and not having X-ray counterpart in the eFEDS cluster catalog (Liu et al. 2022b). As mentioned in Section 2, less than 20% of the optical sample have X-ray counterparts in the eFEDS catalog. Following the procedure described in section 3.3, we then group the clusters at similar redshift and richness into bins such that the total counts of each bin are approximately 500. Next, we compute the average bolometric X-ray luminosity, richness and mass for each stacked bin, weighted by the WL mass calibration. Finally, we fit the $L - M$ and $N - M$ relations simultaneously to powerlaw models using the 2D HiBRECS code. Table 4 shows the best-fit parameters for the scaling relations of X-ray detected and undetected stacked clusters.

As can be seen from Table 4 and Fig. 9, although the normalizations agree within errors, the slope of the X-ray detected group ($b = 1.92^{+0.32}_{-0.25}$) is higher than that of the X-ray undetected group ($b = 1.35^{+0.30}_{-0.20}$), at a $\sim 1.5\sigma$ significance level. At the same time, the $L - M$ relations of both groups are consistent with the best-fit relations of the entire sample (see Section 5.2.1). As for the $N - M$ relations, there is no significant deviation between

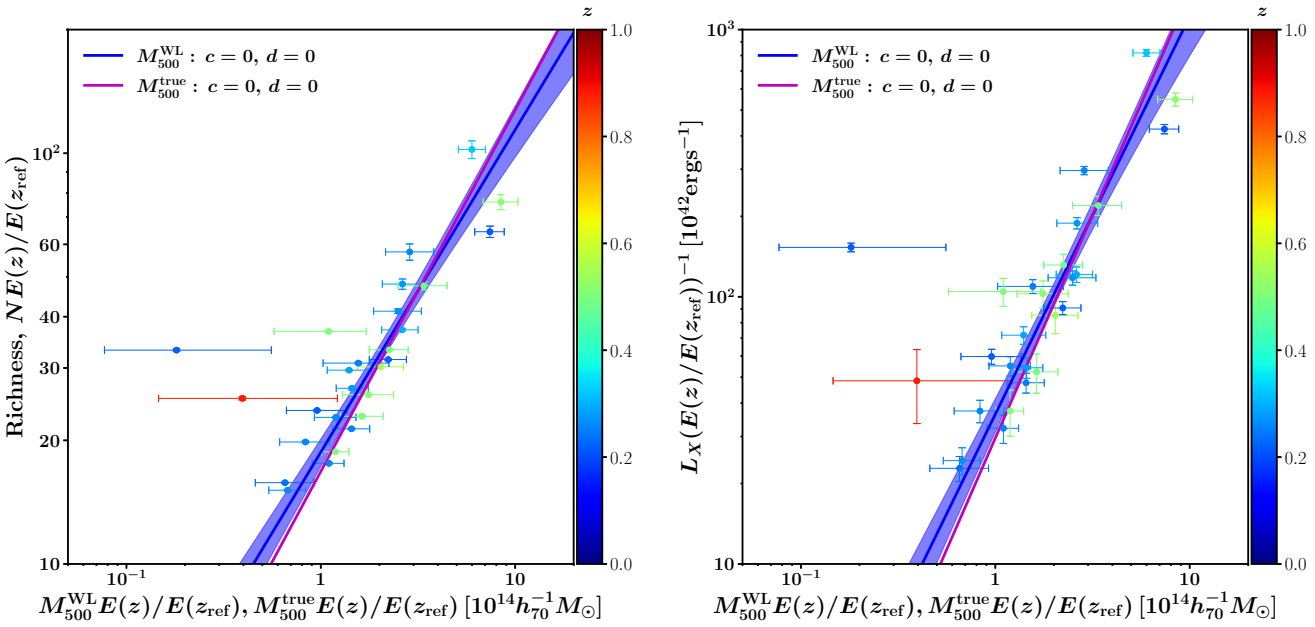

Fig. 6. Scaling relations of the CAMIRA optically selected clusters. Each circle represents a stacked bin described in Section 3.3. Each color is the weighted average redshift of the stacked bin. The best-fit power-law models from the simultaneous fit are plotted. The blue and magenta solid lines are the best-fit scaling relation with respect to the WL masses and the true masses. The blue region is the 1σ uncertainty of the scaling relation with the WL masses.

Table 3. Best-fit parameters for scaling relations of the CAMIRA clusters

Relation	a	b	c	d	σ	ΔAIC	ΔBIC
$LE(z)^{-1} - ME(z)$	$3.39^{+0.15}_{-0.18}$	$1.67^{+0.18}_{-0.15}$	0	0	$< +0.13$	0	0
$NE(z) - ME(z)$	$2.825^{+0.077}_{-0.094}$	$0.878^{+0.099}_{-0.079}$	0	0	$0.076^{+0.020}_{-0.028}$		
$LE(z)^{-1} - ME(z)$	$3.30^{+0.16}_{-0.20}$	$1.77^{+0.21}_{-0.17}$	$-3.46^{+2.78}_{-3.06}$	$3.01^{+3.28}_{-3.13}$	< 0.15	+7.6	+15.6
$NE(z) - ME(z)$	$2.767^{+0.088}_{-0.108}$	$0.942^{+0.115}_{-0.090}$	$-2.08^{+1.51}_{-1.68}$	$1.81^{+1.82}_{-1.72}$	$0.074^{+0.023}_{-0.040}$		
$L - M$	$3.52^{+0.14}_{-0.17}$	$1.50^{+0.17}_{-0.14}$	0	0	< 0.20	+20.2	+12.2
$N - M$	$2.892^{+0.076}_{-0.093}$	$0.794^{+0.093}_{-0.076}$	0	0	$0.134^{+0.032}_{-0.039}$		
$L - M$	$3.47^{+0.15}_{-0.18}$	$1.56^{+0.17}_{-0.14}$	$-0.70^{+2.35}_{-2.79}$	$2.92^{+2.98}_{-2.60}$	< 0.14	0	0
$N - M$	$2.861^{+0.076}_{-0.096}$	$0.828^{+0.098}_{-0.074}$	$-2.06^{+1.25}_{-1.56}$	$1.67^{+1.73}_{-1.42}$	$0.080^{+0.021}_{-0.032}$		
$NE(z) - LE(z)^{-1}$	$1.04^{+0.10}_{-0.12}$	$0.525^{+0.024}_{-0.022}$	0	0	$0.084^{+0.018}_{-0.014}$	0	0
$NE(z) - LE(z)^{-1}$	$1.02^{+0.11}_{-0.13}$	$0.529^{+0.026}_{-0.023}$	$-0.29^{+1.69}_{-1.89}$	$0.05^{+0.39}_{-0.37}$	$0.087^{+0.020}_{-0.015}$	+4.5	+8.5

Notes. L and M are in units of 10^{42} erg s^{-1} and $10^{14}M_\odot$, respectively. The best-fit values of intercept a, slope b, evolution term c in Eq. 22, and the upper limit of the intrinsic scatter σ are shown.

the two considered groups. Both of the sub-groups show similar result to what is reported in 5.2.1.

5.3. Surface brightness profiles

We fit the surface brightness profiles of the stacked X-ray-detected and undetected clusters to a PSF convolved beta model (Eq. 1), with the slope β being fixed to the empirical value of 2/3 (e.g., Ota & Mitsuda 2004). The fit is performed using the python fitting package *lmfit*, employing the least squares minimization method and chi square statistics. The best-fit results are summarized in Table 5. From Fig. 10, it is evident that the central brightness of the stacked X-ray detected clusters is often higher than that of the X-ray undetected counterpart in the same comparison bin. Furthermore, the X-ray radial profiles of the X-ray undetected groups tend to decrease more gradually compared to the X-ray detected ones. In fact, the best-fit parameters show that in 8 out of 9 cases the X-ray detected profiles have higher central brightness values I_0 and smaller core radius r_c, with the exception being the low redshift $0.1 < z < 0.3$, high richness $40 < N < 60$ bin. For this bin, the best-fit beta model of the X-ray undetected clusters implies a higher central brightness and smaller core radius. This is interesting, because if the cluster indeed exhibits a surface brightness of $9.80 \pm 1.09 \times 10^{41}$erg s^{-1} kpc^2 at the center, it is possible for the eFEDS survey to detect it. In contrast to other categories, this category only contains a single

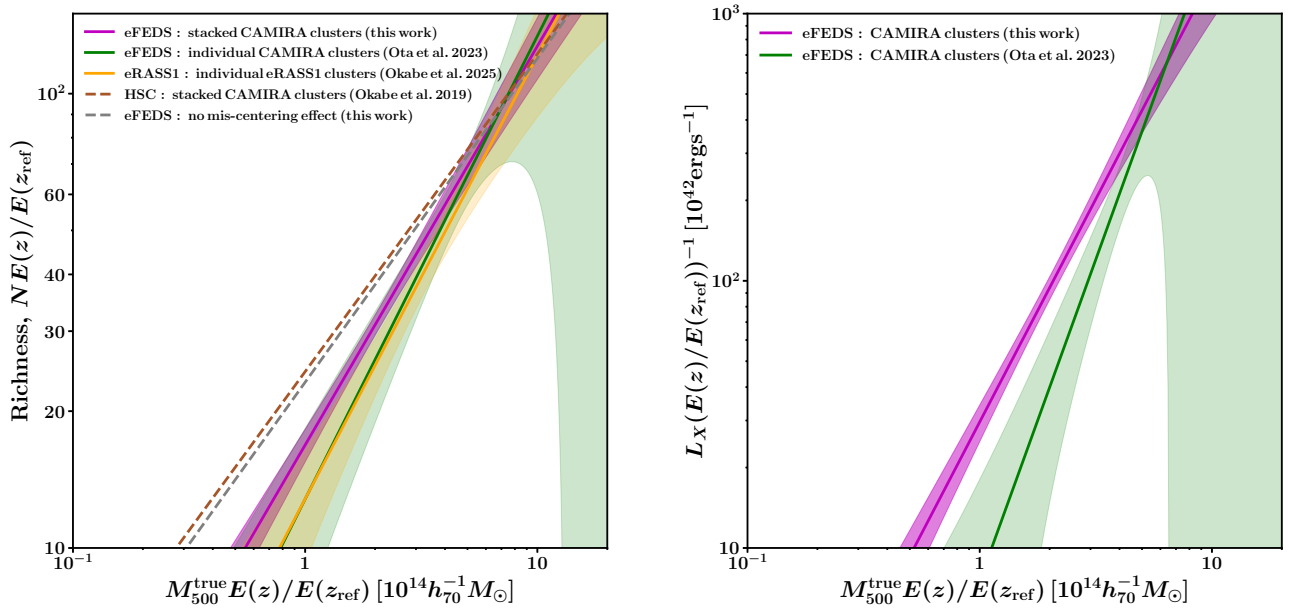

Fig. 7. Scaling relations with the richness (left) and the luminosity (right) with respect to true masses. The magenta solid lines and regions denote the best-fit line and its uncertainty, respectively. The green solid lines and regions are the result from the individual CAMIRA clusters with $N > 40$ (Ota et al. 2023). The orange solid line and region are the result from the eRASS1 clusters (Okabe et al. 2025). The brown and gray dashed lines are the stacked WL result (Okabe et al. 2019) and this work assuming no mis-centering effect. We set $z = 0.35$ for all the baselines.

Table 4. Best-fit scaling relations for X-ray detected and undetected sub-groups obtained from the 2D HIBRECS fitting code.

Sub-group	Relation	a	b	σ
X-ray detected	$LE(z)^{-1} - ME(z)$	$3.19^{+0.26}_{-0.34}$	$1.92^{+0.32}_{-0.25}$	< 0.19
	$NE(z) - ME(z)$	$2.59^{+0.15}_{-0.21}$	$1.07^{+0.20}_{-0.15}$	$0.127^{+0.038}_{-0.049}$
X-ray undetected	$LE(z)^{-1} - ME(z)$	$3.36^{+0.13}_{-0.18}$	$1.35^{+0.30}_{-0.20}$	< 0.11
	$NE(z) - ME(z)$	$2.849^{+0.078}_{-0.109}$	$0.82^{+0.19}_{-0.12}$	< 0.087

Notes. L and M are in units of 10^{42} erg s^{-1} and $10^{14}h_{70}^{-1}M_\odot$, respectively. The best-fit values of intercept a, slope b, and the intrinsic scatter in ln-space σ are shown.

cluster undetected in eFEDS, namely HSC J091352-004535. A point-like contamination near the cluster center likely reduces its detection likelihood, reflected in its surface brightness profile's lack of small-radius data points. A search in the additional catalog of eFEDS galaxy clusters and groups in the eFEDS point source catalog that is under the extent likelihood limit of the extent selected sample (Bulbul et al. 2022b) returns no matching X-ray counterpart.

Furthermore, the above discrepancy could also be explained by the PSF size being much larger than the cluster size. However, for a cluster in such low redshift range, the PSF size (30″, Brunner et al. 2022) is relatively small compared to the emission profile, which indicates that eROSITA observation is sufficient in this case. Finally, it is important to discuss the miscentering effect when studying CAMIRA clusters using multi-wavelength missions. Nevertheless, when inspecting the optical image, galaxy density map and X-ray image of HSC J091352-004535, we found that this cluster center is well constrained. Therefore, we believe that HSC J091352-004535 is a real cluster, which exhibits extended X-ray emission up to 1 Mpc. The main reason why it has not yet been detected in the eFEDS catalog is probably the oversubtraction of the central contamination. In conclusion, with this exception in the low redshift - high richness category, the previously mentioned trends remain valid. That is, CAMIRA clusters with X-ray counterparts follow a brighter and more centrally peaked profile, while the profile of the X-ray undetected clusters is dimmer and flatter.

6. Discussion

6.1. Dynamical status

Our previous study showed that, based on the BCG - X-ray center offset, the relaxed fraction of 43 high richness CAMIRA clusters ($N > 40$) is small, only 2(<16)% (Ota et al. 2023). This result agrees within errors with the relaxed fraction of 17 CAMIRA clusters with $N > 20$ found by using *XMM-Newton* data (Ota et al. 2020), which yields $29 \pm 11(\pm 13)$%. In this work, we extended the calculation to 997 CAMIRA clusters with $N > 15$ using eFEDS data and found that the relaxed fraction is 0(<14%). This value is again in the same ballpark as the two studies mentioned above.

To put this into context, the relaxed fraction measured in this work for the optical CAMIRA sample is significantly lower than

Table 5. Summary of the best-fit single beta model convolved with the eROSITA PSF of the surface brightness of CAMIRA clusters with and without X-ray detection in the eFEDS field.

Subgroup	Richness	Redshift	I_0	r_c	χ^2/d.o.f
X-ray detected	$15 \leq N < 25$	$0.1 \leq z < 0.3$	6.51 ± 0.81	85.99 ± 7.47	51/6
		$0.3 \leq z < 0.6$	25.16 ± 1.97	60.83 ± 3.28	33/7
		$0.6 \leq z < 1.2$	61.36 ± 12.48	74.45 ± 11.26	31/8
	$25 \leq N < 40$	$0.1 \leq z < 0.3$	5.55 ± 0.17	124.36 ± 2.86	6/6
		$0.3 \leq z < 0.6$	27.42 ± 2.55	74.30 ± 4.78	82/8
		$0.6 \leq z < 1.2$	64.22 ± 11.28	58.78 ± 7.67	38/7
	$40 \leq N < 60$	$0.1 \leq z < 0.3$	5.88 ± 0.43	315.98 ± 20.10	31/7
		$0.3 \leq z < 0.6$	16.18 ± 1.42	136.58 ± 9.11	17/8
		$0.6 \leq z < 1.2$	281.96 ± 33.03	43.16 ± 3.48	41/9
Undetected	$15 \leq N < 25$	$0.1 \leq z < 0.3$	0.29 ± 0.11	162.53 ± 61.28	31/5
		$0.3 \leq z < 0.6$	2.74 ± 0.32	124.33 ± 12.58	36/7
		$0.6 \leq z < 1.2$	5.90 ± 0.83	93.32 ± 11.00	25/8
	$25 \leq N < 40$	$0.1 \leq z < 0.3$	0.39 ± 0.088	638.05 ± 401.97	6/4
		$0.3 \leq z < 0.6$	7.84 ± 0.94	89.98 ± 8.00	22/7
		$0.6 \leq z < 1.2$	11.53 ± 1.35	147.74 ± 13.25	12/7
	$40 \leq N < 60$	$0.1 \leq z < 0.3$	9.80 ± 1.09	223.21 ± 13.92	2/3
		$0.3 \leq z < 0.6$	4.93 ± 1.09	234.59 ± 49.67	14/8
		$0.6 \leq z < 1.2$	18.67 ± 6.67	247.62 ± 79.03	60/9

Notes. Central brightness I_0 and core radius r_c are in units of 10^{41}erg s^{-1} kpc^2 and kpc, respectively.

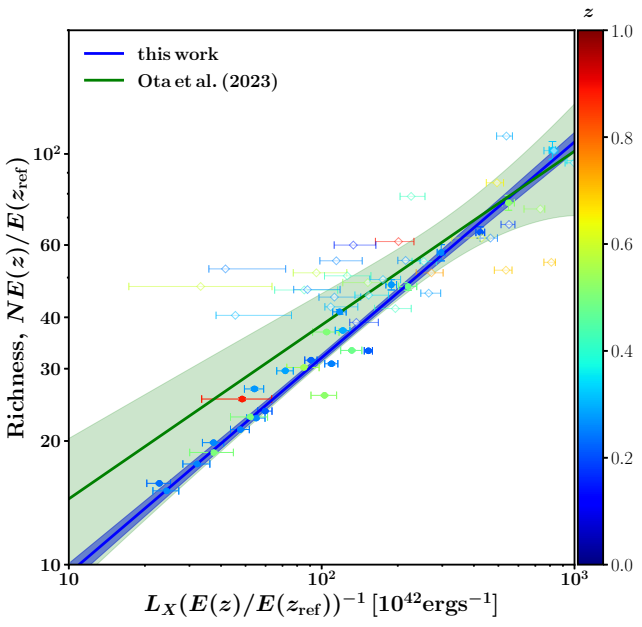

Fig. 8. The richness and scaling relation. The circles and its colors represent stacked quantities and its redshift respectively. The open diamonds are from Ota et al. (2023). The blue and green lines represent the results from this study and Ota et al. (2023), respectively.

that reported for other X-ray constructed samples. Migkas et al. (2021) investigated the X-ray flux limited eeHIFLLUGCS sample compiled from ROSAT data with *XMM-Newton* and *Chandra* follow-ups. They found that around 44% of clusters are relaxed, using the same criteria as in this work ($D_{\rm XP} < 0.02R_{500}$). Rossetti et al. (2016) investigated three X-ray-selected samples (HIFLUGCS, MACS and REXCESS) and concluded that the relaxed fraction is around 74%. This could be explained by the cool-core bias of X-ray observations, which typically results in a higher relaxed fraction. In contrast, optically selected cluster samples are immune to this observational bias, therefore they cover a wider range of morphologies.

At the same time, in the study of the morphology of eFEDS clusters, Ghirardini et al. (2022b) pointed out that the relaxed fraction of the eFEDS clusters at low redshift is about 50%, whilst the ratio at higher redshift $z > 0.2$ is approximately 30-35%. First of all, the study emphasized that, unlike the ROSAT-based samples, the eFEDS cluster catalog has a high completeness and is not biased toward cool-core clusters. This explains the relaxed fraction of the eFEDS sample being lower than that of the other X-ray samples. Secondly, although the method used in Ghirardini et al. (2022b) involved a combination of X-ray concentration and X-ray centroid shift instead of employing the BCG-X-ray peak offset as shown in Section 5.1, the two relaxed fractions are similar for clusters at high redshift $z > 0.2$. Therefore, although the overall relaxed fraction of the sample is low, the fraction for X-ray-detected groups aligns closely with findings from eFEDS cluster studies. This consistency further suggests that X-ray-detected clusters tend to be more relaxed, while X-ray-undetected clusters are generally more disturbed.

Furthermore, Ramos-Ceja et al. (2022) conducted a study on the shear-selected clusters taken from the CAMIRA HSC-SSP S19A catalog that shared sky area with the eFEDS sample. They concluded that the morphology of shear selected clusters is similar to that of the eFEDS sample. The authors also stated that 43% (9/21) of the shear selected clusters lie above the supercluster's detection level, while the ratio for the eFEDS sample is $\sim$ 18%. The high fraction of superclusters in the shear selected sample may lead to the comparable morphological properties between the two samples. In contrast, the percentage of low-mass, X-ray undetected clusters in our CAMIRA sample with N > 15 in the eFEDS field is relatively high, at $\sim$ 80 %, therefore the difference in the dynamical status between our optical sample and the X-ray eFEDS catalog is not surprising.

Our results indicate that the relaxed fraction in optical samples is lower than in X-ray-selected samples. This trend re-

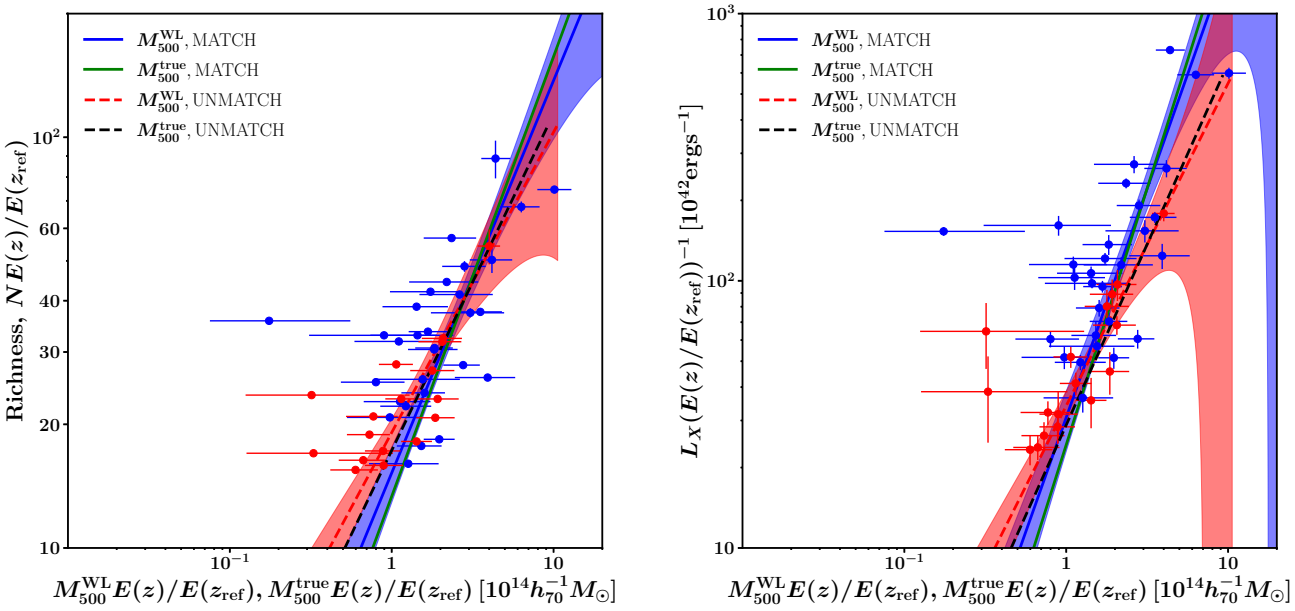

Fig. 9. Scaling relations of the CAMIRA optically selected clusters. Each circle corresponds to a stacked bin, constructed to ensure a total X-ray count of approximately 500. Stacked bins of clusters with X-ray counterparts in eFEDS are shown in blue (MATCH), those without in red (UNMATCH). The best-fit power-law models from the simultaneous fit are plotted. The blue and green solid lines are the best-fit scaling relation with respect to the WL masses and the true masses for the X-ray detected stacked clusters. Similarly, the red and black dashed lines are the best-fit scaling relation for the X-ray undetected stacked clusters. The blue and red regions are the 1σ uncertainty of the scaling relations with the WL masses for the X-ray detected stacked clusters and X-ray undetected clusters, respectively.

flects the cool-core bias inherent to X-ray-based cluster selection and highlights the importance of multiwavelength approaches in cluster studies. The redshift range of the sample may also influence the observed relaxed fraction. According to the hierarchical structure formation model, mergers occur more frequently at earlier epochs, leading to a higher relaxed fraction at lower redshifts. Future work using eRASS:5 data and the latest CAMIRA catalog will enable us to investigate the redshift evolution of cluster morphology in greater detail. Additionally, incorporating other independent morphological diagnostics (e.g., symmetry tests, West et al. 1988; Okabe et al. 2010) and cluster simulations will provide a more comprehensive understanding and help solidify these conclusions.

6.2. Scaling relations

6.2.1. Self-similar models

In this section, we will discuss the results obtained in Sect. 5.2.1 by placing them into context with previous studies.

First, the intrinsic scatters of the two relations, which range from 0.07 to 0.20 (see Table 3), agree well with other studies. The study of the evolution of cluster scaling relations using FABLE simulations by Henden et al. (2019) found that the intrinsic scatter of the bolometric X-ray luminosity and total mass is $0.25^{+0.04}_{-0.03}$ at $z = 0$ and decreases at higher redshift, e.g., 0.11 at $z = 1.0$. Similarly, Truong et al. (2018) conducted an analysis of cosmological hydrodynamical simulations of galaxy clusters using the GADGET-3 code to study the scaling relations between X-ray observables and cluster mass. The authors found an intrinsic scatter around 0.2 at $z = 0$ which decreases to 0.1-0.15 at $z = 2.0$. The scatter of the $N - M$ relation is similar to what we found for the high richness group (Ota et al. 2023). Nevertheless, the intrinsic scatter of the $L - M$ relation in this paper is smaller than the value 0.65 in our previous study. The stacking analysis in this work results in a tighter correlation between X-ray luminosity and cluster mass.

Next, we compare the best-fit power-law obtained in this work with those reported in other studies. Overall, our $L - M$ relation has a best-fit power-law slope of $1.67^{+0.18}_{-0.15}$ with the redshift evolution fixed at self-similar, i.e., $L \propto M^{4/3}E(z)^{7/3}$.When allowed to vary, there is virtually no reported trend in redshift. The $N - M$ slope is $0.878^{+0.099}_{-0.079}$ for a fixed self-similar redshift trend. When it varies, the best-fit indicates a negative redshift trend of $-2.08^{+1.51}_{-1.68}$ compared to self-similarity.

Comparison to other X-ray samples:

- Pratt et al. (2009) investigated the relations between the bolometric X-ray luminosity and other cluster properties using a local sample of clusters. 33 clusters observed by the REXCESS (Representative XMM-Newton Cluster Structure Survey), with redshift ranges up to $z = 0.18$, were examined. The authors found that the $L - M$ relation follows a power-law with the slope $b = 1.90 \pm 0.11$ and scatter $\sigma = 0.38 \pm 0.06$. The authors also used the same cosmological parameters as in this work, therefore it is plausible to directly compare our result to theirs. The best-fit power-law of the $L - M$ relation without redshift evolution in our work (Table 3, row 5-6) has a shallower slope and smaller scatter. The shallower slope aligns with the commonly observed trend where $L - M$ relations in X-ray samples tend to be steeper than predictions from self-similar models. The smaller scatter can likely be attributed to the stacking analysis of nearly 1000 clusters of our sample.
- Akino et al. (2022) studied the scaling relations between various cluster quantities and the true mass ob-

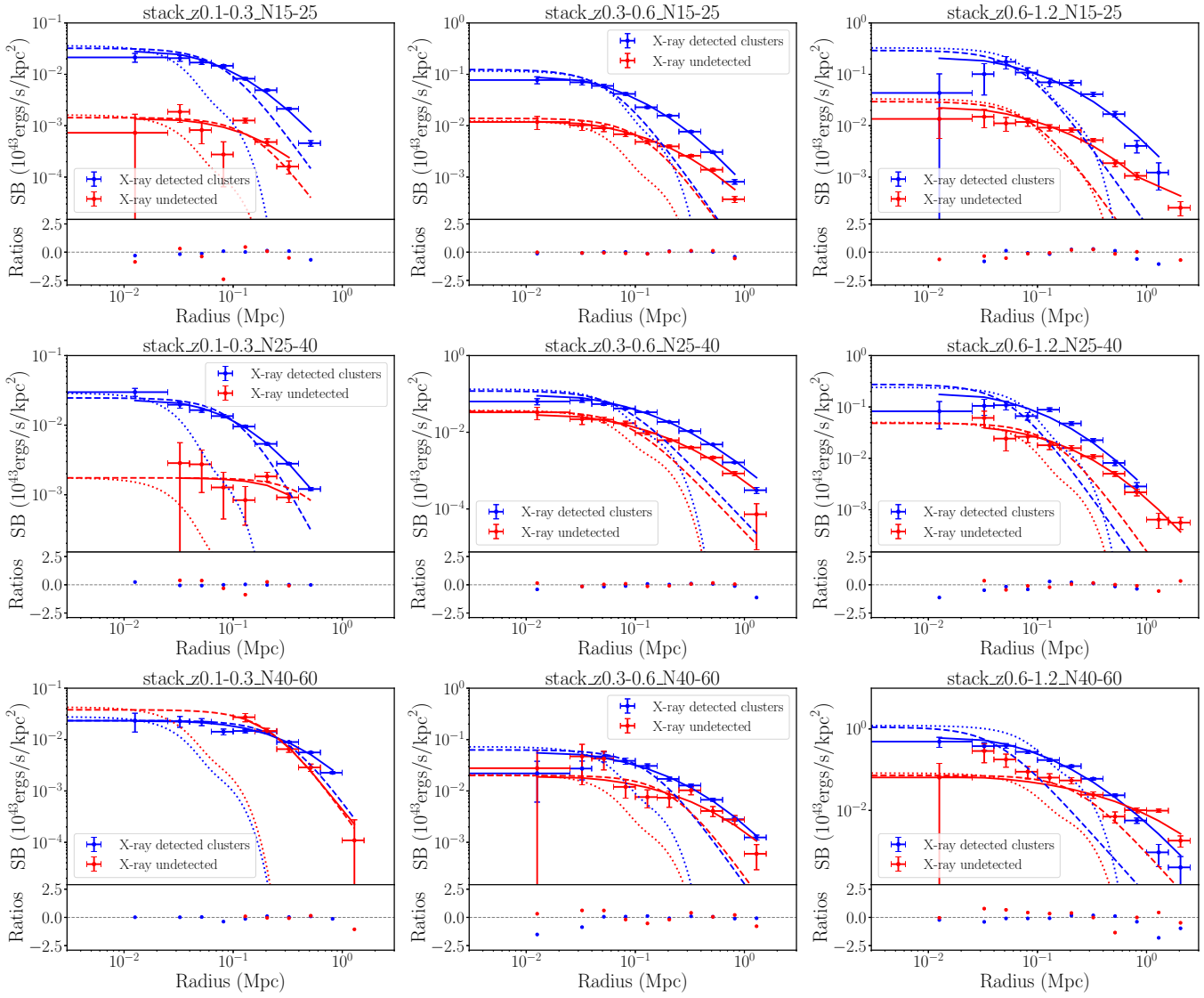

Fig. 10. Radial surface brightness of stacked CAMIRA clusters with and without corresponding X-ray detection are plotted in blue and red circles, respectively. The richness constraint for these groups are: $15 \leq N < 25$ (upper panels), $25 \leq N < 40$ (center panels) and $40 \leq N < 60$ (lower panels). The left panels consist of the $0.1 \leq z < 0.3$ groups, the middle panels show the $0.3 \leq z < 0.6$ groups and the right panels indicate the $0.6 \leq z < 1.2$ groups. The best-fit convolved beta models are depicted in blue and red solid lines. The underlying PSF and beta component are shown in dotted and dashed lines, respectively.

tained from WL calibration for 136 XXL clusters. They found that the slope of the soft-band (0.5-2.0 keV) X-ray luminosity-mass relation is 2.1σ level steeper than predicted by the self-similar model. This result is consistent with previous investigations on the scaling relations of $\sim$ 300 clusters in the XXL survey (Sereno et al. 2020). Similarly, our study of the bolometric luminosity and mass $L-M$ relation shows a steeper slope, at 3.35σ from the self-similar expectation. Direct comparisons between their results and ours are challenging, as their analysis is based on soft-band X-ray luminosity, while our study uses bolometric luminosity. However, both approaches provide meaningful comparisons to the self-similar prediction.

– In addition, a study on the richness-mass relation of 25 ROSAT-based clusters in the redshift range of $0.35 < z < 0.65$ also reported a $N-M$ slope of $0.49^{+0.20}_{-0.15}$ with a scatter of $0.17^{+0.13}_{-0.09}$ (Kiiveri et al. 2021). The authors utilized the redMaPPer method on the Canada-France-Hawaii Telescope (CFHT) data to estimate the optical richness for the selected sample. The richness-mass relation was then fitted to a power-law by a Bayesian approach, considering the selection effect. These values are in good agreement with 1.5σ deviation from our best-fit power-law for the $N-M$ relation.

– The *Chandra* cluster cosmology project (Vikhlinin et al. 2009) makes use of high quality *Chandra* observations of the *ROSAT*-derived samples within the redshift range $0.35 < z < 0.9$ to draw constraints on the cosmological parameters. In contrast to our result, the authors found the redshift trend of the $L-M$ relation to be consistent with the self-similar model. The best-fit relation of the soft band (0.5-2.0 keV) X-ray luminosity and cluster mass is $L \propto M^{1.61\pm0.14}E(z)^{1.85\pm0.42}$, where the cluster mass is derived from the hot gas mass proxy. On the other hand, no redshift evolution is observed for the $L-M$ re-

lation of more than 100 *Chandra*-based X-ray clusters (Maughan 2007).

Comparison to another study of the eFEDS sample:
Chiu et al. (2022) calculated weak-lensing mass calibration and examined the relations of X-ray observables and cluster mass for the eFEDS sample. The authors considered the selection effect and the redshift evolution while establishing the scaling relations. The slope for the bolometric luminosity and mass relation is 1.59 ± 0.14, which is consistent with our result within the error bars. The intrinsic scatter of $0.102^{+0.143}_{-0.043}$ also agrees with ours.

Comparison to another optical sample:
Rozo & Rykoff (2014) conducted a study to evaluate the selection of the optical cluster sample compiled from the Sloan Digital Sky Survey (SDSS) DR8 redMaPPer data. The authors compared the optical catalog to the X-ray and the Sunyaev-Zeldovich (SZ) catalogs in the literature. They found a good correlation between the optical richness to X-ray temperature and gas mass. The slope of the richness and gas mass relation is 0.72 ± 0.12, which agrees well with our reported value.

Comparison to other studies of the HSC-based sample:

- Oguri (2014) computed the mass-richness relation for the CAMIRA clusters and concluded on a slope of $M \propto N^{1.44\pm0.27}$. Similarly, Chiu et al. (2020) also found a slope of 0.92 ± 0.13 for the $N-M$ relation from 3029 CAMIRA clusters and a comparable intrinsic scatter of 0.15. The two studies agree with each other as well as with an independent shear-based calculation of the $N - M$ relation (Murata et al. 2019), where the slope for the $N - M$ relation is 0.86 ± 0.05 using cosmological parameters from Planck observations. The slope of the $N - M$ relation reported in our work is consistent with these studies.
- The negative redshift trend $c = -1.19^{+1.04}_{-1.35}$ when the evolution term is treated as a free parameter reported in our work confirms the finding from Chiu et al. (2020) within the margin of error. By contrast, Bleem et al. (2020) studied the richness-mass relation of an SZ sample and found a weak redshift evolution of $c = 0.29 \pm 0.27$ at pivot redshift $z_{\rm pivot} = 0.6$. Their best-fit slope and intrinsic scatter is similar to our value.

Comparison to other studies of SZ samples:

- SZ-selected samples avoid the cool-core bias inherent in X-ray-selected samples and the projection effects often seen in optical-based samples. These advantages make SZ samples particularly useful for examining how selection effects influence cluster properties. We compare the slope of our $L-M$ relation to the core-included bolometric lumonisity - total mass relation in the work of Bulbul et al. (2019). Their dataset spans a redshift range similar to ours, strengthening the relevance of this comparison. Their slope, $2.15^{+0.24}_{-0.19}$, is steeper than the self-similar model prediction and consistent with our result, although it differs by 2σ. Nevertheless, their best-fit scaling relation agrees with self-similar redshift evolution.
- As for the richness-mass relation, we found that our slope is broadly in good agreement with other SZ-based samples investigations, although the fitting procedures may not be exactly same (e.g., Saro et al. 2015; Grandis et al. 2021).

From the above comparisons, our sample's best-fit $L - M$ slope is shallower than that observed in X-ray flux-limited samples and SZ samples but aligns well with recent findings from the eFEDS sample. The $N - M$ slope of this work, however, is consistent with self-similar prediction and with values reported in the literature. We note that the mis-centering effect of CAMIRA clusters causes one outlier in the $L-M$ and $N-M$ relations. The misfit data point in Fig. 6 and Fig. 9 is a stacked bin that has a member that is visually mis-centered and, at the same time, possesses significantly high weak-lensing weighting. We find that this outlier does not affect the best-fit scaling relation results. Additionally, while other studies attempt to reduce data scatter through selection criteria, we apply a stacking method with weak-lensing signal-to-noise weighting in our analysis.

Compared to theoretical prediction, all the observational results imply a departure from self-similarity, where the $L - M$ slope is steeper than 4/3. X-ray selected samples are known to have a cool-core bias, thus favoring massive clusters with hot, dense gas (Molendi & Pizzolato 2001; Eckert et al. 2011; Käfer et al. 2019). This resulting high fraction of effectively X-ray bright, high mass clusters leads to a steeper slope in the $L - M$ plane. However, the eFEDS cluster sample offers a more complete dataset that spans a wide mass and redshift range without the usual cool-core bias (Ghirardini et al. 2022b). Furthermore, the analyses from this work and other references have already corrected this selection bias to some extent. Either by modifying the selection function (e.g., Clerc et al. 2018; Bahar et al. 2022b) or fitting the relations in a multivariate setting (e.g., this work, Liu et al. 2015; Bulbul et al. 2019; Chiu et al. 2016, 2022; Ota et al. 2023), the impact of the selection method on scaling relations is expected to be minimal. In contrast, nearly mass-limited samples such as SZ-selected ones, albeit having no cool-core bias, usually yield a steep $L - M$ slope as well. Instead of being drawn towards relaxed, centrally concentrated gas systems, SZ samples tend to select more massive, dynamically disturbed clusters. This tendency highlights the importance of non-gravitational processes, such as mergers, AGN feedback, and radiative cooling, in shaping cluster scaling relations. Since these non-gravitational processes violate the assumption of the self-similar model and can not be neglected in most cases, especially for low-mass objects (Lovisari et al. 2015; Schellenberger & Reiprich 2017), they are likely responsible for the observed steep $L - M$ slope. Another possible reason for such deviation from self-similar behavior is that most clusters are not in the hydrostatic equilibrium state. Indeed, various observations and simulations showed that most clusters are not relaxed (Eckert et al. 2011; Hahn et al. 2017; Barnes et al. 2018). Therefore, observations of the $L - M$ relation, which is strongly influenced by the physics of the gas content, can differ from the prediction of self-similarity (see e.g., Lovisari & Maughan 2022 for a recent review).

In addition, hierarchical growth can also modify cluster scaling relations. As discussed in Ota et al. (2023), besides the classic self-similar model (Kaiser 1986), we consider the baseline of the X-ray scaling relation, which takes into account the structure growth (Fujita & Aung 2019). Due to the hierarchical evolution of the Universe, an anti-correlation between mass and halo concentration is expected. That is, the less massive clusters are formed earlier in time, and thus have higher characteristic densities. This results in a higher X-ray luminosity in the low mass end compared to pure self-similarity, which directly translates to shallower slopes in the $L - T_X$ and $L - M$ planes. The authors computed the baseline for the $L - M$ relation at $1.1 - 1.2$ instead of 4/3 for the bolometric X-ray luminosity. To directly compare to their revised baseline, we calculate the best-fit power-law of the $L - M$ relation without the $E(z)$ term (Table 3), which yields $1.50^{+0.17}_{-0.14}$. We find that our result agrees with the revised model

within 2.5σ errors. In conclusion, the $L-M$ slope obtained in our work is slightly shallower or comparable to the slopes reported in previous studies. However, it is marginally steeper than the predictions of both the self-similar model and the baseline model that incorporates the mass-concentration relation (Fujita & Aung 2019).

Finally, current studies show contradictory reports on their redshift evolution. To address these discrepancies, further investigations involving a larger set of data with more high-redshift objects will improve the current understanding of the subject. The use of WL mass is particularly valuable, as it reduces the scaling degeneracy due to the use of two X-ray observables in a scaling relation. Furthermore, including various samples from different selection methods is also important, because the selection bias has an impact on scaling relation studies (e.g., Reichert et al. 2011).

6.2.2. X-ray detected and undetected sub-groups

Significant efforts have been made in the field to understand the properties of galaxy clusters of various selection methods. Many studies suggest that clusters detected in X-rays are biased towards massive and hot ICM gas, therefore they tend to occupy the brighter end of the $L - M$ plane. In this work, we offer a direct comparison between two sub-groups of the same optical cluster sample, with the aid of the eFEDS X-ray cluster catalog. The CAMIRA clusters represent an X-ray unbiased selection and provide a wide range of cluster mass, down to values lower than $10^{14}\mathrm{M}_{\odot}$. At the same time, with an exposure equivalent to eight eROSITA all-sky scans, the eFEDS X-ray data supplements the optical sample with uniform X-ray measurements.

Similar to other investigations on the topic (Andreon et al. 2017; Bahar et al. 2022a), we found that the slope of the $L - M$ relation is steeper for the X-ray detected clusters. Andreon et al. (2017) examined the diversity of gas content of nearby, massive clusters using an X-ray unbiased sample (XUCS) and the REXCESS X-ray sample (Pratt et al. 2009). Their results showed that while the REXCESS sample follows the luminosity-mass relation with a small scatter, the XUCS sample presents a larger diversity in luminosity at a given mass and shows a shallower slope. Bahar et al. (2022a) showed that the low-mass groups preferentially exhibit a shallower $L_X - M_{\mathrm{gas}}$ slope compared to the high-mass clusters in the eFEDS sample. This trend indicates that optical clusters with detected associate hot gas are similar to clusters taken from X-ray based samples, and thus follow a steeper slope in the $L-M$ relation. Furthermore, the clusters with no corresponding X-ray counterparts are often found within the low-mass range. According to the revised scaling relation (Fujita & Aung 2019), these low-mass systems are usually formed at high redshift, therefore represent a higher density. This results in a higher X-ray luminosity of low-mass clusters compared to the self-similar expectation.

The slope of the $N - M$ relation is consistent across different subsamples in this work and aligns with findings from other studies on eFEDS and SDSS redMaPPer clusters (see Section 5.2.1). This consistency suggests that optical richness serves as a reliable mass proxy, irrespective of the cluster selection method. Further observations of the richness-mass relation in X-ray samples are needed for more comprehensive comparisons.

6.3. Surface brightness profiles

In addition to exploiting the scaling relations between X-ray observables and cluster mass, the study of X-ray radial profiles can be used to investigate differences between X-ray detected and undetected clusters. As shown in Section 5.3, CAMIRA clusters with eFEDS counterparts exhibit surface brightness profiles that are brighter and more centrally peaked compared to those of clusters without matching eFEDS clusters. This trend is consistent with previous observations and simulations of eROSITA sources, where clusters undetected in X-rays tend to have flatter and more extended profiles (Comparat et al. 2020; Liu et al. 2022b; Popesso et al. 2024).

Another investigation on the same subject was conducted by Willis et al. (2021) using the XXL and CAMIRA catalogs. Their CAMIRA sample was restricted to $0.1 < z < 0.3$ and $N > 15$, making it comparable to our dataset. However, their study covered an overlapping area of only 22.6 deg^2, smaller than the eFEDS coverage in our work. They found that the X-ray surface brightness of high-flux ($\log f_{\mathrm{X}} > -14.2$ cgs) unmatched CAMIRA clusters was fainter in the central regions compared to high-flux matched clusters. Mis-centering and point-like source contamination were ruled out as potential causes for these unmatched clusters in the XXL catalog. Instead, the discrepancy was attributed to instrumental effects, particularly the reduced detection probability for clusters located near the edge of the XMM-Newton field of view due to vignetting and degraded PSF.

In our work, we similarly rule out mis-centering and misclassification of extended X-ray sources as point-like sources. Moreover, the impact of the eROSITA PSF is negligible in most cases, as its size is smaller than the extension of the X-ray profiles (Fig. 10). However, contamination of point-like sources near cluster centers may reduce the likelihood of these clusters being detected and classified as extended sources in eFEDS. This suggests that unmatched CAMIRA clusters likely represent real systems with overdensities of red-sequence galaxies in optical observations, but they may lack detectable X-ray components in the current catalogs.

It is worth noting that the CAMIRA algorithm achieves a high purity in cluster selection, exceeding 95% down to a richness cut of $\hat{N}\mathrm{mem} = 15$, as estimated using mock catalogs. Its completeness is also high, exceeding 90% in the high-mass regime ($M_{200} \geq 10^{14} h_{70}^{-1} M_{\odot}$). However, completeness decreases for lower-mass systems, particularly at high redshift (Oguri et al. 2018). Potential contamination and incompleteness at high redshift thus remains a possibility. This factor could contribute to deviations between X-ray and optical samples. While investigating these discrepancies is beyond the scope of this paper, deeper X-ray observations are necessary to further assess the completeness of optical samples. On the other hand, while X-ray surveys may be more effective than optical surveys at identifying nearby clusters, as they are less affected by projection effects, the high completeness of CAMIRA-selected samples at low redshifts suggests that this explanation alone cannot account for the discrepancy in the number of matched clusters.

The difference in X-ray surface brightness between the two sub-samples aligns with the findings from scaling relation analyses (Section 5.2.2). In particular, the $L - M$ scaling relations reveal a modest deviation between the X-ray detected and undetected sub-samples, although this deviation remains within 2σ. In contrast, their optical richness-mass $N - M$ relations are similar. Consequently, the CAMIRA clusters, comprising both X-ray detected and undetected sub-samples, exhibit differences in X-ray properties (e.g., $L - M$ relation, radial profile, and detectabil-

ity) but share similar optical characteristics (e.g., $N - M$ relation and red-sequence overdensity). This suggests that the CAMIRA sample represents a complete cluster population with diverse X-ray properties. This highlights the importance of multiwavelength surveys in cluster studies, as combining clusters identified through different methods is essential to capturing the complete cluster population. A recent study by Andreon et al. (2024) found that approximately one-quarter of clusters in a complete sample exhibit low X-ray surface brightness, representing a population missing from both X-ray and SZ samples. This aligns with our findings, as optical samples, being unaffected by ICM physics, can include these faint X-ray clusters.

7. Summary

We selected a sample of 997 HSC optically detected clusters in the eFEDS footprint, with a richness threshold of $N > 15$ and a redshift constraint of $0.10 < z < 1.34$. We investigated the X-ray properties of our sample and below are our main findings:

1. We examined the dynamical status of CAMIRA clusters in the eFEDS field using the X-ray–BCG offset and found the relaxed cluster fraction to be $0(< 14)\%$. This fraction is lower than that of X-ray-selected cluster samples but is comparable to values found in optical catalogs.
2. We measured the weak-lensing mass, estimated X-ray luminosity from count rates, and derived the scaling relations using the hierarchical Bayesian regression method. The bolometric X-ray luminosity-mass relation agrees with our previous study of the high richness CAMIRA clusters and with several investigations of X-ray constructed samples. The $L - M$ relation has a steeper slope compared to the self-similar prediction and the new baseline model considering the mass-concentration connection, which is in good agreement with values in the literature. The $N-M$ relation found in this work is consistent with other estimates of the CAMIRA sample, and broadly agrees with other samples. Additionally, we observe a negative redshift trend in the $N - M$ relation, while no significant redshift evolution is found for the $L - M$ relation.
3. We investigated the deviation between X-ray detected and undetected clusters in our optical sample. First, the slope of the $L - M$ scaling relation of the X-ray detected clusters is steeper than that of the X-ray undetected ones, indicating different X-ray properties between the optical and X-ray samples. However, the optical richness–mass relation shows consistency across both sub-samples. Second, the X-ray surface brightness profiles of X-ray matched clusters appear to be brighter in the center and decrease more rapidly.

Our findings reveal that the X-ray properties of optically identified clusters generally differ from those of X-ray-selected clusters. The observed scaling relations between mass and other properties align well with recent observations and confirm our previous work (Ota et al. 2023). We plan to extend this analysis using the deeper five stacked eROSITA all-sky survey (eRASS:5), which covers a far larger area than the eFEDS field, potentially increasing our sample size fivefold despite lower exposure depth. Stacking analysis will again enhance statistical robustness. This series of studies demonstrates eROSITA's potential, especially when combined with HSC data, to refine our understanding of scaling relations and selection effects, ultimately contributing to the development of comprehensive cluster samples for cosmological constraints.

Table A.1. WL mass calibrations for $M_{500}^{\rm WL}$.

$a_{\rm WL}$	$-0.138^{+0.003}_{-0.003}$
$b_{\rm WL}$	$1.121^{+0.007}_{-0.007}$
$c_{\rm WL}$	$-1.549^{+0.041}_{-0.041}$
$d_{\rm WL}$	$1.672^{+0.091}_{-0.090}$
$\sigma_{\rm WL,0}$	$0.174^{+0.003}_{-0.003}$
c_σ	$-0.980^{+0.116}_{-0.110}$

Appendix A: WL mass calibrations

Stacked lensing profiles average out cluster properties such as elliptical halo structures and subhalos, and thus the assumption of a spherically symmetric halo is well established. On the other hand, the number of background galaxies is important in cluster WL analysis. Since the observed ellipticities are composed of coherent WL pattern synthesized to the intrinsic ones, if the number of background galaxies were not enough, the measured mass would be deviated from the true one. The typical number density of background galaxies in the HSC-SSP Survey, decreases from ~ 10 to ~ 1 arcmin^{-2} by changing the cluster redshift from ~ 0.1 to ~ 1. Therefore, when we make a subsample in redshift bins, there might be bias in measured WL masses.

We assess accuracy of our stacked lensing masses using a mock shape catalogue realizing our observing conditions. We first make parent catalog of 10,000 clusters assuming a spherical NFW model. The mock clusters are uniformly distributed $[0.1, 1.4]$ in a redshift. Then, we make 7695 subsamples of which the number of clusters and the redshift range are the same as those in our study, and the mass ranges are similar to those in our samples. When making the sub-samples, we randomly select from the parent catalogue and do not allow overlapping clusters. We repeated the same analysis in real data and found that mass measurements failed in $\sim 1\%$ of the samples. The resulting mass bias is shown in Figure A.1. To evaluate the mass bias, we introduce the following equation,

$$\ln x^{\rm WL} = a_{\rm WL} + (b_{\rm WL} + d_{\rm WL} ev(z)) \ln x^{\rm ture} + c_{\rm WL} ev(z) \quad \text{(A.1)}$$

where $x = \ln(M_{500}(E(z)/E(z_{\rm ref}))$ and $ev(z) = \ln(E(z)/E(z_{\rm ref}))$ with $z_{\rm ref} = 0.35$. The intrinsic scatter of the WL mass is specified by

$$\sigma_{\rm WL} = \exp\left[\ln \sigma_{\rm WL,0}(1 + c_{\ln\sigma} ev(z))\right]. \quad \text{(A.2)}$$

The best-fit parameters are shown in Table A.1. We use the WL mass calibration as fixed parameters in the regression analysis.

Acknowledgements. This work is based on data from eROSITA, the soft X-ray instrument aboard SRG, a joint Russian-German science mission supported by the Russian Space Agency (Roskosmos), in the interests of the Russian Academy of Sciences represented by its Space Research Institute (IKI), and the Deutsches Zentrum für Luft- und Raumfahrt (DLR). The SRG spacecraft was built by Lavochkin Association (NPOL) and its subcontractors, and is operated by NPOL with support from the Max Planck Institute for Extraterrestrial Physics (MPE). The development and construction of the eROSITA X-ray instrument was led by MPE, with contributions from the Dr. Karl Remeis Observatory Bamberg & ECAP (FAU Erlangen-Nuernberg), the University of Hamburg Observatory, the Leibniz Institute for Astrophysics Potsdam (AIP), and the Institute for Astronomy and Astrophysics of the University of Tübingen, with the support of DLR and the Max Planck Society. The Argelander Institute for Astronomy of the University of Bonn and the Ludwig Maximilians Universität Munich also participated in the science preparation for eROSITA. The eROSITA data shown here were processed using the eSASS/NRTA software system developed by the German eROSITA consortium. The Hyper Suprime-Cam (HSC) collaboration includes the astronomical communities of Japan and Taiwan, and Princeton University. The HSC instrumentation and software were developed by the National Astronomical Observatory of Japan(NAOJ), the Kavli Institute for the Physics and Mathematics of the Universe (Kavli IPMU), the University of Tokyo, the

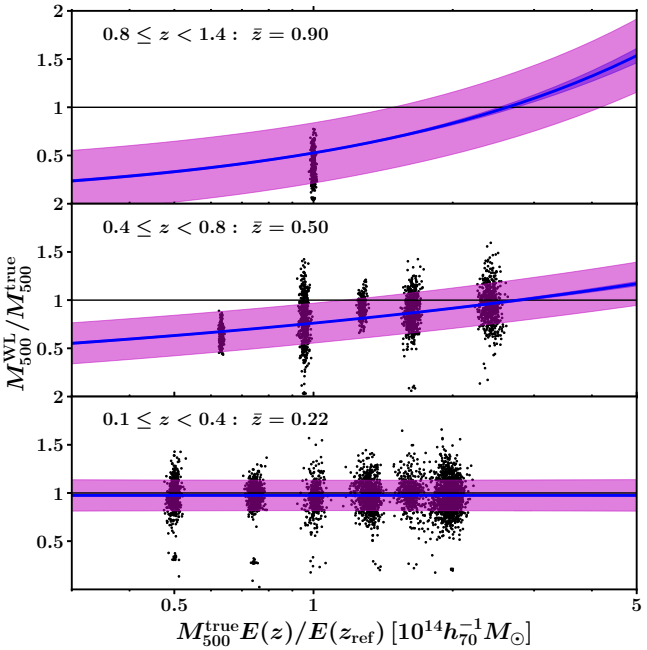

Fig. A.1. The mass bias, $M_{500}^{\rm WL}/M_{500}^{\rm true}$, in three redshift bins. The black points are the mass bias for stacked mock clusters without their errors. The blue lines and regions are the baselines and their uncertainties, respectively. The magenta regions denotes the baseline including the intrinsic scatter.

High Energy Accelerator Research Organization (KEK), the Academia Sinica Institute for Astronomy and Astrophysics in Taiwan (ASIAA), and Princeton University. Funding was contributed by the FIRST program from Japanese Cabinet Office, the Ministry of Education, Culture, Sports, Science and Technology (MEXT), the Japan Society for the Promotion of Science (JSPS), Japan Science and Technology Agency (JST), the Toray Science Foundation, NAOJ, Kavli IPMU, KEK,ASIAA, and Princeton University. This work was supported in part by the Fund for the Promotion of Joint International Research, JSPS KAKENHI Grant Number 16KK0101, 20K04027(NO), 20H05856, 20H00181, 19KK0076(NO and MO), 22H01260 (MO).

References

Adami, C., Giles, P., Koulouridis, E., et al. 2018, A&A, 620, A5
Akino, D., Eckert, D., Okabe, N., et al. 2022, PASJ, 74, 175
Andreon, S. & Moretti, A. 2011, A&A, 536, A37
Andreon, S., Trinchieri, G., & Moretti, A. 2024, A&A, 686, A284
Andreon, S., Trinchieri, G., Moretti, A., & Wang, J. 2017, A&A, 606, A25
Asplund, M., Grevesse, N., Sauval, A. J., & Scott, P. 2009, ARA&A, 47, 481
Bahar, Y. E., Bulbul, E., Clerc, N., et al. 2022a, A&A, 661, A7
Bahar, Y. E., Bulbul, E., Clerc, N., et al. 2022b, A&A, 661, A7
Balucinska-Church, M. & McCammon, D. 1992, ApJ, 400, 699
Barnes, D. J., Vogelsberger, M., Kannan, R., et al. 2018, MNRAS, 481, 1809
Bhattacharya, S., Habib, S., Heitmann, K., & Vikhlinin, A. 2013, ApJ, 766, 32
Bleem, L. E., Bocquet, S., Stalder, B., et al. 2020, ApJS, 247, 25
Bocquet, S., Grandis, S., Bleem, L. E., et al. 2024, Phys. Rev. D, 110, 083510
Böhringer, H., Chon, G., Retzlaff, J., et al. 2017, AJ, 153, 220
Böhringer, H., Schuecker, P., Guzzo, L., et al. 2001, A&A, 369, 826
Brunner, H., Liu, T., Lamer, G., et al. 2022, A&A, 661, A1
Bruzual, G. & Charlot, S. 2003, MNRAS, 344, 1000
Bulbul, E., Chiu, I. N., Mohr, J. J., et al. 2019, ApJ, 871, 50
Bulbul, E., Liu, A., Kluge, M., et al. 2024, A&A, 685, A106
Bulbul, E., Liu, A., Pasini, T., et al. 2022a, A&A, 661, A10
Bulbul, E., Liu, A., Pasini, T., et al. 2022b, A&A, 661, A10
Carlberg, R. G., Yee, H. K. C., Ellingson, E., et al. 1996, ApJ, 462, 32
Carrasco Kind, M. & Brunner, R. J. 2014, MNRAS, 438, 3409
Cavaliere, A. & Fusco-Femiano, R. 1978, A&A, 70, 677
Chen, K.-F., Chiu, I.-N., Oguri, M., et al. 2024, arXiv e-prints, arXiv:2406.11966
Chiu, I., Mohr, J. J., McDonald, M., et al. 2018, MNRAS, 478, 3072
Chiu, I., Saro, A., Mohr, J., et al. 2016, MNRAS, 458, 379

Chiu, I. N., Chen, K.-F., Oguri, M., et al. 2024, The Open Journal of Astrophysics, 7, 90
Chiu, I. N., Ghirardini, V., Liu, A., et al. 2022, A&A, 661, A11
Chiu, I. N., Klein, M., Mohr, J., & Bocquet, S. 2023, MNRAS, 522, 1601
Chiu, I. N., Umetsu, K., Murata, R., Medezinski, E., & Oguri, M. 2020, MNRAS, 495, 428
Clerc, N., Ramos-Ceja, M. E., Ridl, J., et al. 2018, A&A, 617, A92
Comparat, J., Eckert, D., Finoguenov, A., et al. 2020, The Open Journal of Astrophysics, 3, 13
Dauser, T., Falkner, S., Lorenz, M., et al. 2019, A&A, 630, A66
Ebeling, H., Edge, A. C., Bohringer, H., et al. 1998, MNRAS, 301, 881
Ebeling, H., Edge, A. C., Mantz, A., et al. 2010, MNRAS, 407, 83
Eckert, D., Molendi, S., & Paltani, S. 2011, A&A, 526, A79
Finoguenov, A., Tanaka, M., Cooper, M., et al. 2015, A&A, 576, A130
Fonseca, J., Viljoen, J.-A., & Maartens, R. 2019, J. Cosmology Astropart. Phys., 2019, 028
Foster, A. R., Ji, L., Smith, R. K., & Brickhouse, N. S. 2012, ApJ, 756, 128
Fujita, Y. & Aung, H. 2019, ApJ, 875, 26
Ghirardini, V., Bahar, Y. E., Bulbul, E., et al. 2022a, A&A, 661, A12
Ghirardini, V., Bahar, Y. E., Bulbul, E., et al. 2022b, A&A, 661, A12
Ghirardini, V., Bulbul, E., Artis, E., et al. 2024, A&A, 689, A298
Giodini, S., Lovisari, L., Pointecouteau, E., et al. 2013, Space Sci. Rev., 177, 247
Grandis, S., Mohr, J. J., Costanzi, M., et al. 2021, MNRAS, 504, 1253
Hahn, O., Martizzi, D., Wu, H.-Y., et al. 2017, MNRAS, 470, 166
Henden, N. A., Puchwein, E., & Sijacki, D. 2019, MNRAS, 489, 2439
Heymans, C., Van Waerbeke, L., Bacon, D., et al. 2006, MNRAS, 368, 1323
Hirata, C. & Seljak, U. 2003, MNRAS, 343, 459
Hubble, E. 1929, Contributions from the Mount Wilson Observatory, 3, 23
Hudson, D. S., Mittal, R., Reiprich, T. H., et al. 2010, A&A, 513, A37
Jansen, F., Lumb, D., Altieri, B., et al. 2001, A&A, 365, L1
Käfer, F., Finoguenov, A., Eckert, D., et al. 2019, A&A, 628, A43
Kaiser, N. 1986, MNRAS, 222, 323
Kaiser, N., Aussel, H., Burke, B. E., et al. 2002, in Society of Photo-Optical Instrumentation Engineers (SPIE) Conference Series, Vol. 4836, Survey and Other Telescope Technologies and Discoveries, ed. J. A. Tyson & S. Wolff, 154–164
Kaiser, N., Burgett, W., Chambers, K., et al. 2010, in Society of Photo-Optical Instrumentation Engineers (SPIE) Conference Series, Vol. 7733, Ground-based and Airborne Telescopes III, ed. L. M. Stepp, R. Gilmozzi, & H. J. Hall, 77330E
Kiiveri, K., Gruen, D., Finoguenov, A., et al. 2021, MNRAS, 502, 1494
Kravtsov, A. V. & Borgani, S. 2012, ARA&A, 50, 353
Lau, E. T., Bogdán, Á., Nagai, D., Cappelluti, N., & Shirasaki, M. 2024, arXiv e-prints, arXiv:2410.22397
Lavoie, S., Willis, J. P., Démoclès, J., et al. 2016, MNRAS, 462, 4141
Li, X., Miyatake, H., Luo, W., et al. 2022, Publications of the Astronomical Society of Japan, 74, 421
Liu, A., Bulbul, E., Ghirardini, V., et al. 2022a, A&A, 661, A2
Liu, J., Mohr, J., Saro, A., et al. 2015, MNRAS, 448, 2085
Liu, T., Buchner, J., Nandra, K., et al. 2022b, A&A, 661, A5
Lovisari, L. & Maughan, B. J. 2022, in Handbook of X-ray and Gamma-ray Astrophysics, ed. C. Bambi & A. Sangangelo, 65
Lovisari, L., Reiprich, T. H., & Schellenberger, G. 2015, A&A, 573, A118
Mandelbaum, R., Lanusse, F., Leauthaud, A., et al. 2017, ArXiv e-prints [arXiv:1710.00885]
Mandelbaum, R., Miyatake, H., Hamana, T., et al. 2018, PASJ, 70, S25
Massey, R., Heymans, C., Bergé, J., et al. 2007, MNRAS, 376, 13
Maturi, M., Bellagamba, F., Radovich, M., et al. 2019, MNRAS, 485, 498
Maughan, B. J. 2007, ApJ, 668, 772
Medezinski, E., Oguri, M., Nishizawa, A. J., et al. 2018, PASJ, 70, 30
Merloni, A., Lamer, G., Liu, T., et al. 2024, A&A, 682, A34
Migkas, K., Pacaud, F., Schellenberger, G., et al. 2021, A&A, 649, A151
Miyazaki, S., Oguri, M., Hamana, T., et al. 2018, PASJ, 70, S27
Molendi, S. & Pizzolato, F. 2001, ApJ, 560, 194
Molham, M., Clerc, N., Takey, A., et al. 2020, MNRAS, 494, 161
Murata, R., Oguri, M., Nishimichi, T., et al. 2019, PASJ, 71, 107
Navarro, J. F., Frenk, C. S., & White, S. D. M. 1996, ApJ, 462, 563
Nishizawa, A. J., Hsieh, B.-C., Tanaka, M., & Takata, T. 2020, arXiv e-prints, arXiv:2003.01511
Oguri, M. 2014, MNRAS, 444, 147
Oguri, M., Lin, Y.-T., Lin, S.-C., et al. 2018, PASJ, 70, S20
Oguri, M., Miyazaki, S., Li, X., et al. 2021, PASJ, 73, 817
Okabe, N., Oguri, M., Akamatsu, H., et al. 2019, PASJ, 71, 79
Okabe, N. & Smith, G. P. 2016, MNRAS, 461, 3794
Okabe, N., Zhang, Y. Y., Finoguenov, A., et al. 2010, ApJ, 721, 875
Okabe et al., I.-N. 2025, arXiv e-prints
Ota, N. & Mitsuda, K. 2004, A&A, 428, 757
Ota, N., Mitsuishi, I., Babazaki, Y., et al. 2020, PASJ, 72, 1
Ota, N., Nguyen-Dang, N. T., Mitsuishi, I., et al. 2023, A&A, 669, A110
Pacaud, F., Pierre, M., Adami, C., et al. 2007, MNRAS, 382, 1289
Pierre, M. 2022, arXiv e-prints, arXiv:2205.05499
Planck Collaboration, Ade, P. A. R., Aghanim, N., et al. 2016, A&A, 594, A24
Popesso, P., Biviano, A., Bulbul, E., et al. 2024, MNRAS, 527, 895
Pratt, G. W., Croston, J. H., Arnaud, M., & Böhringer, H. 2009, A&A, 498, 361
Predehl, P., Andritschke, R., Arefiev, V., et al. 2021, A&A, 647, A1
Ramos-Ceja, M. E., Oguri, M., Miyazaki, S., et al. 2022, A&A, 661, A14
Reichert, A., Böhringer, H., Fassbender, R., & Mühlegger, M. 2011, A&A, 535, A4
Rossetti, M., Gastaldello, F., Ferioli, G., et al. 2016, MNRAS, 457, 4515
Rozo, E. & Rykoff, E. S. 2014, ApJ, 783, 80
Rykoff, E. S., Rozo, E., Busha, M. T., et al. 2014, ApJ, 785, 104
Sanderson, A. J. R., Edge, A. C., & Smith, G. P. 2009, MNRAS, 398, 1698
Saro, A., Bocquet, S., Rozo, E., et al. 2015, MNRAS, 454, 2305
Schellenberger, G. & Reiprich, T. H. 2017, MNRAS, 469, 3738
Schneider, P., van Waerbeke, L., Jain, B., & Kruse, G. 1998, MNRAS, 296, 873
Seppi, R., Comparat, J., Nandra, K., et al. 2023, A&A, 671, A57
Sereno, M. 2016, MNRAS, 455, 2149
Sereno, M., Umetsu, K., Ettori, S., et al. 2020, MNRAS, 492, 4528
Skrutskie, M. F., Cutri, R. M., Stiening, R., et al. 2006, AJ, 131, 1163
Smith, R. K., Brickhouse, N. S., Liedahl, D. A., & Raymond, J. C. 2001, ApJ, 556, L91
Sunyaev, R., Arefiev, V., Babyshkin, V., et al. 2021, A&A, 656, A132
Takey, A., Schwope, A., & Lamer, G. 2013, A&A, 558, A75
Tanaka, M., Coupon, J., Hsieh, B.-C., et al. 2018, PASJ, 70, S9
Truemper, J. 1993, Science, 260, 1769
Truong, N., Rasia, E., Mazzotta, P., et al. 2018, MNRAS, 474, 4089
Vakili, M., Hoekstra, H., Bilicki, M., et al. 2023, A&A, 675, A202
Vikhlinin, A., Burenin, R. A., Ebeling, H., et al. 2009, ApJ, 692, 1033
West, M. J., Oemler, Augustus, J., & Dekel, A. 1988, ApJ, 327, 1
Willis, J. P., Oguri, M., Ramos-Ceja, M. E., et al. 2021, MNRAS, 503, 5624
Wright, E. L., Eisenhardt, P. R. M., Mainzer, A. K., et al. 2010, AJ, 140, 1868
Xu, W., Ramos-Ceja, M. E., Pacaud, F., Reiprich, T. H., & Erben, T. 2018, A&A, 619, A162
Xu, W., Ramos-Ceja, M. E., Pacaud, F., Reiprich, T. H., & Erben, T. 2022, A&A, 658, A59
Yang, X., Mo, H. J., van den Bosch, F. C., et al. 2006, MNRAS, 373, 1159
York, D. G., Adelman, J., Anderson, John E., J., et al. 2000, AJ, 120, 1579
Zou, H., Gao, J., Xu, X., et al. 2021, ApJS, 253, 56

[1] Institut für Astronomie und Astrophysik Tübingen (IAAT), Universität Tübingen, Sand 1, 72076 Tübingen, Germany
e-mail: nguyen@astro.uni-tuebingen.de
[2] Argelander-Institut für Astronomie (AIfA), Universität Bonn, Auf dem Hügel 71, 53121 Bonn, Germany
[3] Department of Physics, Nara Women's University, Kitauoyanishi-machi, Nara, 630-8506, Japan
[4] Physics Program, Graduate School of Advanced Science and Engineering, Hiroshima University, 1-3-1 Kagamiyama, Higashi-Hiroshima, Hiroshima 739-8526, Japan
[5] Hiroshima Astrophysical Science Center, Hiroshima University, 1-3-1 Kagamiyama, Higashi-Hiroshima, Hiroshima 739-8526, Japan
[6] Core Research for Energetic Universe, Hiroshima University, 1-3-1, Kagamiyama, Higashi-Hiroshima, Hiroshima 739-8526, Japan
[7] Center for Frontier Science, Chiba University, 1-33 Yayoi-cho, Inage-ku, Chiba 263-8522, Japan
[8] Department of Physics, Graduate School of Science, Chiba University, 1-33 Yayoi-Cho, Inage-Ku, Chiba 263-8522, Japan
[9] Kavli Institute for the Physics and Mathematics of the Universe (Kavli IPMU, WPI), University of Tokyo, Chiba 277-8582, Japan
[10] Graduate School of Science, Division of Particle and Astrophysical Science, Nagoya University, Furo-cho, Chikusa-ku, Nagoya, Aichi, 464-8602, Japan
[11] Max Planck Institute for Extraterrestrial Physics, Giessenbachstrasse 1, 85748 Garching, Germany
[12] University of Hamburg, Hamburger Sternwarte, Gojenbergsweg 112, 21029 Hamburg, Germany
[13] Tsung-Dao Lee Institute, and Key Laboratory for Particle Physics, Astrophysics and Cosmology, Ministry of Education, Shanghai Jiao Tong University, Shanghai 200240, China
[14] Department of Astronomy, School of Physics and Astronomy, and Shanghai Key Laboratory for Particle Physics and Cosmology, Shanghai Jiao Tong University, Shanghai 200240, China

[15] Academia Sinica Institute of Astronomy and Astrophysics (ASIAA), 11F of AS/NTU Astronomy-Mathematics Building, No.1, Sec. 4, Roosevelt Rd, Taipei10617, Taiwan
[16] Universität Innsbruck, Institut für Astro- und Teilchenphysik, Technikerstr. 25/8, 6020 Innsbruck, Austria
[17] Leiden Observatory, Leiden University, PO Box 9513, 2300 RA Leiden, the Netherlands
[18] SRON Netherlands Institute for Space Research, Niels Bohrweg 4, NL-2333 CA Leiden, the Netherlands
[19] Kobayashi-Maskawa Institute for the Origin of Particles and the Universe (KMI), Nagoya University, Nagoya, 464-8602, Japan
[20] National Astronomical Observatory of Japan, 2-21-1 Osawa, Mitaka, Tokyo 181-8588, Japan
[21] SOKENDAI (The Graduate University for Advanced Studies), Mitaka, Tokyo, 181-8588, Japan

CHAPTER 4

Results and Discussion

4.1 Multiwavelength study of Galactic Supernova remnants

As the detailed findings of the related research are summarized in Chapter 3, this chapter focuses on discussing the key insights gained from this thesis.

4.1.1 Analysis of the Galactic supernova remnants...

HESS J1534-571 and HESS J1614-518 are prominent TeV sources with distinguishable shell-like structures, suggesting efficient particle acceleration activities at their sites. Since these sources were initially discovered in TeV, their emission in other wavebands, such as radio and X-rays, may either be faint or remain undetected. Therefore, a systematic search for emission in other wavebands was conducted to confirm their SNR nature and enable broadband SED analysis.

HESS J1534-571

HESS J1534-571 was observed in X-ray by *Suzaku* (Mitsuda et al., 2007; Koyama et al., 2007) shortly after its initial discovery (H.E.S.S. Collaboration et al., 2018a; Saji et al., 2018). However, the four pointings did not cover the entire SNR. Both studies from the H.E.S.S. Collaboration et al. (2018a) and Saji et al. (2018) reported no significant X-ray emission from the source. Although further observations using *Suzaku* were planned, they could not be executed before the mission ended. To address the gap in coverage, we proposed *XMM-Newton* observations with an approximate 25 ks exposure, targeting the region of the SNR that was not covered by Suzaku. Notably, this region coincides with the highest peak in the TeV surface brightness map, suggesting a promising site for detecting an X-ray synchrotron component. Similar correlation between TeV peaks and X-ray synchrotron emission have been observed in e.g., SN 1006 (Rothenflug et al., 2004; Acero et al., 2007; Naumann-Godó et al., 2008; Acero et al., 2010) and RX J1713.7-3946 (Cassam-Chenai et al., 2004; Aharonian et al., 2006), further supporting our observational strategy. However,

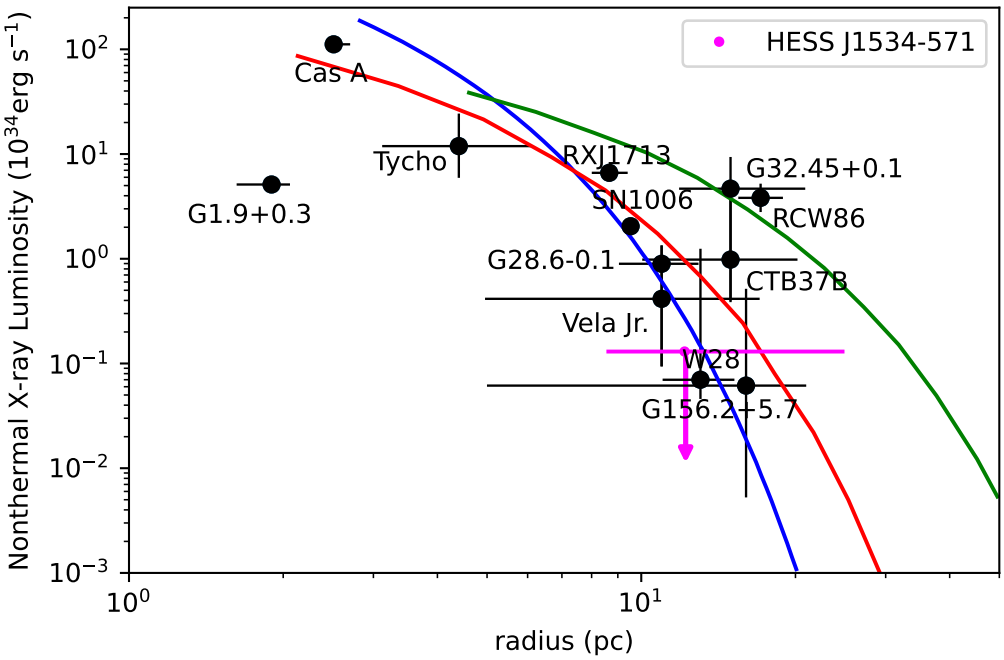

Figure 4.1: Relation between non-thermal X-ray luminosity and the radius of Galactic SNRs. The predicted models for the time evolution of SNR synchrotron X-rays are plotted in blue, red, and green, corresponding to different ambient densities: $5.0\,\mathrm{cm}^{-3}$ (blue), $1.0\,\mathrm{cm}^{-3}$ (red), and $0.1\,\mathrm{cm}^{-3}$ (green). The upper-limit non-thermal X-ray flux for HESS J1534-571 is $F_{2-10\,\mathrm{keV}} = 9.03 \times 10^{-13}\,\mathrm{erg\,cm^{-2}\,s^{-1}}$ at the 95% confidence level (magenta arrow, this work). Data for 12 other SNRs are adopted from Nakamura et al. (2012).

the *XMM-Newton* observation also did not detect significant thermal (typically dominant in the soft X-ray band) or non-thermal (hard X-ray band) X-ray emission. This result positions HESS J1534-571 as a rare example of an SNR that exhibits strong TeV but lacks X-ray synchrotron emission detectable with current X-ray satellite sensitivities. If the high-energy CR production follows a purely leptonic model, the absence of X-ray synchrotron emission suggests that the CR electrons have likely escaped the acceleration site, rendering synchrotron emission at X-ray energies inefficient. This scenario bears similarity to the case of relic PWNe.

Assuming a power-law spectrum, we estimated the non-thermal X-ray flux of HESS J1534-571 to constrain its VHE γ-ray production. To assess the robustness of this estimation, we compared the computed flux to those of other SNRs. Figure 4.1 illustrates the relationship between the non-thermal X-ray flux (in the 2–10 keV band) and the radius of SNRs, where the radius serves as an indicator of the SNR's age. As an SNR evolves, it expands further into space while its X-ray flux gradually decreases. As shown in the plot, the computed value for HESS J1534-571 is consistent with the general trend observed for other SNRs. Additionally, theoretical models describing the relationship between non-thermal X-ray flux and SNR's radius are overlaid. These models demonstrate that higher ambient gas densities lead to a faster decline in the X-ray flux as the SNR evolves (Nakamura et al., 2012). The location of HESS J1534-571 in the plot indicates an ambient gas density in the range of 1-5 cm^{-3}, which is consistent with the assumed gas density in the construction of the broadband SED (Araya, 2017; H.E.S.S. Collaboration et al., 2018a; Nguyen-Dang et al., 2023).

Another intriguing finding is that the clumpy emission observed in the X-ray narrow band at 6.4 keV exhibits a morphology similar to the TeV brightness map. This fluorescence line, originating from the neutral Fe Kα shell transition, is theoretically associated with interactions between CR protons at energies around $\sim$ 100 MeV and ambient cool gas. Hints of such clumpy molecular clouds in the vicinity of the SNR have been reported by Maxted et al. (2018a), revealing a highly inhomogeneous gas structure with spatially clumpy gas in the northwestern region of the SNR. However, the morphology of this associated gas only partially matches either the TeV profile or the 6.4 Fe Kα line emission (Fig. 4.2). This raises an open question for future investigations: can next-generation telescopes and further searches for molecular clouds in this region confirm the MeV CR-gas interaction scenario?

HESS J1614-518

For the first time, HESS J1614-518 has been confirmed as an SNR, thanks to the discovery of its faint, shell-like emission in both radio and X-ray surveys. Figure 4.3 shows the eRASS:4 image in the 1.3–2.5 keV energy band of a portion of the sky tile containing this source. Overlaid are the best-fit shell structures reported by H.E.S.S. Collaboration et al. (2018a) in the TeV waveband and by our work in the radio waveband. Despite the fact that several bright sources are present near our target, the X-ray emission from HESS J1614-518 appears as a faint, diffuse shell with a broader

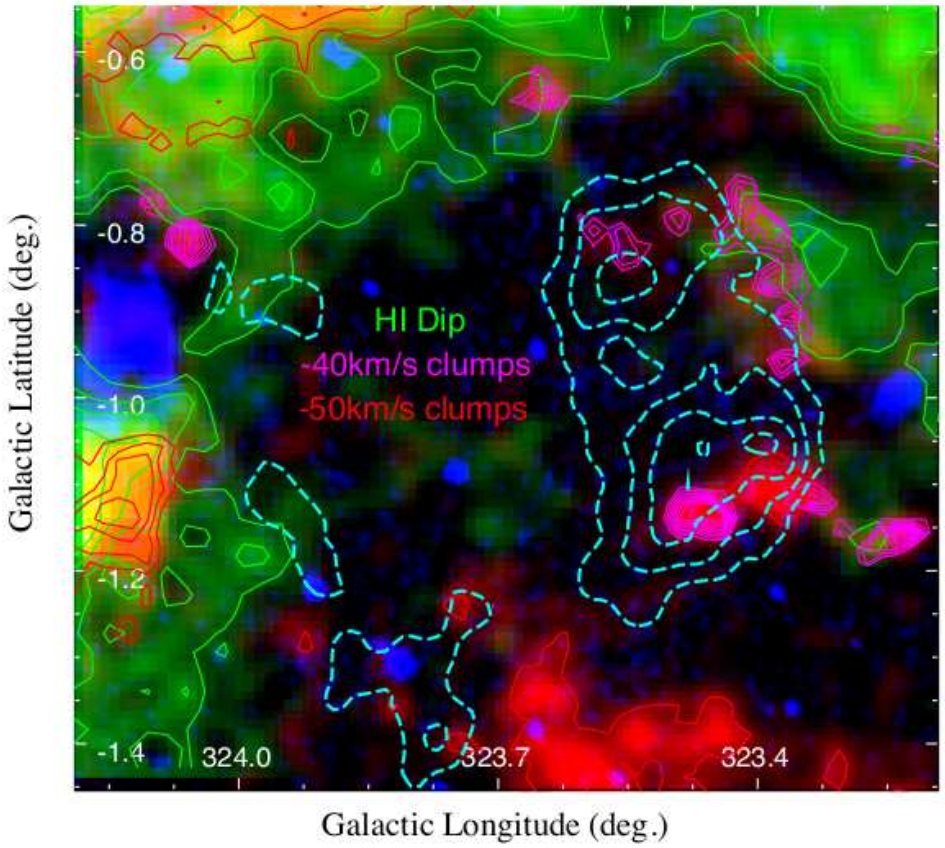

Figure 4.2: Potential gas association of HESS J1534-571 indicated in magenta contours (Maxted et al., 2018a).

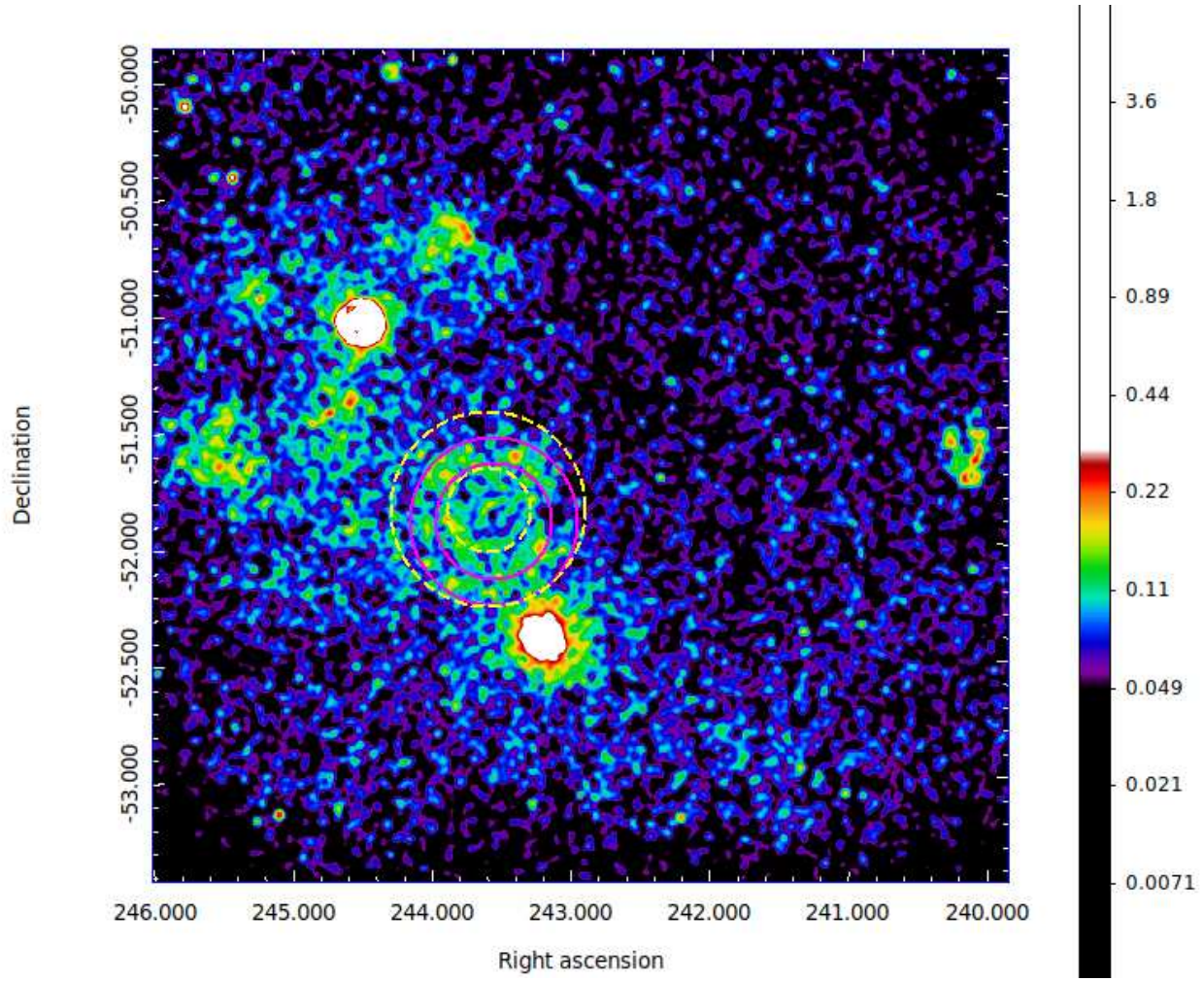

Figure 4.3: eRASS:4 sky map of HESS J1614-518 in the energy range 1.3-2.5 keV. Overlaid are the best-fit shells in TeV (dashed yellow contours, values taken from H.E.S.S. Collaboration et al., 2018a) and radio (solid magenta contours, this work).

extension compared to the radio thin shell (see Fig. 11 in Pühlhofer et al. 2025). The agreement in multiwavelength morphology suggests that the observed electromagnetic radiation originates from the same population of particles. The non-thermal X-ray spectrum is well described by a power-law model. The derived radio and X-ray fluxes are then employed for broadband γ-ray SED analysis, assuming a one-zone model.

It is only natural to ask: Why was an X-ray counterpart of HESS J1614-518 not reported in the literature? Previous X-ray observations with *Swift*, *Suzaku*, and *XMM-Newton* included several pointings, yet no significant non-thermal X-ray emission was detected (H.E.S.S. Collaboration et al., 2018a). The lack of reported X-ray emission could be attributed to two factors: the large sky coverage required to fully encompass the source (the TeV shell spans 0.8 degrees in diameter) and contamination from nearby diffuse sources. The soft band (0.3-1.0 keV) *XMM-Newton* image shows significant stray light contamination from the nearby SNR RCW 103 in the northern region of HESS J1614-518. Meanwhile, the hard band (3-7 keV) *XMM-Newton* image reveals a possible diffuse emission in the northern region, spatially coincident with the northeastern TeV component of HESS J1614-518, with an angular scale of approximately 20 arcminutes; however, it was not sufficient to confirm the source's nature. This highlights the crucial role of eROSITA, with its large sky coverage, in identifying extended X-ray sources such as SNRs.

4.1.2 ...and what do they tell us about CRs?

Overview

The primary aim of the first half of this dissertation is to address the question: **How can CRs be accelerated to such extreme energies?**[1]

Achieving VHE levels for CRs requires the injection of energy from extreme astronomical sources such as SNRs, PWNe, or AGNs. Observations of γ-ray emission from SNRs like RX J1713.7-3946 and W44 (Butt et al., 2001; Aharonian et al., 2006; Ackermann et al., 2013; Abe et al., 2025) provide direct evidence of efficient particle acceleration at these sites. While the well-established diffusive shock acceleration mechanism generally explains the acceleration of particles to the "knee" of the CR spectrum (Schure et al., 2012; Blasi, 2013), alternative processes such as CR streaming instability (Bell, 2004; Oh, 2011) have also been proposed.

Despite significant progress, confirming SNRs as the primary energy sources for Galactic CRs remains challenging due to observational constraints (e.g., Bell et al., 2013) and theoretical uncertainties (e.g., Cristofari et al., 2020). To address the main question posed at the beginning of this chapter, we can break it down into the following sub-questions:

- Can SNRs accelerate particles to PeV energies, and if so, up to what ages? (Refer to Fig. 4.4 for an illustration of how the CR-induced γ-ray spectrum in the VHE range evolves with SNR age.)

[1] Up to PeV for Galactic CRs and even to 10^{20} eV overall; see Fig. 1.6.

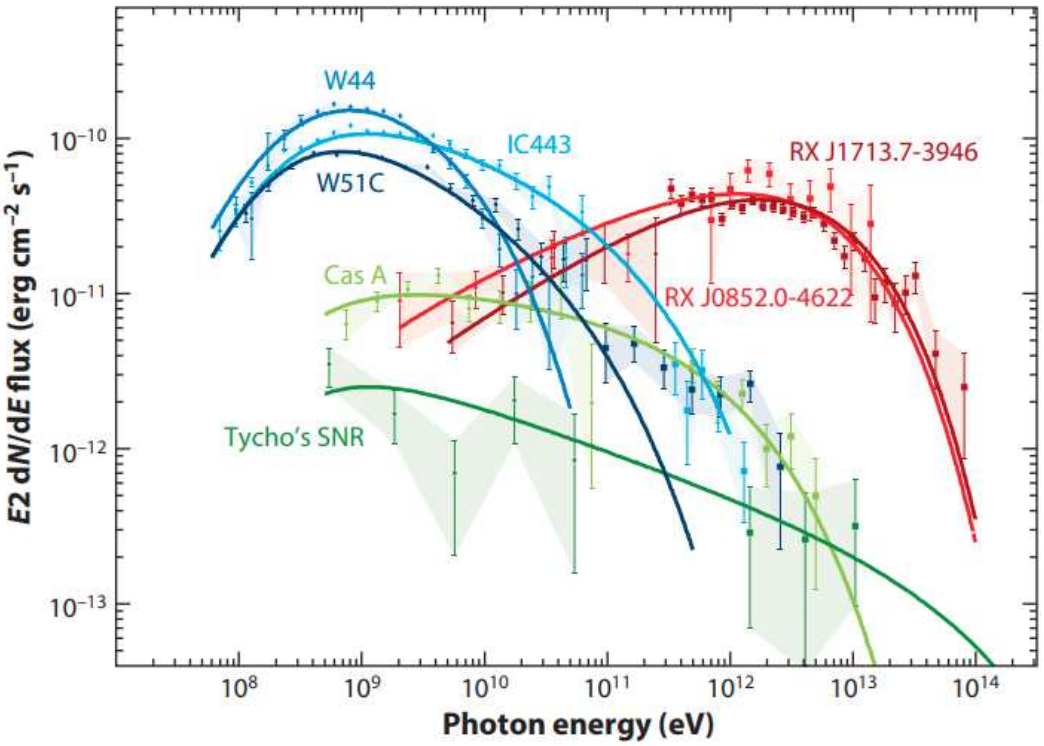

Figure 4.4: γ-ray spectra of well-known SNRs with corresponding best-fit hadronic models. The overall shapes of the γ-ray spectra exhibit distinct characteristics depending on the SNR age, ranging from very young to young and middle-aged SNRs (green, red, and blue, respectively). Credit: Funk (2015).

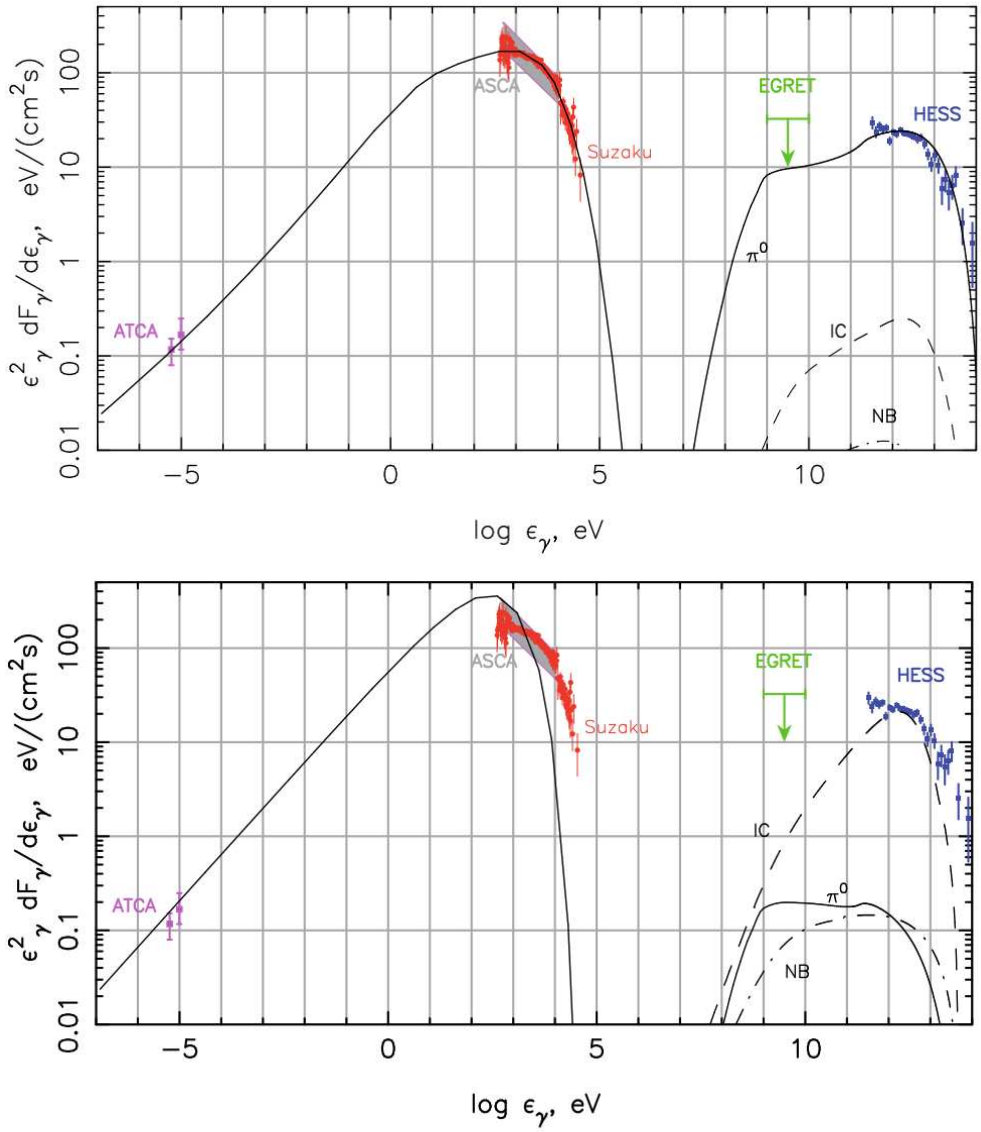

Figure 4.5: Broadband SED of SNR RX J1713.7-3946. Data are shown in 4 electromagnetic wavebands: radio, X-ray, very high energy (GeV), and VHE (TeV). Overlaid are the spectral models for hadronic (*top*) and leptonic (*bottom*) induced γ-rays. Credit: Berezhko & Völk (2008).

- What are the dominant acceleration mechanisms? (Diffuse shock acceleration, CR streaming instability, etc.)
- What is the relative energy contribution to leptonic and hadronic CRs? (See Fig. 4.5 for an example of disentangling these mechanisms using broadband SED analysis.)
- Up to what energies do Galactic CRs contribute to the total all-particle CR spectrum?
- How do CRs propagate through and modify the ISM?
- Ultimately, can SNRs be confirmed as the primary Galactic CR factories, or is it essential to consider alternative candidates? There are discussion that SNRs inject CRs into large stellar clusters, and these clusters (at large cluster shocks) then accelerate CRs to PeV (e.g., Aharonian et al., 2022, 2024).

In this study, we focus on two newly discovered SNRs and SNR candidates, both exhibiting strong TeV emission. Consequently, the most effective strategy moving forward is to conduct a broadband SED analysis of their γ-ray emissions. This approach directly addresses the third question listed above and indirectly helps answer the overarching question about CR acceleration. Our analysis indicates a leptonic origin for the observed VHE γ-rays can not be ruled out for both sources. The GeV data (from *Fermi*-LAT) and TeV measurements (from the H.E.S.S. Galactic Plane Survey) combine to form a steep spectrum, lacking the classical π^0 decay "bump" typically associated with hadronic scenarios (See Fig. 4.5, top panel). In both cases, the constructed emission models favor IC radiation produced by CR electrons over interactions between CR protons and surrounding material (see Fig. 4.6 and 4.7). This suggests that these SNRs can effectively accelerate CR electrons to TeV energies, producing synchrotron radiation that extends into the X-ray range, but the hadronic content can not be seen with current observations.

To construct the pure leptonic model, the required magnetic field strengths are $6\,\mu$G and $25\,\mu$G for HESS J1534-571 and HESS J1614-518, respectively (Fig. 4.6 and 4.7, top panels). These values are constrained by the radio and VHE γ-ray flux and are consistent with expectations from simple shock compression in SNRs (Ferriere, 2009). As reported by Ferriere (2009), the average magnetic field near the Galactic plane is typically around $10\,\mu$G, though localized filaments or dense interstellar clouds can reach much higher field strengths, sometimes exceeding 1 mG. However, the magnetic field values inferred here raise challenges as they are somewhat lower than expected for recent effective particle acceleration, suggesting potential inconsistencies or additional complexities in the modeling. Alternatively, if hadronic CRs contribute minimally, a high magnetic field is not required, and a value only a few times the typical ISM level ($3\,\mu$G) would be sufficient for CR electron acceleration via DSA.

For the hadronic models of VHE γ-ray emission, a significantly higher magnetic field is required to suppress the contribution of IC radiation at these frequencies. Specifically, the magnetic field strengths needed are $25\,\mu$G for HESS J1534-571 and $50\,\mu$G for HESS J1614-518 (Fig. 4.6 and 4.7,

bottom panels). The hadronic scenario for HESS J1614-518 is unlikely, as the required total energy input into CR protons exceeds the typical kinetic energy available from SNs, which is around 10^{51} erg. In contrast, for HESS J1534-571, the hadronic γ-ray production could be argued based on the similarity of the TeV brightness map and the gas tracer (e.g., the narrow band 6.4 keV map) on a large scale level. In fact, additional evidence for the presence of molecular clouds has been observed, showing a degree of spatial similarity. The characteristics of the ambient environment are indeed crucial in shaping the observed photon spectra from SNRs. For instance, the VHE emission could follow the hadronic case unless the gas density in the vicinity of the SNR is particularly low ($< 0.1\,\mathrm{cm}^{-3}$) or the photon background is enhanced ($u_{rad} \sim 10\,\mathrm{eVcm}^{-3}$) (Corso et al., 2023).

Although identifying hadronic SNRs remains a challenging task, our findings emphasize the importance of detailed and comprehensive analyses, complemented by multiwavelength observations across various instruments, to disentangle the γ-ray production mechanisms at SNRs. A deeper understanding of the local conditions such as photon fields, ambient gas density, and magnetic turbulence will be critical to refining these models and constraining the scenarios. With sufficient hadronic SNRs observed, we would move one step closer to determining whether SNRs can be the primary accelerators of Galactic CRs.

Discussion

The results presented in this thesis demonstrate the capability of recent and current X-ray observatories (*Suzaku*, *XMM-Newton*, eROSITA) in studying particle acceleration activities in SNRs. In particular, eROSITA, even at current survey depth, serves as an excellent SNR finder in X-ray wavelengths, thanks to its unprecedented sensitivity in the soft X-ray range and large sky coverage. This opens a new era for the study of SNRs and extended X-ray sources.

However, the all-sky survey mode necessitates deep X-ray follow-ups to investigate the hot plasma content and CR acceleration mechanisms in greater detail. Even with eROSITA's large coverage, discovering the faint X-ray shell was not straightforward. In our analysis, we observed X-ray emission from the source only when we suppressed energies below 1.3 keV (Pühlhofer et al. 2025). Nonetheless, the morphological analysis of the SNR in X-ray wavelengths requires deeper targeted observations to achieve more robust results. Future X-ray observations, with appropriate strategies, will significantly enhance our understanding of the hot gas physics at the SNR site, particularly by defining the shock region and improving spectral constraints with better-controlled backgrounds. In the context of studying SNRs (with diameters typically on the order of degrees), eROSITA can serve as a source finder and diagnostic tool, paving the way for deeper targeted observations, especially with complementary high spatial and spectral resolution instruments like *Chandra* (Weisskopf et al., 2000) and XRISM (Tashiro et al., 2020).

On the other hand, as shown in our analysis of these two sources, and in other cases such as SNR Cassiopeia-A (e.g., Abdo et al., 2010b), distinction between leptonic and hadronic models

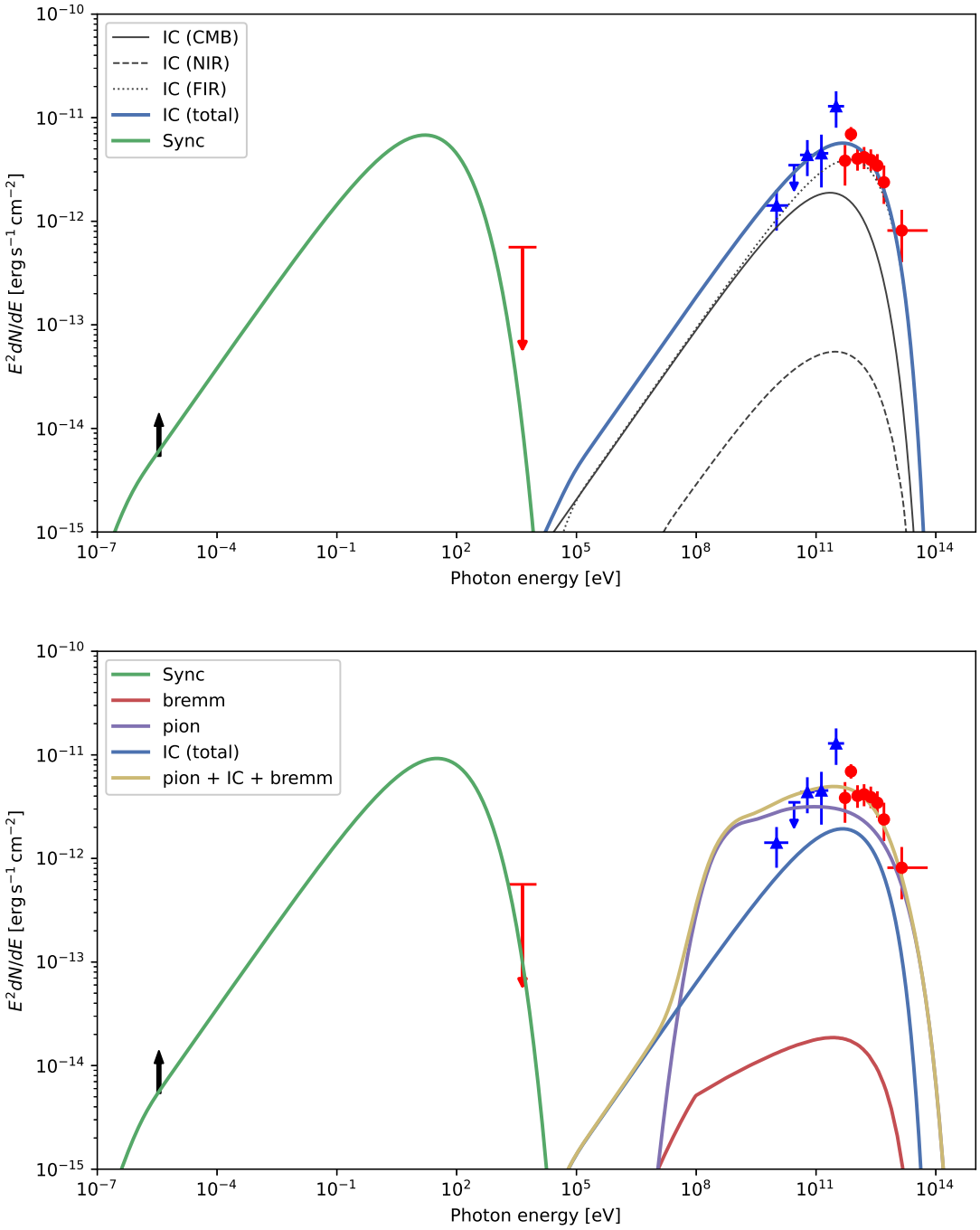

Figure 4.6: Broadband SED of SNR HESS J1534-571. Overlaid are constructed models for a pure leptonic γ-ray production (*Top*) and a hadronic scenario (*Bottom*). Figure taken from Nguyen-Dang et al. (2023).

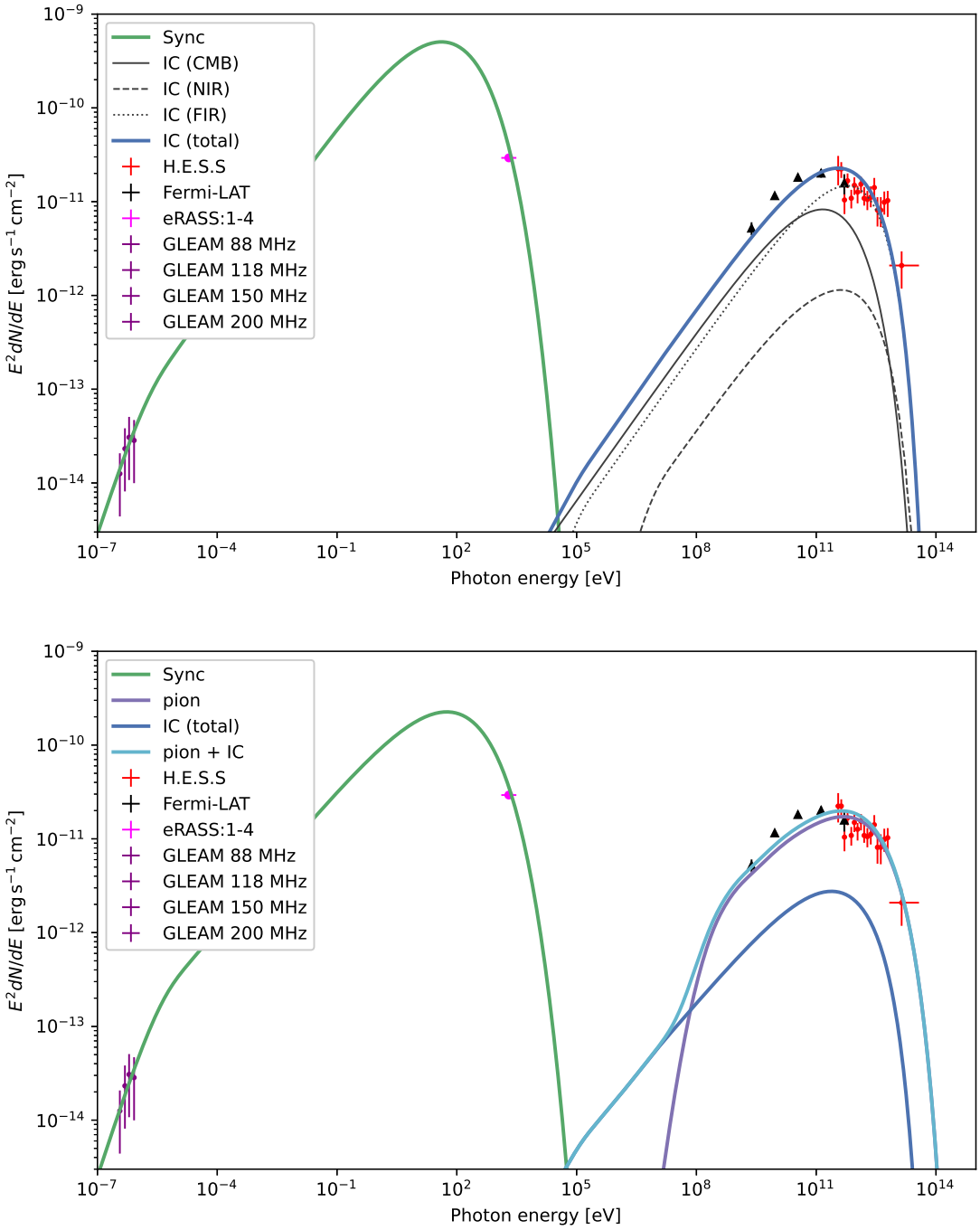

Figure 4.7: Broadband SED of SNR HESS J1614-518. Overlaid are constructed models for a pure leptonic γ-ray production (*Top*) and a hadronic scenario (*Bottom*). Figure taken from Pühlhofer et al. (2025).

for VHE emission can be ambiguous. For Cassiopeia-A, the proposed leptonic model involves both IC and bremsstrahlung radiation in a highly amplified magnetic field (0.1-0.3 mG) and high effective density ($\sim 26\,\mathrm{cm}^{-3}$). Although the hard spectrum below 1 GeV favors a hadronic origin, ruling out the leptonic model is not conclusive (Abdo et al., 2010b). Therefore, having sufficient measurements in the MeV-GeV range is crucial for investigating the origin of high energy and VHE γ-rays. This challenge is expected to be addressed by future telescopes such as AMEGO-X (covering from 100 keV to 1 GeV, Caputo et al., 2022) or eASTROGAM (covering from 0.3 MeV to 3 GeV, de Angelis et al., 2018). With its PSF approximately two times smaller than *Fermi*-LAT, AMEGO-X will be able to measure the γ-ray spectra of the most promising Galactic hadronic sources, including SNRs such as IC,443, W44, and W51C (Caputo et al., 2022). Fig. 4.8 illustrates the contribution of AMEGO-X for a case of a γ-ray blazar[2]. Complemented by radio observations, AMEGO-X will help estimate the magnetic field in these hadronic accelerator candidates and improve our understanding of particle acceleration in the Milky Way.

In conclusion, the open questions regarding the when (up to what age of SNRs) and how (which population, how much energy is injected per particle) Galactic CRs are produced remain to be addressed. Answering these questions requires multiwavelength efforts and enhanced instrumentation. Using shock-heated plasma as the primary diagnostic tool, X-ray observatories with large coverage, such as eROSITA, will provide more X-ray counterparts of TeV-selected SNRs as well as searching for new SNRs. These will complement high-resolution instruments such as *Chandra*, XRISM, and ATHENA to study the shock more exhaustively. Furthermore, with the aid of complementary observations, such as CO(1–0) emission maps, the search for molecular clouds near these sources will provide direct hints for the hadronic scenario. Finally, expanding measurements of the spectra of SNRs at medium and ultra-high frequencies with AMEGO-X (Caputo et al., 2022) and LHAASO (from 20 TeV to 1 PeV, Cao et al., 2019) will complete the radiation models and offer improved constraints on the origin of high to VHE γ-ray emission from SNRs.

[2] A type of AGN that emits extremely high-energy γ-rays (e.g., Abdo et al., 2010a)

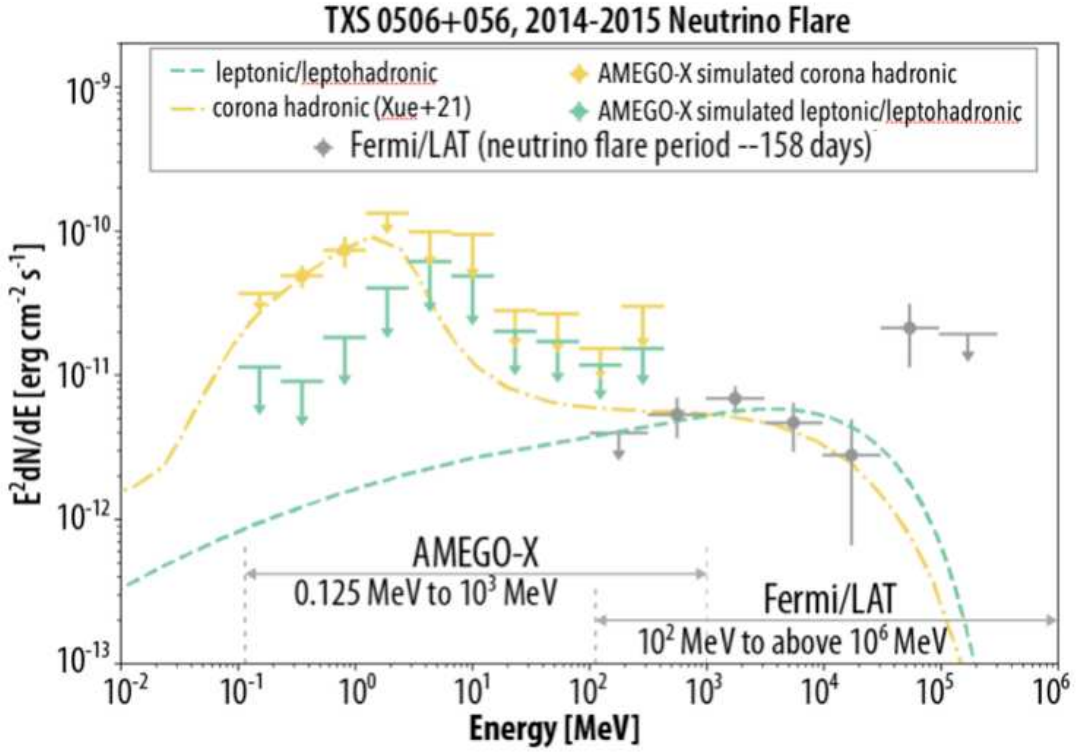

Figure 4.8: Simulated SED of the γ-ray blazar TXS 0506+056 (2014). Simulated data and models for different component are shown in yellow and green markers and lines. Gray data points are observations from *Fermi*-LAT. As can be seen, AMEGO-X is poised to fill in the gap in the medium energy frequencies right below the current range of *Fermi*-LAT. Figure taken from Caputo et al. (2022).

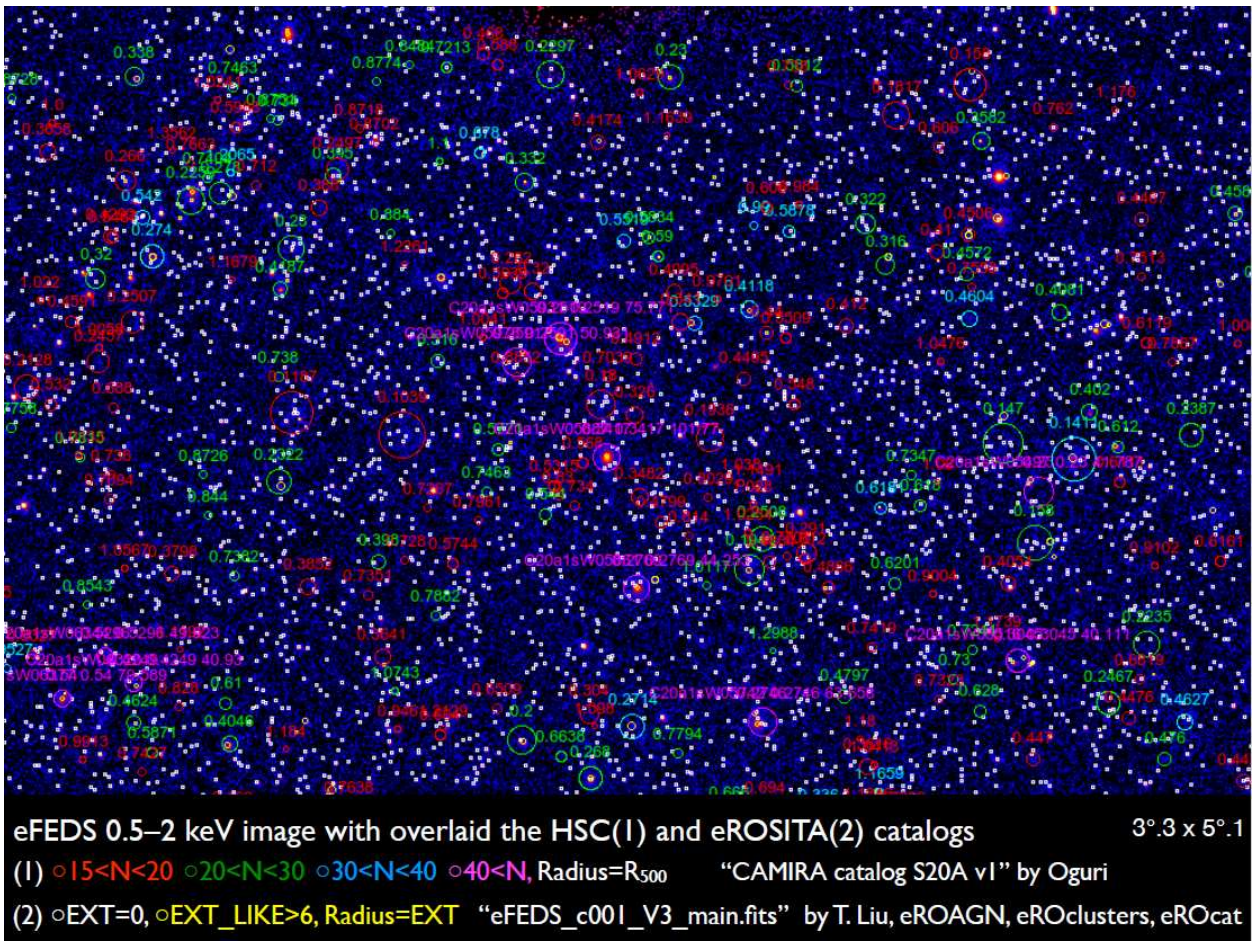

Figure 4.9: eFEDS image in the soft-band energy (0.5-2.0 keV), overlaid are the sources detected with the HSC and eROSITA survey (Oguri et al., 2018; Liu et al., 2022). Credit: Naomi Ota.

4.2 Multiwavelength study of galaxy clusters

4.2.1 Overview

The CAMIRA optical sample

The CAMIRA algorithm (**C**luster finding **A**lgorithm based on **M**ulti-band **I**dentification of **R**ed-sequence g**A**laxies) is a technique for detecting galaxy clusters (Oguri, 2014). It was developed for application in ongoing and future wide-field optical imaging surveys, such as the Subaru Hyper Suprime-Cam (Subaru HSC; Miyazaki et al., 2012). The CAMIRA algorithm was applied to the HSC Wide S16A dataset, covering 232 $\deg^2$, to construct a catalog of 1,921 clusters in the redshift range $0.1 < z < 1.1$ with a richness[3] threshold of $\hat{N}_{\rm mem} > 15$, which is approximately equivalent to $M_{200} > 10^{14} h^{-1} \mathrm{M}_\odot$.

For a given cluster sample, completeness and purity address the following questions:

[3]Cluster richness refers to the number of member galaxies detected.

- **Completeness:** Does the sample cover the full mass range of the cluster population? For example, are low-mass or faint clusters missing due to a high detection threshold?
- **Purity:** How many clusters in the sample are genuine, rather than false detections caused by factors such as projection effects?

The CAMIRA optical cluster catalog exhibits high completeness and purity ($> 90\%$) for massive systems, as confirmed by an analysis using mock cluster catalogs (Oguri et al., 2018). Nevertheless, the completeness estimation is constrained by the limited size of available X-ray samples, therefore future analyses with larger X-ray datasets will be valuable.

In this work, we utilize the latest HSC imaging (S20A), combined with high-quality X-ray data from the eFEDS survey (Predehl et al., 2021; Liu et al., 2022), to investigate the global properties of optically selected clusters. Our goal is to establish cluster scaling relations and assess different cluster selection methods.

Stacking analysis

Only about one-fifth of the CAMIRA optical clusters have at least one X-ray counterpart in the eFEDS field. Figure 4.9 shows the spatial distribution of clusters in a $3.3^\circ \times 5.1^\circ$ region of the eFEDS sky area. CAMIRA clusters of different richness (marked by red, green, blue, and magenta circles) appear significantly more abundant than the extended sources from the eFEDS X-ray catalog (denoted by yellow circles). To identify eFEDS counterparts of CAMIRA clusters, we cross-matched the two catalogs. A match was considered valid if an X-ray extended source was located within R_{500}[4] of the CAMIRA cluster center and had a redshift difference $|\Delta z| < 0.02$ relative to the CAMIRA cluster redshift. The absence of X-ray counterparts suggests that approximately $\sim 80\%$ of CAMIRA clusters in the eFEDS footprint are undetected at the current X-ray sensitivity.

If a real cluster exists in a given direction but is not listed in the eFEDS X-ray cluster catalog, this could be due to its X-ray emission being below the detection threshold or its compact and faint emission causing it to be misclassified as a point source. Additionally, contamination from a nearby bright X-ray point source (e.g., an AGN) could reduce the likelihood of the cluster being detected as an extended source. Bulbul et al. (2022) investigated this issue and compiled an additional catalog of eFEDS galaxy clusters and groups from the eFEDS point source catalog, which includes sources below the extent likelihood threshold of the extent-selected sample (see Fig. 4.11). When we applied our cross-matching criteria to this supplementary catalog, the matched fraction increased only slightly from $\sim 17\%$ to $\sim 25\%$, and our subsequent analyses remained unchanged.

Therefore, we applied a stacking analysis to improve the statistical significance of our results. This approach is widely used in other studies (e.g., Oguri, 2014; Murata et al., 2019; Chiu et al.,

[4]The radius within which the average density is 500 times the critical density ρ_c of the Universe at that redshift.

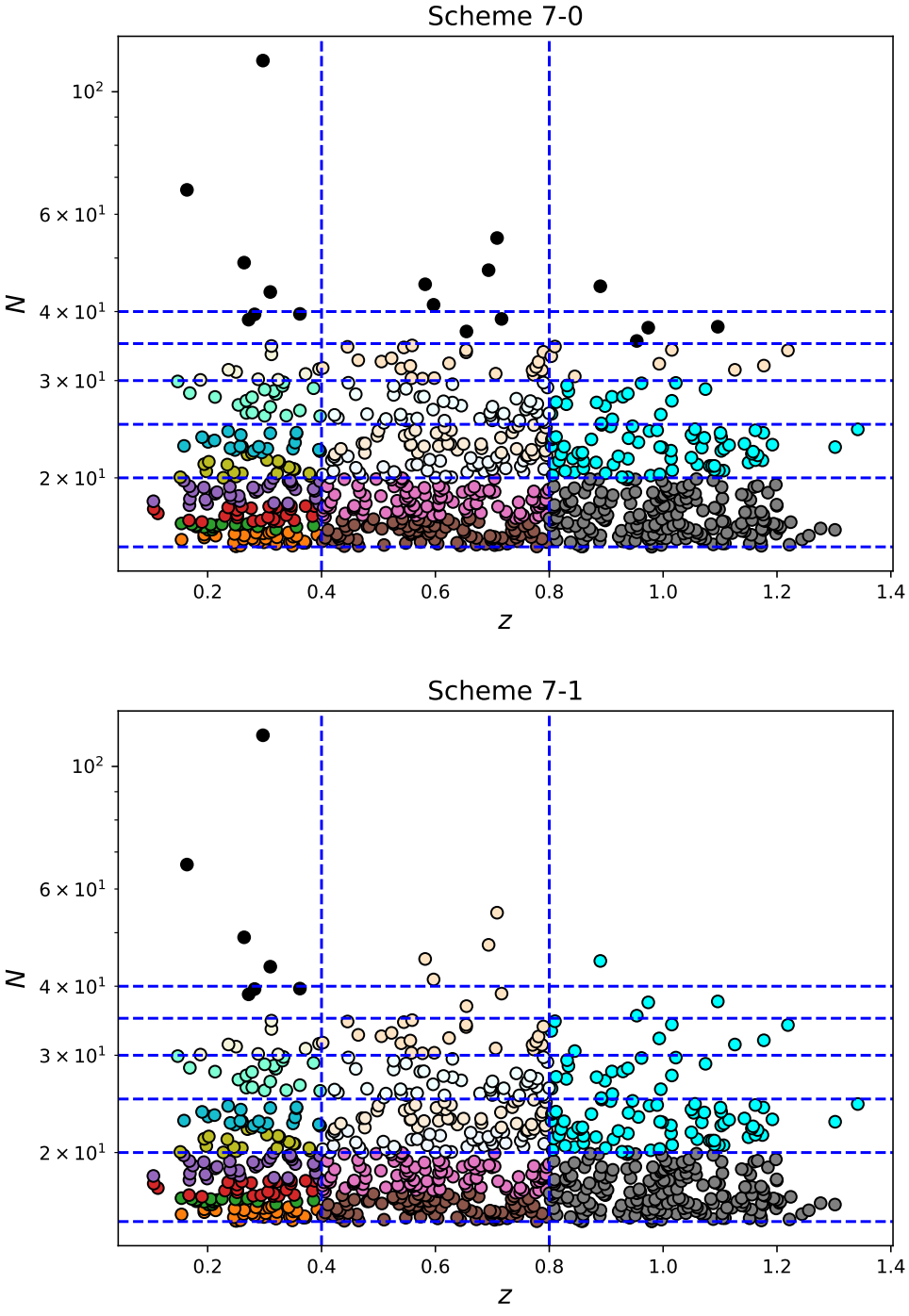

Figure 4.10: Examples of testing the binning schemes. See text for more details.

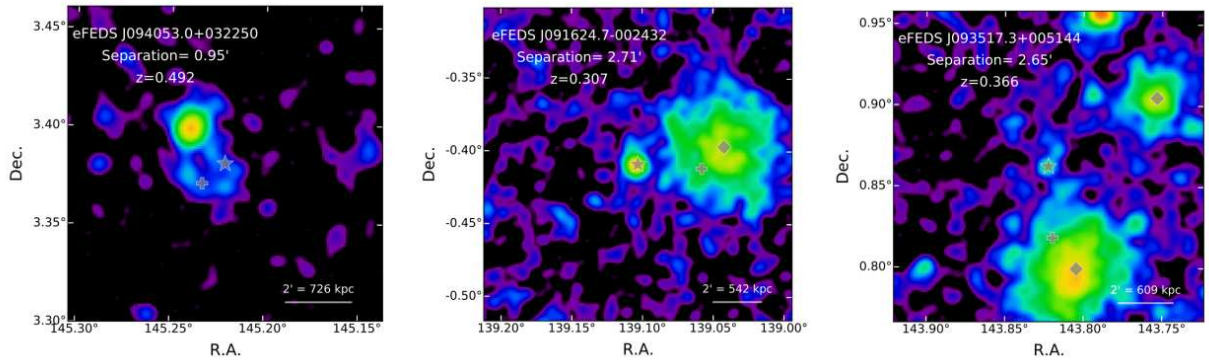

Figure 4.11: Examples of eROSITA clusters that were listed in the point source catalog, matched with the public SZ catalogs using a matching radius of 3 arcmin (Planck Collaboration et al., 2016; Bulbul et al., 2022). In each image, the gray star indicates the X-ray position of the cluster as listed in the point source catalog, which also serves as the center of the image. Extended sources in the field, belonging to the extended catalog (Liu et al., 2022), are marked with gray diamonds. The SZ centroid from the Planck catalog is denoted by a cross. Figure taken from Bulbul et al. (2022).

2020). Our goal was to group the clusters into bins such that each bin contained at least 500 total counts. We tested different thresholds and found that this count limit provides a good balance between statistical robustness and maintaining a sufficient number of stacked bins. To define an optimal binning scheme, we first divide the clusters into initial groups based on their richness and redshift. For redshift, we broadly categorize clusters into low, medium, and high redshift with $z < 0.4$, $0.4 \leq z < 0.8$, and $z \geq 0.8$, respectively. In terms of richness, clusters are divided into bins as follows: $15 \leq N < 20$, $20 \leq N < 25$, $25 \leq N < 30$, $30 \leq N < 35$, $35 \leq N < 40$, and $N \geq 40$. If we simply stack clusters based on this initial division, we would have 18 bins. However, there are two reasons why this may not be the optimal approach. First, fewer clusters are detected at higher redshifts (see Fig. 4.10), meaning the total counts in such bins may fall below the threshold of 500. To meet the minimum count requirement, it is necessary to combine high redshift clusters from adjacent bins. Meanwhile, clusters in the low redshift and low richness regime are abundant, often exceeding the required count. Hence, it is beneficial to further divide these initially large groups into smaller subsets.

With this flexible binning strategy, that is merging adjacent bins when the total count is insufficient (< 500) and splitting bins when the total count is excessive ($\gg 500$), we divided the CAMIRA clusters into 27 stacked bins of similar redshift and richness (see Fig. 1, Nguyen-Dang et al. 2025). The scaling relation analysis was then conducted using the averaged stacked observables, weighted by the signal-to-noise ratios from weak lensing measurements.

When merging clusters from adjacent initial groups, a key question arises: should the clusters be combined based on similar N or similar z? To address this, we tested both approaches by comparing their binning outcomes and the resulting best-fit scaling relations. Fig. 4.10 illustrates the binning schemes for $\sim$ 200 CAMIRA clusters that have X-ray counterparts in eFEDS, where

the upper and lower panels show stacking by similar N and similar z, respectively. Fig. 4.12 presents the best-fit power-law for the $L-N$ and $L/E(z)-NE(z)$ relations of the stacked clusters, obtained using a Bayesian regression method (Kelly, 2007). While the best-fit results do not differ significantly between the two binning methods, the scatter is notably lower when a redshift evolution factor, $E(z)$, is applied. We further validated the consistency of these binning schemes using simulations with the SIXTE program (Dauser et al., 2019).

Other works apply stacking based on simple redshift divisions (e.g., Oguri, 2014) or use the Voronoi technique (e.g., Bahar et al., 2024). In our case, the sample spans a wide range of richness and redshift, allowing for a finer division that incorporates both N and z as criteria. Stacking schemes have proven effective in compensating for the low counts of distant objects. However, the stacking objects in our work are weighted using the weak lensing signal-to-noise ratios, which may introduce a bias towards higher-mass and lower-redshift objects. These objects are more likely to be detected using the red-sequence method and also tend to have better weak lensing measurements. When comparing the best-fit scaling relations reported in Nguyen-Dang et al. (2025) to those in Ota et al. (2023), we find that the log-normal intrinsic scatters are reduced through stacking analysis. While stacking is a powerful method for tackling the low-count regime, simulations such as those by Popesso et al. (2024) show that this technique introduces potential uncertainties that must be carefully considered for precision cosmology applications.

Uncertainties of morphological analysis

In Ota et al. (2023), we focused on a set of 43 high-richness clusters ($N > 40$), i.e., massive systems. The X-ray emission from such massive clusters is easily detected in the eFEDS X-ray catalog, allowing the BCG - X-ray peak offset to serve as a reliable morphological indicator. Furthermore, the sufficient X-ray detection of these clusters enables the use of additional X-ray derived morphological parameters, such as X-ray concentration index (Maughan et al., 2012; Ghirardini et al., 2022).

However, in our extended work (Nguyen-Dang et al. 2025), as mentioned above, approximately 80% of clusters show no prominent X-ray detection, even with an exposure equivalent to eight sky scans by eROSITA. Consequently, the estimation of their dynamical state is affected by the high uncertainties associated with X-ray peak measurements. This poses a challenge in determining the relaxed fraction of the sample, leading us to report a conservative upper limit. To strengthen our results, we calculate the BCG - X-ray peak offsets for different subgroups, allowing a direct comparison with the morphological results of the eFEDS clusters reported by Ghirardini et al. (2022). The consistency between these analyses, along with agreement with the simulations by Seppi et al. (2023), supports the dynamical state conclusions presented in our second paper.

Additionally, challenges arise in the identification of the BCGs. In fact, 229 out of 997 CAMIRA clusters in the eFEDS field lack photometric and/or redshift measurements in current optical/NIR databases. This is not unexpected, as the Subaru HSC survey is among the deepest and most

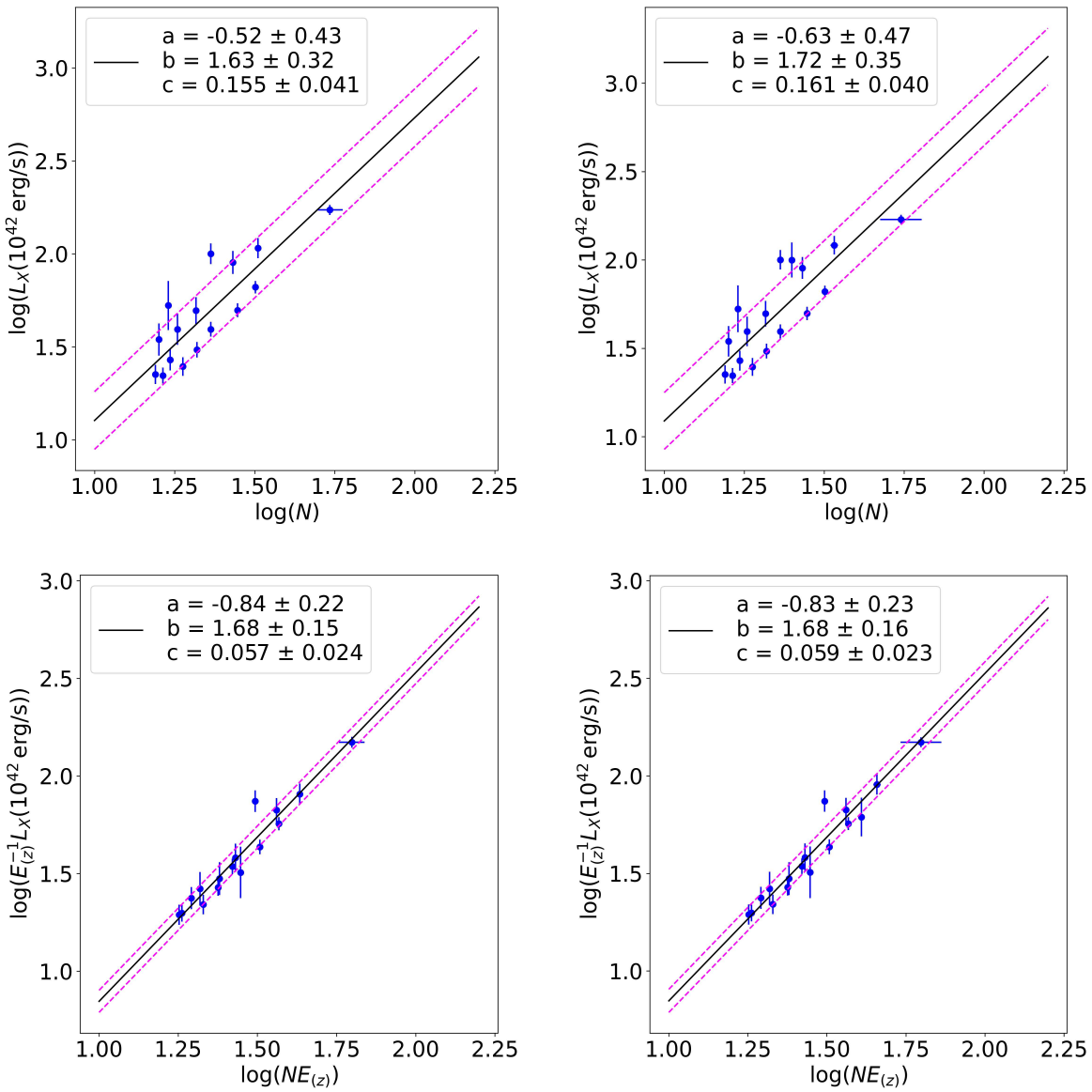

Figure 4.12: Test results of fitting the $L-N$ and $L/E(z)-NE(z)$ relations of stacked clusters to a power-law function using a Bayesian regression method. The best-fit parameters a, b, c indicate the intercept, normalization, and log-normal intrinsic scatter, respectively.

efficient cluster finders. Misidentification of the BCGs introduces another source of uncertainty in the morphological analysis. To account for these uncertainties, we estimate statistical errors via bootstrap resampling, address systematic errors by varying the smoothing scale of the X-ray images, and incorporate instrumental resolution effects.

4.2.2 Conclusion remarks

The best-fit slopes of the $L-T$, $L-M$, and $N-M$ scaling relations in our work (Ota et al., 2023; Nguyen-Dang et al. 2025) show good agreement with previous studies. Table 4.1 summarizes recent best-fit slopes of scaling relations, with the results from our study highlighted in bold. The prediction from self-similar model for the slope of the X-ray relations are $L_{\rm bol} \propto T^2$ and $L_{\rm bol} \propto M^{4/3}$ (Equation 1.15 and 1.13). While the exact fitting methods and corrections for selection bias may vary between studies, the overall values remain within a similar range. Below is a summary of our findings:

First, our results confirm that stacking analysis is an effective approach for enhancing statistical robustness when applied to a uniform dataset spanning a wide range of properties.

Second, the dynamical state analysis of the CAMIRA clusters in the eFEDS field indicates that only a small fraction ($\ll 50\%$) are relaxed. This fraction is significantly lower than typical values reported in X-ray-selected samples (e.g., Rossetti et al., 2016) but is consistent with the eFEDS sample and other optical samples (e.g., Ota et al., 2020). When applying the same analysis only to CAMIRA clusters with eFEDS counterparts, the relaxed fraction aligns with the value reported by Ghirardini et al. (2022). This suggests that our morphology analysis, despite its challenges, provides reasonable results. This conclusion is further supported by the simulation study of eFEDS clusters by Seppi et al. (2023).

Third, the best-fit slopes of the scaling relations in our work and other studies show small variations. In most cases, the observed slopes are steeper than those predicted by self-similarity. This implies that non-gravitational effects, such as AGN feedback and recent mergers, play a non-negligible role in cluster evolution, particularly in low-mass groups and clusters (Lovisari & Maughan, 2022). A better understanding of these effects, and improved calibration, is crucial for cosmological applications.

Fourth, the use of X-ray data to complement the CAMIRA optical sample has enabled a direct and uniform comparison between optical clusters with and without X-ray counterparts. The results from both the $L-M$ scaling relation and the X-ray radial profiles indicate that optical clusters with X-ray counterparts differ from optical clusters that remain undetected in current X-ray surveys. At the same time, the optical $N-M$ relation, which connects optical richness to cluster mass (obtained from WL calibration in our work), does not show a distinct trend between the two categories. This suggests that the optical sample presented in this work is highly complete and includes a diverse population of clusters, even those with ICM properties unsuitable for X-ray detection. In other words, the optically selected sample consists of genuine clusters with

consistent optical properties, while their varying X-ray properties affect their detectability in X-ray surveys.

Finally, our work emphasizes the importance of a multiwavelength approach in cluster studies. Looking ahead, the deeper, five-stacked eROSITA all-sky survey (eRASS:5), which covers a much larger area than eFEDS, has the potential to significantly expand our sample size. Our studies have demonstrated that eROSITA, particularly in combination with HSC data, is a powerful tool for improving our understanding of scaling relations and selection effects. This, in turn, is essential for constructing comprehensive cluster samples to refine cosmological constraints.

Table 4.1: Overview of observed scaling relations.

Relation	Observed	Comments	Reference
$L_{\rm bol} - T$	$\mathbf{2.08 \pm 0.46}$	43 clusters, z = 0.16-0.89	Ota et al. (2023)
	2.26 ± 0.29	50 clusters, z = 0.15-0.55	Mahdavi et al. (2013)
	2.72 ± 0.18	114 clusters, z = 0.10-1.30	Maughan et al. (2012)
	2.64 ± 0.20	64 clusters, z = 0.01-0.15	Mittal et al. (2011)
	2.53 ± 0.15	232 clusters, z = 0.04-1.46	Reichert et al. (2011)
	2.70 ± 0.24	31 clusters, z = 0.06-0.17	Pratt et al. (2009)
	2.61 ± 0.32	37 clusters, z = 0.14-0.30	Zhang et al. (2008)
$L_{\rm bol} - M$	$\mathbf{1.67 \pm 0.18}$	27 stacked clusters, z = 0.1-1.4	Nguyen-Dang et al. (2025)
	$\mathbf{1.52 \pm 0.34}$	38 clusters, z = 0.16-0.89	Ota et al. (2023)
	1.59 ± 0.14	434 clusters, z = 0.01-1.3	Chiu et al. (2022)
	2.15 ± 0.24	59 clusters, z = 0.2-1.5	Bulbul et al. (2019)
	1.51 ± 0.09	232 clusters, z = 0.04-1.46	Reichert et al. (2011)
	1.90 ± 0.11	31 clusters, z = 0.06-0.17	Pratt et al. (2009)
	2.33 ± 0.70	37 clusters, z = 0.14-0.30	Zhang et al. (2008)
$N - M$	$\mathbf{0.88 \pm 0.10}$	27 stacked clusters, z = 0.1-1.4	Nguyen-Dang et al. (2025)
	0.49 ± 0.20	25 clusters, z = 0.35-0.65	Kiiveri et al. (2021)
	0.92 ± 0.13	$\sim$ 20 stacked clusters, z = 0.2-1.1	Chiu et al. (2020)
	0.86 ± 0.05	$\sim$ 12 stacked clusters, z = 0.1-1.0	Murata et al. (2019)
	0.72 ± 0.12	$\sim$ 200 clusters, $z < 0.35$	Rozo & Rykoff (2014)
	1.44 ± 0.27	5 stacked clusters, z = 0.1-0.3	Oguri (2014)

CHAPTER 5

Future projects

Upon completing my doctoral projects, I plan to pursue several related topics as a continuation of the results presented in this dissertation. Below are the ongoing and future projects I aim to undertake during my first postdoctoral years.

5.1 Multiwavelength study of another Galactic Supernova remnant

As mentioned in Section 4.1, current deep-imaging telescopes such as *Chandra* (Weisskopf et al., 2002) provide powerful tools to study the detailed physics at SNR regions. At shock fronts, matter is compressed, and strong magnetic fields are generated. The streaming instability of CRs further amplifies these shock-induced magnetic fields. Synchrotron radiation, emitted by relativistic electrons moving in these amplified magnetic fields, produces thin, sharp filaments observed in X-rays. A notable example is SNR HESS J1731-347 (Fig. 5.1).

HESS J1731-347 is a shell-type SNR with distinct non-thermal X-ray spectra that has been extensively studied (H.E.S.S. Collaboration et al., 2011; Doroshenko et al., 2017, 2023). In this work, we focus on investigating the shock-induced filaments of the SNR to understand the mechanism of interaction between relativistic electrons and magnetic fields. The origin of such X-ray filaments in SNRs remains debated; they may result from synchrotron losses (Berezhko & Völk, 2004) or magnetic field decay (Pohl et al., 2005). With the derived lower limit of the local magnetic field being significantly higher than the average Galactic ISM value of approximately a few μG (Beck, 2001), we prove the presence of efficiently amplified magnetic fields. This suggests that HESS J1731-347 could serve as a site for cosmic ray proton acceleration under such conditions. Furthermore, we aim to present a morphological study of the filament near the CCO, although the origin of this filament remains unresolved (See Fig. 5.2 for the best-fit morphology of the filament arc near the CCO, usingthe `sherpa` tool[1].). The findings of this study will be

[1] `https://cxc.cfa.harvard.edu/sherpa/`

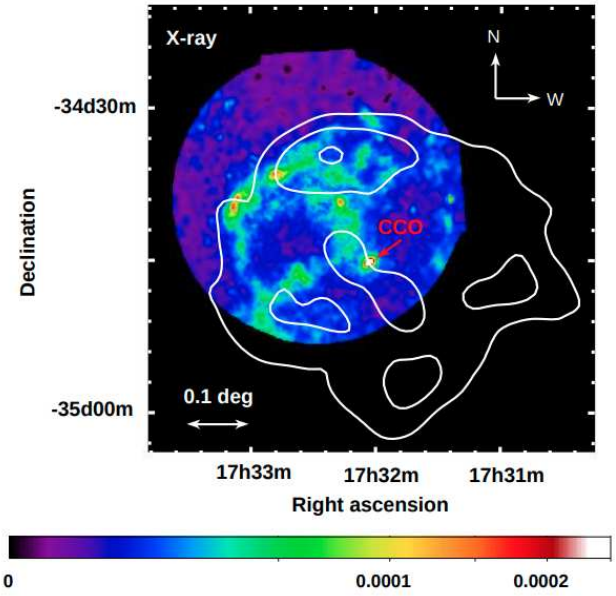

Figure 5.1: *XMM − Newton* observation of a sub-region of HESS J1731-347, in the 0.5–4.5 keV energy band. Overlaid is the TeV map in white contour. The position of the suspected CCO is marked by the red arrow. Figure taken from H.E.S.S. Collaboration et al. (2011).

reported in a forthcoming paper (Nguyen-Dang et al., 2025).

5.2 Multiwavelength study of galaxy clusters

Studying X-ray properties of the CAMIRA optical sample utilizing eRASS:5

Following the submission of our reports on the study of X-ray properties of the CAMIRA optically selected cluster sample (Oguri, 2014; Oguri et al., 2018) using the eFEDS data (coverage of $\sim$ 140 deg^2, depth = 8 eROSITA scans, Predehl et al., 2021; Liu et al., 2022), we plan to extend the investigation using the upcoming eRASS:5 data. As an all-sky survey, eRASS:5 will significantly increase the coverage compared to the test field of eFEDS. The overlap between the HSC-based catalog and eRASS:5 is expected to be approximately 4-5 times larger than the current sample. However, the depth of eRASS:5, equivalent to 5 eROSITA scans, may pose challenges in terms of X-ray uncertainties. Nevertheless, we have demonstrated that stacking analysis is a powerful tool for addressing issues with low-count objects.

With improvements in both sample size and uniformity, we aim to study the ICM characteristics of the optical sample, establish scaling relations, and shed light on the effects of cluster selection methods. The expected results will contribute to understanding the observed cluster population and preparing cluster samples with high completeness, tailored for various purposes of cosmological and astrophysical research.

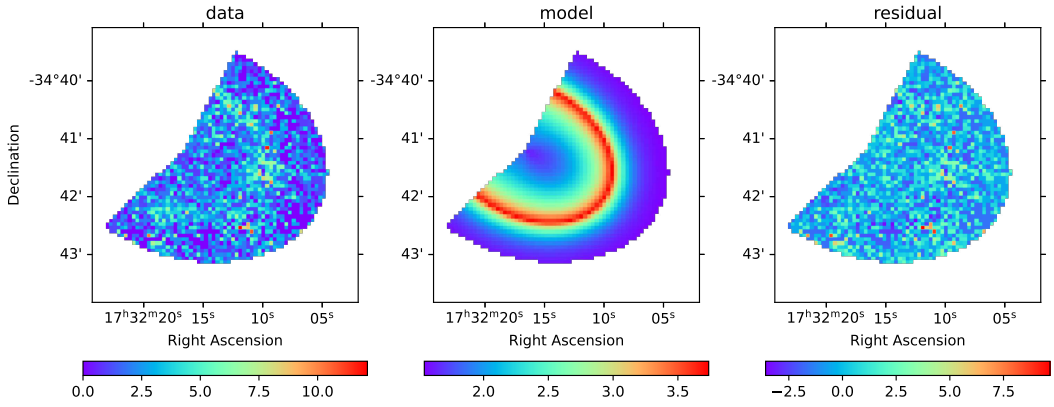

Figure 5.2: 2D fitting of the filament near the CCO of HESS J1731-347, assuming a rotational elliptical model for spatial morphology and a general exponential for the emission profile.

Investigating the causes of scaling relation deviations

Non-gravitational processes, such as AGN (Pounds et al., 1990; Nandra & Pounds, 1994) feedback, introduce significant deviations in observed scaling relations from the predictions of self-similar models by heating and redistributing the ICM. AGN-driven mechanisms, including cavity and shock heating, suppress cooling flows and modify the ICM's density and temperature profiles, ultimately affecting scaling relations like the X-ray luminosity-temperature ($L-T$) relation. Clusters with strong AGN heating often exhibit reduced X-ray luminosities compared to self-similar predictions, placing them as outliers below the best-fit line in the $L-T$ plane. The recently launched XRISM mission[2] is poised to build upon advancements made by Hitomi (Hitomi Collaboration et al., 2016; Tashiro et al., 2020; Ishisaki et al., 2022; Tashiro, 2023; Kilbourne et al., 2024), offering an unprecedented opportunity to study AGN-driven gas motions and their implications for cluster evolution with remarkable precision.

AGN eruptions produce bipolar bubbles of relativistic plasma in the ICM, visible as cavities in X-ray images (Fig. 5.3). These bubbles rise buoyantly, driving turbulence and bulk motions in the surrounding medium. Understanding AGN heating mechanisms requires detailed measurements of gas velocities, which XRISM will achieve using its high-resolution microcalorimeter with an energy resolution of ~ 5 eV. Observations of (highly ionized) Fe XXV emission lines at 6.7 keV (e.g., Reeves, 2003; Bianchi et al., 2007, 2009) will enable line-of-sight velocity measurements with accuracies better than 100 $\mathrm{km\,s^{-1}}$ (XRISM Science Team, 2020). Our simulation have demonstrated that XRISM can reliably detect gas motions on the order of a few hundred $\mathrm{km\,s^{-1}}$ with high precision.

Through the measurement of gas motions in galaxy clusters, this research aims to quantify the

[2]September 7, 2023

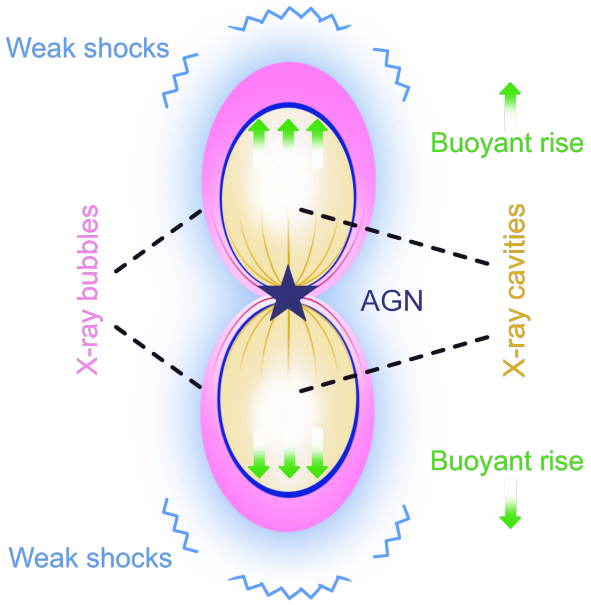

Figure 5.3: Schematic diagram of AGN induced gas motion.

effects of AGN heating on the ICM and assess their contribution to scatter in scaling relations. These findings will provide valuable insights into the activity of AGN in brightest cluster galaxies (BCGs), elucidate the origins of deviations from self-similar scaling relations, and enhance cluster mass calibration, which is a critical factor in cosmological studies (e.g., Ota et al., 2018; Chadayammuri et al., 2021). Recent studies on galaxy cluster topic can be found in XRISM Science Team (2020); Hitomi Collaboration et al. (2018a,b); XRISM Collaboration (2025). Finally, this research will allow us to exploit the capacity of the XRISM observatory and prove its role as one of the highest resolution X-ray facilities to date.

Bibliography

Abdo, A. A., Ackermann, M., Agudo, I., et al. 2010a, , 716, 30 → [p109]

Abdo, A. A., Ackermann, M., Ajello, M., et al. 2010b, , 710, L92 → [p106], [p109]

Abe, S., Abhir, J., Abhishek, A., et al. 2025, arXiv e-prints, arXiv:2501.03889 → [p37], [p102]

Acero, F., Aharonian, F., Akhperjanian, A. G., et al. 2010, , 516, A62 → [p97]

Acero, F., Ballet, J., & Decourchelle, A. 2007, , 475, 883 → [p97]

Ackermann, M., Ajello, M., Albert, A., et al. 2016, , 819, 149 → [p18]

Ackermann, M., Ajello, M., Allafort, A., et al. 2013, Science, 339, 807 → [p102]

Ade, P. A., Aghanim, N., Arnaud, M., et al. 2011, Astronomy & Astrophysics, 536, A8 → [p21]

Aglietta, M., Alessandro, B., Antonioli, P., et al. 2004, Astroparticle Physics, 21, 583 → [p13]

Aharonian, F., Akhperjanian, A. G., Bazer-Bachi, A. R., et al. 2006, , 449, 223 → [p97], [p102]

Aharonian, F., Ashkar, H., Backes, M., et al. 2022, , 666, A124 → [p105]

Aharonian, F., Benkhali, F. A., Aschersleben, J., et al. 2024, , 970, L21 → [p105]

Aharonian, F. A., Akhperjanian, A. G., Aye, K. M., et al. 2004, , 432, 75 → [p9]

Albert, A., Alfaro, R., Alvarez, C., et al. 2024, , 972, 21 → [p13]

Allen, S. W., Evrard, A. E., & Mantz, A. B. 2011, , 49, 409 → [p22]

Allen, S. W. & Mantz, A. B. 2019, in The Chandra X-ray Observatory, 2514-3433 (IOP Publishing), 10–1 to 10–32 → [p17], [p18]

Aloisio, R., Berezinsky, V., Blasi, P., et al. 2007, Astroparticle Physics, 27, 76 → [p13]

Alvarez, G. E., Randall, S. W., Bourdin, H., Jones, C., & Holley-Bockelmann, K. 2018, The Astrophysical Journal, 858, 44 → [p30]

Andreon, S. & Moretti, A. 2011, , 536, A37 → [p20]

Antoni, T., Apel, W. D., Badea, A. F., et al. 2005, Astroparticle Physics, 24, 1 → [p13]

Araya, M. 2017, The Astrophysical Journal, 843, 12 → [p99]

Bahar, Y. E., Bulbul, E., Clerc, N., et al. 2022, , 661, A7 → [p28]

Bahar, Y. E., Bulbul, E., Ghirardini, V., et al. 2024, , 691, A188 → [p115]

Beck, R. 2001, , 99, 243 → [p119]

Bell, A. R. 2004, , 353, 550 → [p102]

Bell, A. R., Schure, K. M., Reville, B., & Giacinti, G. 2013, , 431, 415 → [p37], [p102]

Berezhko, E. G. & Völk, H. J. 2004, , 427, 525 → [p119]

Berezhko, E. G. & Völk, H. J. 2007, , 661, L175 → [p10]

Berezhko, E. G. & Völk, H. J. 2008, , 492, 695 → [p104]

Bianchi, S., Guainazzi, M., Matt, G., & Fonseca Bonilla, N. 2007, , 467, L19 → [p121]

Bianchi, S., Guainazzi, M., Matt, G., Fonseca Bonilla, N., & Ponti, G. 2009, , 495, 421 → [p121]

Blasi, P. 2013, , 21, 70 → [p102]

Bleem, L. E., Bocquet, S., Stalder, B., et al. 2020, , 247, 25 → [p29]

Blumenthal, G. R., Faber, S. M., Primack, J. R., & Rees, M. J. 1984, , 311, 517 → [p17]

Böhringer, H. 1994, in NATO Advanced Study Institute (ASI) Series C, Vol. 441, Cosmological Aspects of X-Ray Clusters of Galaxies, ed. W. C. Seitter, 123–138 → [p18]

Böhringer, H., Schuecker, P., Guzzo, L., et al. 2004, , 425, 367 → [p21]

Bourne, M. A. & Sijacki, D. 2021, , 506, 488 → [p34]

Bradač, M., Clowe, D., Gonzalez, A. H., et al. 2006, , 652, 937 → [pxiv]

Bradač, M., Treu, T., Applegate, D., et al. 2009, , 706, 1201 → [pxiv]

Brandenberger, R. H. 2010, in American Institute of Physics Conference Series, Vol. 1268, Graduate School in Astronomy: XIV Special Courses at the National Observatory of Rio de Janeiro, ed. R. Dupke, J. Alcaniz, R. de La Reza, & S. Daflon (AIP), 3–70 → [p17]

Bromm, V., Yoshida, N., Hernquist, L., & McKee, C. F. 2009, , 459, 49 → [p17]

Brunetti, G. & Jones, T. W. 2014, International Journal of Modern Physics D, 23, 1430007 → [p18]

Bulbul, E., Chiu, I.-N., Mohr, J. J., et al. 2019, , 871, 50 → [p28], [p118]

Bulbul, E., Liu, A., Pasini, T., et al. 2022, , 661, A10 → [p112], [p114]

Burenin, R. A. & Vikhlinin, A. A. 2012, Astronomy Letters, 38, 347 → [p17]

Butt, Y. M., Torres, D. F., Combi, J. A., Dame, T., & Romero, G. E. 2001, , 562, L167 → [p102]

Bykov, A. M., Churazov, E. M., Ferrari, C., et al. 2015, , 188, 141 → [p18]

Cao, Z., Aharonian, F., Axikegu, et al. 2024, Science Bulletin, 69, 2833 → [p13]

Cao, Z., della Volpe, D., Liu, S., et al. 2019, arXiv e-prints, arXiv:1905.02773 → [p109]

Caprioli, D., Blasi, P., & Amato, E. 2009, , 396, 2065 → [p10]

Caputo, R., Ajello, M., Kierans, C. A., et al. 2022, Journal of Astronomical Telescopes, Instruments, and Systems, 8, 044003 → [p109], [p110]

Carlstrom, J., Ade, P. A., Aird, K., et al. 2011, Publications of the Astronomical Society of the Pacific, 123, 568 → [p21]

Cassam-Chenai, G., Decourchelle, A., Ballet, J., Sauvageot, J. L., & Dubner, G. 2004, in IAU Symposium, Vol. 218, Young Neutron Stars and Their Environments, ed. F. Camilo & B. M. Gaensler, 73 → [p97]

Chadayammuri, U., Tremmel, M., Nagai, D., Babul, A., & Quinn, T. 2021, , 504, 3922 → [p122]

Che, H. & Zank, G. P. 2019, in Journal of Physics Conference Series, Vol. 1332, Journal of Physics Conference Series (IOP), 012003 → [p11]

CHEX-MATE Collaboration, Arnaud, M., Ettori, S., et al. 2021, , 650, A104 → [p25]

Chiu, I., Mohr, J. J., McDonald, M., et al. 2018, , 478, 3072 → [p28]

Chiu, I., Umetsu, K., Murata, R., Medezinski, E., & Oguri, M. 2020, , 495, 428 → [p29], [p112], [p118]

Chiu, I.-N., Chen, K.-F., Oguri, M., et al. 2024, The Open Journal of Astrophysics, 7, 90 → [p20]

Chiu, I.-N., Klein, M., Mohr, J., & Bocquet, S. 2023, , 522, 1601 → [p18]

Cho, J. 2014, The Astrophysical Journal, 797, 133 → [p20]

Chowdhury, D., Martin, J., Ringeval, C., & Vennin, V. 2019, , 100, 083537 → [p17]

Clowe, D., Schneider, P., Aragón-Salamanca, A., et al. 2006, , 451, 395 → [pxiv]

Corso, N. J., Diesing, R., & Caprioli, D. 2023, , 954, 1 → [p106]

Cristofari, P., Blasi, P., & Amato, E. 2020, Astroparticle Physics, 123, 102492 → [p102]

Danese, L. & Burigana, C. 1994, in Present and Future of the Cosmic Microwave Background, ed. J. L. Sanz, E. Martinez-Gonzalez, & L. Cayon, Vol. 429, 28 → [p21]

Dauser, T., Falkner, S., Lorenz, M., et al. 2019, , 630, A66 → [p115]

de Angelis, A., Tatischeff, V., Grenier, I. A., et al. 2018, Journal of High Energy Astrophysics, 19, 1 → [p109]

De Lucia, G. & Blaizot, J. 2007, Monthly Notices of the Royal Astronomical Society, 375, 2 → [p21]

Diehl, R. L. 2009, European Physical Journal D, 55, 509 → [p12]

Diesing, R. 2023, , 958, 3 → [p13]

Doroshenko, V., Pühlhofer, G., Bamba, A., et al. 2017, , 608, A23 → [p119]

Doroshenko, V., Pühlhofer, G., & Santangelo, A. 2023, , 679, A152 → [p119]

Drury, L. O., Aharonian, F. A., & Voelk, H. J. 1994, , 287, 959 → [p10]

Dubinski, J. 1998, The Astrophysical Journal, 502, 141 → [p21]

Eckert, D., Molendi, S., & Paltani, S. 2011, , 526, A79 → [p20]

El Bourakadi, K. & Otalora, G. 2024, arXiv e-prints, arXiv:2412.13090 → [p17]

Evans, L. & Bryant, P. 2008, Journal of Instrumentation, 3, S08001 → [p13]

Evrard, A. E. & Henry, J. 1991 → [p25]

Fabian, A. C., Willingale, R., Pye, J. P., Murray, S. S., & Fabbiano, G. 1980, , 193, 175 → [p9]

Fermi, E. 1949, Physical Review, 75, 1169 → [p10]

Ferreira, P. G. & Magueijo, J. 2008, , 78, 061301 → [p17]

Ferriere, K. 2009, Astronomy & Astrophysics, 505, 1183 → [p105]

Filippenko, A. V. 1997, , 35, 309 → [p1]

Foglizzo, T., Kazeroni, R., Guilet, J., et al. 2015, , 32, e009 → [p1]

Funk, S. 2015, Annual Review of Nuclear and Particle Science, 65, 245 → [p103]

Gal-Yam, A., Mazzali, P., Ofek, E. O., et al. 2009, , 462, 624 → [p2]

Gallo, S., Douspis, M., Soubrié, E., & Salvati, L. 2024, , 686, A15 → [p18]

Ghirardini, V., Bahar, Y. E., Bulbul, E., et al. 2022, , 661, A12 → [p115], [p117]

Giodini, S., Lovisari, L., Pointecouteau, E., et al. 2013, , 177, 247 → [p24]

Giuffrida, R., Miceli, M., Caprioli, D., et al. 2022, Nature Communications, 13, 5098 → [p37]

Grandis, S., Klein, M., Mohr, J. J., et al. 2020, , 498, 771 → [p18]

Grandis, S., Mohr, J. J., Costanzi, M., et al. 2021, , 504, 1253 → [p29]

Green, A., Reeves, S., & Murphy, T. 2014, Publications of the Astronomical Society of Australia, 31 → [p14]

Gull, S. F. & Northover, K. J. E. 1975, , 173, 585 → [p20], [p21]

Guo, X. & Xin, Y. 2024, , 965, 28 → [p13]

Guth, A. H. 1981, , 23, 347 → [p17]

Hachisu, I., Kato, M., & Nomoto, K. 1996, , 470, L97 → [p1]

Haungs, A., Rebel, H., & Roth, M. 2003, Reports on Progress in Physics, 66, 1145 → [p13]

Helder, E. A., Vink, J., Bykov, A. M., et al. 2012, , 173, 369 → [p13]

Henry, J. P., Evrard, A. E., Hoekstra, H., Babul, A., & Mahdavi, A. 2009, , 691, 1307 → [p24]

H.E.S.S. Collaboration et al. 2011, , 531, A81 → [p119], [p120]

H.E.S.S. Collaboration et al. 2018a, , 612, A8 → [p14], [p16], [p97], [p99], [p101], [p102]

H.E.S.S. Collaboration et al. 2018b, , 612, A6 → [p10], [p14]

H.E.S.S. Collaboration et al. 2018c, , 612, A1 → [p9]

H.E.S.S. Collaboration et al. 2018d, , 612, A2 → [p15]

H.E.S.S. Collaboration et al. 2023, , 675, A138 → [p18]

Hillas, A. M. 2005, Journal of Physics G Nuclear Physics, 31, R95 → [p9], [p10]

Hinton, J. A. & Hofmann, W. 2009, , 47, 523 → [p9]

Hitomi Collaboration et al. 2016, , 535, 117 → [p121]

Hitomi Collaboration et al. 2018a, , 70, 9 → [p122]

Hitomi Collaboration et al. 2018b, , 70, 10 → [p122]

Hudson, D. S., Mittal, R., Reiprich, T. H., et al. 2010, , 513, A37 → [p20]

Ishisaki, Y., Kelley, R. L., Awaki, H., et al. 2022, in Society of Photo-Optical Instrumentation Engineers (SPIE) Conference Series, Vol. 12181, Space Telescopes and Instrumentation 2022: Ultraviolet to Gamma Ray, ed. J.-W. A. den Herder, S. Nikzad, & K. Nakazawa, 121811S → [p121]

Jansen, F., Lumb, D., Altieri, B., et al. 2001, , 365, L1 → [p29], [p31]

Jarzebowski, T. 1991, Postepy Astronomii Krakow, 39, 53 → [p23]

Jones, C. & Forman, W. 1990, Advances in Space Research, 10, 209 → [p18]

Jones, C., Forman, W., & Fabian, A. 1992, NATO ASI Series, Kluwer Academic, Dordrecht, 366, 49 → [p24]

Kahn, F. D. 1980, Highlights of Astronomy, 5, 365 → [p5]

Kaiser, N. 1986, , 222, 323 → [p24]

Kaiser, N. 1991, Astrophysical Journal, Part 1 (ISSN 0004-637X), vol. 383, Dec. 10, 1991, p. 104-111., 383, 104 → [p25]

Kargaltsev, O., Pavlov, G. G., & Durant, M. 2012, in Astronomical Society of the Pacific Conference Series, Vol. 466, Electromagnetic Radiation from Pulsars and Magnetars, ed. W. Lewandowski, O. Maron, & J. Kijak, 167 → [p15]

Katayama, H., Hayashida, K., Takahara, F., & Fujita, Y. 2003, The Astrophysical Journal, 585, 687 → [p21]

Keisler, R., Reichardt, C. L., Aird, K. A., et al. 2011, , 743, 28 → [p17]

Kelly, B. C. 2007, , 665, 1489 → [p115]

Kiiveri, K., Gruen, D., Finoguenov, A., et al. 2021, , 502, 1494 → [p29], [p118]

Kilbourne, C., Chiao, M., Costantini, E., et al. 2024, in AAS/High Energy Astrophysics Division, Vol. 21, AAS/High Energy Astrophysics Division, 303.04 → [p121]

Klessen, R. S. & Glover, S. C. O. 2023, , 61, 65 → [p17]

Knop, R. A., Aldering, G., Amanullah, R., et al. 2003, , 598, 102 → [p17]

Koester, B. P., McKay, T. A., Annis, J., et al. 2007, , 660, 239 → [p20]

Komatsu, E., Smith, K. M., Dunkley, J., et al. 2011, , 192, 18 → [p17]

Koyama, K., Hyodo, Y., Inui, T., et al. 2007, , 59, 245 → [p97]

Lazendic, J. S., Slane, P. O., Gaensler, B. M., et al. 2004, , 602, 271 → [p9]

Leahy, D. A. & Filipović, M. D. 2022, The Astrophysical Journal, 931, 20 → [p5]

Lemaitre, G. 1931, Publications du Laboratoire d'Astronomie et de Geodesie de l'Universite de Louvain, 8, 101 → [p17]

Li, Y., Liu, S., & He, Y. 2023, , 953, 100 → [p15]

Liddle, A. R. 1999, in High Energy Physics and Cosmology, 1998 Summer School, ed. A. Masiero, G. Senjanovic, & A. Smirnov, 260 → [p17]

Liu, A., Bulbul, E., Ghirardini, V., et al. 2022, , 661, A2 → [p31], [p112], [p114], [p120]

Liu, T., Buchner, J., Nandra, K., et al. 2022, Astronomy & Astrophysics, 661, A5 → [p111]

Loewenstein, M. 2000, The Astrophysical Journal, 532, 17 → [p20]

Lovisari, L. & Maughan, B. J. 2022, in Handbook of X-ray and Gamma-ray Astrophysics, ed. C. Bambi & A. Sangangelo, 65 → [p24], [p25], [p117]

Mahdavi, A., Hoekstra, H., Babul, A., et al. 2013, , 767, 116 → [p118]

Majumdar, S. & Mohr, J. J. 2004, , 613, 41 → [p17]

Makino, N. 1996, , 48, 573 → [p18]

Manolakou, K., Horns, D., & Kirk, J. G. 2007, , 474, 689 → [p15]

Mantz, A., Allen, S. W., Ebeling, H., & Rapetti, D. 2008, , 387, 1179 → [p17]

Mantz, A., Allen, S. W., Ebeling, H., Rapetti, D., & Drlica-Wagner, A. 2010, , 406, 1773 → [p24]

Mantz, A. B., von der Linden, A., Allen, S. W., et al. 2015, , 446, 2205 → [p34]

Mastichiadis, A. 1996, , 305, L53 → [p6]

Maughan, B. J. 2007, , 668, 772 → [p28]

Maughan, B. J., Giles, P. A., Randall, S. W., Jones, C., & Forman, W. R. 2012, , 421, 1583 → [p115], [p118]

Maxted, N. I., Braiding, C., Wong, G. F., et al. 2018a, , 480, 134 → [p10], [p99], [p100]

Maxted, N. I., Filipović, M. D., Sano, H., et al. 2018b, , 866, 76 → [p9]

Merloni, A., Lamer, G., Liu, T., et al. 2024, , 682, A34 → [p31]

Merloni, A., Predehl, P., Becker, W., et al. 2012, arXiv e-prints, arXiv:1209.3114 → [p31]

Migkas, K. 2024, arXiv e-prints, arXiv:2406.01752 → [p18], [p24]

Miralda-Escudé, J. 2003, Science, 300, 1904 → [p17]

Mitsuda, K., Bautz, M., Inoue, H., et al. 2007, , 59, S1 → [p97]

Mittal, R., Hicks, A., Reiprich, T. H., & Jaritz, V. 2011, Astronomy & Astrophysics, 532, A133 → [p118]

Miyazaki, S., Komiyama, Y., Nakaya, H., et al. 2012, in Ground-based and Airborne Instrumentation for Astronomy IV, ed. I. S. McLean, S. K. Ramsay, & H. Takami, Vol. 8446, International Society for Optics and Photonics (SPIE), 84460Z → [p111]

Mohr, J. J., Evrard, A. E., Fabricant, D. G., & Geller, M. J. 1995, , 447, 8 → [p24]

Molnar, S. 2016, Frontiers in Astronomy and Space Sciences, 2, 7 → [p34]

Murata, R., Oguri, M., Nishimichi, T., et al. 2019, , 71, 107 → [p29], [p112], [p118]

Nakamura, R., Bamba, A., Dotani, T., et al. 2012, , 746, 134 → [p98], [p99]

Nakano, T. 1981, Progress of Theoretical Physics Supplement, 70, 54 → [p17]

Nalewajko, K., Yuan, Y., & Chruślińska, M. 2018, Journal of Plasma Physics, 84, 755840301 → [p15]

Nandra, K. & Pounds, K. A. 1994, , 268, 405 → [p121]

Nastase, H. & Skenderis, K. 2020, , 101, 021901 → [p17]

Natarajan, P., Williams, L. L. R., Bradač, M., et al. 2024, , 220, 19 → [pxiv]

Naumann-Godó, M., Beilicke, M., Hauser, D., Lemoine-Goumard, M., & de Naurois, M. 2008, in American Institute of Physics Conference Series, Vol. 1085, American Institute of Physics Conference Series, ed. F. A. Aharonian, W. Hofmann, & F. Rieger (AIP), 304–307 → [p97]

Nguyen-Dang, N. T., Pühlhofer, G., Sasaki, M., et al. 2023, , 679, A48 → [pv], [pvii], [pxii], [p99], [p107]

Nobukawa, K. K., Nobukawa, M., Koyama, K., et al. 2018, , 854, 87 → [p8]

Nomoto, K., Thielemann, F. K., & Yokoi, K. 1984, , 286, 644 → [p1]

Norman, M. L. 2010, arXiv e-prints, arXiv:1005.1100 → [p18]

Oguri, M. 2014, , 444, 147 → [p20], [p28], [p111], [p112], [p115], [p118], [p120]

Oguri, M., Lin, Y.-T., Lin, S.-C., et al. 2018, , 70, S20 → [p20], [p111], [p112], [p120]

Oh, S. P. 2011, Turbulence and Cosmic Rays in Clusters of Galaxies, NASA Proposal id.11-ATP11-132 → [p102]

Ota, N., Mitsuishi, I., Babazaki, Y., et al. 2020, , 72, 1 → [p117]

Ota, N., Nagai, D., & Lau, E. T. 2018, , 70, 51 → [p122]

Ota, N., Nguyen-Dang, N. T., Mitsuishi, I., et al. 2023, , 669, A110 → [pvi], [pviii], [pxii], [p34], [p64], [p115], [p117]

Pacaud, F., Pierre, M., Adami, C., et al. 2007, , 382, 1289 → [p20], [p28]

Parekh, V., van der Heyden, K., Ferrari, C., Angus, G., & Holwerda, B. 2015, , 575, A127 → [p24]

Peebles, P. J. E. 1984, , 277, 470 → [p17]

Peebles, P. J. E. 2022, Annals of Physics, 447, 169159 → [p17]

Peters, B. 1961, Il Nuovo Cimento, 22, 800 → [p13]

Planck Collaboration, Ade, P. A. R., Aghanim, N., et al. 2011, , 536, A1 → [p21]

Planck Collaboration, Ade, P. A. R., Aghanim, N., et al. 2016, , 594, A27 → [p114]

Planck Collaboration, Aghanim, N., Akrami, Y., et al. 2020, , 641, A6 → [p17]

Pohl, M., Yan, H., & Lazarian, A. 2005, , 626, L101 → [p119]

Popesso, P., Marini, I., Dolag, K., et al. 2024, arXiv e-prints, arXiv:2411.16546 → [p115]

Postolak, M. 2024, arXiv e-prints, arXiv:2404.18503 → [p17]

Pounds, K. A., Nandra, K., Stewart, G. C., George, I. M., & Fabian, A. C. 1990, , 344, 132 → [p121]

Pratt, G., Croston, J., Arnaud, M., & Böhringer, H. 2009, , 498, 361 → [p118]

Pratt, G. W., Arnaud, M., Biviano, A., et al. 2019, , 215, 25 → [p18]

Predehl, P., Andritschke, R., Arefiev, V., et al. 2021, , 647, A1 → [p30], [p31], [p112], [p120]

Principe, G., Mitchell, A. M. W., Caroff, S., et al. 2020, , 640, A76 → [p15]

Puehlhofer, G., Brun, F., Capasso, M., et al. 2015, in International Cosmic Ray Conference, Vol. 34, 34th International Cosmic Ray Conference (ICRC2015), 886 → [p15]

Ramos-Ceja, M. E., Oguri, M., Miyazaki, S., et al. 2022, , 661, A14 → [p20]

Rasia, E., Meneghetti, M., & Ettori, S. 2013, The Astronomical Review, 8, 40 → [p24]

Rees, M. J. 2000, , 333, 203 → [p17]

Reeves, J. 2003, in Astronomical Society of the Pacific Conference Series, Vol. 290, Active Galactic Nuclei: From Central Engine to Host Galaxy, ed. S. Collin, F. Combes, & I. Shlosman, 35 → [p121]

Reich, W. & Sun, X.-H. 2019, Research in Astronomy and Astrophysics, 19, 045 → [p15]

Reichert, A., Böhringer, H., Fassbender, R., & Mühlegger, M. 2011, , 535, A4 → [p118]

Reiprich, T. H., Basu, K., Ettori, S., et al. 2013, , 177, 195 → [p18], [p22], [p26]

Reiprich, T. H. & Böhringer, H. 2002, , 567, 716 → [p17], [p25]

Reynolds, S. P. 1996, , 459, L13 → [p6]

Roncarelli, M., Ettori, S., Dolag, K., et al. 2006, , 373, 1339 → [p26]

Rosati, P., Borgani, S., & Norman, C. 2002, , 40, 539 → [p24]

Rossetti, M., Gastaldello, F., Ferioli, G., et al. 2016, , 457, 4515 → [p117]

Rosswog, S. & Brüggen, M. 2007, Introduction to High-Energy Astrophysics → [p4]

Rothenflug, R., Ballet, J., Dubner, G., et al. 2004, , 425, 121 → [p97]

Rozo, E., Bartlett, J. G., Evrard, A. E., & Rykoff, E. S. 2014, , 438, 78 → [p25]

Rozo, E. & Rykoff, E. S. 2014, , 783, 80 → [p28], [p118]

Rozo, E., Wechsler, R. H., Rykoff, E. S., et al. 2010, , 708, 645 → [p24]

Ruszkowski, M. & Pfrommer, C. 2023, , 31, 4 → [p18]

Saha, P., Bharadwaj, S., Chakravorty, S., et al. 2021, , 502, 5313 → [p9]

Saji, S., Matsumoto, H., Nobukawa, M., et al. 2018, Publications of the Astronomical Society of Japan, 70, 23 → [p8], [p16], [p37], [p97]

Santos, J. S., Rosati, P., Tozzi, P., et al. 2008, , 483, 35 → [p24]

Saro, A., Bocquet, S., Rozo, E., et al. 2015, , 454, 2305 → [p29]

Schartel, N., González-Riestra, R., Kretschmar, P., et al. 2022, in Handbook of X-ray and Gamma-ray Astrophysics, ed. C. Bambi & A. Sangangelo, 114 → [p29]

Schure, K. M., Bell, A. R., O'C Drury, L., & Bykov, A. M. 2012, , 173, 491 → [p102]

Seppi, R., Comparat, J., Nandra, K., et al. 2023, , 671, A57 → [p24], [p115], [p117]

Springel, V., Frenk, C. S., & White, S. D. M. 2006, , 440, 1137 → [p17]

Springel, V. & Hernquist, L. 2003, , 339, 312 → [p17]

Starobinsky, A. A. 1998, Soviet Journal of Experimental and Theoretical Physics Letters, 68, 757 → [p17]

Sun, X.-N., Yang, R.-Z., & Liang, E.-W. 2022, , 659, A83 → [p15]

Sunyaev, R. & Zeldovich, Y. B. 1972, Astronomy and Astrophysics, Vol. 20, p. 189 (1972), 20, 189 → [p21]

Takada, M. 2010, in American Institute of Physics Conference Series, Vol. 1279, Deciphering the Ancient Universe with Gamma-ray Bursts, ed. N. Kawai & S. Nagataki (AIP), 120–127 → [p20]

Tashiro, M., Maejima, H., Toda, K., et al. 2020, in Society of Photo-Optical Instrumentation Engineers (SPIE) Conference Series, Vol. 11444, Space Telescopes and Instrumentation 2020: Ultraviolet to Gamma Ray, ed. J.-W. A. den Herder, S. Nikzad, & K. Nakazawa, 1144422 → [p106], [p121]

Tashiro, M. S. 2023, in The Sixteenth Marcel Grossmann Meeting. On Recent Developments in Theoretical and Experimental General Relativity, Astrophysics, and Relativistic Field Theories, ed. R. Ruffino & G. Vereshchagin, 95–103 → [p121]

The Pierre Auger Collaboration, Aab, A., Abreu, P., et al. 2015, arXiv e-prints, arXiv:1509.03732 → [p13]

Thielemann, F. K., Nomoto, K., & Yokoi, K. 1986, , 158, 17 → [p1]

Truemper, J. 1982, Advances in Space Research, 2, 241 → [p21]

Tsuji, N., Tanaka, T., Safi-Harb, S., et al. 2024, , 967, 138 → [p13]

Tümer, A., Wik, D. R., Gaspari, M., et al. 2022, The Astrophysical Journal, 930, 83 → [p30]

Unger, M., Farrar, G. R., & Anchordoqui, L. A. 2015, , 92, 123001 → [p13]

Vanderlinde, K., Crawford, T., De Haan, T., et al. 2010, The Astrophysical Journal, 722, 1180 → [p21]

Veronica, A., Reiprich, T. H., Pacaud, F., et al. 2024, , 681, A108 → [p31]

Veronica, A., Su, Y., Biffi, V., et al. 2022, , 661, A46 → [p31]

Vikhlinin, A., Burenin, R. A., Ebeling, H., et al. 2009, , 692, 1033 → [p24], [p28]

Vikhlinin, A., Voevodkin, A., Mullis, C. R., et al. 2003, , 590, 15 → [p17]

Vink, J. 2012, , 20, 49 → [p3], [p4], [p5]

Vink, J. 2020, Physics and Evolution of Supernova Remnants → [p1], [p3]

Voit, G. M. 2005, Reviews of Modern Physics, 77, 207 → [p18], [p24]

von der Linden, A., Allen, M. T., Applegate, D. E., et al. 2014, , 439, 2 → [p34]

Weiler, K. W. & Sramek, R. A. 1988, , 26, 295 → [p1]

Weisskopf, M. C., Brinkman, B., Canizares, C., et al. 2002, , 114, 1 → [p119]

Weisskopf, M. C., Tananbaum, H. D., Van Speybroeck, L. P., & O'Dell, S. L. 2000, in Society of Photo-Optical Instrumentation Engineers (SPIE) Conference Series, Vol. 4012, X-Ray Optics, Instruments, and Missions III, ed. J. E. Truemper & B. Aschenbach, 2–16 → [p31], [p106]

White, S. D. M. & Frenk, C. S. 1991, , 379, 52 → [p17]

Woosley, S. & Janka, T. 2005, Nature Physics, 1, 147 → [p1]

XRISM Collaboration. 2025, arXiv e-prints, arXiv:2501.05514 → [p122]

XRISM Science Team. 2020, arXiv e-prints, arXiv:2003.04962 → [p121], [p122]

Xu, W., Ramos-Ceja, M. E., Pacaud, F., Reiprich, T. H., & Erben, T. 2018, , 619, A162 → [p20]

Yamazaki, R., Kohri, K., Bamba, A., et al. 2006, , 371, 1975 → [p15]

York, D. G., Adelman, J., Anderson, John E., J., et al. 2000, , 120, 1579 → [p20]

Zacharias, M. 2014, , 443, 3001 → [p15]

Zeng, H., Xin, Y., Zhang, S., & Liu, S. 2021, , 910, 78 → [p15]

Zhang, Y. Y., Andernach, H., Caretta, C. A., et al. 2011, , 526, A105 → [p21]

Zhang, Y.-Y., Finoguenov, A., Böhringer, H., et al. 2008, Astronomy & Astrophysics, 482, 451 → [p118]

Zwicky, F. 1937, , 86, 217 → [p20]

Acknowledgements

This PhD has been an exciting yet challenging journey, which would not have been possible without the guidance, encouragement, and support of many individuals. I would like to express my deepest gratitude to those who were always there for me and helped me complete this work.

First and foremost, I would like to thank Dr. Gerd Pühlhofer and Prof. Andrea Santangelo for giving me the incredible opportunity to conduct my doctoral research at IAAT on the topic of supernova remnants. Gerd, I am especially grateful for your patience, thoroughness, and scientific inspiration. Thank you for also taking care of other aspects of my PhD life, such as ensuring my visa was granted on time, helping me to get my early COVID vaccination, or encouraging me to take holidays. I feel lucky to have had you as my supervisor. Andrea, thank you for your scientific guidance and for the fascinating cultural discussions, I have learned so much from you in both areas. I also sincerely thank Victoria for forwarding my interest to Andrea and Gerd and for your continuous support afterward.

I am grateful to Gerd and to professor Klaus Werner for reviewing my thesis and preparing the reports. I am grateful to the doctoral committee: professor Lachenmaier, professor Werner, professor Wharam, and Gerd for the valuable questions and comments.

I would also like to thank the senior scientists at IAAT who answered many of my questions and made IAAT a friendly, vibrant workplace: Dennys, Victor, Ji Long, and Lorenzo. Chris, thank you for always welcoming my questions and helping me with the paperwork. Frau Lauer, I deeply appreciate your swift and effective secretary work, which made our lives so much easier.

My gratitude extends to the teachers and colleagues outside IAAT who collaborated with me during the preparation of the part of the thesis on galaxy clusters. Naomi-san, you have been an incredible source of inspiration, and I am grateful for the opportunity to join the eROSITA-HSC projects. Your scientific mentorship and cultural discussions have been invaluable to me. Professor Reiprich, thank you for allowing me to be part of the eeHIFLUGCS team and for your insightful advice. I truly enjoyed the dynamic atmosphere of your dark energy research group. Thank you, Florian, Kostas, Lorenzo, and Gerrit, for sharing your wisdom and for encouraging me. A special thanks to Miriam, who has always been an incredible help, whether in scientific matters or life decisions.

I am grateful to thầy Tân and anh Quang for introducing me to this exciting scientific field. Anh Điệp, thank you for giving me my first astronomy lectures and for your constant support.

Thao and Florian, you have been my moral support, always listening to my complaints about

literally anything and making sure I was well-fed so I wouldn't flee back to Vietnam due to food cravings. I am also endlessly thankful to my friends from Bonn, Yvonne and Ji, who made this journey much more bearable, not just through scientific discussions but also through our extensive cat-related conversations, game nights and trips. My Mexican friends, Luis and Iveth, thank you for always brightening up my mood instantly. Ngọc and Ngân, starting this astronomy journey together with you gave me strength along the way. Chị Thanh and Đạt, thank you for your warm encouragement. A huge thank you to Angie and the students in the Ota Lab (Nara Women's University) for their motivation and support during my visits to Bonn, Germany, and Nara, Japan. Anuvind, thank you for making me world-class cocktails in Bonn and for constantly sending me PhD memes in my last PhD year, something I did not know that I really needed. Hannah, thank you for sending cats videos regularly. Thank you, Gleb for showing me around Munich when I was there for a conference. Thank you, Huong, Vy, Tuấn, Vân, Thuong, for your love from Vietnam.

I express my heartfelt thanks to the bachelor's, master's, and PhD students at IAAT. Although our interactions were limited due to my peculiar living situation and also thanks to the *amazing* Deutsche Bahn, I truly enjoyed our time together. Special thanks to Charles for the metal music recommendations and for your great support toward the end of my PhD. Heiko, thank you for our non-Pythonic conversations and for never correcting my German (it is *unglaubbar*). Inga, I appreciate your hospitality whenever my last train home was canceled, your introduction to my all-time favorite honey cereal brand, and, of course, for correcting my German. Fabian, thanks for the drinks and stories we shared at the gamma-ray conference. Camille, I still cherish your crepe recipe. Robbie, I appreciate you recording my voice for our animation project and giving me a taste of celebrity life. Aafia, thank you for being nice to me in our Among Us games. Martina, Alberta, Enza, and Stefanie, thank you for sharing the ground-floor kitchen with me. Yujia (and many others), thank you for letting me practice my broken Chinese with you. Miltos and Andreas, I appreciate sharing an office with you. Thank you, Aditya for our productive discussions on X-ray data analysis. Marvin, thanks for our interesting talks about Japan. Bastian, thanks for helping me with my defense preparation. I thank Paul, Christian, Wilhelmina, Moritz, Daniela, Xianqi, Antonio, Miriam, and many others for our lunch break chats. Abarna and Diego, you were my office mates before COVID-19. I never saw you again after the pandemic, but I hope you are doing well.

During the post-COVID phase of my PhD, I also had the chance to meet with many bright and friendly young scientists from other institutes. Thank you, Fabian, Xueying, Alena, Emre, Jonathan and Federico for our scientific and personal discussions, they meant a lot to me.

I thank my family for giving me the challenges that forge me into the person I am today.

I also want to express my thanks to the Stamer family for granting me the trust and for giving me the biggest support in my life. Without you, I would not be able to write this thesis. Thank you for making Germany my new home.

Figure 5.1: Various distributions of my cats. *Upper left:* symmetric; *upper right:* parallel; *lower left:* quantized; *lower right:* occupying the same energy level.

Finally, my biggest thanks go to my husband and my cats. I came to Germany for a degree, but I gained something even more valuable: a family. Baby, thank you for letting me pull the *"I am writing my thesis"* card to get whatever I want, you are simply the best, and I don't even need a reference to back that statement up. Thank you for taking care of me and letting me turn off my brain whenever we travel together. And mega thanks to Lumi and Simba (Fig. 5.1) for being the weirdest, craziest, fluffiest, hungriest furballs who fill my heart with love.

Có công mài sắt, có ngày nên kim.[1]

– Vietnamese idiom

I began my academic journey studying high school physics education in Vietnam. After a few unexpected, life-changing events, I now find myself writing a PhD thesis in Astrophysics. To me, this is quite a leap. This journey has taught me the power of perseverance and education, and I hope it serves as a source of inspiration for young students from remote areas in Vietnam, like myself, to pursue their dreams without giving up.

I would like to conclude this thesis with a quotation from Bác Pierre Darriulat[2], from a presentation that he gave on cosmic rays in Hồ Chí Minh city in 2011. During the early stages of my astronomy studies, I had the privilege of meeting and talking with Bác Pierre, along with a few other Vietnamese researchers in the field. These conversations gave me the confidence to take my first steps into the world of astrophysics.

"For now 50 years astrophysics has made fascinating and spectacular progress
The whole of physics is invited to the banquet:
particle, nuclear, atomic, molecular, plasma, solid state
The whole of physics and also the whole world
Only a few privileged countries can afford to launch space missions
or to build giant telescopes
But any country can, in principle, access the data
This is an opportunity that developing countries should not miss
The sky belongs to all of us
We are all made of the same star dust"

[1]This directly translates to: "With effort in grinding iron, one day it will become a needle".
[2]Department of Astrophysics, Vietnam National Space Center, Hanoi, Vietnam.